6-23-2015

Spectroscopic and Computational Studies of Molybdenum Enzymes and Models

Chao Dong

Chao Dong
Candidate

Chemistry and Chemical Biology
Department

This dissertation is approved, and it is acceptable in quality and form for publication:

Approved by the Dissertation Committee:

Dr. Martin L. Kirk, Chairperson

Dr. Hua Guo

Dr. Wei Wang

Dr. Changjian Feng

SPECTROSCOPIC AND COMPUTATIONAL STUDIES OF MOLYBDENUM ENZYMES AND MODELS

by

CHAO DONG

B.S. Chemistry, Fuyang Normal College 2004
M.S. Chemistry, University of Science & Technology of China 2007

DISSERTATION

Submitted in Partial Fulfillment of the
Requirements for the Degree of

Doctor of Philosophy
Chemistry

The University of New Mexico
Albuquerque, New Mexico

May, 2015

DEDICATION

To my parents, Wenping Dong and Surong Yang,
and my brother and my sister.

ACKNOWLEDGEMENTS

I would like to thank my graduate advisor Dr. Martin L. Kirk for support and mentorship. I have learned how to be an efficient, independent and professional scientific researcher. He always teaches me with patience and professionalism. The valuable experience I gained from him will enlighten me in my future career.

I would also like to thank former and current graduate students and postdoctoral fellows in Prof. Kirk's research group: Dr. Regina Peter Mtei, Dr. Joseph Sempombe, Dr. Diana Habel Rodriguez, Benjamin W. Stein, Dominic Kofl Kersi, Ju Chen, Ranjana Dangi, Khadanand Kc, Amrit Pokhrel, Dr. Jing Yang, and Dr. Logan J. Giles. Thank you guys for encouragement, suggestions and assistance.

I would also like to thank Dr. Silke Leimkühler from the University of Potsdam for providing xanthine dehydrogenase enzymes and Dr. H. Sugimoto from Osaka University for providing DMSO reductase model compounds. Additional thanks to Dr. Hua Guo, Dr. Wei Wang and Dr. Changjian Feng who are my committee members and provided advice on the completion of my doctoral thesis.

SPECTROSCOPIC AND COMPUTATIONAL STUDIES OF MOLYBDENUM ENZYMES AND MODELS

by

Chao Dong

B.S. Chemistry, Fuyang Normal College, 2004
M.S. Chemistry, University of Science &Technology of China, 2007
Ph.D. Chemistry, University of New Mexico, 2015

ABSTRACT

In this dissertation spectroscopic methods such as electronic absorption (EAS), resonance Raman (rRaman), electron paramagnetic resonance (EPR), and MCD spectroscopies have been used in combination with DFT calculations for the interpretation of experimental results. These methods have been used to investigate the molybdenum coordination environment in enzymes and model complexes.

Xanthine oxidase (XO), one of the canonical molybdenum enzyme families, hydroxylizes heterocyclic substrates by inserting an oxygen atom from molybdenum-activated water into a substrate C-H bond. This generates reducing equivalents that pass through two iron sulfur clusters and then to FAD, where oxidation of the FAD takes place. In this catalytic cycle there are ongoing arguments about whether a proton or hydride is transferred to the terminal sulfido during the reductive half reaction. Additionally, in the reductive half reaction the pyranotperin dithiolene cofactor (PDT) is proposed to modulate the transfer of

electron out of molybdenum center to the proximal iron sulfur cluster. Due to the interference from the Fe-S and FAD chromophores, the observance of vibrational modes inherent to the PDT-Mo has not been achieved. Such evidence would support the involvement of the PDT as an integral component of the enzyme electron transfer regeneration pathway. Finally, no spectroscopic data has been obtained that directly probes amino acids around the active site of XO, although kinetic data are reported to show their role in substrate orientation and lowering activation energy of transition state. Here, the observation of an intense metal to ligand charge transfer (MLCT) band from the reduced molybdenum enzyme/product complex, combined to DFT calculations of the transition state, are presented and discussed. The results indicate that the PDT is intimately involved in one-electron transfer, and the Mo-O-$C_{product}$ linkage in two-electron transfer to oxidize substrate and reduce the molybdenum center. Reduced XO-thione-violapteirn complexes shift the MLCT band to the near-infrared region of the spectrum, and this removes the interference from FAD and FeS clusters, resulting in the appearance of high quality resonance Raman spectra that reveal the low frequency vibrational region. Heavy atom substitution on these new substrates affects both the electronic absorption and resonance Raman spectra. Resonance Raman spectra of variants that are anticipated to affect the PDT through hydrogen bonding show small perturbations on the Raman frequencies of PDT-Mo vibrational modes. EPR studies on “aldehyde inhibited” XO, a Mo(V) species formed during XO catalysis, display second coordination sphere effects from amino acids that interact with the active site of XO. The new hybrid

substrates, incuding analogs of the drug FYX051(C), display an intense MLCT band after the enzyme reacting with substrates. This potentially provides an opportunity to probe the effects of second coordination sphere perturbations in the substrate-binding pocket using resonance Raman spectroscopy.

Arsenite Oxidase, a member of the dimethyl sulfoxide reductase (DMSOr) enzyme family, differs from other DMSOR family members. The Mo site in arsenite oxidase is not coordinated by any amino acid residues. This enzyme facilitates the transfer of an oxygen atom from water to the arsenite substrate. Electronic structure studies of dioxomolybdenum (VI) complexes with ene-1, 2-dithiolate ligands have been performed using a combination of electronic absorption and resonance Raman spectroscopies, and bonding calculations. The similar frequencies of molybdenum–sulfur vibrational modes and the similar origin of the lowest energy ligand to metal charge transfer band indicate these complexes possess the similar catalytic activities, and this is supported by their oxygen atom transfer (OAT) rates.

The active site of sulfite oxidase (SO) catalyzes the oxidation of sulfite to sulfate through oxygen atom transfer for detoxifying the excessive sulfite or in the final step of degrading the sulfur containing amino acids. A conserved cysteine thiolate ligand is proposed to modulate the reduction potential of redox orbital by control the covalency of Mo-S(cysteine) bond through the O_{oxo}-Mo-S-C dihedral angle. An $\sim 90^{\circ}$ O_{oxo}-Mo-S-C dihedral angle results in poor Mo(d_{X2-Y2})-S covalency, while an ~ 0 or 180° O_{oxo}-Mo-S-C dihedral angle leads to appreciable

Mo(d_{X2-Y2})-S orbital mixing. Our spectroscopic and computational studies of molybdenum model complexes with chalcogen ligands not only confirms prior assignments of the S → Mo charge transfer occuring at 22500cm^{-1} in chicken sulfite oxidase (CSO) enzyme, but also supports a hypothesis that the O_{oxo}-Mo-S-C varies between ~90° and 65° in selenocysteine substituted Human sulfite oxidase (HSO) enzyme. EPR and MCD spectra for small molecule model complexes that mimic this interaction if SO family enzymes is discussed.

Table of Contents

List of Figures

List of Tables

Chapter 1 Physical Methods

1.1 Transition Metal Complexes And Spectroscopic Methods

Metalloproteins play important roles in biological systems. Metalloproteins perform broad functions such as molecular transport (iron-contained myoglobin-hemerythrin O_2 carrier),[1 2-4] structure support (zinc fingers)[5] and electron transfer (iron-sulfur clusters and cytochromes)[6,7] and catalysis of a chemical reaction (Molybdenum enzymes, Copper, Iron and Manganese oxidase enzymes etc. al).[8-10 11,12] Metalloenzymes that containing transition metal are an important subclass of metalloproteins, and these enzymes oxidize or reduce substrates at their active sites in order to transform substrate into products.

Determining how these metalloenzymes function is a challenging task. Understanding the catalytic mechanism can give guidance in their potential applications in chemical engineering, biology and pharmacy. Knowledge of gene sequences and X-ray crystal structures have opened the door for researchers to understand the role of the transition metal coordination sphere at the active site.[13,14 15-17] Generally the transition metal is coordinated with O, N, and S donors from amino residues located at the active site. The active site is poised for high reactivity due to the electronic structure and the nature of metal-ligand bonds. Compared with typical covalent bonds in organic chemistry, these metal-ligand bonds are relatively easily broken and re-formed to create low energy

pathways for chemical reactions. Most of transition metals can display more than one oxidation state, and are said to be redox active. The potential of $1e^-/2e^-$ reactions is so sensitive to the nature of the ligands and the coordination geometry that the ligands can effectively modulate the reactivity. Also, different spin states can lead to different reactivities. Above all, the transition metal coordination sphere possesses partially occupied d-shells and variable strength of metal-ligand bonds that result in a variety of spectroscopic properties. Synthetic small molecule transition metal analog complexes with geometries and reactivities that mimic the active sites of metalloenzymes have been developed. Spectroscopic methods such as electronic absorption (EAS), Infrared (IR),[18] resonance Raman (rRaman),[19,20] electron paramagnetic resonance (EPR),[21 22,23] x-ray absorption (XAS)[24-26] and magnetic circular dichroism (MCD)[27 28,29] are employed to gain sight into the relationships between function, electronic structure and geometry of enzyme active sites and analog model compounds.[1,30-32 33]

This chapter will introduce the basic principles of important spectroscopic and magnetic methods that are mentioned in the following chapters of the dissertation. Based on Einstein's theory, light possesses a quantized energy for a photon and is considered as a radiant electromagnetic wave with an oscillating electric and magnetic field. When light is absorbed by a molecule, transitions exist between its quantized electronic, vibrational and rotational energy states as the absorbed photons satisfy the relationship $\Delta E=hc/l$ (h is Planck's constant) shown in Figure 1.1. A molecular spectrum is characterized by the intensity of

electromagnetic incident light emitted or absorbed by molecules as a function of frequency, wavenumber, or some related quantity.

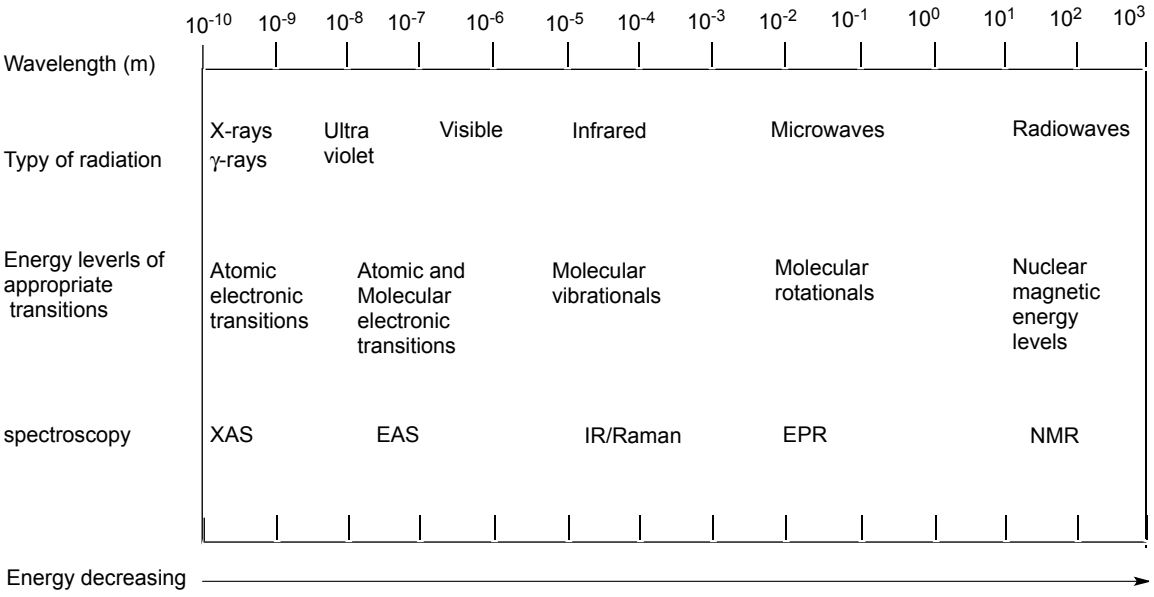

Figure 1.1 Regions of electromagnetic spectrum.

1.2 Electronic Absorption Spectroscopy (EAS)

1.2.1 The Beer-Lambert Absorption Law, Transition Diploe Moment and Electronic Transition Moment Strength

In equation 1.1 the Lambert-Beer absorption law shows the percent of transmittance (I_0: intensity of incident light; I: intensity after the light passes through the sample). The absorption intensity is defined as absorbance (A) from the height of an absorption peak in equation 1.2, which is related to the molar extinction coefficient (ε: L Mol $^{-1}$ cm $^{-1}$), optical path length of the sample (b: usually 1 cm) and the concentration of the sample (c).

$$\%T = \frac{I}{I_0}100\% \quad \text{.....(1.1)}$$

$$\log_0(\frac{I}{I_0}) = A = \varepsilon bc \quad \text{.....(1.2)}$$

$$f = 4.32\times10^{-9}\int \varepsilon(\bar{\nu})d\bar{\nu} \\ = 9.6\times10^{-9}\times\varepsilon(\bar{\nu})\times\Delta\bar{\nu} \quad \text{.....(1.3)}$$

The molar extinction coefficient, ε, is an intrinsic property of the species in the sample solution, and it is proportional to the square of transition dipole moment integral describing a transition between two electronic energy states in the molecule, and can be used to calculate the oscillator strength (f) in equation 1.3 ($\Delta\bar{\nu}$ is the full width at half maximum in wavenumbers, where the molar extinction coefficient has a value of half its maximum ε_{max}). Light incident on the sample induces a transition dipole moment, which is the electric dipole moment that is associated with the electronic transition between two states in the molecule.

Two principles are often used in the analysis of electronic absorption spectra. The first is the Born Oppenheimer approximation, where the electronic and nuclear (vibrational and rotational) components of the wave functions in a molecule are treated separately, since there is a large mass ratio between the nucleus and the electron as shown in equation 1.4.

$$\Psi_{total} = \psi_{electronic}\times\psi_{nuclear} \quad \text{.....(1.4)}$$

$$E_{total} = E_{electronic} + E_{vibrational} + E_{rotational} \quad \text{.....(1.5)}$$

$$E_{electronic} \approx 1000 * E_{vibrational} \approx 1000000 * E_{rotational} \quad \text{.....(1.6)}$$

$$E_{total} = E_{electronic} + E_{vibrational} \quad \text{.....(1.7)}$$

From this approximation the electronic, vibrational and rotational energies can be considered independent each other (equation 1.5). Due to the large-scale order differences of the energies in equation 1.6, the Born-Oppenheimer approximation can be approximated as in equation 1.7. The Franck-Condon Principle states that electronic transitions take place on a very short time scale (about 10^{-15} s), so that during an electronic transition, changing from a vibrational energy level in the ground state to another vibrational level in an excited state will be more probable if the two vibrational wave functions possess significant overlap (Figure 1.2 a). The transition dipole strength directly relates the integral of overlap of ground state and excited state wave functions in equation 1.8 (μ is the transition dipole moment operator). Considering the Born Oppenheimer approximation, equation 1.8 can be rewritten as in equation 1.9, in which the first integral belongs to the electronic transition moment and the second integral is for the vibrational overlap as shown in Figure 1.2.[34] In order for an allowed transition to occur, equation 1.10 is required not to equal to zero.

$$R = \int \psi_b \hat{\mu} \psi_a d\tau = \langle \psi_b | \hat{\mu} | \psi_a \rangle \quad \text{.....(1.8)}$$

$$\begin{aligned} R &= \langle \psi_{el}^g \psi_{vib}^g | \hat{\mu} | \psi_{el}^e \psi_{vib}^e \rangle \\ &= \int \psi_{el}^g \psi_{el}^e dr \int \psi_{vib}^g \psi_{vib}^e dR \end{aligned} \quad \text{.....(1.9)}$$

$$f \propto R^2 \propto \left(\int \psi_{el}^g \psi_{el}^e dr \right)^2 \left(\int \psi_{vib}^g \psi_{vib}^e dR \right)^2 \quad \text{.....(1.10)}$$

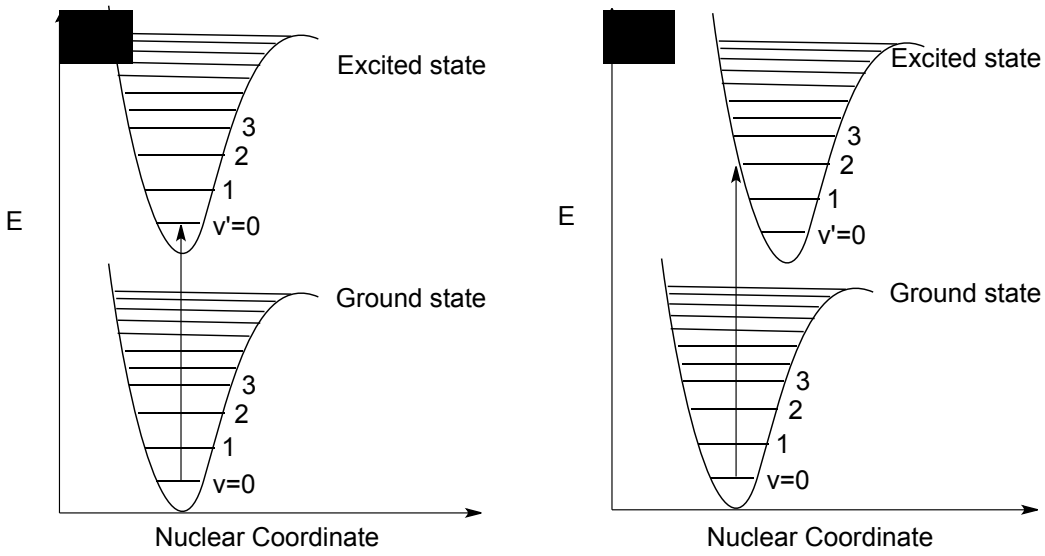

Figure 1.2 Scheme of a (without) and b (with) a nuclear distortion between potential energy surfaces.

1.2.2 Selection Rules

The selection rules for a nonzero electronic transition moment integral in equations 1.9 and 1.10 derive from the properties of orbital and electron spin wave functions, respectively.

<1> spin selection rule $\Delta S=0$

This requires that during an electron transition the spin multiplicity remains the same $\Delta S=0$ in the ground and excited state. This means that a transition from a singlet to a triplet is spin-forbidden and not allowed.

Spin-orbit coupling can relax the spin selection rule by coupling the orbital angular momentum and spin angular momentum. For example, 4d and 5d heavy metals with large spin-orbit coupling constants can cause a relaxing of the spin selection rule. However, the intensity of a formally spin-forbidden transition is

much weaker than a spin allowed transitions (Table 1.1).

<2> Laporte (orbital) selection rule ∆l=±1

The Laporte selection rule is important for molecules with inversion centers. The requirement that the parity must change during an electronic transition from ground state a to excited state b is shown in equation 1.11. The totally symmetric representation can only be obtained from a direct product of the type of Γ_i^2 not from $\Gamma_i \times \Gamma_j$ (*i≠j*). Hence, the transition dipole moment is zero unless the product of the representation of the ground state and excited state possesses a representation of the dipole moments operator μ (i.e. must transform as x, y, z). For centrosymmetric molecules the g (gerade) to u (ungerade) transition is allowed, and vice versa. The g to g and u to u transitions are said to be Laporte forbidden. Since all d orbitals are of g symmetry, the d-d transitions in transition metal complex are formally Laporte forbidden.

$$\Gamma(\psi_a) \times \Gamma(\mu) \Gamma(\psi_b) \subset A_1(g) \quad \text{.....(1.11)}$$

$$\Gamma(\psi_a) \times \Gamma(\mu) \Gamma(\psi_b) \times \Gamma(\psi^e_{vib}) \subset A_1(g) \quad \text{.....(1.12)}$$

The Laporte selection rule can be relaxed by the static or dynamic removal of perfect centrosymmetric symmetry. The electronic-vibrational coupling can also relax the parity selection rule through asymmetric vibrations (see the equation 1.9 and Figure 2b). Since all vibrational ground states are totally symmetric, , for the integral not to be zero the direct product of ground state and excited electronic wave functions with the dipole moment operator μ must have the same

representation of one of the asymmetric vibrations of the molecule as shown in equation 1.12.

1.2.3 Band Intensities

Table 1.1 Intensities of absorption bands in 3d metal complexes.[35]

Molecular extinction coefficient ε_{max} ($Lmol^{-1}\,cm^{-1}$)	Types of transition
<1	Spin forbidden and Laporte forbidden
20-100	Spin allowed and Laporte forbidden
Ca 500	Spin forbidden and Laporte allowed
103-5x104	Spin allowed and Laporte allowed

Table 1.1 shows approximate extinction coefficients for different types of electronic transitions. In centrosymmetric molecules the asymmetric vibrations from electronic-vibrational coupling allow the mixture d orbital wave functions with p orbitals on the metal or those associated with the ligands. In this way the Laporte selection rule is relaxed. In non-centrosymmetric molecules the mixing the d orbitals with p orbitals can occur by symmetry. The greater the mixing between d orbitals and p orbitals, the more the Lapore selection rules are relaxed and the intensities of the d-d transitions will be increased.

1.2.4 Band Shape

Broad bands are often observed in electronic absorption spectra. Vibronic

coupling, distortion to lower symmetry, the Jahn-Teller effect, spin-orbit coupling, and solvent effects can all contribute to the broadness of an absorption band. Generally, the width of a given band is determined by one or more of these factors.[35]

1.2.5 Effect of Temperature on the Absorption Spectrum

Broad bands with tails are almost always seen in an electronic absorption spectrum at room temperature. When the temperature decreases, band tails will tend to disappear and the band often become sharper and more resolved. In addition the molar extinction coefficient of the 0-0' line is increased since the population of higher vibrational levels of the ground state are decreased with a concomitant increased population of v =0 (Figure 1.2b).[36] The total oscillator strength is unchanged. For vibronically allowed transitions, since the 0-0' is forbidden, an increase in the population of 0 can't make up for the loss of intensity. Thus, the oscillator strength of a vibrationally allowed (Lapporte forbidden) band decreases with decreasing temperature.

1.2.6 Types of Electronic Transitions in Metal Complexes

In electronic absorption spectroscopy, there are three types of transitions that are usually encountered as shown in Figure 1.3.

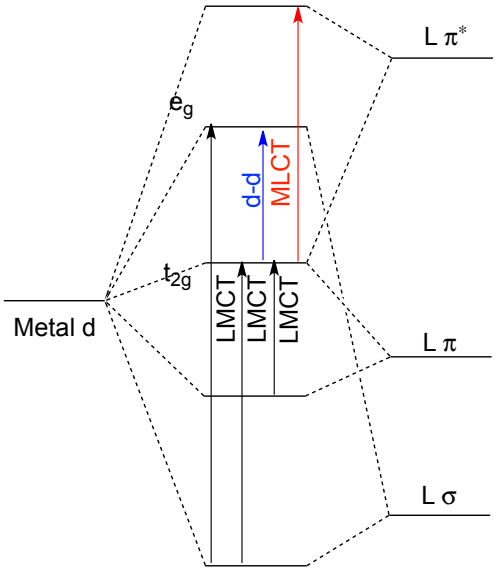

Figure 1.3 Diagram of various transitions in transition metal complexes with octahedral geometry. (d-d: ligand field transition between d orbitals of a transition metal; LMCT: ligand to metal charge transfer; MLCT: metal to ligand charge transfer)

Since the intensities of absorption bands in an electronic absorption spectrum were discussed above, we discuss here the transition energies of various transitions. Usually the d-d transitions occur at lower energies compared with MLCT and LMCT transitions. Analysis of the d-d bands in transition metal complexes can yield the ligand filed splitting parameter Dq (octahedral complex: Δ=10Dq). A partial spectrochemical series follows the order: $I^-<Br^-<S^{2-}<SCN^-<Cl^-<SCN^-<NO_3^-<F^-<OH^-<H_2O<SCN^-<NCS^-<NH_3<$bipy$< NO_2^-< CN^-<$CO and there is an increase in Δ as we move from left to right in this series.[37] This order reflects the bonding properties of the metal and the ligand: weak σ-donor, strong π donor< moderate σ-donor<strong σ-donor, π acceptor. For a given ligand at parity of the metal, there is an increase in Δ as the oxidation state increases and as we go from 3d to 4d and 5d. Partially transferring an electron from the ligand

to the metal can be regarded as the ligand being oxidized and the metal being reduced.[38] For a given ligand we observe for MLCT transitions: (i) an increase in energy as 3d<4d<5d and (ii) a decrease in energy as the metal oxidation state increases. The same optical electronegativity arguments can be used to interpret MLCT transitions. It is easily to infer the relative redox properties of metal and ligand based on the transition energy of LMCT and MLCT transitions.

1.3 Raman Spectroscopy

Raman spectroscopy is a type of the vibrational spectroscopy that is used to probe the metal ion environment in metalloenzymes and their small molecule analogs. Resonance Raman spectroscopy is well-suited for studies of the transition metal environment in proteins due to resonance enhancement of Raman intensity when optically pumping into intense LMCT and MLCT electronic absorption bands.

1.3.1 Origin of Raman

When laser light impinges on a sample two types of scattered lights are obtained: Rayleigh light with no energy loss (elastic collision) and Raman scattering with $\nu_0 \pm \nu_m$ after an inelastic collision (ν_0 is frequency of the incident laser line; ν_m is vibrational frequency of a molecule) as shown in Figure 1.4. Only about 1 in 10 million photons that hit a sample are scattered by inelastically by Stokes or anti-Stokes processes. As a result, under non-resonant conditions, Raman scattering is an inefficient process.

Figure 1.4 Mechanism of Raman.

The oscillating electric field of electromagnetic wave (laser line) (equation 1.11) can create an induced dipole moment (equation 1.12) by distorting the electron cloud of a molecule. The distortion of the electron cloud is expressed as the polarizability α. The nuclear displacement q is defined in equation 1.13 with respect to a vibrating with a frequency ν_m. If we take a diatomic molecule as example we have just with one degree of vibrational freedom, and α is simply expressed as in equation 1.14. Combining equation 1.12 with equations 1.13 and 1.14, we obtain equation 1.15. The first tem represents Rayleigh scattering with shifting. The change in polarizability is described by the polarizability derivative $(\frac{\partial\alpha}{\partial q})_0 \neq 0$.[39] The n_0+n_m from second item corresponds to a thermally populated upper vibrational level that transfers energy to the incident light. This is called anti-Stokes scattering. The Stokes scattering n_0-n_m results in a shift to lower frequency

$$P = E_0 \cos 2\pi\nu_0 t + \frac{1}{2}(\frac{\partial\alpha}{\partial q})_0 q_0 E_0[\cos\{2\pi(\nu_0+\nu_m)t + \cos\{2\pi(\nu_0+\nu_m)t\}] \quad \text{.....(1.15)}$$

compared with the incident light. Based on the Maxwell-Boltzmann distribution law the population of molecules at n=0 much larger than at n=1 (Figure 1.5). Therefore, the Stokes lines are more intense than anti-Stokes lines. The Raman spectrum is plotted as a function of intensity *vs* frequency difference between the Stokes scattering and the incident light. The Raman shift is expressed in units of wavenumbers, cm^{-1}.

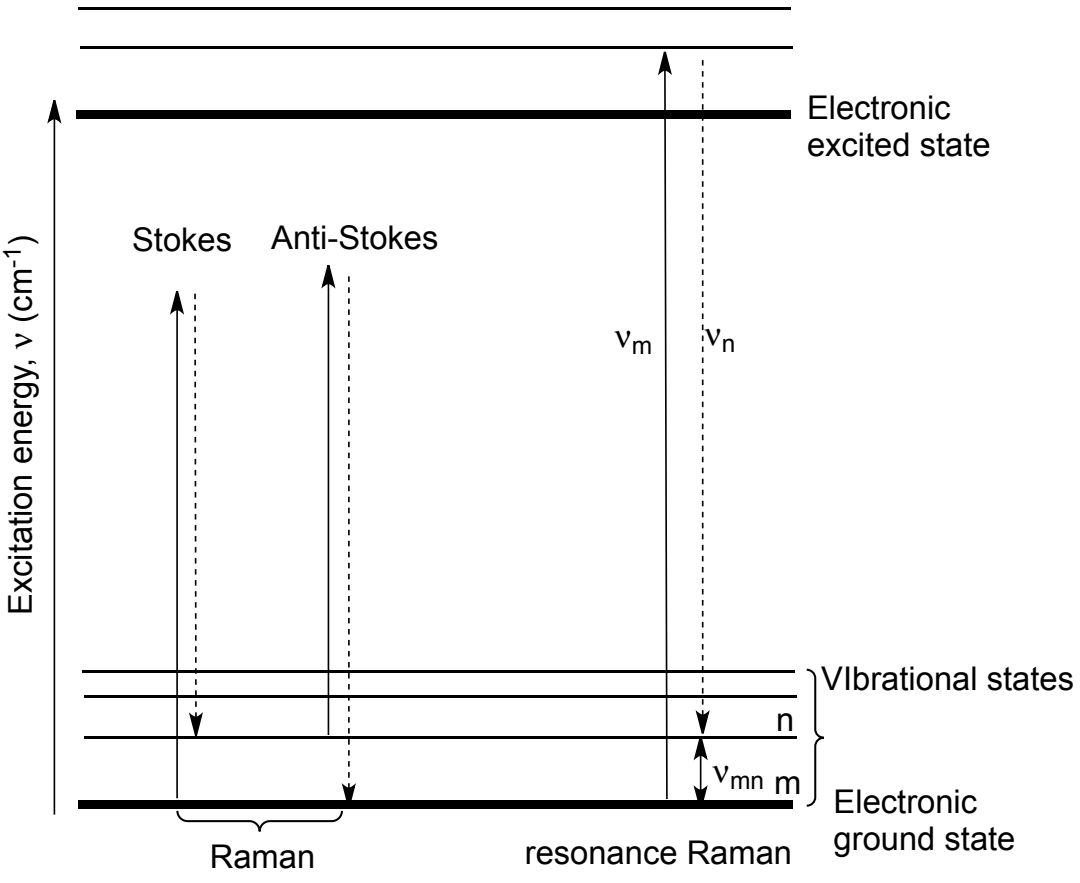

Figure 1.5 Energy level diagram for Raman and resonance Raman spectroscopy.

1.3.2 Intensity of Raman Spectra and Symmetry Selection Rules [39 40]

The intensity for normal Raman scattering is given in equation 1.16, where I_0 is the intensity of the laser line, n is the frequency of scattered radiation, and C is

the concentration of sample.

$$I \propto const.I_0 \nu^4 C \quad \text{.....(1.16)}$$

$$I_{ij} = \int \psi_0(Q_a)\alpha_{ij}\psi_1(Q_a)dQ_a \quad \text{.....(1.17)}$$

Equation 1.12 can be recast in the form of $\begin{bmatrix} P_x \\ P_y \\ P_z \end{bmatrix} = \begin{bmatrix} \alpha_{xx} & \alpha_{xy} & \alpha_{xz} \\ \alpha_{yx} & \alpha_{yy} & \alpha_{yz} \\ \alpha_{zx} & \alpha_{zy} & \alpha_{zz} \end{bmatrix} \begin{bmatrix} E_x \\ E_y \\ E_z \end{bmatrix}$. The change in the orientation, size and shape of the polarizability ellipsoid can lead to a Raman-active normal vibrational mode. In complex and/or large molecules that possess symmetry, the Raman selection rule is given in equation 1.17 where Q_a is normal coordinate, ψ is the vibrational wave function, and α_{ij} (*I, j* =x, y, z) is the component of polarizability tensor. In order for a vibration to be Raman active, one component of I_{ij} is required to be non-zero. Thus, in order for a vibration to be Raman active, the vibration must transform the same as the polarizabilty tensor in the point group of the molecule.

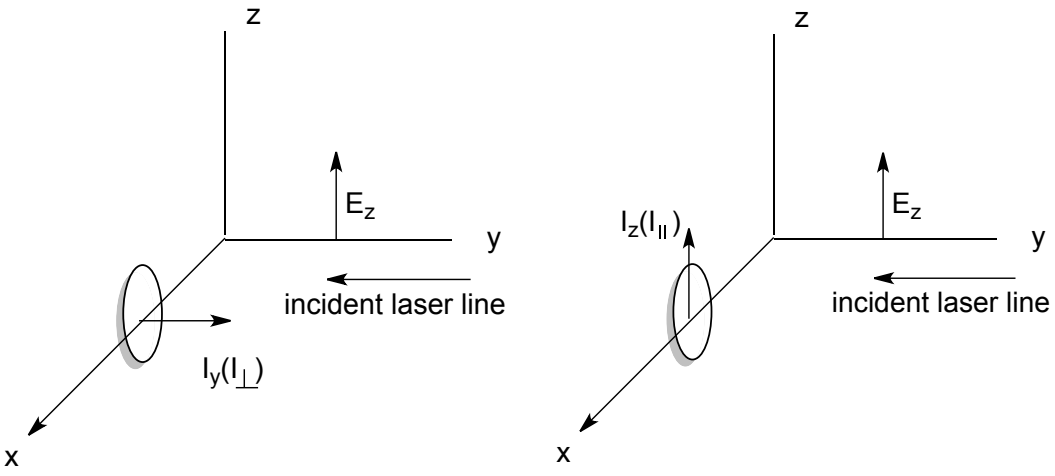

Figure 1.6 Determination of depolarization ratios in a 90º scattering geometry.

1.3.3 Depolarization Ratios

Raman depolarization ratios can provide additional information about the symmetry of a vibration and are helpful for making accurate band assignments. In Figure 1.6 a polarization analyzer is used to obtain the y or z polarization of the scattered light. Equation 1.18 defines the depolarization ratio. When its value is in the range of 0≤ ρ <3/4, this indicates a total symmetric vibrations. Ratios in the range ρ =3/4 define depolarized bands from non-totally symmetric vibrations. In short, as an additional parameter in Raman spectroscopy, the polarization information can help determine the symmetry of vibrations in a molecule and also help to interpret their electronic structure of materials.[40]

$$\rho = \frac{I_{\parallel}}{I_{\perp}} \quad \text{.....(1.16)}$$

1.3.4 Resonance Raman Spectroscopy [39, 42]

When the exciting laser line is under the envelop of an electronic absorption band, the intensity of Raman scattering is enhanced by ~10^6 times in comparison with normal Raman. The intensity of a Raman band is given in the equation 1.16. Here, m and n represent the initial and final vibronic states of the electronic ground state shown in Figure 1.5. The polarizability, $(\alpha_{ij})_{mn}$, can be rewritten as in equation 1.17 where M is electronic transition moment between different states, Γ_e is band width of eth state and iΓ_e is the damping constant. It is obvious that $(\alpha_{ij})_{mn}$ is frequency dependent. If the incident light frequency, ν_0, is

close to the transition energy, ν_m, the denominator in the first item will be very small and the intensity of a Raman band $\nu_{em} - \nu_0$ increases tremendously. This is the origin of resonance Raman enhancement. In equation 1.18, $(\alpha_{ij})_{mn}$ is divided into A and B terms that correspond to total symmetric vibrations and non-total symmetric vibrations, respectively. That contributes to the intensities of the resonance Raman spectrum. Here we just briefly discuss A term resonance Raman (equation 1.19).

$$I \propto const.I_0 \nu^4 C \sum_{ij} |(\alpha_{ij})_{mn}|^2 \quad \text{.....(1.16)}$$

$$(\alpha_{ij})_{mn} = \frac{1}{h} \sum_e \left(\frac{M_{me} M_{en}}{\nu_{em} - \nu_0 + i\Gamma_e} + \frac{M_{me} M_{en}}{\nu_{em} + \nu_0 + i\Gamma_e} \right) \quad \text{.....(1.17)}$$

$$(\alpha_{ij})_{mn} = A + B \quad \text{.....(1.18)}$$

$$A = M^2 \frac{1}{h} \sum_e \frac{< n|e >< e|m >}{\nu_{em} - \nu_0 + i\Gamma_e} \quad \text{.....(1.19)}$$

The numerator contains two integrals that correspond to Franck-Condon overlap. According to the previous discussion and equations 1.9 and 1.10, this term is zero unless the equilibrium position changes upon the electronic excitation. If a large distortion occurs on the excited state potential energy surface, vibrational modes coupled to the distortion will be enhanced based on the A term mechanism.

1.4 Electron Paramagnetic Resonance Spectroscopy (EPR)

Electron paramagnetic resonance (EPR) spectroscopy is a very powerful tool for

application in the studying paramagnetic reaction intermediates, organic radicals, paramagnetic transition model complexes and biological systems with unpaired electrons. The interpretation of EPR spin-Hamiltonian parameters can provide the information regarding the relationship between geometric and electronic structure in these systems.

1.4.1 Zeeman Effect (Zeeman Interaction)

The electron spins along its own axis and has its magnetic field like that of a small magnet, The magnetic dipole moment, μ, is given in equation 1.20 where β is the Bohr magneton and S is the spin angular momentum. The variable g is called splitting factor or the g factor and contains information regarding how the electron interacts with the applied external magnetic field B (equation 1.23). The g-value for a free electron is g= 2.0023. For an S=1/2 system, the energy of the spin states in an external magnetic field shown is given by equations 1.21 -1.24. The unpaired electron interacts with the applied external field B_0 and gives rise to separation of two different energy levels for the two spin states (m_s =½ and m_s =-½) as shown in Figure 1.7. The lower energy level corresponds to the case where the magnetic dipole moment is parallel to external magnetic field. The higher energy level corresponds to the case where this moment is opposite the external magnetic field. This is called the Zeeman effect or the Zeeman interaction.

$$\mu = -g\beta S \quad \text{.....(1.20)}$$

$$E = -\mu \bullet B \quad \text{.....(1.21)}$$

$$E = g\beta m_S B \quad \text{.....(1.22)}$$

$$E = \frac{1}{2} g_e \beta B_0 \quad \text{.....(1.23)}$$

$$E = -\frac{1}{2} g_e \beta B_0 \quad \text{.....(1.24)}$$

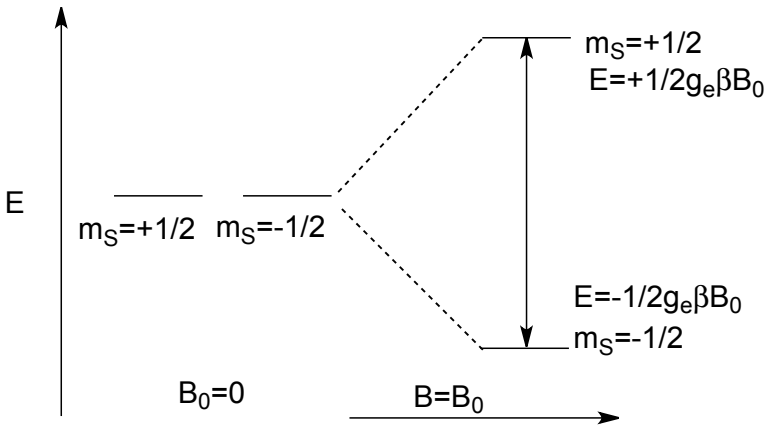

Figure 1.7 Energy level diagram of spin states as a function of external magnetic field.

1.4.2 Resonance Conditions and Selection Rules

$$E = h\nu \quad \text{.....(1.25)}$$

$$\Delta E = h\nu = g_e \beta B_0 \quad \text{.....(1.26)}$$

The absorption of the appropriate quantum of electromagnetic radiation leads to absorption and the occurrence of a transition between these two different energy levels. This occurs only if the following conditions are satisfied. <1> the photon energy matches the energy difference between the two spin states of the electron (equations 1.25 and 1.26), and <2> during the transition the

reorientation of electron magnetic dipole moment is induced by the oscillating magnetic field that is perpendicular to the external magnetic field.[41] Cases <1> and <2> can be met at microwave frequencies. The selection rules are <a> for an isolated spin increase $\Delta m_s = \pm 1$, <b> for a strong electron-electron dipole interaction $\Delta m_s = \pm 1$ and $\Delta m_s = \pm 2$, and <c> for an electron-nuclear interaction $\Delta m_s = \pm 1$ and $\Delta m_I = 0$. The resonant absorption in a paramagnetic sample can be detected in two ways. One is by holding the external magnetic field constant and sweeping the microwave frequency. The second is to scan the external magnetic field at a constant microwave frequency. Considering the sensitivity of the microwave of cavity in the experimental setup and the range of variation of the parameters, υ and B_0, the second case commonly adopted for EPR.

1.4.3 Origin of g-tensor Anisotropy

The magnetic dipole moment produced from the spin and orbital angular momenta is shown in equation 1.27. Generally the orbital angular momentum is nearly zero due to the spin being quenched by the ligand field in the ground state. However, the mixing of orbital angular momentum from excited states into the ground state can still take place. This process is known as spin-orbit coupling $\lambda \vec{L} \bullet \vec{S}$ and is given in equation 1.28. This will cause the perturbation to the ground state wave function and results in deviation from the g_e value (equation 1.29). The new g value gives important chemical information regarding chemical bonding, symmetry, and the electronic structure of the molecule. This g-

$$\vec{\mu} = -\beta < \psi_g | \vec{L} + g_e \vec{S} | \psi_g > \quad \text{.....(1.27)}$$

$$\vec{\mu} = -\beta[<\psi_g|g_e\vec{S}|\psi_g> + <\psi_g|\lambda\vec{L}\bullet\vec{S}|\psi_e>] \quad \text{.....(1.28)}$$

$$h\nu = (g_e + \delta g)\beta B_0 = g\beta B_0 \text{.....(1.29)}$$

tensor can be represented as a 3x3 matrix (g matrix) $g = \begin{bmatrix} g_x & 0 & 0 \\ 0 & g_y & 0 \\ 0 & 0 & g_z \end{bmatrix}$. In an x, y, z Cartesian coordinate system the principle axes are labeled as g_x , g_y and g_z as they are measured along these directions. When in diagonal form, the off-diagonal terms are zero. Most of the paramagnetic species in biological systems of low symmetry are recorded as frozen solution samples. Here, the individual paramagnets are randomly oriented. If all the g values are the same $g_x = g_y = g_z$ then the spectrum is said to be isotropic. At room temperature low symmetry molecules in solution also display an isotropic EPR spectrum since they rotate rapidly and average the anisotropic effect. An axial spectrum is present when $g_x = g_y \neq g_z$ (the g factor parallel to the unique axis is $g_z = g_{\|}$ and the remaining two perpendicular to have $g_{x,y} = g_{\perp}$). A rhombic spectrum appears if the g values are all different ($g_x \neq g_y \neq g_z$). In general the g values of d orbital ground state are given by equation 1.30[34] where $i = x, y, z, \psi_e$.

$$g_i = 2 - 2\lambda\sum_{e\neq g}\frac{<\psi_g|\overrightarrow{L_i}|\psi_e><\psi_e|\overrightarrow{L_i}|\psi_g>}{E_g - E_e} \text{.....(1.30)}$$

are the d orbitals. The spin-orbit coupling constant, $\lambda = \pm\frac{\xi}{2S}$, gives different values for different elements. Usually the heavy metals with spin-orbit coupling constants create large deviations from g_e. Half-filled and less than half-filled d shells are represented by + and -. Here, ξ is the one-electron spin-orbit coupling constant and S is the total spin of the transition metal ion. The orbital angular momentum operator acts on individual d orbital functions as shown in Table 1.2, and $E_g - E_e$ is obtained from the optical transition energy in electronic absorption spectroscopy.

1.4.4 Hyperfine Tensor and Super-hyperfine Interaction

The nuclear spin can couple with the electron spin to produce an electron-nuclear hyperfine interaction. Since the magnitude of Zeeman interaction is usually large compared to the hyperfine interaction, the latter can be considered as the perturbation to the electron spin Hamiltonian in equation 1.31. A is hyperfine tensor with a traceless 3x3 matrix. The hyperfine tensor can be divided into an isotropic and an anisotropic term in a molecule with an axis of trigonal or higher symmetry as shown in equation 1.32. In lower symmetry ligand fields, the hyperfine tensor is rhombic. In the spin Hamiltonian expressed in equation 1.33, the g and A tensors are assumed to be collinear, but this is usually not the case. The hyperfine term is included in the spin-Hamiltonian as shown in equation 1.34. The hyperfine coupling constant, A, is usually expressed with the unit cm^{-1} or MHz. On this basis the Zeeman splitting the EPR spectrum is further split into (2I+1) lines with equal intensity due to the hyperfine coupling with a nucleus with

I≠0. If the electron spin couples with the nuclear spin of the ligand, this is referred to as a superhyperfine or ligand hyperfine interaction. The splitting of the lines goes as 2nI+1 with the number of n ligand nucleii.

$$H = \beta B \bullet g \bullet \vec{S} + A \bullet I \bullet \vec{S} \quad \text{.....(1.31)}$$

$$A = \begin{bmatrix} A_{\perp} & 0 & 0 \\ 0 & A_{\perp} & 0 \\ 0 & 0 & A_{\parallel} \end{bmatrix} = \begin{bmatrix} A_{iso} & 0 & 0 \\ 0 & A_{iso} & 0 \\ 0 & 0 & A_{iso} \end{bmatrix} + \begin{bmatrix} A_{aniso} & 0 & 0 \\ 0 & A_{aniso} & 0 \\ 0 & 0 & A_{aniso} \end{bmatrix} \quad \text{.....(1.32)}$$

$$H = \beta B[g_{\parallel}\vec{S}_z + g_{\perp}(\vec{S}_x + \vec{S}_y)] + A_{\parallel}\vec{I}_z\vec{S}_z + A_{\perp}(\vec{I}_x\vec{S}_x + \vec{I}_y\vec{S}_y) \quad \text{.....(1.33)}$$

$$h\nu = g\beta B_0 + Am_s m_I \quad \text{.....(1.34)}$$

Contributions to the A tensor derive from three terms.[34] The first is the pure isotropic interaction known as the Femi contact term. The symmetry allowed mixing of the s orbital into the ground state has positive contributions to Femi contact term. The indirect Femi contact comes from contribution from spin polarization of core s electrons by the unpaired d electron in the ground state (3d

Table 1.2 Effect of rotation on real d orbitals.[42]

	Orbital Angular Momentum Operator L		
	X	Y	Z
Initial Orbital	Final Orbital		
$d_{x^2-y^2}$	$-id_{yz}$	$-id_{xz}$	$2id_{xy}$
d_{z^2}	$-i\sqrt{3}\ d_{yz}$	$i\sqrt{3}\ d_{yz}$	0

d_{xy}	$-id_{xz}$	$-id_{yz}$	$-2id_{x^2-y^2}$
d_{xz}	$-id_{xy}$	$id_{x^2-y^2} - i\sqrt{3}\ d_{z^2}$	$-id_{yz}$
d_{yz}	$id_{x^2-y^2} + i\sqrt{3}\ d_{z^2}$	id_{xy}	$-id_{xz}$

Table 1.3 Anisotropic hyperfine contributions due to the dipolar interaction of nucleus with a single d electron.[42]

	X	Y	Z
Z^2	4	4	-2
$x^2- y^2$	-2	-2	4
yz	4	-2	-2
xz	-2	4	-2
xy	-2	-2	4

electron contributes negative indirect Femi contact). The second contribution to the A-tensor is the dipolar coupling and indirect dipolar coupling that derives from the spin and orbital angular momenta of the electron interacting with the nuclear angular momentum. The former dominates the anisotropic contribution to hyperfine coupling constant and is traceless as shown in the Table 1.3.

1.4.5 Multiple Frequency EPR at Low Temperature and Spin Relaxation

The Zeeman splitting of an S=1/2 system produces two separated energy levels of electron spin states in an applied external magnetic field. At the room temperature according to Boltzmann distribution (equation 1.35), the spin

population ratio is about 0.9986 with B_0=2000G, T=298K, and g=2.0. The slightly spin population difference between the upper and lower levels gives rise to an EPR signal. In the equation 1.36 the difference in the spin population of the two energy levels is proportional to the applied external magnetic field and inversely proportional to temperature and this affects the intensity of the EPR signal accordingly in the absence of relaxation phenomena. From the spin Hamiltonian expressions in equation 1.33 the Zeeman splitting is magnetic filed dependent and band width is frequency independent while the hyperfine coupling tensor is magnetic field independent. Using high magnetic fields (i.e. at W-band, Table 1.4) the Zeeman interaction is large relative to the the hyperfine terms and this

$$\frac{N_{upper}}{N_{lower}} = e^{\frac{-\Delta E}{k_B T}} = e^{-\frac{g\beta B_0}{k_B T}} = 1 - \frac{g\beta B_0}{k_B T} = 0.9986 \quad \text{.....(1.35)}$$

$$N_{lower} - N_{upper} = N_{lower}[1-(1-\frac{g\beta B_0}{k_B T})] = \frac{Ng\beta B_0}{k_B T} \text{.....(1.36)}$$

results in first-order effects dominating the EPR spectra. Higher frequency EPR also allows one to resolve of two partially overlapping lines that are magnetic field dependent. The use of S-band and L-band EPR is useful for resolving hyperfine splitting.

Relaxation effects derive from both spin-lattice relaxation and spin-spin relaxation [41,43]. The spin–lattice relaxation (longitudinal relaxation time Γ_{1e}) is responsible for the spin population difference on the two energy levels through rapidly dissipating the energy to surrounding molecules or the lattice. With longer Γ_{1e},

the electron doesn't have time to go back the ground state and the population difference disappears resulting in a decrease in the EPR signal. Spin-spin relaxation Γ_{2e} (transverse relaxation time) can result from dipolar and energy exchange between electrons with a higher energy spin state or lower-energy nucleus. Since the Γ_{2e} is usually much shorter than Γ_{1e}, the spin-spin relaxation often dominates the contribution to the line width in an EPR spectrum.

Table 1.4 Frequently used microwave bands and corresponding magnetic field strengths.[44]

Microwave band	Frequency (GHz)	B_0 (Gauss)
L	1.1	392
S	3.0	1070
X	9.5	3389
Q	35	12485
W	90	32152

1.5 Magnetic Circular Dichroism Spectroscopy (MCD)

Magnetic circular dichroism spectroscopy plays an important role in the determination of geometric and electronic structure of transition metal complexes and metalloenzyme active sites. It is complimentary to the electronic absorption spectroscopy, resonance Raman, and EPR sepectroscopies. MCD has been used to gain insight into the ground state and excited state electronic structures of paramagnetic species in biological systems that contain copper,[45] molybdenum,[46] cobalt,[47] and iron,[48,49] nickel.[50] MCD possesses a higher

resolution than electronic absorption spectroscopy and can often resolve the overlapping bands. In MCD, one measures the differential absorption of left circularly polarized light (LCP, $\Delta M_j = +1$) and right circularly polarized light (RCP, $\Delta M_j = -1$) from circular dichroism with the sample in an applied static magnetic field oriented parallel to the propagation of the incident light. The selection rules for MCD are $\Delta M_j = \pm 1$ and $\Delta M_s = 0$. The contributions to the MCD intensity are given in equation 1.37 [51] where E is the energy of the incident light, $\Delta\varepsilon$ is the differential molar absorptivity for LCP and RCP radiation, γ is a collection of constants, β is the Bohr magneton, H is the applied static magnetic field, and $f(E)$ is the bandwidth function. The A term and B term are magnetic field dependent and temperature independent. A principal

$$\frac{\Delta\varepsilon}{E} = \gamma\beta H[A_1(-\frac{\partial f(E)}{\partial E}) + (B_0 + \frac{C_0}{kT})f(E)] \quad \text{.....(1.37)}$$

difference between them is that the former possesses a derivative band shape and the latter has an absorptive band shape. The C term possesses a dependent $1/T$ and dominates the MCD spectrum at low temperatures. The A term requires a non-degenerate ground state $|\mathrm{A}>$ and a degenerate excited state $|J>$. The latter is Zeeman split due to the interaction with applied static magnetic field. The oppositely signed and equal components lead to an MCD spectrum with a derivative shape. The intensity of the A term is typically very weak as shown in Figure 1.8.[46]

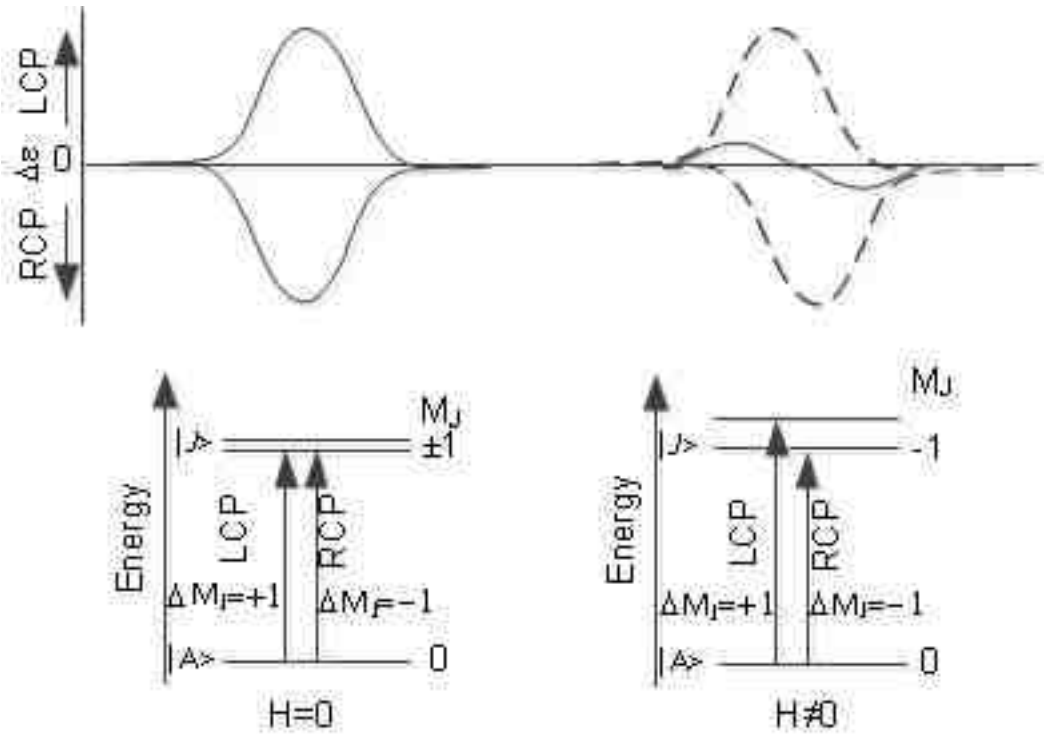

Figure 1.8 Origin of derivative shaped A term MCD intensity. A term derives from LCP and RCP transitions from the ground state M_J=0 (orbitally non-degenerate) to M_J=+1 and M_J=-1 (orbital degenerate) due to Zeeman splitting by with the applied magnetic field. LCP and RCP represent left circularly polarized light and right circularly polarized light, respectively. |A> and |J> are the ground state wave function and excited state wave function respectively. The selection rule of transition is ΔM_J=±1.

The B term arises from transitions involving the non-degenerate ground state $|\mathrm{A}>$ to an excited state $|J>$ that is coupled to an intermediate state $|K>$ by out-of-state Zeeman mixing. The intensity from the B term is proportional to the magnetic field and inversely proportional to energy difference, ΔE, between these states (Figure 1.9).[46]

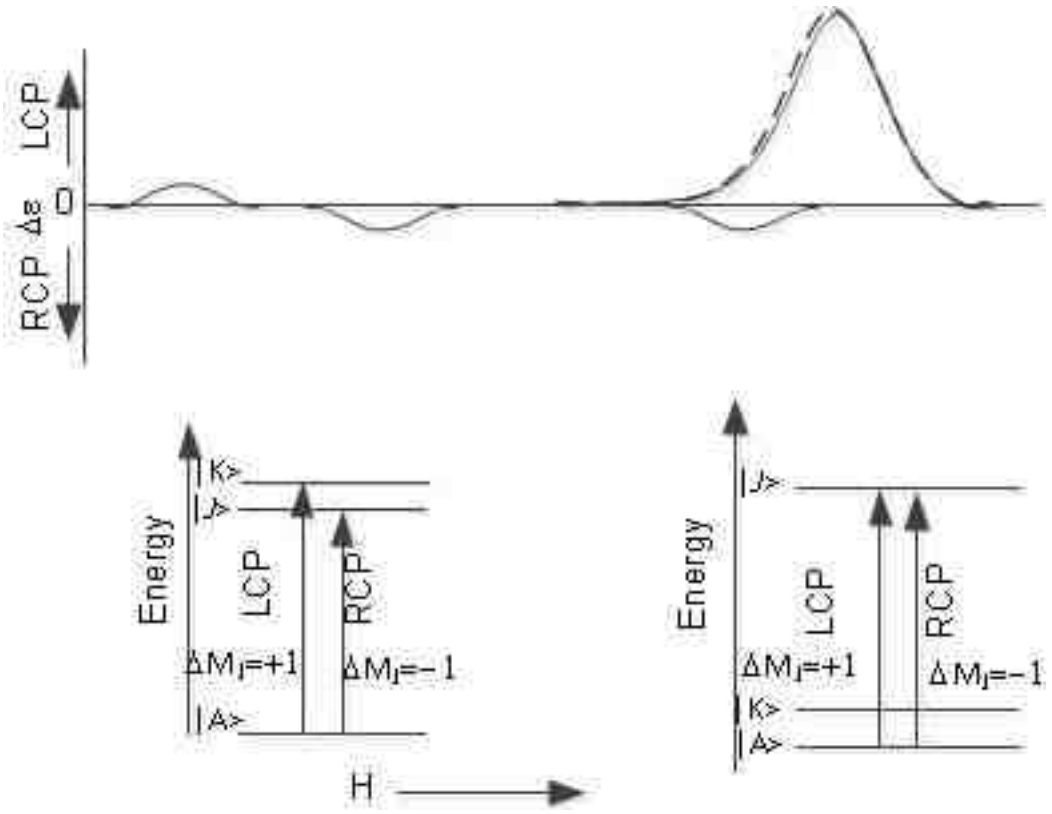

Figure 1.9 Origin of B term is due to out state spin orbit coupling involving excited state |K> and |J> and the intensity is related to the energy difference between these states and applied magnetic field. The stronger applied magnetic field and the small the energy difference lead to increasing the intensity of B term.

The C term requires degeneracy in the ground state $|\mathrm{A}>$. At high temperatures ($kT \doteq g\beta H$), the oppositely signed components form a derivative shaped band like an A term.[46] This is often called a pseudo A term. However at low temperature an absorptive C-term feature arises due to the fact that the lower energy m_s components are selectively populated according to the Boltzmann distribution (Figure 1.10). With respect to paramagnetic species, the spin degeneracy in the ground state can result in transitions with $\Delta M_j = \pm 1$ and $\Delta M_s = 0$ occur through spin orbit coupling with excited degenerate orbital states as shown in Figure 1.11.[52] This type of mixing often dominates the contribution to

the C term compared with spin-orbit coupling of excited state with ground state.

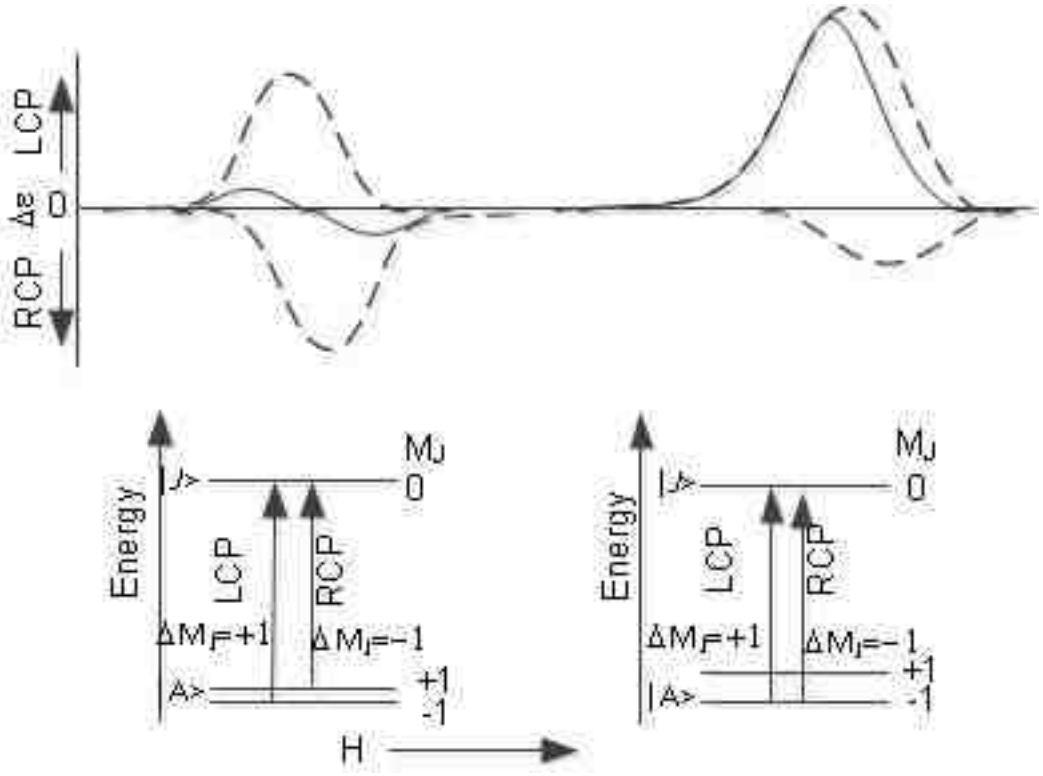

Figure 1.10 Origin of C term MCD intensity arises from the differential absorption of LCP and RCP light from the orbital degenerate ground state to non-degenerate excited state. Increasing the applied magnetic field and decreasing the temperature produces a large Boltzmann population distribution difference on lower energy level and the band shape changes from a derivative absorption to an absorptive shape.

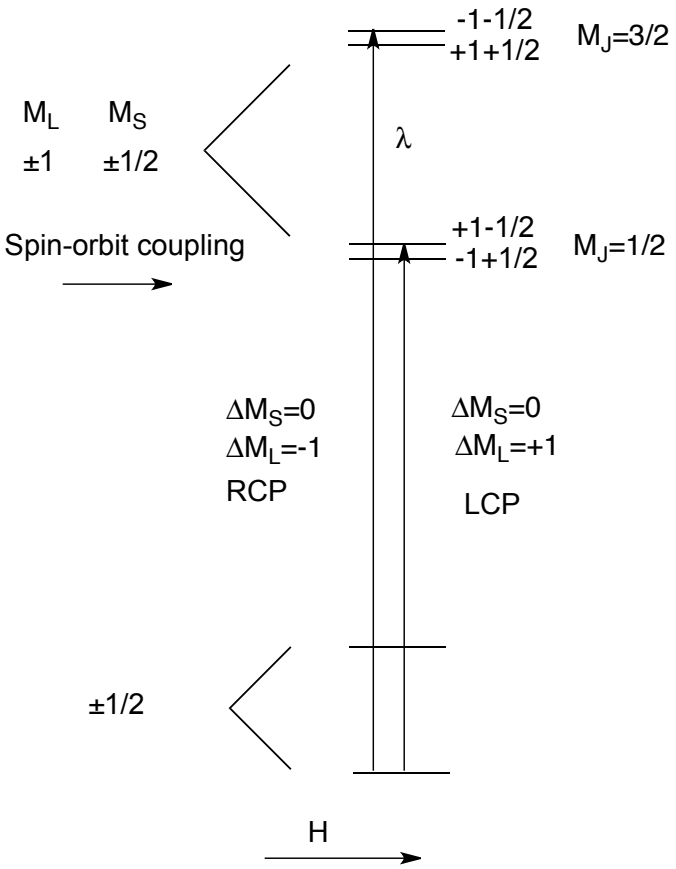

Figure 1.11 Diagram of spin-orbit coupling between excited states that contribute to C term intensity when the ground state is orbitally non-degenerate.

1.6 Summary

In the above sections, the basic principles and selection rules for EAS, resonance Raman, EPR and MCD are briefly introduced. Depending on the species under study (paramagnetic or diamagnetic) some of these techniques are more useful than others. Often, these techniques are combined in order to obtain greater information regarding the geometry and electronic structure of transition metal model complexes and the metal ion coordination environment at the active sites of metalloenzymes (Table 1.5). Therefore, they can provide us with deep insight into the understanding of an enzyme's catalytic mechanism.

Table 1.5 Summary of spectroscopic and magnetic methods used for the study of inorganic complexes and metallobiomolecules.[53]

Method	Parameters	Information content
EPR	ground state g, A^M, D, E; ligand superhyperfine coupling A^L	low symmetry of d orbital splitting and their relative covalency; orbital angular momentum and metal covalency of ground state; covalency electron spin density on ligand
EAS	Ligand field and charge transfer excited states: energies/intensities/band shapes	Ligand field splitting o d orbitals Geometry distortion of site from centrosymmetric/excited state distortion-probes change in bonding on excitation/nature of L-M bond and ligand donor strength
MCD	Ligand field and charge transfer excited states: energies/band shapes/intensities (A, B, C terms)	d orbitsl splitting (geometry)/ distortion of site from centrosymmetric/ nature of excited state and spin-orbit coupling intensity mechanism/nature of L-M bond and ligand donor strength
rRaman	Charge transfer excited states: depolarization ratio/enhancements profiles (A and B terms)	Assignments of vibrations/ excited state distortion

1.7 References

(1) Fu, L.; Stanford University. Dept. of Chemistry. *Functional and structural models of myoglobin and cytochrome c oxidase*; 1997.

(2) Klotz, I. M.; Klippenstein, G. L.; Hendrickson, W. A. *Science* **1976**.

(3) Kim, H. W.; Greenburg, A. G. *Hemoglobin-Based Oxygen Carriers as Red Cell Substitutes and Oxygen Therapeutics*; Springer Science & Business Media, 2013.

(4) Stenkamp, R. E. *Chem. Rev.* **1994**, *94*, 715–726.

(5) Berg, J. M. *Annu Rev Biophys Biophys Chem* **1990**, *19*, 405–421.

(6) McLean, K. J.; Sabri, M.; Marshall, K. R.; Lawson, R. J.; Lewis, D. G.; Clift, D.; Balding, P. R.; Dunford, A. J.; Warman, A. J.; McVey, J. P.; Quinn, A.-M.; Sutcliffe, M. J.; Scrutton, N. S.; Munro, A. W. *Biochem. Soc. Trans.* **2005**, *33*, 796–801.

(7) Brzóska, K.; Meczyńska, S.; Kruszewski, M. *Acta Biochim. Pol.* **2006**, *53*, 685–691.

(8) Groysman, S.; Holm, R. H. *Biochemistry* **2009**, *48*, 2310–2320.

(9) Hille, R. *Chem. Rev.* **1996**, *96*, 2757–2816.

(10) Machonkin, T. E.; Quintanar, L.; Palmer, A. E.; Hassett, R.; Severance, S.; Kosman, D. J.; Solomon, E. I. *JACS* **2001**, *123*, 5507–5517.

(11) Costas, M.; Mehn, M. P.; Jensen, M. P.; Que, L. *Chem. Rev.* **2004**, *104*, 939–986.

(12) Requena, L.; Bornemann, S. *Biochem. J.* **1999**, *343 Pt 1*, 185–190.

(13) Colman, P. M.; Freeman, H. C.; Guss, J. M.; Murata, M. *Nature* **1978**.

(14) Cate, J. H.; Yusupov, M. M.; Yusupova, G. Z.; Earnest, T. N. *Science* **1999**.

(15) Karahanian, E.; Corsini, G.; Lobos, S.; Vicuna, R. *Biochimica Et Biophysica Acta-Gene Structure and Expression* **1998**, *1443*, 65–74.

(16) Sayers, Z.; Brouillon, P.; Vorgias, C. E.; Nolting, H. F.; Hermes, C.; Koch, M. H. *Eur. J. Biochem.* **1993**, *212*, 521–528.

(17) Spritz, R. A.; Ho, L.; Furumura, M.; Hearing, V. J. *J. Invest. Dermatol.* **1997**, *109*, 207–212.

(18) Barth, A. *Biochim. Biophys. Acta* **2007**, *1767*, 1073–1101.

(19) Clark, R.; Dines, T. J. *Angewandte Chemie International …* **1986**.

(20) Garton, S. D.; Temple, C. A.; Dhawan, I. K.; Barber, M. J.; Rajagopalan, K. V.; Johnson, M. K. *J. Biol. Chem.* **2000**, *275*, 6798–6805.

(21) Han, J.; Adman, E. T.; Beppu, T.; Codd, R.; Freeman, H. C.; Huq, L. L.; Loehr, T. M.; Sanders-Loehr, J. *Biochemistry* **1991**, *30*, 10904–10913.

(22) Wilson, G. L.; Greenwood, R. J.; Pilbrow, J. R.; Spence, J. T.; Wedd, A. G. *JACS* **1991**, *113*, 6803–6812.

(23) González, P. J.; Rivas, M. G.; Brondino, C. D.; Bursakov, S. A.; Moura, I.; Moura, J. J. G. *J Biol Inorg Chem* **2006**, *11*, 609–616.

(24) George, G. N.; Pickering, I. J.; Kisker, C. *Inorg Chem* **1999**, *38*, 2539–2540.

(25) Izumi, Y.; Glaser, T.; Rose, K.; McMaster, J.; Basu, P.; Enemark, J. H.; Hedman, B.; Hodgson, K. O.; Solomon, E. I. *J. Am. Chem. Soc.* **1999**, *121*, 10035–10046.

(26) Sarangi, R. *Coordination Chemistry Reviews* **2013**, *257*, 459–472.

(27) Fridén, H.; Cheesman, M. R.; Hederstedt, L. *… Acta (BBA)-Protein …* **1990**.

(28) Mack, J.; Bunya, M.; Shimizu, Y.; Uoyama, H.; Komobuchi, N.; Okujima, T.; Uno, H.; Ito, S.; Stillman, M. J.; Ono, N.; Kobayashi, N. *Chemistry* **2008**, *14*, 5001–5020.

(29) Sempombe, J.; Elmore, B. O.; Sun, X.; Dupont, A.; Ghosh, D. K.; Guillemette, J. G.; Kirk, M. L.; Feng, C. *JACS* **2009**, *131*, 6940–6941.

(30) He, C.; Mishina, Y. *Curr Opin Chem Biol* **2004**, *8*, 201–208.

(31) Qiu, D.; Kilpatrick, L.; Kitajima, N.; Spiro, T. G. *JACS* **1994**, *116*, 2585–2590.

(32) Tshuva, E. Y.; Lippard, S. J. *Chem. Rev.* **2004**, *104*, 987–1012.

(33) Enemark, J. H.; Cooney, J. J. A.; Wang, J.-J.; Holm, R. H. *Chem. Rev.* **2004**, *104*, 1175–1200.

(34) Solomon, E. I. *Comments Inorg Chem* **1984**, *3*, 225–320.

(35) Ed, J. L.; Joint Ed, R. G. W. *Modern Coordination Chemistry*; 1967.

(36) Lever, A. B. P. *Inorganic electronic spectroscopy*; Elsevier Science Ltd, 1984.

(37) *Inorganic Electronic Structure and Spectroscopy Ed. by Edward I. Solomon*; 2006.

(38) Karlin, K. D.; Stiefel, E. I. *Progress in Inorganic Chemistry, Dithiolene Chemistry*; John Wiley & Sons, 2004.

(39) Ferraro, J. R.; Nakamoto, K. *Introductory Raman Spectroscopy*; Academic Press, 2012.

(40) Eichhorn, G. L.; Marzilli, L. G. *Methods for Determining Metal Ion Environments in Proteins*; 1980.

(41) Atherton, N. M. *Principles of electron spin resonance*; Ellis Horwood Limited, 1993.

(42) Que, L. *Physical Methods in Bioinorganic Chemistry*; Sterling Publishing Company, 2000.

(43) Weil, J. A.; Bolton, J. R. *Electron Paramagnetic Resonance*; John Wiley & Sons, 2007.

(44) Misra, S. K. *Handbook of Multifrequency Electron Paramagnetic Resonance*; John Wiley & Sons, 2014.

(45) Solomon, E. I.; Szilagyi, R. K.; George, S. D.; Basumallick, L. *Chem. Rev.* **2004**, *104*, 419–458.

(46) Kirk, M. L. *Paramagnetic Resonance of Metallobiomolecules* **2003**, *858*, 340–357.

(47) Kaden, T. A.; Holmquist, B.; Vallee, B. L. *Biochemical and biophysical research …* **1972**.

(48) Agui, A.; Mizumaki, M.; Matsushita, T.; Kawamura, N.; Nakatani, T. *Physica Scripta* **2005**, *T115*, 611–613.

(49) Chow, M. S. Y. *Reactions of Non-heme Iron Active Sites with Dioxygen: Mechanistic Insights Through Spectroscopy, Kinetics and Computations*; ProQuest, 2008.

(50) Craft, J. L.; Horng, Y.-C.; Ragsdale, S. W.; Brunold, T. C. *J Biol Inorg Chem* **2004**, *9*, 77–89.

(51) Kirk, M. L.; Peariso, K. *Curr Opin Chem Biol* **2003**, *7*, 220–227.

(52) Neese, F.; Solomon, E. I. *Inorg Chem* **1999**, *38*, 1847–1865.

(53) Solomon, E. I. *Inorg Chem* **2005**, *44*, 723–726.

Chapter 2 Spectroscopic and Computational Studies of the Mo Coordination Environment of Xanthine Oxidase Family Enzymes

2.1 Introduction

2.1.1 Molybdenum Hydroxylase Family

Molybdenum is the only transition metal in the second row of periodic table that is ubiquitous in nature due to its high solubility at high oxidation state. As one class of molybdenum enzymes, the Mo hydroxylase have continued to draw broad research interest ever since it was discovered eighty years ago. In comparison with the monooxygenases (flavin-containing *p*-hydroxybenzoate hydroxylase, heme-containing cytochrome P450, non-heme-containing methane monooxygenase, and copper-containing dopamine-β-monooxygenase),[1] the Mo hydroxylase possess a unique oxygen atom source from metal-activated water rather than dioxygen. When an oxygen atom is incorporated into a C-H bond of a given substrate, two reducing equivalents are generated instead of being consumed according to the following reaction stoichiometry (equation 2.1).

$$RH+H_2O \rightarrow ROH+2H^{+}+2e^{-} \quad \text{(2.1)}$$

The molybdenum hydroxylases include xanthine oxidoreductase (XO), xanthine dehydrogenase (XDH), aldehyde oxidoreductase (AO), carbon monoxide dehydrogenase (CODH), and quinoline 2-oxidoreductase (Qor).[2] They are found in a wide range of eukaryotic, prokaryotic, archaeal and bacterial organisms.

Crystal structural and genetic characterizations show that they possess a great deal of structure similarity as shown in Figure 2.1. The redox active centers of the molybdenum hydroxylase enzymes are organized as dimers $(\alpha)_2$ in eukaryotic enzymes and oligomers $(\alpha\beta\gamma)_2$.

Differences among these enzymes are related to the nature of reactions that they catalyze, the conserved amino residues at the substrate binding pocket, the type of redox centers present, the nature of the electron acceptor, the geometric structure of Molybdenum center, or some combination of these factors. The reactions catalyzed by Molybdenum hydroxylase members are:

XO: Xanthine+H_2O → Uric acid+$2H^+$+$2e^-$……(2.2)

XDH: Xanthine+H_2O → Uric acid+$2H^+$+$2e^-$……...(2.3)

AO: Aldehyde+H_2O → carboxyic acid+$2H^+$+$2e^-$……(2.4)

CODH: CO+H_2O → CO_2+$2H^+$+$2e^-$……...(2.5)

Qor: Quinoline+H_2O → 2-hydroxyquinoline+$2H^+$+$2e^-$……..(2.6)

XO/XDH catalyzes the oxidation of a broad range of purine, and aromatic and aliphatic aldehyde substrates. In mammals, there are two inter-convertible forms of xanthine oxidoreductase, xanthine dehydrogenase and xanthine oxidase. Eukaryotic XDH can be easily and reversibly converted to the oxidase form by sulfhydryl oxidation or converted irreversibly by proteolysis. Prokaryotic xanthine oixdoreductase exists in a stable dehydrogenase form like the RcXDH isolated from bacterial *Rhodobacter capsulatus.*[3] XO differs XDH in the various electron acceptors that it can use during catalysis. XO prefers dioxygen as the oxidizing substrate at the FAD site while XDH shows a preference for NAD+ reduction.

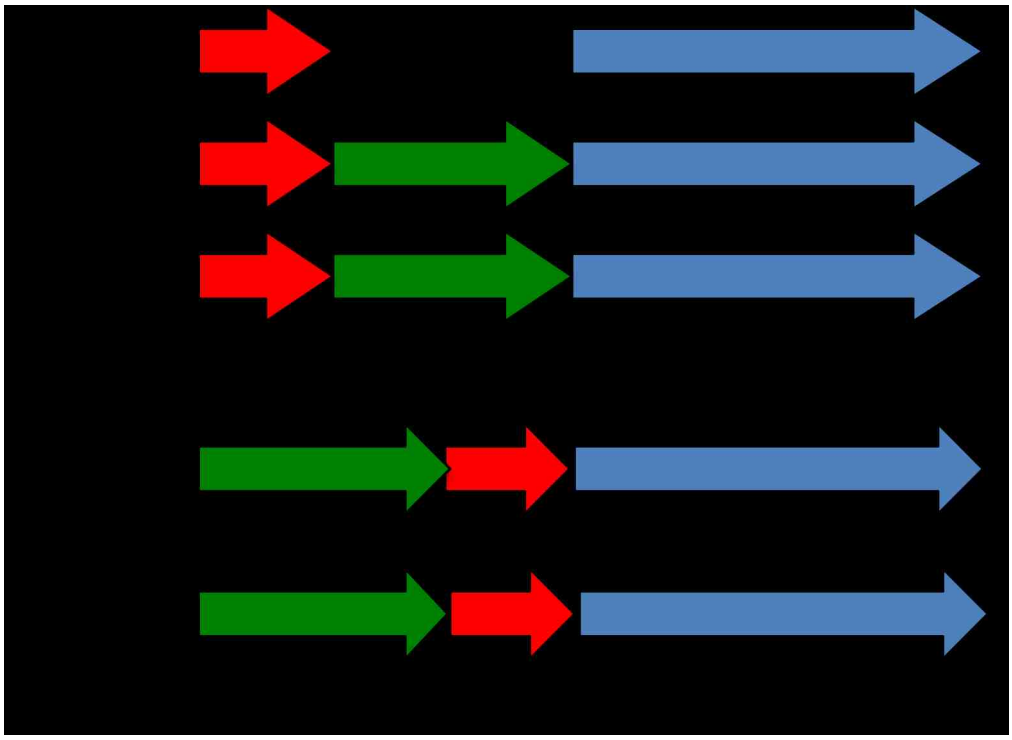

Figure 2.1 Schematic organization of operons of Molybdenum hydroxylase enzymes (AO is from bacterial *Desulfovibrio gigas*; XO from *Bos Taurus*; XDH from *Rhodobacter capsulatus;* Qor from *Pseudomonas putida* 86; CODH from *Oligotropha carboxidovorans*). The short red arrow represents 2Fe-2S I and 2Fe-2S II clusters; the medium green arrow is for the FAD subunit and the large blue arrow is for the Mo active site domain.[2]

Aldehyde oxidoreductase uses aldehyde and aromatic hetero-cycles as reducing substrates but more efficiently catalyzes the oxidation of the former. The bacterial aldehyde oxidoreductase isolated from *Desulfovibrio gigas* is the first member of the molybdenum hydroxylase enzyme family that had its crystal structural determined.[4] The square-pyramidal geometry of the molybdenum site and the conserved glutamate are observed in the crystal structures of other Molybdenum hydroxylase family members. The presence of a terminal sulfido ligand bound to Mo is essential for XO/XDH to oxidize substrates. AO is distinguished from XO/XDH by two aspects: the pyranopterin cofactor possesses a dinucleotide

usually cytosine) and there is no FAD domain (Figure 2.1). The Ferredoxin 4Fe-4S is the electron acceptor rather than NAD^+ or O_2.

Compared with XO/XDH the physiological role of human aldehyde oxidoreductase is still not clear. The conserved glutamate and phenylalanine amino residues, combined with the nature of the molybdenum coordination sphere, allow the mammalian aldehyde oxidoreductase to catalyze the oxidation of a broad variety of substrates. This includes the metabolism of some drugs in humans.[5] For example, human AO can oxidize anticancer agents like acridine carboxamide to an acridone derivative (an antitumor agent) and the reduction of sulfoxide compounds such as sulindac (an anti-inflammatory agent). The activation of pro-drugs for anticancer agents can also be performed by human AO. For example, 8-hydroxythioguanine is activated from thioguanine by human AO. However, the catalytic mechanism of aldehyde oxidoreductase is believed to be that proposed for XO/XDH.

The CODH enzyme catalyzes the oxidation of CO to CO_2 as part of the carbon and energy resources for biological systems in nature. Its structure is a dimer of heterotrimers.[6] Each heterotrimer ($\alpha\beta\gamma$) consists an iron-sulfur protein (CoxS), FAD domain (CoxM), and a molybdenum active site (CoxL). This is shown in Figure 2.1. It is noticeable that the order of genes in the operon (FAD-2Fe/2S-Mo) is different from those of XO and XDH (2Fe/2S-FAD-Mo). A distinct feature in CODH compared to other XO family members is the presence of a binuclear active site where Mo and Cu ions are bridged by μ-sulfido ligand. The Qor (quinoline 2-oxidoreductase) enzyme from *Pseudomonas putida* 86 is of interest,

as it catalyzes the 2-hydroxylation of quinoline in the catalytic reaction.[7] Although Qor possesses only a mononuclear molybdenum center instead of the binuclear Mo-Cu center in the active site of CODH, Qor possesses the same structural organization in the operon-encoding pattern (qorMSL) as that in CODH (Figure 2.1).

2.1.2 Crystal Structure of XO

The four redox centers are linearly arranged in the each subunit (Figure 2.2 Bottom). Substrate oxidation occurs at the Mo active site and electron transfer occurs through the iron sulfur clusters to FAD, where the electron acceptor is either NAD^+ or O_2. The Pyranopterin cofactor (Figure 2.3 left) is coordinated to molybdenum in the mononuclear molybdenum enzyme families such as sulfite oxidase and DMSO reductase and xanthine hydroxylase.[9] It is proposed that the pyranopterin cofactor mediates electrons out of the molybdenum center during the enzymatic turnover and also modulates the reduction potential of molybdenum center.[10] The 2Fe-2S I and II clusters are distinguished by their EPR g values and their individual reduction potentials.[11] The FAD domain is in a hydrogen-bonding environment and is buried deeply in a cleft. The loop formed by amino acids in the XDH form of the enzyme is oriented to have enough space for NAD^+ binding. After conversed to XO, the rearrangement of the loop blocks the NAD^+ access to the cleft and eliminates the activity of XDH.[2] The conformation change in the surface of the FAD domain is one of the differences between XO and XDH.

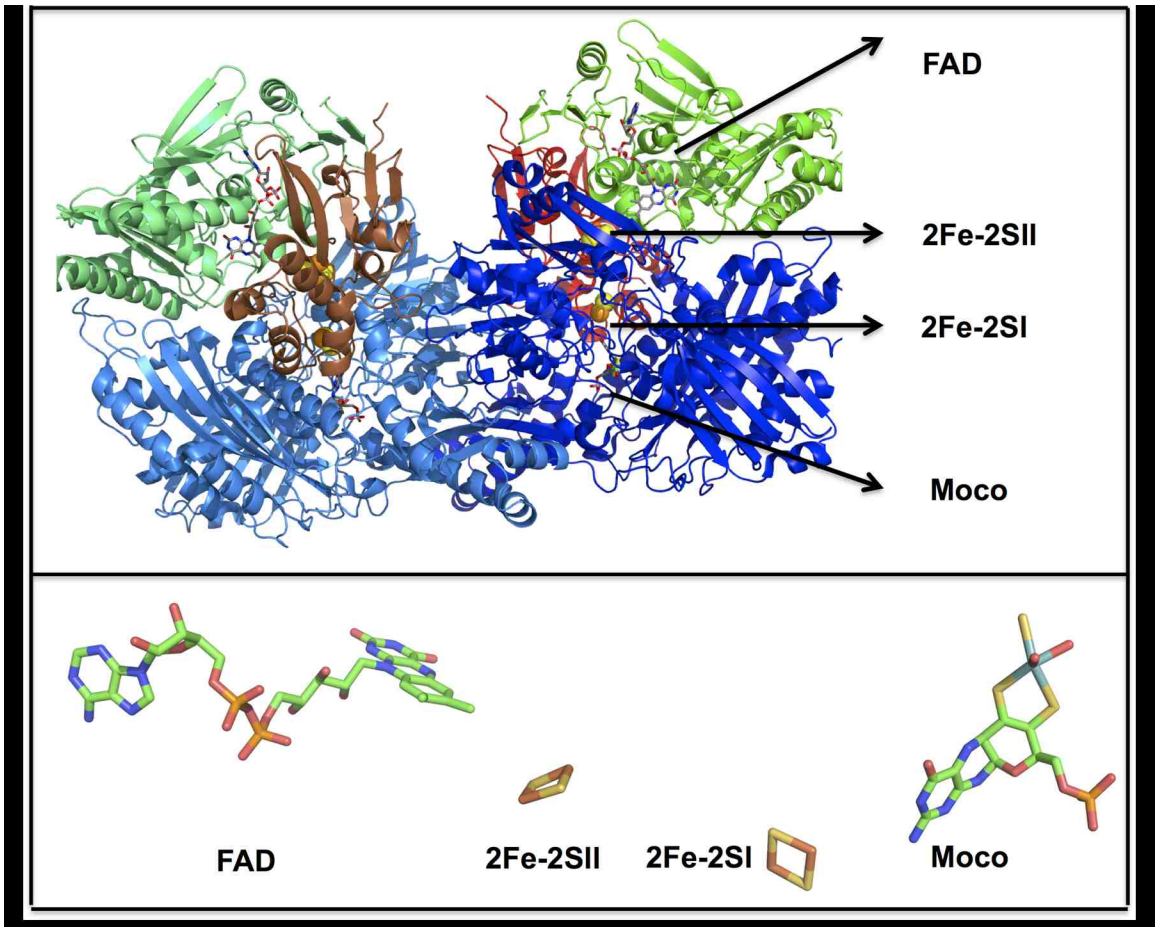

Figure 2.2 Top: the dimer crystal structure of isolated xanthine oxidase from bovine milk (PDB code 3ETR with 2.2 A).[8] Bottom: the illustration of the electron transfer pathway with a linear arrangement of redox centers.

Figure 2.3 Left: the structure of pyranopterin cofactor (PDT); right: coordination geometry of XO as a function of oxidation state.

2.1.3 Active Site of XO/XDH

In addition to coordination with pyranopterin cofactor the molybdenum metal

center is also equatorially bound to a terminal sulfido and a labile OH. XO/XDH also possesses an apical oxo ligand (Figure 2.3 right). This results in a square-pyramidal geometry. In Figure 2.1 and Figure 2.4 the overall structures of the XO and XDH forms are essentially identical with no significant changes in the Mo coordination environment or the substrate-binding pocket. The rectangular shape of the substrate binding pocket with opening is built by face and side edges from Phe-1009 and Phe-914, the bottom from Arg-880 and Glu-1261, the top from Glu-802.[12] The hydrophobic and charged chains apppear to establish a good environment for access of planar heterocyclic substrates since hydrogen bonding interactions with Arg-880 and Glu-802 may be formed. Based on the structural similarity of the XO/XDH active sites, many spectroscopic and kinetic studies have been performed to probe the enzymatic mechanism of XO/XDH hydroxylation of substrates. Particularly, the bacterial enzyme from *R. capsulatus* XDH can work as enzyme model for human XO and allows for site-specific mutants to be studied.

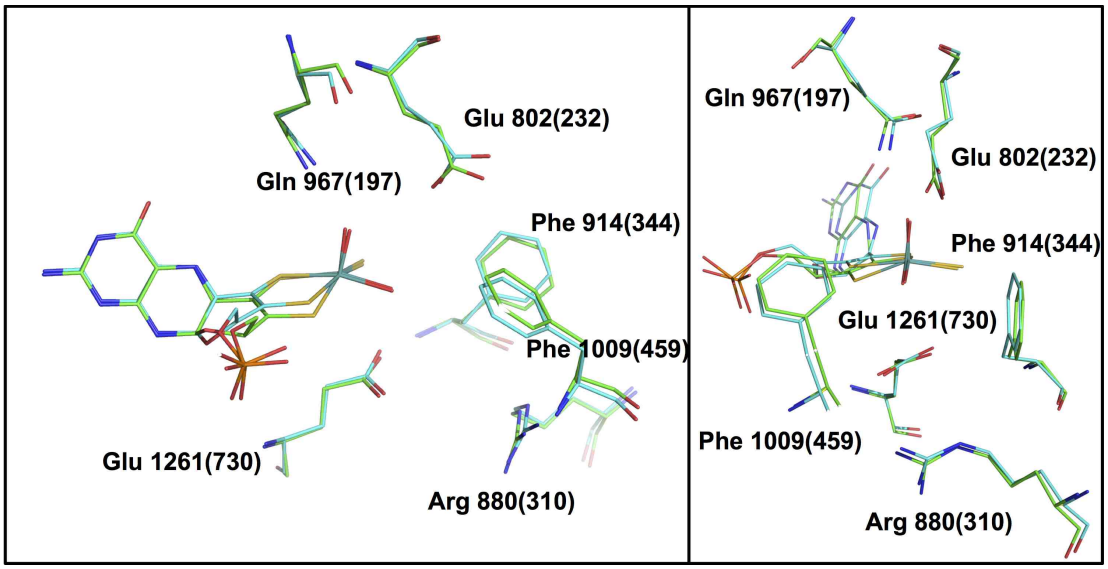

Figure 2.4 The active site comparison of XO (isolated from bovine milk, PDB code 3NRZ)[13] and XDH (isolated from *R. capsulatus* XDH, PDB code 2W54).[14] Left and right are views along the different orientations corresponding to the front and side of the substrate binding pocket. The numbers in parentheses are conventions for *R. capsulatus* XDH amino residues.

2.1.4 Clinical Studies of XO/XDH

The clinical significance of XO/XDH is very important for humans. Xanthinuria,[15] is a rare genetic disease resulting in a lack of XO activity. The disease is divided into three types: xanthinuria I (mutations in the gene coding of XO), xanthinuria II (lack of ability of inserting sulfur into the active site), and xanthinuria III (lack of ability of biosynthesis pyranopterin cofactor). In mammals XDH exists in a normal xanthine oxidoreductase enzyme. However the oxidase form of xanthine oxidoreductase can be converted from the XDH form. The electron acceptor, O_2, in XO can produce peroxide and superoxide when reduced by XO, which is ascribed to oxidative stress and the post ischemia reperfusion for heart attack and stroke.[16,17] A common disease related to xanthine oxidoreductase is the gout caused by the deposition of excessive uric acid crystals in the vessels and joints.

Due to its inhibition effect on the xanthine oxidoreductase allopurinol is prescribed for the treatment of gout and inhibits substrate turnover.[18]

2.1.5 Spectroscopic Studies of XO/XDH

2.1.5.1 Electronic Absorption Spectroscopy

Figure 2.5 displays the absorption spectra of oxidized and reduced XO from bovine milk and XDH from *R. capsulatus* XDH. The absorption maximum of XDH is 465nm, shifted 15nm from the XO absorption maximum at 450nm. The corresponding extinction coefficient for XDH and XO are 37800 M^{-1} cm^{-1} and 31600 M^{-1} cm^{-1}[19]. The intense peaks are contributed from FAD and iron-sulfur clusters. The 550nm peak is exclusively from iron-sulfur clusters. It is difficult to obtain the information about the molybdenum center due to interference from absorption bands due to FAD and 2Fe-2S clusters. The electronic absorption maxima of XO and XDH can be bleached by the addition of the dithionite. With certain substrates a low-energy charge-transfer spectrum can be obtained that results from a relatively stable product bound reduced molybdenum complex. To understand the origin of this charge-transfer transition in electronic absorption spectroscopy is helpful and can be used to understand details regarding the catalytic mechanism. In 1982 Davis et al. determined that a charge transfer complex could be formed by lumazine as reducing substrate or inversely with violapterin product bound to dithionite reduced enzyme.[20] The reduced enzyme product complex possesses a charge transfer band at 650nm and is identified as a true intermediate species.[21] In 2004, the Nishino research group obtained the crystal structure of the intermediate during oxidation of the inhibitor FYX051 by

bovine XDH.[22] This new intermediate also shows a stable broad absorption peak at 640nm analogous to that of the violapterin complex. Recently, a tri-hydroxy-FYX051 product bound reduced xanthine oxidase complex has been shown to produce an intense band at 590nm.[23]

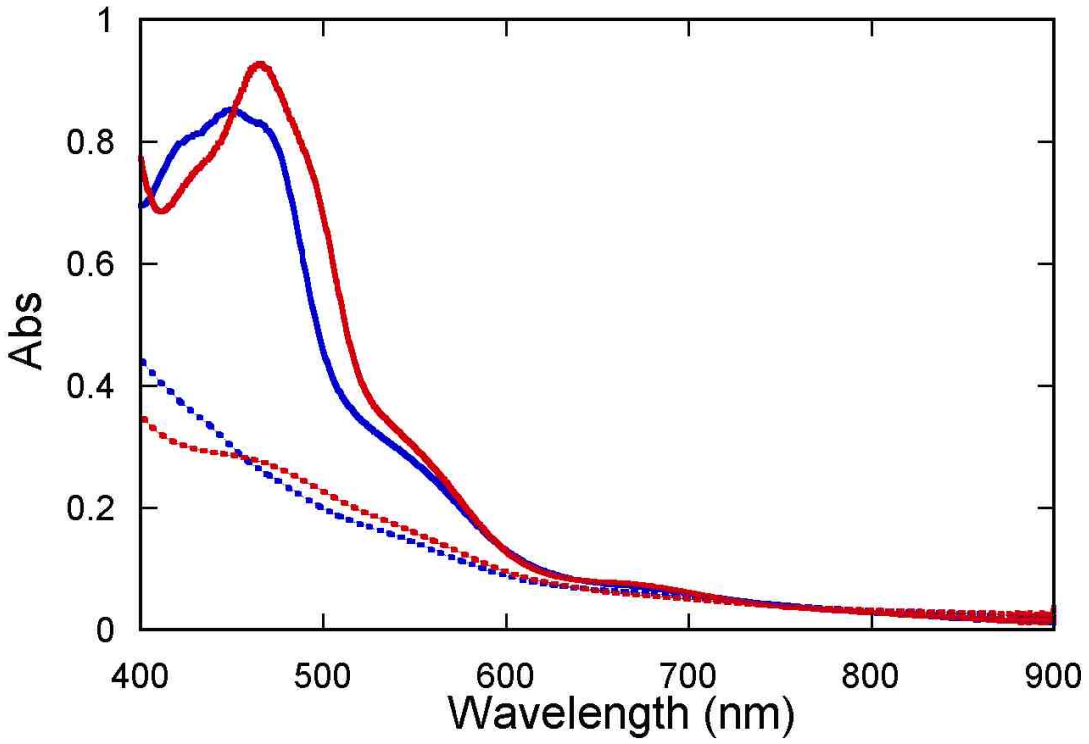

Figure 2.5 Electronic absorption spectra of oxidized (solid line) and reduced (dotted line) XO (bovine milk) (blue) and XDH (*R. capsulatus*) (red). The reduced form is obtained by addition of dithionite.

2.1.5.2 Resonance Raman Spectroscopy

The existence of highly absorbing and/or fluorescent FAD and 2Fe-2S clusters in molybdenum hydroxylase enzymes makes the application of resonance Raman in investigation of molybdenum-ligand vibrations quite difficult. The appearance of charge transfer complexes of reduced molybdenum species

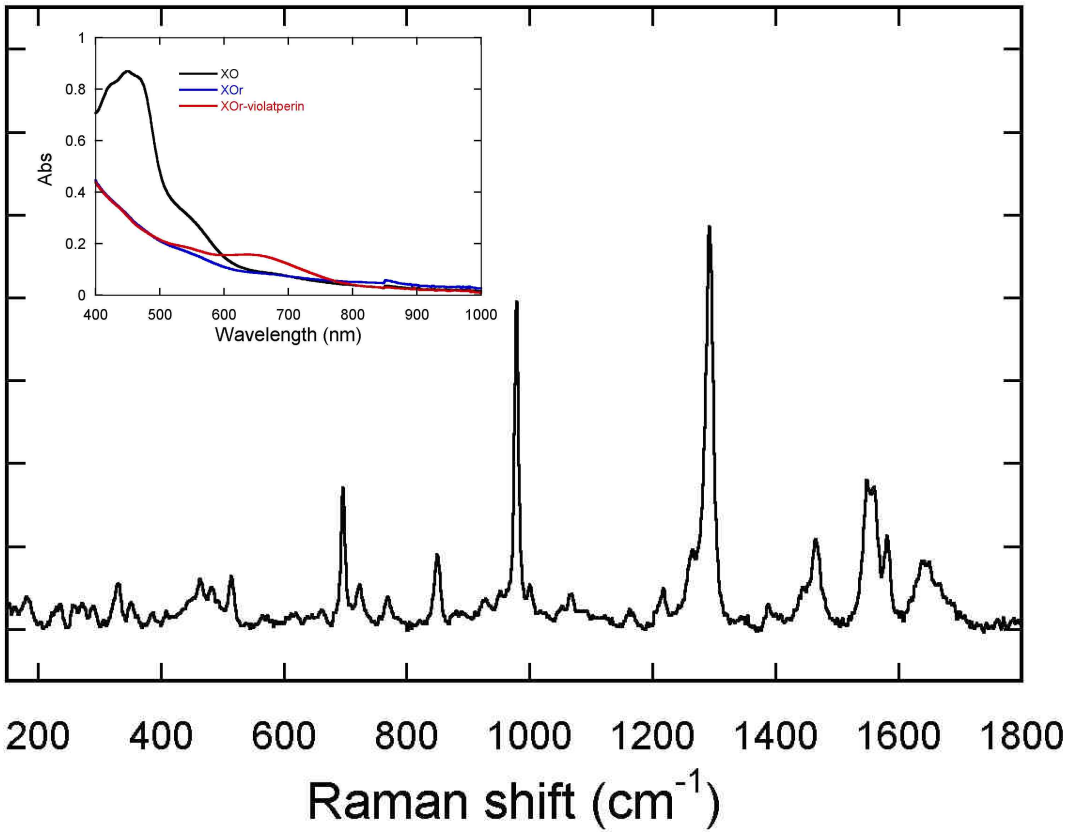

Figure 2.6 Resonance Raman spectrum of reduced XO-violapterin complex (laser line for excitation is 647.1nm). The inset is the electronic absorption spectra of oxidized XO in black, reduced XO in blue and the enzyme-product complex in red. The charge transfer band is located at 650nm.

in XDH opens the door for using the resonance Raman to further probe the molybdenum active site coordination and electronic structure. Hille and coworkers performed resonance Raman studies of a violatperin bound reduced XO enzyme complex.[25,26] With the help of ^{18}O isotope labeling and calculations numerous vibrational modes have been identified. As a result, an end-on binding mode between violapterin and molybdenum at active site is supported while a side-on binding can be eliminated. This conclusion is consistent with ENDOR experiments and is further corroborated by the crystal structure of XO bound with

the inhibitor FYX051.[22] However, until now identification of pyranopterin molybdenum dithiolene vibrational mode in molybdenum hydroxylase enzymes family has not been accomplished due to the interferences with the iron-sulfur clusters and FAD (Figure 2.6).

2.1.5.3 Electron Paramagnetic Resonance Spectroscopy

EPR, one of the most powerful tools to probe the paramagnetic metal ion environment in biological systems, can be used to characterize the redox centers of XDH. The parameters of the 2Fe-2S I cluster are similar to that of spinach ferridoxin observed at temperature of 40-70K. The 2Fe-2S II cluster possesses higher EPR g values in EPR and is observed at temperatures bellow 20K. Leimkühler's and coworker show that the EPR spectrum of 2Fe-2S I in *R. capsulatus* XDH possesses an axial signal that is different from that of bovine milk XO with rhombic g values [11]. This can explain the absorbance intense peak shift around 10nm from 450nm in bovine milk XO to 465nm in *R. capsulatus* XDH.

EPR is mostly used to study the Mo(V) oxidation state either poised or during enzyme turnover. The "very rapid" species has been studied by EPR and it is considered as an important catalytic intermediate without proton hyperfine in EPR signal.[27] No proton hyperfine indicates existence of the Mo=S and proton hyperfine couplings in EPR signal of "rapid" species are interpreted as arising from a Mo-SH site. The isotopic substitution EPR experiments further help to understand the "very rapid" species. The ^{18}O labeled water has been employed

to elucidate how product binds to reduced enzyme.[28] A large hyperfine coupling from ^{17}O is seen in the EPR spectra. The ERP related ENDOR experiment also shows that there is a 2.8Å distance between molybdenum and the ^{13}C carbon (C8) on the xanthine substrate in the "very rapid" species. This strongly suggests that an oxygen bridges the product and reduced molybdenum center.[27]

2.1.6 Oxidative Half Reaction of XO/XDH and Electron Transfer

The electron acceptors O_2 or NAD^+ (dependent on enzyme form of xanthine oxidoreductase) are reduced at the FAD site. Generally electron transfer from $FADH_2$ to O_2 is complicated. The final products are peroxide and superoxide. Six reducing equivalents from molybdenum produce 2 equivalents of H_2O_2 in the former two steps by $2e^-$ oxidation, and two equivalents of $O_2^{\bullet-}$ are produced by $1e^-$ oxidation in the last two steps.[2]

As a part of intramolecualr electron transfer chain, the iron sulfur clusters mediate electron transfer between molybdenum and FAD. The reducing equivalents distribute themselves among the redox centers with different reduction potentials. The electron transfer rate from molybdenum to FAD is much higher than that of enzyme turnover rate. The electron transfer rate between FAD and 2Fe-2S I increases from 155 s^{-1} at pH 6 to 330 s^{-1} at pH 9 in pH jump experiments.[2] From pulse radiolysis studies, the electron transfer from molybdenum to 2Fe-2S I takes place at 8500 s^{-1} while from 2Fe-2S I to FADS the rate is just 125 s^{-1}.[53] The electron transfer rate observed from pulse radiolysis is consistent with the results from the pH jump experiment. The pattern of Mo-

2Fe/2S-FAD electron transfer is supported by the crystal structure of the protein with 2Fe/2S clusters mediating electron transfer between FAD and molybdenum.

2.1.7 Reductive Half Reaction of XO/XDH

The generally accepted mechanism of the reductive half reaction of XO is shown in Figure 2.7.[53] Catalysis starts with conserved Glu-1261 abstracting a proton from the equatorial Mo-OH concomitant with nucleophile attack on the C8 of the xanthine substrate. The formal hydride transfer to the terminal sulfido results in a reduced $LMo^{IV}O(SH)(OR)$ product bound enzyme complex intermediate where L is the pyranopterin cofactor and OR is hydroxylated product coordinated to the molybdenum by a bridging oxygen derived from water. Subsequently this intermediate breaks down by the displacement of product with water and two electrons transfer from molybdenum to other redox active centers in the enzyme. With 6-methyl-xanthine as reducing substrate the “very rapid” species is observed during the catalytic process. However, for a wide range of substrates under a variety of conditions the EPR signal of the “very rapid” species is small or unobservable. Possibly the product dissociates from the intermediate before the one electron oxidation of reduced molybdenum (IV) enzyme-product complex.

In the tetrahedral transition state/intermediate the hydrogen atom has been suggested to be transferred as a hydride because it bears the calculated negative charge when formamide is used as a model substrate.[29] However, recent density functional calculations[30] show that the hydrogen atom transferred to the terminal sulfido in the tetrahedral transition state possesses nearly neutral

charge, which is consistent with C-H activation by the mechanism of Mo=S $\pi\rightarrow$ C-H σ^* and C-H $\sigma^* \rightarrow$Mo=S $\pi*$.[31]

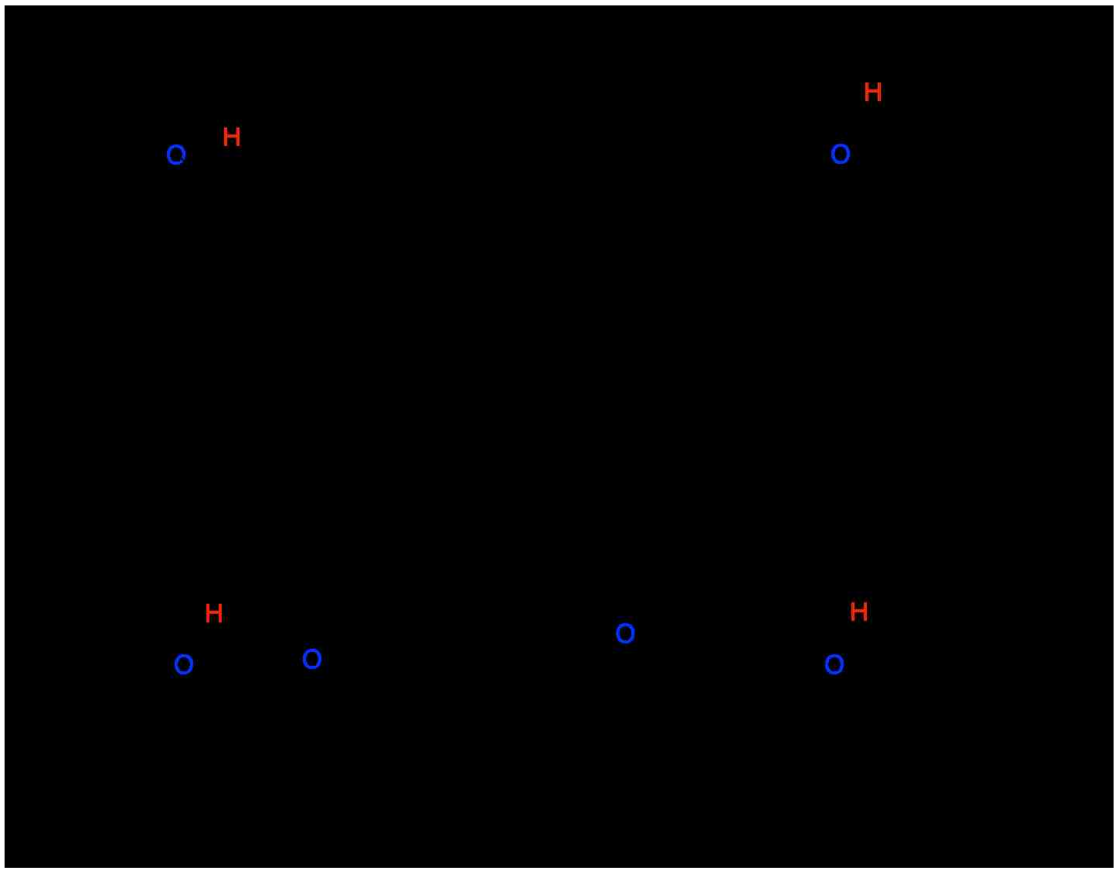

Figure 2.7 Proposed reaction mechanism of xanthine oxidase.

2.2 Objectives

2.2.1 The Nature of the Transition State in XO/XDH

Figure 2.8 Proton transfer (left) and hydride transfer (right) mechanism.

The detailed interpretation of the charge transfer band in product bound reduced XOR species coupled with DFT calculations on excited states and the transition state will provide us the insight into how the C-H hydrogen is transferred to the terminal sulfido.

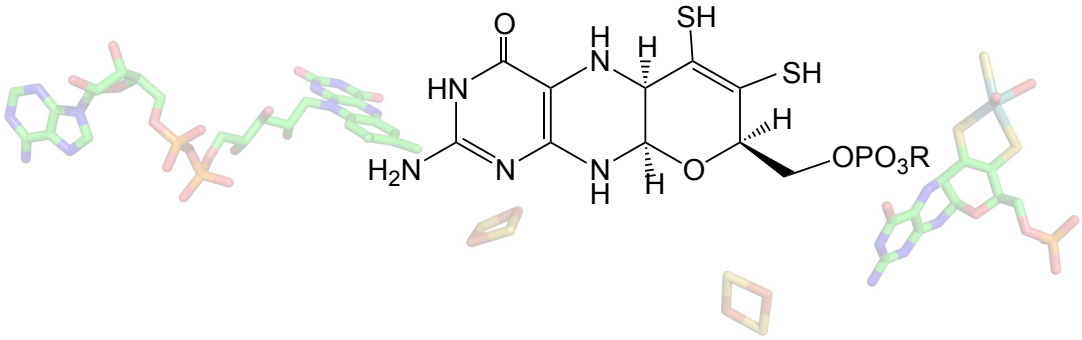

Figure 2.9 Pyranopterin dithiolene (PDT) cofactor and the electron transfer pathway in molybdenum hydrolase enzymes.

2.2.2 The Pyranopterin Dithiolene (PDT) Cofactor in Electron Transfer

The pyranopterin ditholene ligand is believed to modulate the reduction potential of the Mo ion and mediate electron transfer reactivity (Figure 2.9). Resonance Raman characterization of the vibrational modes of pyranopterin dithiolene is one

way to probe its potential involvement in the catalytic cycle. Until now only the pyranopterin dithiolene in DMSO reductase enzymes has been reasonably characterized by rRaman without interference from other redox centers (FAD and 2Fe/2S clusters).[32] Hille and coworkers obtained good quality rRaman spectra of the reduced XO enzyme complex with violapterin when excitating under the charge transfer band 650nm.[26] However, the signal from the iron sulfur clusters in the low energy region makes the identification of vibrational modes of the pyranopterin dithiolene ligands difficult. The new substrate molecules in Figure 3.0 have been synthesized to move the charge transfer absorption peak into the near infrared region and prevent the deleterious effects from the FAD and 2Fe-2S chromophores. The signal/noise ratio is enhanced in these resonance Raman spectra and this shows that Raman can provide the rich information in the low energy region.

Figure 2.10 Lumazine derivatives.

2.2.3 The Conserved Amino Residues at the Active Site

In Figure 2.11, Glutamine Q197 is located on the top of the molybdenum oxo with a hydrogen bond length of 2.8 Å. At such a distance, the molybdenum reduction potential might be able to be adjusted by hydrogen bonding in order to facilitate the redox reaction. Q102 and Q663 hydrogen bond with the PDT and may affect

electron transfer reactivity. Varients of Q102 and Q663 may affect the PDT in its electron transfer role and these hydrogen bonding perturbations may be investigated by spectroscopic studies. Xanthine (left) with a downside orientation and hypoxanthine (right) with an upside orientation are in the channel of the binding pocket built by amino acid residues Glutamate E802, E1261 and Arginine R880. Based on the crystal structure[8,12,14,33-35] and kinetic studies[19,36,37] of xanthine oxidase, xanthine dehydrogenase, and their variants these amino residues play important roles in the substrate reorganization, orientation and hydroxylation. The role of E1261 is to initiate the catalysis and no enzymatic reactivity is detected if it is mutated to alanine. The E802 contributes less to the catalytic reductive half reaction than R880 as shown from the kinetic data of HIlle and Leimkühler.[37] Therefore, it has been proposed that the substrate prefers to bind in the upside orientation for catalysis. An alternative augment has been presented from Nishino and coworkers and from Thiel and coworkers. These researchers suggest that it is the downside orientation of substrates that is catalytically active based on crystal structures and QM/MM calculations.[38] Regardless of the productive substrate orientation, it is clear that these two amino acid residues make different contributions to the reactivity, and this may be able to be probed by resonance Raman and electron paramagnetic resonance spectroscopies of specific enzyme variants. We have hypothesized that E1261 not just initiates the reaction, but also contributes to substrate binding. Therefore, E232, E730, and R310 of xanthine dehydrogenase and their variants (correspondingly E802, E1261, R880 and their variants of xanthine

oxidase) will be used to study their respective perturbations on enzyme resonance Raman and EPR spectra.

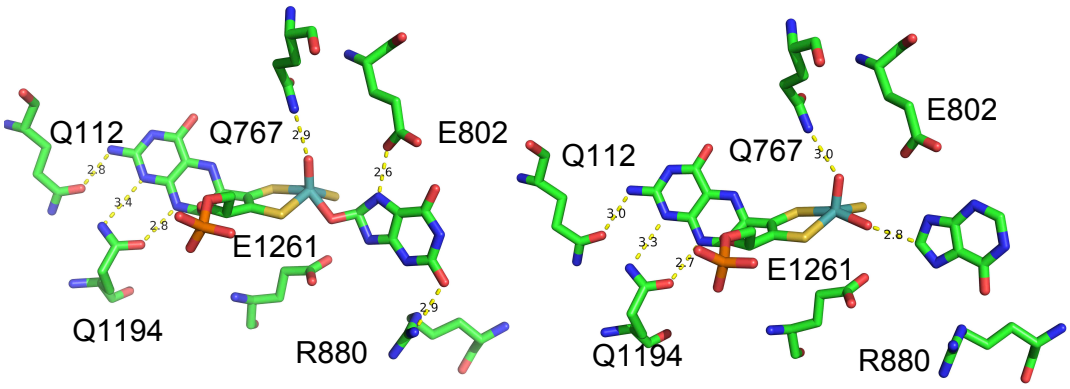

Figure 2.11 The active sites residues of Xanthine Oxidase. Left: Glutamine Q112, Q1194 hydrogen bonding with PDT; Q767 on the top of molybdenum oxo with 2.8-3.0Å hydrogen bond length. Glutamate E802, E1261 and Arginine R880 located in the substrate-binding pocket. Left: downside orientation of xanthine (PDB code 3AMZ; 2.1Å).[33] Right: upside orientation of the substrate hypoxanthine (PDB code 3NRZ; 1.8 Å).[13]

Kinetic studies of xanthine dehydrogenase and its variants show that specific site specific mutations may affect the binding ability of the substrate and decrease or even abolish reactivity.[19,36,37] It is difficult to investigate the spectroscopic properties of these variants due to the fact that they severely reduce the catalytic efficiency of the enzyme. However the hybrid substrate FYX051 possesses the dual properties of mechanism-based purine inhibitors like alloxanthine and structural-based substrate like Febuxosat (a drug for treating gout).[39] More importantly, the tri-hdroxy-FYX051 bound reduce XO product intermediate has an intense charge transfer band at 590nm, which provides a spectroscopic opportunity to study the above-mentioned questions. The substrate FYX051 and its analog FYX051 have been synthesized in case these mechanism-based

inhibitors can't bind to the active sites of the XDH variants (Figure 2.12).

The spectroscopic studies of product bound reduced XO/XDH and variants could provide insight into the role of conserved amino residues on active site catalysis. The Mo(V) aldehyde inhibited species can also be used to probe the catalytic mechanism of XO/XDH using EPR spectroscopy as a probe. The molecules formaldehyde and 3-pyridinecarboxyaldehyde are used to inhibit wild type and variant XDH so that the aldehyde inhibited paramagnetic species can be formed for EPR study. The perturbation from wild type and variants on the geometry of inhibited species can be observed through the signal-sensitive EPR spectra.

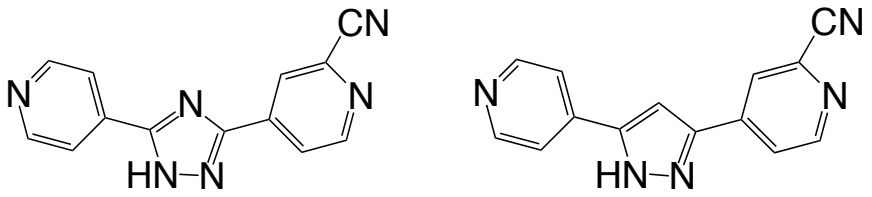

Figure 2.12 FYX051 (left) and its analog FYX051C (right).

2.3 Experimental Methods

2.3.1 Synthesis of Lumazine Derivatives

2-thione-lumazine: 2-thione-pterindine (2-thione-lumazine) is synthesized from the reaction of 2-thio-6-hydroxy diamine pyrimidine with glyoxal.[40] 1g 2-thio-6-hydroxy diamine pyrimindine (purchased from Sigma-Aldrich) is dissolved in concentrated 100ml H_2SO_4. The mixture is heated to reflux to facilitate the solubility of diamine pyrimidine for a few minutes. 0.5g glyoxal in 20ml of H_2O is added into the warm mixture. After few minutes, brown/yellow crystals are precipitated out and then filtered. Crystals are then dissolved in 25ml of 2M

NaOH and decolored in charcoal. The solution is filtered while warm and then a hot solution of HCl (2M, 50ml) is added. This operation is repeated three times to produce 0.8g of yellow crystals. Finally they are washed several times with water and dried. The ESI-MS (MeOH): m/z calc =181, m/z exp = 203 (M+Na). ^{1}H NMR (δ, ppm): 13.31 (s), 12.78 (s), 8.72 (d), 8.60(d). ^{13}C NMR: 176.23, 159.08, 149.35, 149.17, 141.93, 130.25.

4-thiolumazine: 4-thiopterindine (4-thiolumazine) is synthesized using a modified method.[41-43] The starting material lumazine (Alfar Aesar) and Lawesson's (Sigma Aldrich) regent are obtained commercially and used without further purification. Under dry nitrogen, a slightly excess Lawesson's reagent (0.51 g, 1.25 mmol) is added into a stirred suspension of lumazine (0.61 g, 2.50 mmol) in dioxane (25 mL) in a three-neck flask at 100 ^{o}C. The mixture is refluxed at this temperature for 15 minutes during which time the solution color changes from pale yellow to dark red. The reaction is monitored by thin layer chromatography. Upon completion, the reaction mixture is cooled to room temperature and evaporated to dryness in vacuum. The crude product was washed with acetic acid followed by water. After drying in vacuum, it yields 300 mg (75%) of dark red powder. Crystals are obtained by slow evaporation of a saturated 4-thione-lumazine dimethylformamide solution. The ESI-MS (HCOOH): m/z calc =181.02, m/z exp = 181.02 (M+H). 1H NMR (δ, ppm): 13.94 (s), 13.68 (s), 8.73 (d), 8.59(d). 13C NMR (δ, ppm): 191.00, 148.55, 147.67, 146.47, 141.07, 130.98.

2,4-dithiolumazine: The starting material 2-thiolumazine is prepared as described.[41-43] Under dry nitrogen, a slightly excess Lawesson's reagent (0.51 g, 1.25 mmol) is added into a stirred suspension of 2-thiolumazine (0.45 g, 2.50 mmol) in dioxane (25 mL) in a three-neck flask at 100 °C. The mixture is refluxed for 15 minutes during which time the solution color changes from pale yellow to dark red. Upon completion, the reaction mixture is cooled to room temperature and evaporated to dryness in vacuum. The crude product is washed with acetic acid followed by water. After dried in vacuum, it yields 245 mg (50%) of orange powder. The ESI-MS (HCOOH): m/z calc =196, m/z exp = 196.99 (M+H). 1H NMR (δ, ppm): 13.08 (s), 13.27 (s), 8.66 (d), 8.55(d). 13C NMR (δ, ppm): 187.73, 172.75, 149.27, 144.73, 142.56, 133.49.

2.3.2 Synthesis of FYX051 and Its Analog FYX051C

All the procedures performed under a nitrogen atmosphere and solvents are dried with 4Å molecular sieves. The chemicals used in the following procedure were obtained from Sigma Aldrich. The synthesis follows scheme 1 and 2.

Synthesis of FYX051

In 30mL MeOH 5.9 mmol cynao pyridine is transformed to the iminoether after the addition of sodium methoxide (1.18mmol) with stirring 1h, then followed by addition of 5.9mmol nicotinic acid hydrazide **1**. This is refluxed for 12h until the reaction is complete. The solid is washed from the mixture with MeOH and gives **2**. 3 equivalents of dimethylcarbamoyl chloride are added to the **2** in 50ml DMF solution at 40 °C. The mixture is stirred for 1h and 2 equivalent NaCN is added. After 4h of reaction at 40 °C, decant the liquid on the top and then add

10equivalents water, filter the mixture and keep the solid. The final product is obtained by heating the solid **3** at 200°C until evolved gas deceases. 1H NMR (DMSO-d6): δ δ=8.0 (d, 2 H), 8.3 (s, 1 H), 8.6 (s, 1H), 8.8 (d, 2 H), 8.9 (d, 1H) 15.4 (s, 1 H). MS(ESI): calculated (M+H) C12N6H8 249; found 249.0

Synthesis of FYX051C

1. Synthesis of 3-(4-pyridine)-5-(4-pyridine-N-oxide)-pyrazole **5**.

The di-ketone is synthesized from N-oxide ethyl isopicolinate **1** and 4-cetylpyridine using the following the procedure. 2.68mmol **1** is dissolved in 40ml dried MeOH, then followed by the addition of hydrazine hydrate, 1.5 equivalents (50 g/moL, 0.2ml) at room temperature. The mixture is stirred at room temperature for 1h and then refluxed for 2h. After cooling to room temperature the solvent is removed by reduced pressure. The remaining solid is washed by MeOH or EtOH 1-2 times and 0.32g of pure product is obtained. The yield of **2** is ~55%. ^{1}H NMR (DMSO-d6): δ = 7.55 (s, 1 H), 7.7 (d, 2 H), 7.8 (d, 2H), 8.3 (2 H), 8.6 (2 H) ppm. MS(ESI): calculated (M+H) C13N5H9 228; found 248.0

2. Synthesis of 3-(4-pyridine)-5-(4-pyridine-N-oxide)-pyrazole **6**.

1mmol **5** is dissolved in 10 ml dried DMF and followed by adding of 3 equivalents of dimethylcarbamoyl chloride at 40 °C. At the same temperature the mixture is stirred for 1h and then sodium cyanide is added. This is kept refluxing for 4h and cooled to room temperature. Water is added to the mixture and the precipitated solid is washed by DMF. The yield of pure product is ~30%. ^{1}H NMR (DMSO-d6): δ=7.8-7.9 (d, 3 H), 8.1 (d, 1H), 8.5 (s, 1 H), 8.7 (d, 2 H), 8.8 (d, 1H) 14.2 (s, 1

H) ppm.

2.3.3 Sample Preparation

2.3.3.1 Reduced XO/XDH and Its Variants with Violapterin Derivatives

Oxidized *B. taurus* XO was purchased from Sigma Aldrich. The XO_{red}-product complex can be prepared in one of two methods. In the first method, the enzyme-product complex is produced by reacting oxidized xanthine oxidase with the substrate (4-thiolumazine or 2,4-dithiolumazine), followed by addition of dithionite. The formation of XO_{red}-4-thioviolapterin is initiated by adding 15 µL 7.8 mM 4-thiolumazine to a solution containing 70 µL 72 µM XO_{OX} and 60 µL 50mM sodium bicine-NaOH (pH=8.3) buffer. The solution mixture was incubated for 5 minutes at room temperature under aerobic conditions, and then bubbled with nitrogen gas for 15 minutes to make anaerobic. The reaction mixture is titrated with 15 µL 0.04 M sodium dithionite in an anaerobic environment. Spectrophotometric measurements have established the formation of the XO_{red}-4-thioviolapterin complex through the appearance of an absorbance maximum in the electronic absorption spectrum at 758 nm.

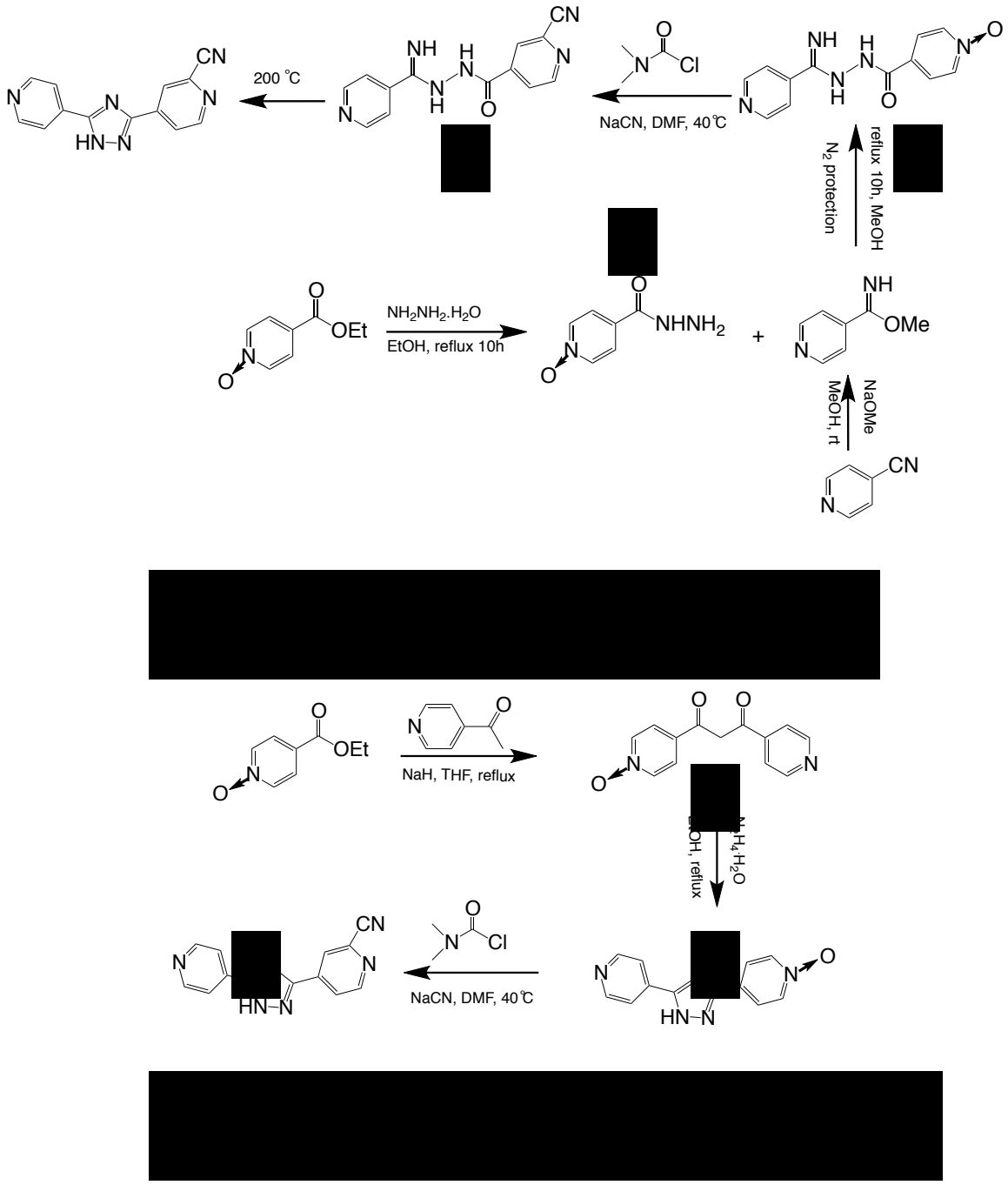

A second method may also be used to generate the enzyme-product complex. Here, 15 µL 7.8 mM of 4-thiolumazine is added to 70 µL of 72 µM XO_{OX} and buffer solution for 2 hours. This mixture is then separated using an Amicon Ultra

0.5mL centrifugal filter (Sigma-Aldrich: MWCO 3kDa). The separated product solution is then quickly added to a fresh, anaerobic, dithionite reduced XO sample (15 µL 0.4 M), after which the electronic absorption spectrum is collected. The appearance of the 758 nm band confirms the presence of the enzyme-product complex.

Wild-type *R. capsulatus* XDH, and E232A, E730A, R310M, Q197A and Q102A variant were provided by Professor Silke Leimkühler, University of Potsdam, Germany. The concentrations of the enzymes were determined by the absorbance at 450nm with an extinction coefficient of 37800 $M^{-1}cm^{-1}$ in xanthine oxidase and at 465 nm with extinction coefficient of 31600 $M^{-1}cm^{-1}$ in xanthine dehydrogenase (ε is the molar absorptivity of the enzyme bound FAD). The $wtXDH_{red}$-product complexes were generated using the same methods that were used for XO. Alternatively, a second method using XO enzyme generated product (produce from XO and centrifuged) was added to the reduced variants.

The concentration of the lumazine substrate derivatives varied from 7mM-10mM. In order to ensure that the reaction went to completeness, an excess of substrate was added.

2.3.3.2 Reduced XO/XDH and Its Variants with FYX051 and FYX051C Complexes

The substrates FYX051 and FYX051C were dissolved in the 0.1N HCl respectively at a concentration 1mM. FYX-051 (1mM, 2.6µL) and half active XO (27.6µM, 120µL) were mixed anaerobically in 280µl 50 mM bicine buffer, pH 8.3 (total volume is about 400µL). After 120hours incubations the enzyme is treated

with added dithionite (0.04M 15µl) and is then ready for electronic absorption data collection. For XDH variants the “backward” reaction has been adapted by adding the product produced from XO to the reduced XDH variants.

2.3.3.3 Inhibited XO/XDH and Its Variants with Formaldehyde and 3-pyridinecarboxyaldehyde

The concentrations of wild type enzymes and their variants are 70-90mmol. The concentrations of formaldehyde and 3-pyridinecarboxyaldehyde are 0.3mol and 0.03mol respectively (pH 8.3 bicine buffer). An excess of inhibitors is added into the enzyme solution in bicine buffer. The mixture is kept in a open EPR tube and bubbled with oxygen gas for 10-20 minutes. The sample is then frozen in liquid nitrogen and made ready for EPR data collection.

2.3.4 Spectroscopy

2.3.4.1 Electronic Absorption Spectroscopy

Electronic absorption spectra were collected on a double-beam Hitachi U-4100 UV-vis-NIR spectrophotometer (Hitachi High-Technologic Corporation) capable of scanning a wavelength region between 185 and 3200 nm. The samples are measured in a 1 cm path length, black-masked, quartz cuvette (Starna Cells, Inc.) equipped with a Teflon stopper. The instrument is calibrated with reference to the 656.10 nm deuterium line.

2.3.4.2 Resonance Raman Spectroscopy

Solution resonance Raman spectra (rR) were collected on a commercial DXR Smart Raman Instrument (Thermo Fisher Scientific Inc.). All aqueous samples were sealed in capillary tubes of diameter 1.5-1.8 mm and mounted onto the

capillary tube holder in the 180° back scattering geometry of the accessory chamber. A 780 nm diode laser was used as the excitation sources and the laser power was 140 mW. A buffer background and a standard sample (Na_2SO_4) were collected before the enzyme data collection. Raman shifts are calibrated against the standard sulfate peak at 992 cm^{-1}. Spectral subtraction of the buffer background yields the final Raman spectrum.

2.3.4.3 Electron Paramagnetic Resonance Spectroscopy

A Bruker EMX EPR spectrometer with an Oxford instruments liquid helium flow cryostat was used to collect EPR spectra of frozen samples. The parameters of experiments were 20dB power attenuation at a temperature of 70K. The spectra simulations are performed with the EasySpin software program.

2.3.4.4 X-ray Crystallography

A orange rod-like specimen of $C_9H_{11}N_5O_2S$, was cut to the approximate dimensions 0.074 mm x 0.127 mm x 0.205 mm, coated with Paratone oil and mounted on a CryoLoop that had been previously attached to a metallic pin using epoxy for the X-ray crystallographic analysis. The X-ray intensity data were measured on an APEX II CCD system equipped with a graphite monochromator and a Mo Kα sealed tube (λ = 0.71073 Å). The frames were integrated with the Bruker SAINT software package using a narrow-frame algorithm. The integration of the data using a triclinic unit cell yielded a total of 5627 reflections to a maximum θ angle of 26.41° (0.80 Å resolution), of which 2269 were independent (average redundancy 2.480, completeness = 99.1%, R_{int} = 2.69%, R_{sig} = 4.08%) and 1733 (76.38%) were greater than $2\sigma(F^2)$. The final cell constants of $\underline{a}$ =

5.5656(3) Å, b = 8.5877(4) Å, c = 12.2172(7) Å, α = 95.751(4)°, β = 98.795(3)°, γ = 101.942(3)°, volume = 559.30(5) $Å^3$, are based upon the refinement of the XYZ-centroids of reflections above 20 σ(I). The calculated minimum and maximum transmission coefficients (based on crystal size) are 0.9433 and 0.9790.

The structure was solved and refined using the Bruker SHELXTL Software Package, using the space group P -1, with Z = 2 for the formula unit, $C_9H_{11}N_5O_2S$. Non-hydrogen atoms were refined anisotropically. Hydrogen atoms, except for the N-H protons that were located in the diffraction map, were placed in geometrically calculated positions with U_{iso} = 1.2U_{equiv} of the parent atom (U_{iso} = 1.5U_{equiv} for methyl groups). The final anisotropic full-matrix least-squares refinement on F^2 with 162 variables converged at R1 = 3.92%, for the observed data and wR2 = 9.64% for all data. The goodness-of-fit was 1.039. The largest peak in the final difference electron density synthesis was 0.315 $e^-/Å^3$ and the largest hole was -0.210 $e^-/Å^3$ with an RMS deviation of 0.051 $e^-/Å^3$. On the basis of the final model, the calculated density was 1.504 g/cm^3 and F(000), 264 e^-.

2.3.5 Computational Methods

2.3.5.1 Softwares Used and Density Functional Theory with Basis Sets

Spin-restricted gas phase geometry optimizations, numerical frequency calculations, and excited states computations for the XO_{red}-product complexes are performed at the density functional theory (DFT; TDDFT) level using the Gaussian 03W and ORCA (version 2.9.1) software packages. All Gaussian 03W calculations use the B3LYP hybrid exchange-correlation functional and SDD

basis set. ORCA calculations used the BP86 functional with the def2-TZVP basis set for Mo and S, and a def2-SVP basis set for all light atoms to optimize the geometry and compute vibrational frequencies. The B3LYP functional with SDD basis set were also used in Gaussian calculations. ChemCraft (version 1.7) and Gaussian view were utilized to visualize and render the vibrational modes and the electron density difference maps (EDDMs) and orbitals. Excited states calculations were run using the CASSCF based on preliminary geometries and time dependent calculations with the B3LYP hybrid functional and def2-TZVPP basis set for Mo and S, and def2-SVP for all light atoms. Active spaces of CASSCF were chosen to be an 8-electron and 7-orbital except for 8-electron and 8-orbital calculations for XOR-4-thioviolapterin.

Transition state calculations: Transition state (TS) calculations were conducted in using Gaussian 03W software. First XOox-4-thiolumazine (intermediate 1: oxygen from Mo-O connected to 4-thiolumazine without H-transfer to sulfido) and XOr-4-thioviolapterin (intermediate 2: H transfer to sulfide and product bound with molybdenum through bridging oxygen) were optimized in the gas phase. Then the TS guess-searching was performed by varying the C-H bond length. The TS geometry optimization was performed using the structures of optimized intermediate 1, intermediate 2, and the TS guess. Finally, the TS was proved to be viable by the observation of a negative vibrational mode in the frequency calculation, which corresponds to the S-H or C-H stretching mode. Single point energy calculations were also run just after the optimization of intermediates 1 and 2 and the TS. All of these computations were performed at the B3LYP level.

A 6-31G* basis set was used for all atoms except for molybdenum, where the LANL2DZ basis set was used, The LANL3DZ basis set includes an effective core potential.

2.3.5.2 Models

Both upside A and downside B orientations of product/substrate exists in crystal structures with reduced enzyme[13,33,35]. In calculations with the three conserved amino residues E802, E1261 and R880 the enzyme complex is modified by bound 4-thioviolapterin and vinyl replacement of phosphate group. The initial gas

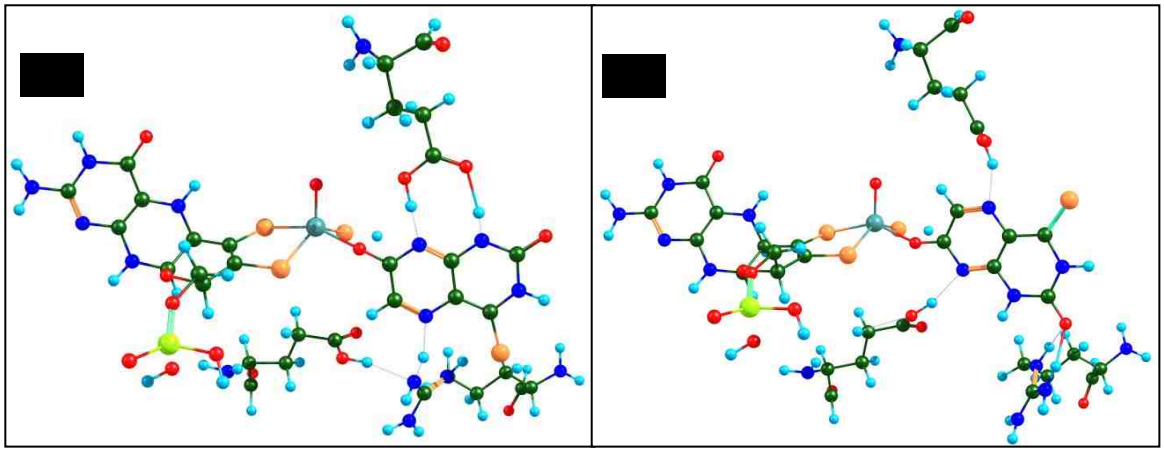

Figure 2.13 Models of reduced xanthine oxidase bound with 4-thioviolapterin in the upside A and the downside orientation B. A is 0.63eV energy stable than B.

phase geometry optimization is performed with the B3LYP function and SDD basis set. The A structure is found to be 0.63eV more stable than B (Figure 2.13). The calculations of the other three XOr-violapterin derivative complexes also show that orientation A is 0.5-0.7eV more stable compared with orientation B. In the following section, geometry optimization, ground state, excited state and transition state calculations have been performed on the upside orientation of bound product without three conserved amino acid residues.

2.4 Results, Analysis and Discussion

2.4.1 Crystal Structure of 4-thiolumazine

ORTEP diagrams of the 4-thione-lumazine molecule and 4-thione-lumazine·DMF dimers are shown in Figure 2.14. The perspective view illustrates the general atomic numbering scheme used for defining the molecular structure parameters. The solvent DMF molecules were incorporated into the crystal structures in a ratio of 1:1. It forms a H-bonded 4-thione-lumazine·DMF dimer in each unit.

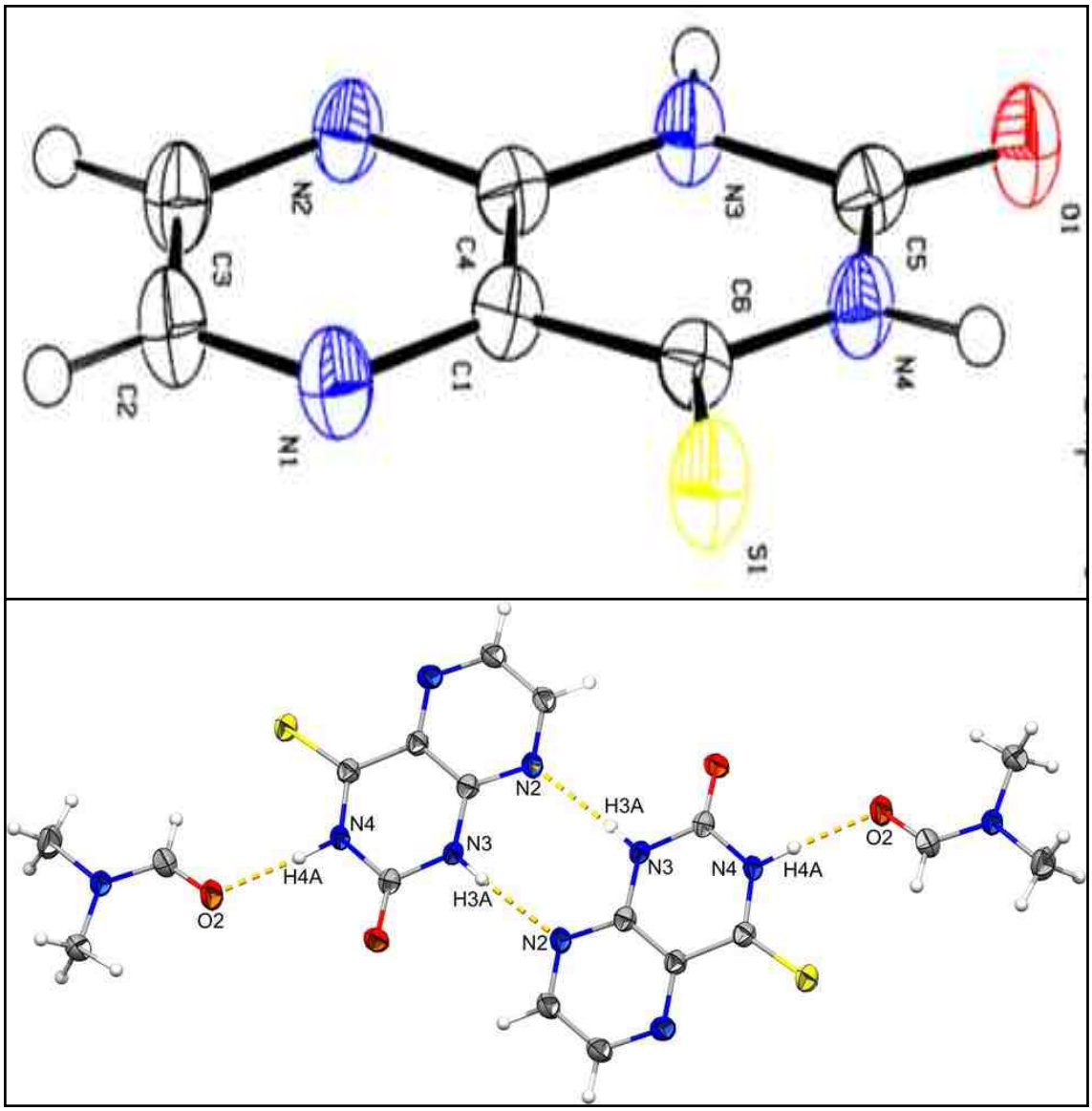

Figure 2.14 Thermal ellipsoid plots for 4-thione-lumazine (A) and hydrogen-bonded 4-thione-lumazine-DMF dimer (B). Hydrogen bonding distance: N3H3—N2: 2.881(2) Å; N4H4—O2: 2.772(2) Å.

No symmetry is crystallographic-ally imposed on 4-thiolumazine·dimer by the P1 space group. Table 2.1 presents the selected crystallographic molecular structural parameters. The bond lengths are similar to those reported for 2,4-dithioluamzine[44]. The bond angles are slight deviated from 120^{o}. This is greater than in 2,4-dthioluamzine, but it still leads to an approximately planar geometry in

the dimers. The hydrogen bonding is not of the form C=O•••H-N or N-H•••S as is typically seen. Two hydrogen bonds N3-H3A•••N2 with the bond length 2.881(2) Å and 2.772(2) Å are responsible for the dimerization of 4-thiolumazine. Each of them orients to DMF with an O2•••H4A-N4 hydrogen bond.

Table 2.1 Selected bond lengths (Å) and bond angles (degree).

Bond	Bond Distance (Å)	Angle	Angle (^{o})
S1-C6	1.6486(19)	C2-N1-C1	116.37(17)
N1-C1	1.341(2)	C4-N3-C5	123.65(17)
N2-C3	1.330(2)	C5-N3-H3A	114.4(15)
N3-C4	1.367(2)	C6-N4-H4A	119.3(13)
N4-C5	1.392(2)	N1-C1-C4	121.36(17)
N3-H3A	0.80(2)	C4-C1-C6	118.85(17)
C1-C4	1.393(2)	C3-C2-H2	119.0
C2-C3	1.392(3)	N2-C3-H3	118.9
O1-C5	1.215(2)	C3-N2-C4	115.80(16)
N1-C2	1.330(2)	C4-N3-H3A	122.0(15)
N2-C4	1.344(2)	C6-N4-C5	127.32(16)
N3-C5	1.370(2)	C5-N4-H4A	113.4(13)
N4-C6	1.369(2)	N1-C1-C6	119.79(17)
N4-H4A	0.89(2)	N1-C2-C3	122.03(19)
C1-C6	1.473(3)	N2-C3-C2	122.21(18)
C2-H2	0.95	C2-C3-H3	118.9

The unusual hydrogen bond interactions in 4-thiolumazine indicate the preferential acceptor property of the nitrogen atom is over the sulfur atom in the lumazine derivatives. This unique pattern is also observed in the 2,4-dithiolumaizne dimer[44] and in luamzine with water as the proton medium[45]. N-H hydrogen bond is important to the enzyme activity. For example, similar molecules like purines shown in Figure 2.15 display hydrogen bonding with amino residues E730, E232 and R310 in the binding pocket. The best orientation is taken to have maximum hydrogen bonding with the N and O atoms of substrates so as to facilitate oxidation of the substrates.

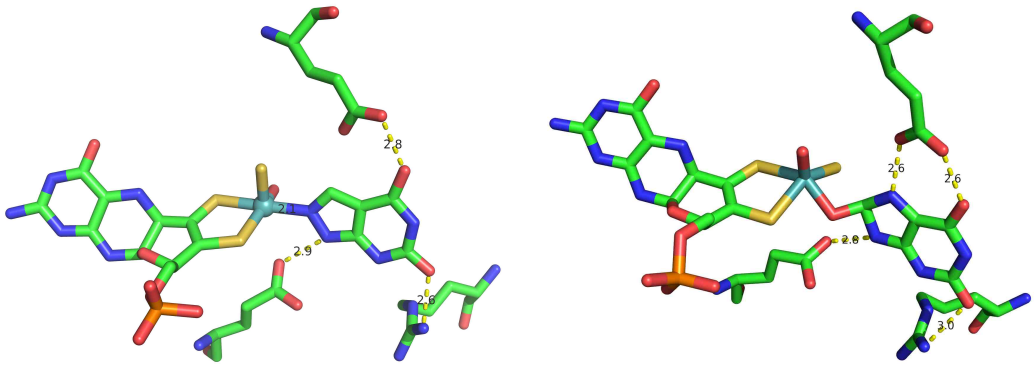

Figure 2.15 Substrates alloxanthine (left)[12] and xanthine (right) bound to the molybdenum center with hydrogen bonding with conserved amino acid residues.[33] The dashed dot line represents hydrogen bond length between 2.5-3.0 Å.

2.4.2 Violapterin Derivatives Bound to Reduced Xanthine Oxidase

2.4.2.1 Electronic Absorption Spectroscopy

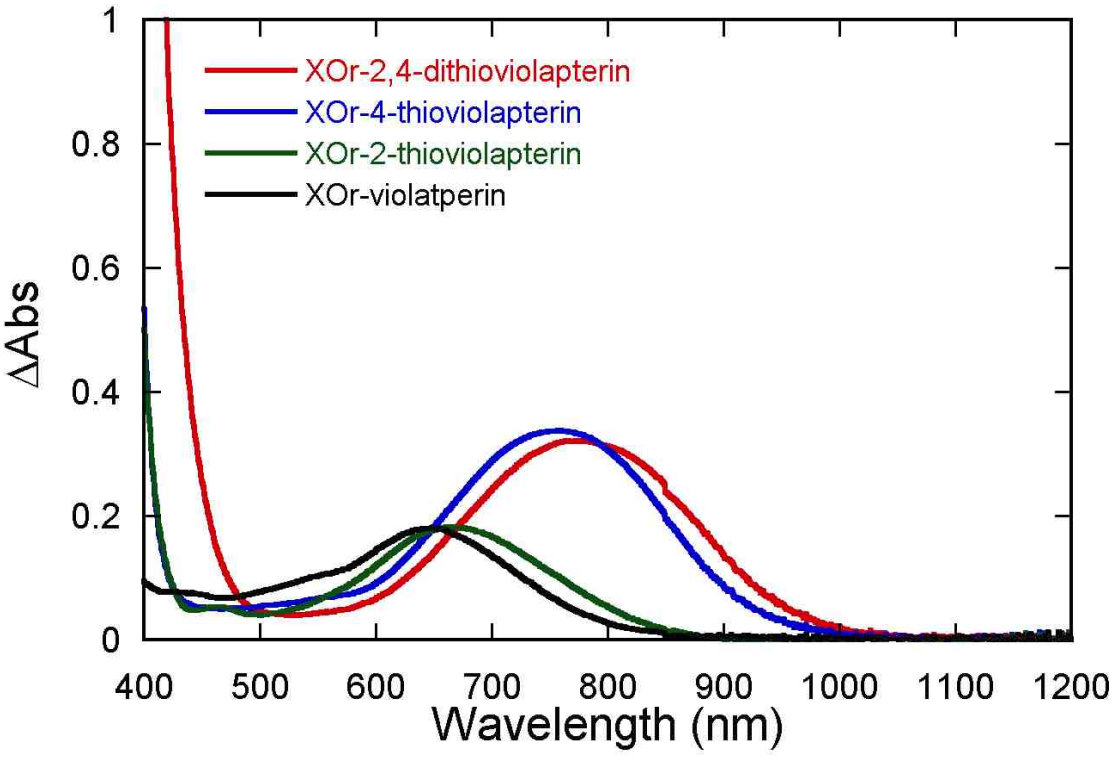

Figure 2.16 Room temperature electronic absorption spectra of XOr-violapterin derivative complexes (violapterin derivatives are the products).

Room temperature difference electronic absorption spectra of XOr-product complexes are collected and displayed in the Figure 2.16. The absorbance along y-axis is subtracted from reduced enzyme for the violapterin derivatives (products) bound to reduced enzyme complexes. All four spectra possess only one strong, low-energy band ranging from 650 nm to 780 nm. It is noticeable that in Figure 2.16 the four complexes fall into two groups based on their charge transfer energiesand extinction coefficients. In one group, the XOr-violapterin CT band is at 650nm and the XOr-2-thioviolapterin CT band is at 668nm with similar

absorbance. A second group consists of XOr-4-thioviolapterin at 758nm and XOr-2,4-dithioviolapterin at 780nm with similar absorbance. Compared with XOr-violapterin and XOr-2-thioviolapterin, the intensity of the XOr-4-thioviolapterin and XOr-2, 4-dithioviolapterin is approximately twice as large.

Table 2.2 Experimental and CASSCF calculated electronic absorption spectroscopy parameters.

Complex	ABS Energy (nm/cm^{-1}) (*exp*)	*f* (*exp*)	ABS Energy (nm/cm^{-1}) (*cal*)	*f* (*cal*)
XOr-violapterin	650/15,380	0.22	638 /15,670	0.28
XOr-2-thiovio	665/14,970	0.22	658/15,200	0.32
XOr-4-thiovio	758/13,200	0.38	782/12,790	0.39
XOr-2, 4-dithiovio	774/12,840	0.36	787/12,710	0.53

2.4.2.2 Metal to Ligand Charge Transfer Band

The room temperature Gaussian resolved electronic absorption spectrum of XOr-4-thioviolapterin is shown in Figure 2.17. The measured extinction coefficient and bandwidth at half peak maximum yields the experimental oscillator strength f = 0.19. Take into account the enzyme activity is only ~50-60%, the actual oscillator strength value should be doubled (~0.38). The 8-electron 8-orbital CASSCF calculations result in excellent agreement with the experimental data in terms of transition energy and oscillator strength. The detailed experimental and computational parameters for all four enzyme-product complexes are provided in Table 2.2. The computed frontier molecular orbitals at the DFT level of theory for

the reduced enzyme-product complex can provide sight into the nature of the charge transfer band shown in the Figure 2.16. The highest occupied molecular orbital (HOMO) is doubly occupied in the reduced Mo(IV) enzyme-product complex and is primarily comprised of the Mo dxy redox active orbital

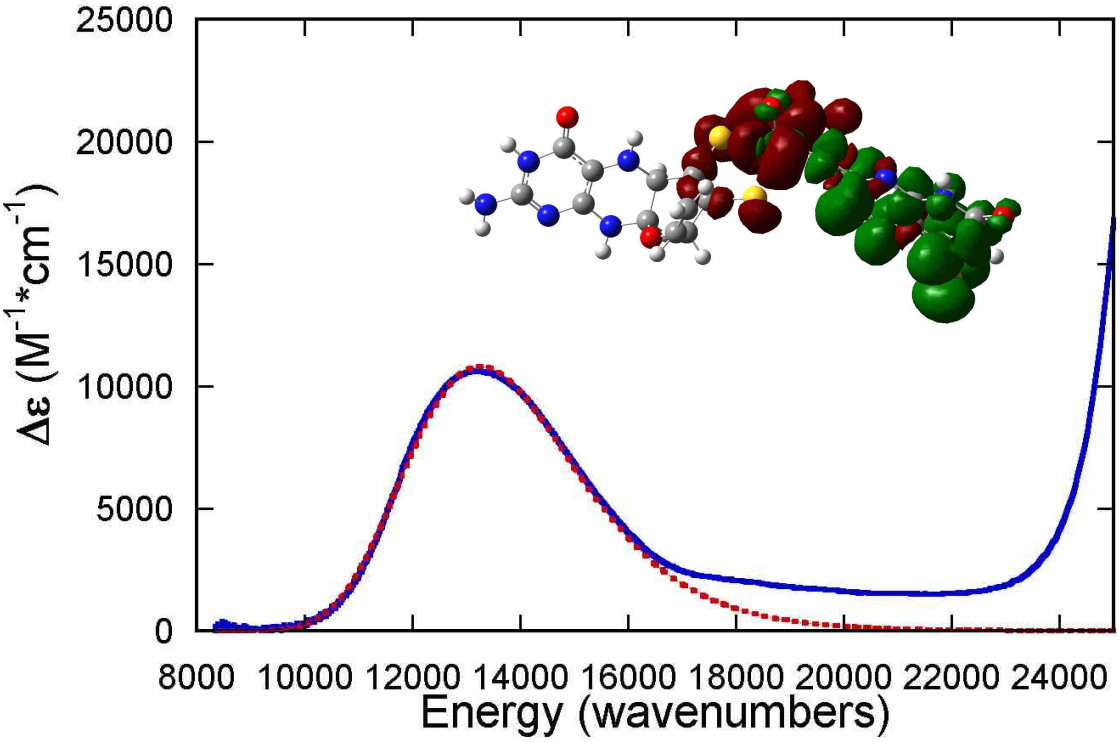

Figure 2.17 Gaussian resolved electronic absorption spectrum of XOr-4-thioviolapterin complex. Inset is the electron density difference map (EDDM).

(69%) with a significant contribution from the π orbitals of the product ring (18%). The lowest lying unoccupied molecular orbital (LUMO) possesses primarily 4-thioviolapterin π* character (84%), but it also mixes with the Mo(dxy) redox active orbital (6%) as shown in Table 2.3. The resulted electron density difference map (EDDM) for this band is presented in Figure 2.17 an inset. Using this information, we can confidently assign this low-energy transition as metal-to-

ligand charge transfer (MLCT) from the Mo(IV) dxy orbital to the 4-thioviolapterin π* orbitals.

Thus, a one-electron promotion from HOMO to LUMO is responsible for the charge transfer band. The Mullikan orbital contributions to the HOMO and LUMO after geometry optimization are listed in table 2.3. The HOMOs are highly similar to one another with the majority of the electron density being localized in the Mo dxy orbital. However, appreciable differences result from the LUMOs of XOr-4-thiovio and XOr-2, 4-dithiovio which each possess ~15% S character at the 4 sulfur position. This can be seen more clearly in Figure 2.18. The bridging oxygen in XOr-2-thioviolapterin has a particularly low contribution to the LUMO.

Table 2.3 Computated Mullikan charge contributions.

E-P complex	Orbital	Mo	O(bridge)	4-O/S	2-O/S	ring
XOr-violapterin	HOMO	73.62	2.20	1.30	0.03	13.32
	LUMO	3.93	8.05	9.95	1.35	86.84
XOr-2-thiovio	HOMO	73.10	1.83	1.46	0.06	14.07
	LUMO	1.93	2.91	6.67	9.65	93.15
XOr-4-thiovio	HOMO	69.65	1.79	3.57	0.06	17.75
	LUMO	6.37	8.08	14.88	1.09	84.18
XOr-2, 4-dithiovio	HOMO	68.64	1.54	4.06	0.13	18.98
	LUMO	6.36	6.55	14.60	4.00	85.74

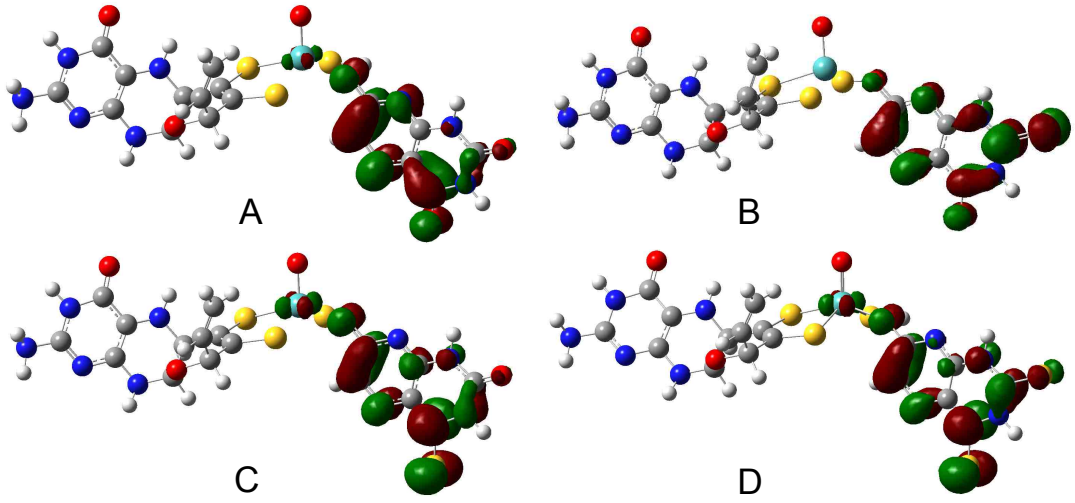

Figure 2.18 LUMOs for all four XOr-Product complexes. A: XOr-violapterin; B: XOr-2-thioviolapterin; C: XOr-4-thioviolapterin; D: XOr-2, 4-dithioviolapterin.

2.4.2.3 Resonance Raman Spectroscopy

Solution resonance Raman spectra of the XOr-violapterin derivatives have been collected using 780nm excitation (Figure 2.19). The enhanced Raman intensity of XOr-4-thioviolapterin and XOr-2, 4-dithioviolapterin is greater than those of XOr-violapterin and XO4-2-thioviolapterin. Also the spectral resolution is enhanced greatly. To compare these spectra more clearly, they have all been normalized to the intensity of 1293 cm^{-1} mode. The resonance Raman spectra for the XOr-product complexes can be divided into a high energy (1200-1700 cm^{-1}) and low energy (200-600 cm^{-1}) for analysis.

2.4.2.3.1 Low Frequency Region (200-600 cm^{-1})

Because 780nm excitation is on resonance for XOr-4-thioviolapterin and XOr-2,4-dithioviolapterin their signals are relatively stronger, especially in the low frequency end in Figure 2.19. The most intense vibrational bands in the low frequency region are highlighted with straight lines (234, 259, 328, 352 cm^{-1}), and

are very similar for all four complexes (Figure 2.20). The most resonantly enhanced band occurs at ~327 cm^{-1} and is assigned as arising from Mo-PDT (pyranopterin dithiolene) half of the Mo (IV)-4-thioviolapterin and Mo (IV)-2, 4-dithioviolapterin. This band is the Mo-dithiolene core vibration that possesses symmetric S-Mo-S stretching and bending character coupled with pyranopterin

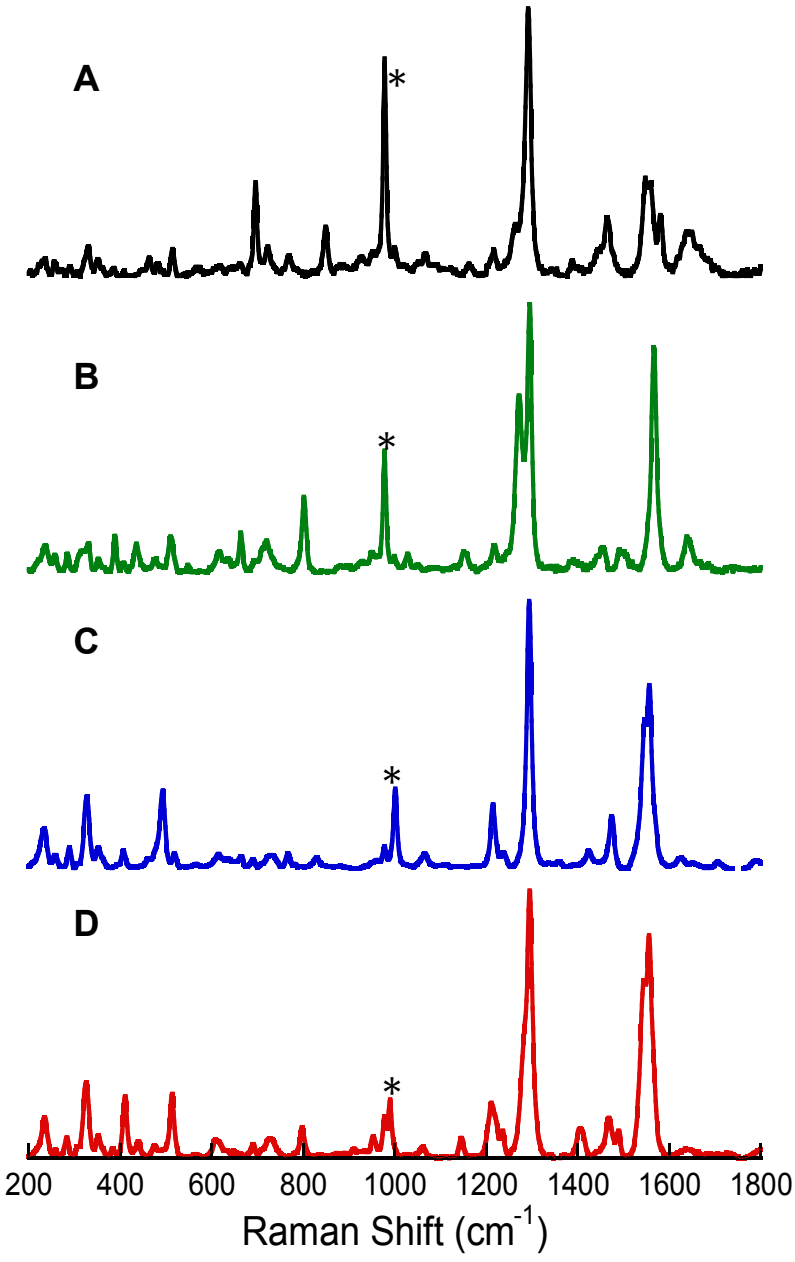

Figure 2.19 Normalized Raman and resonance Raman spectra of XOr-product complexes: (A) XOr-violapterin (black); (B) XOr-2-thioviolapterin (green); (C) XOr-4-thioviolapterin (blue); (D) XOr-2, 4-dithioviolapterin (red). The peak with an asterisk is from the internal standard $(NH_4)_2SO_4$. Note C and D are highly enhanced under 780 nm excitation, and the raw intensity of C and D are about one order of magnitude stronger than those of A and B. For comparison, every spectrum is normalized to its maximum peak 1293 cm^{-1}.

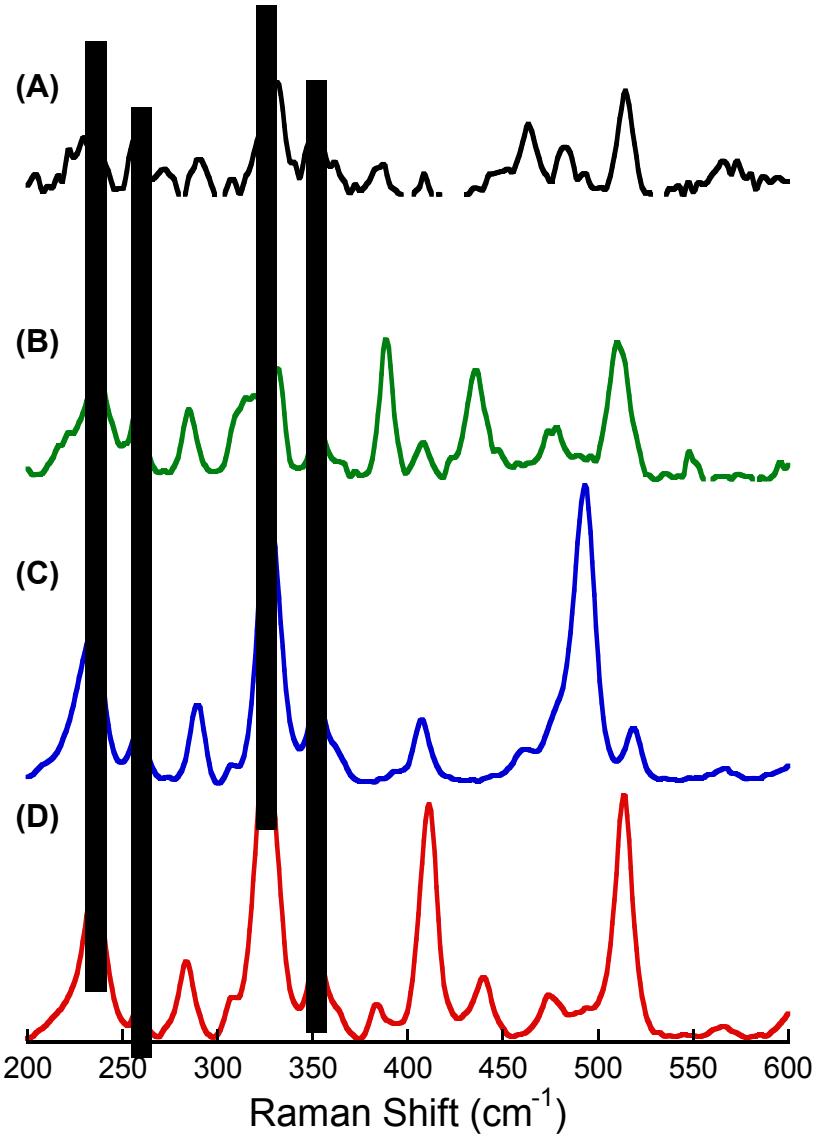

Figure 2.20 Low frequency region of the Raman spectra for XOr-violatperin derivatives. XOr-violapterin is in black; XOr-2-thioviolapterin is in dark green; XOr-4-thioviolapterin is in blue and XOr-2, 4-dithioviolapterin is in red.

Table 2.4 The vibrational frequencies in the low energy region (cm^{-1}). C-S stretching modes are represented in red color. Blue color represents intense Mo-PDT involved vibrational modes.

XOr-2-thiovio			XOr-4-thiovio			XOr-2, 4-dithiovio		
Mode	Exp	Cal	Mode	Exp	Cal	Mode	Exp	Cal
28	237	245	28	235	240	29	234	244
30	257	272	29	259	269	30	259	272
32	285	291	31	290	290	32	283	292
36	328	337	36	328	337	36	326	337
39	356	356	39	352	357	39	352	357
40	389	372				41	384	373
42			43	408	402	46	411	419
46	435	455	46	461	458	47	440	433
47	474	474	47	474	475	49	474	475
			48	493	486			
50	509	509	51	518	515	52	513	515

motion (Figure 21). The vibrational band at 234 cm^{-1} is assigned as a dithiolene folding + Mo≡O rocking mode, also with appreciable PDT character. The weak 259 and 352 cm^{-1} weak bands likely also possess Mo-PDT character. A band located at ~290 cm^{-1} is assigned as the 2/4-position ketone/thione bending mode coupled with the pyranopterin to some degree. C-S stretching modes of XOr-2-thioviolaterpin and XOr-4-thioviolapterin are assigned at 389 and 408 cm-1. They both appear at 384 and 411 cm^{-1} in the XOr-2,4-dithioviolapterin data compiled in Table 2.4. The latter mode with a higher intensity is due to two C-S stretching modes which couple together (Figure 21). Vibrational modes at 435 and 440 cm^{-1} belong to C-S stretches involved in an in-plane ring distortion in the XOr-2-thioviolapterin and XOr-2,4-dithioviolapterin systems. While C-O motion is

involved in the in-plane ring distortion for the XOr-4-thioviolapterin and XOr-violapterin samples occurring at 461 and 481 cm^{-1}, respectively.

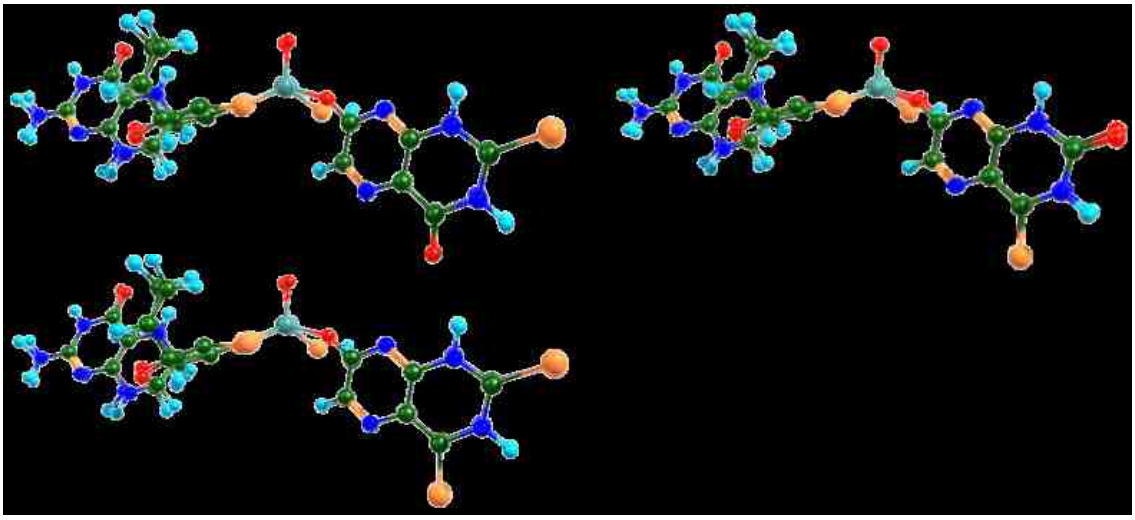

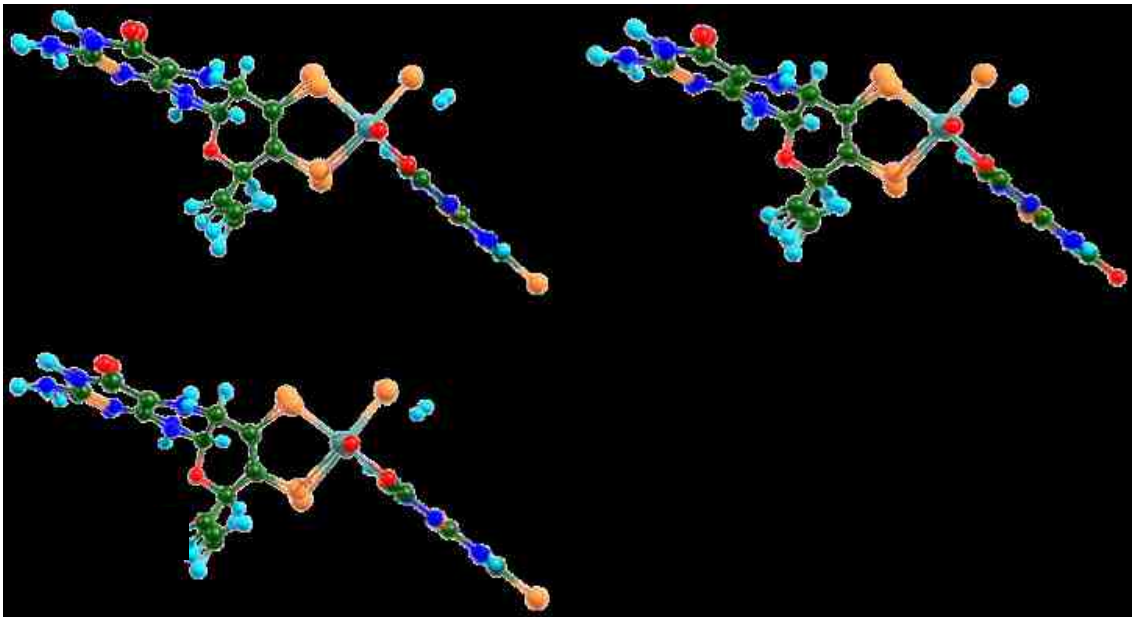

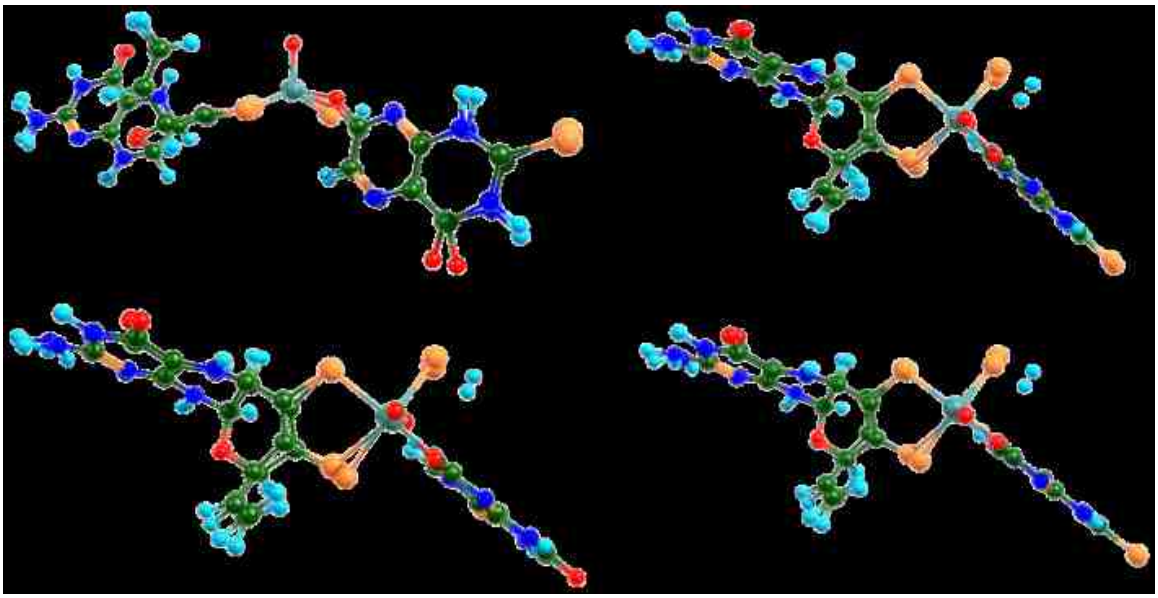

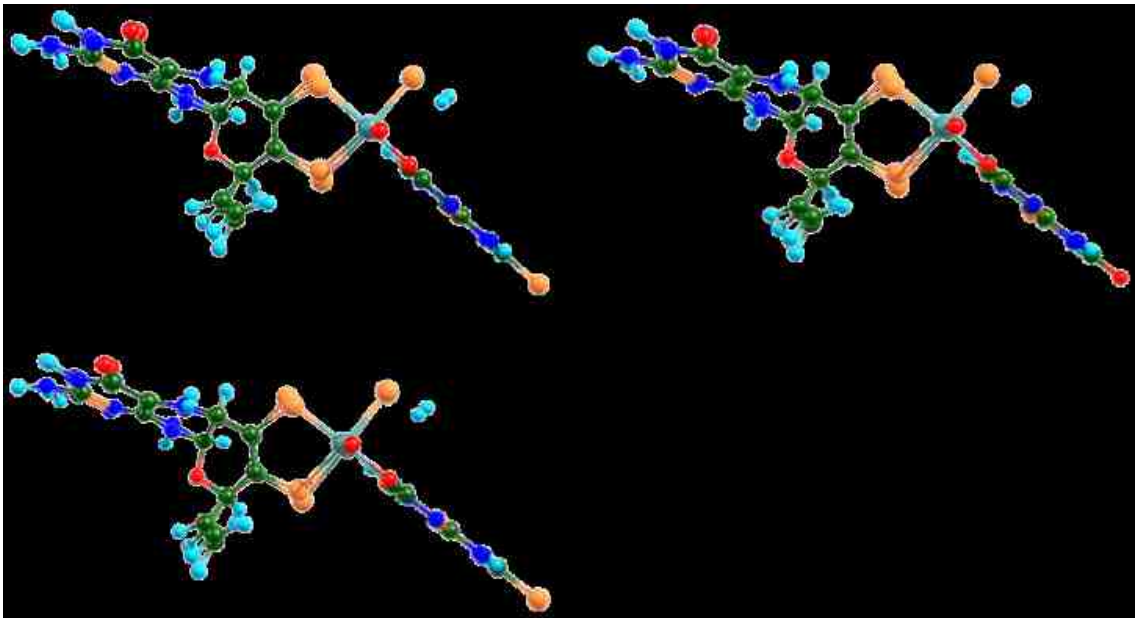

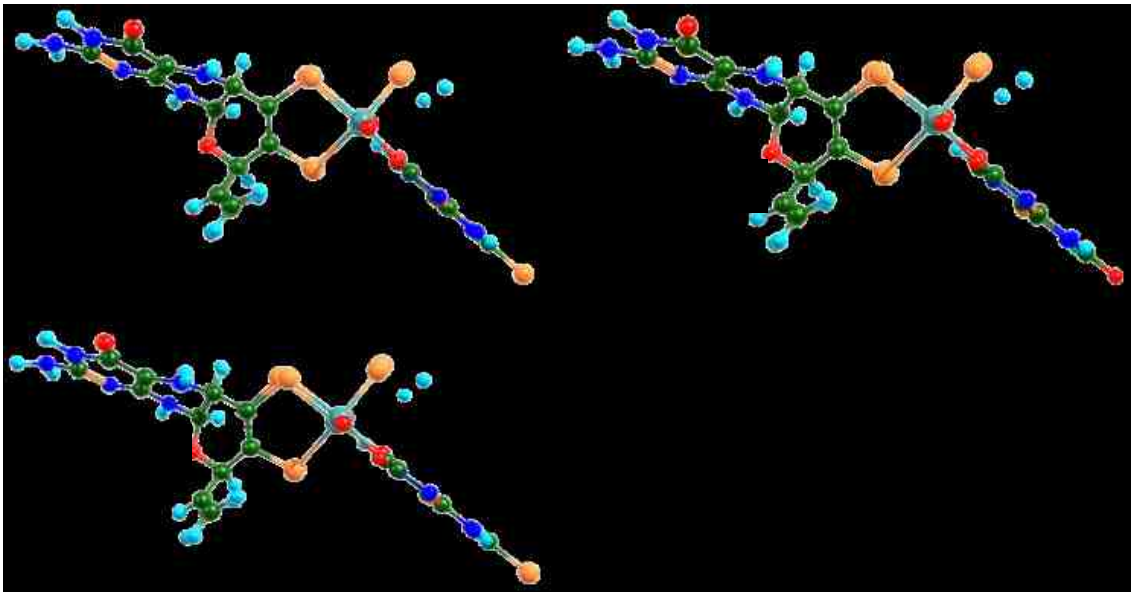

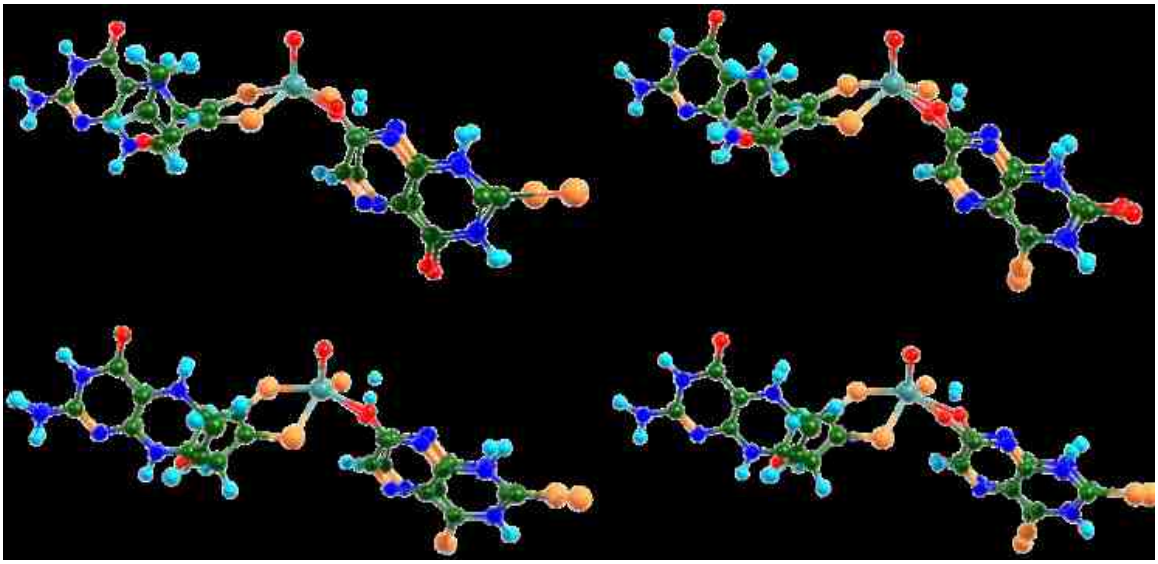

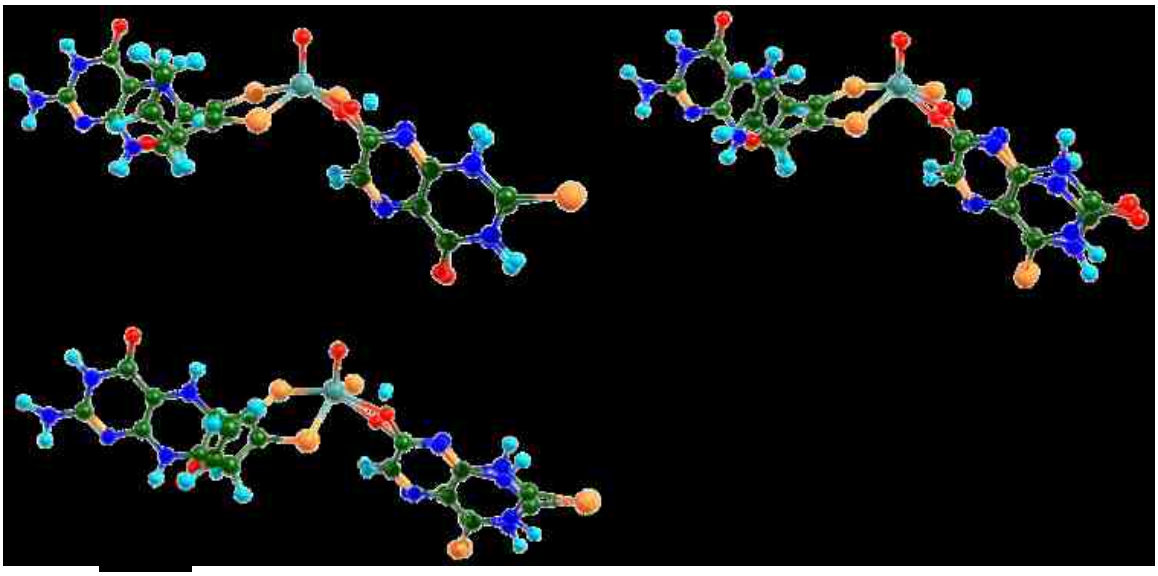

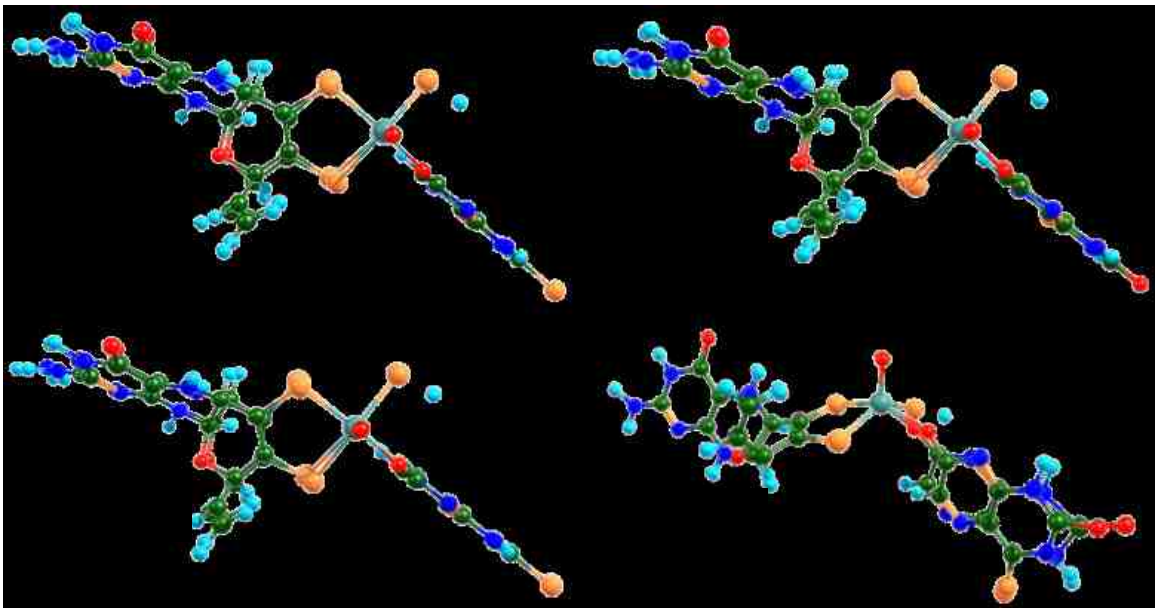

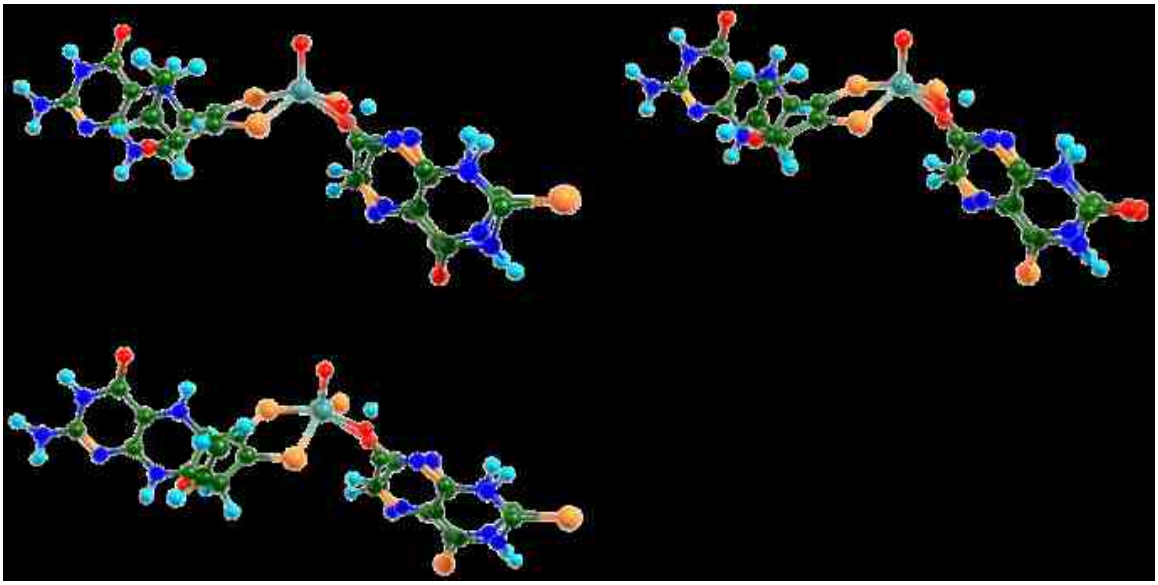

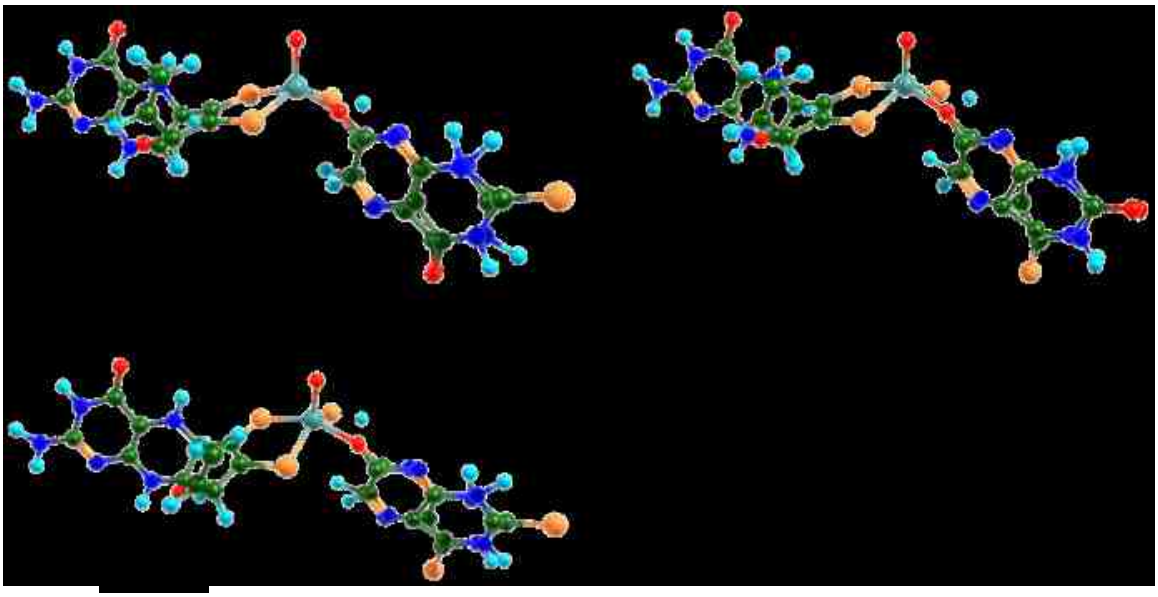

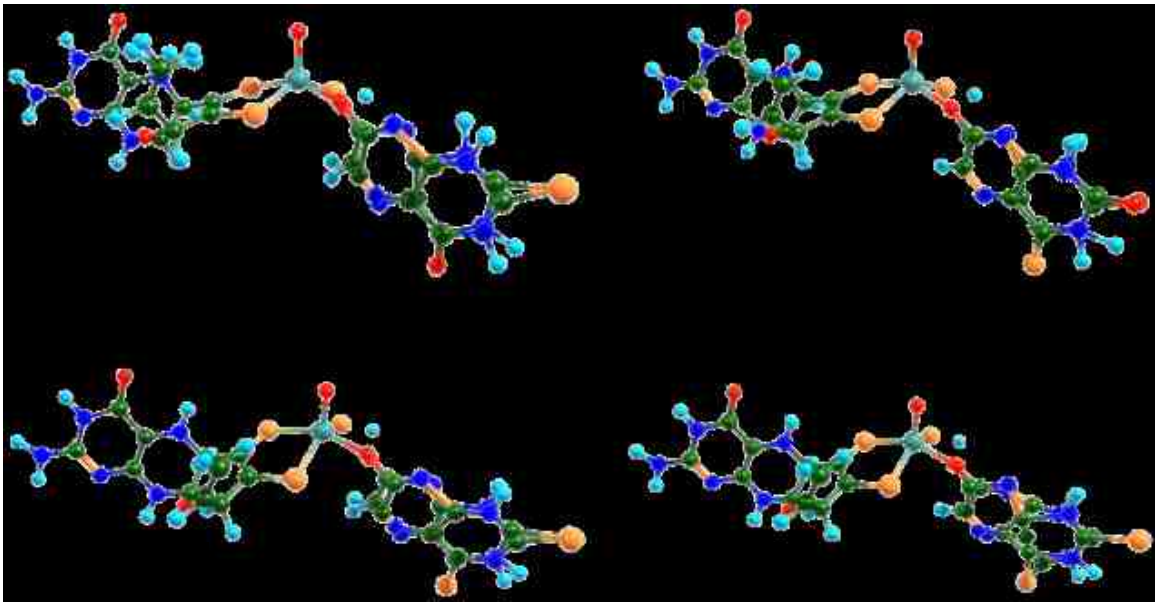

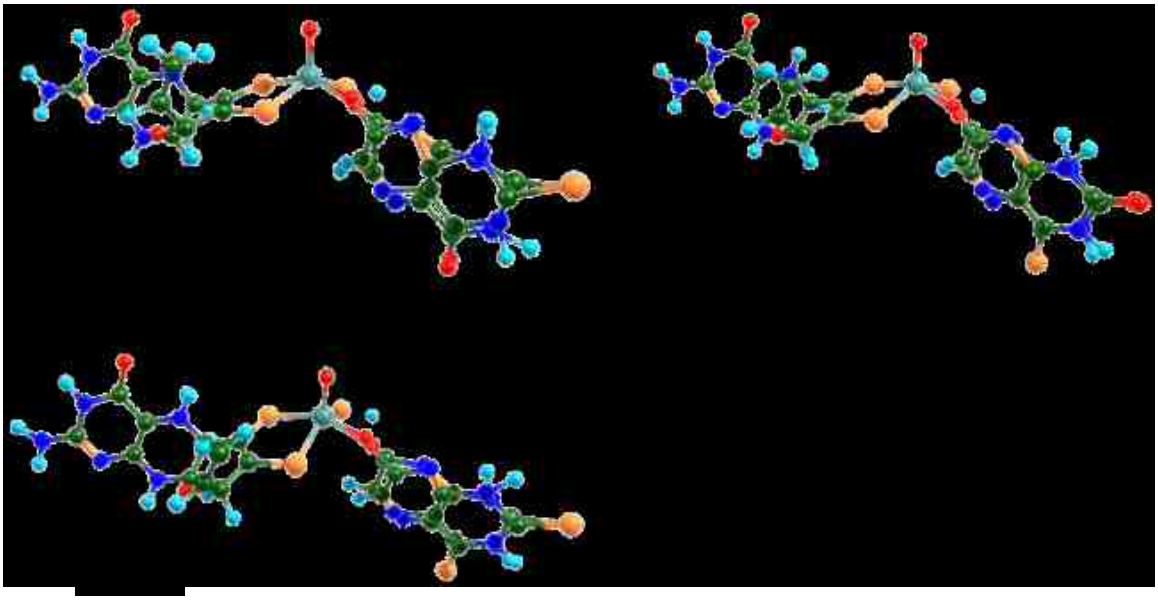

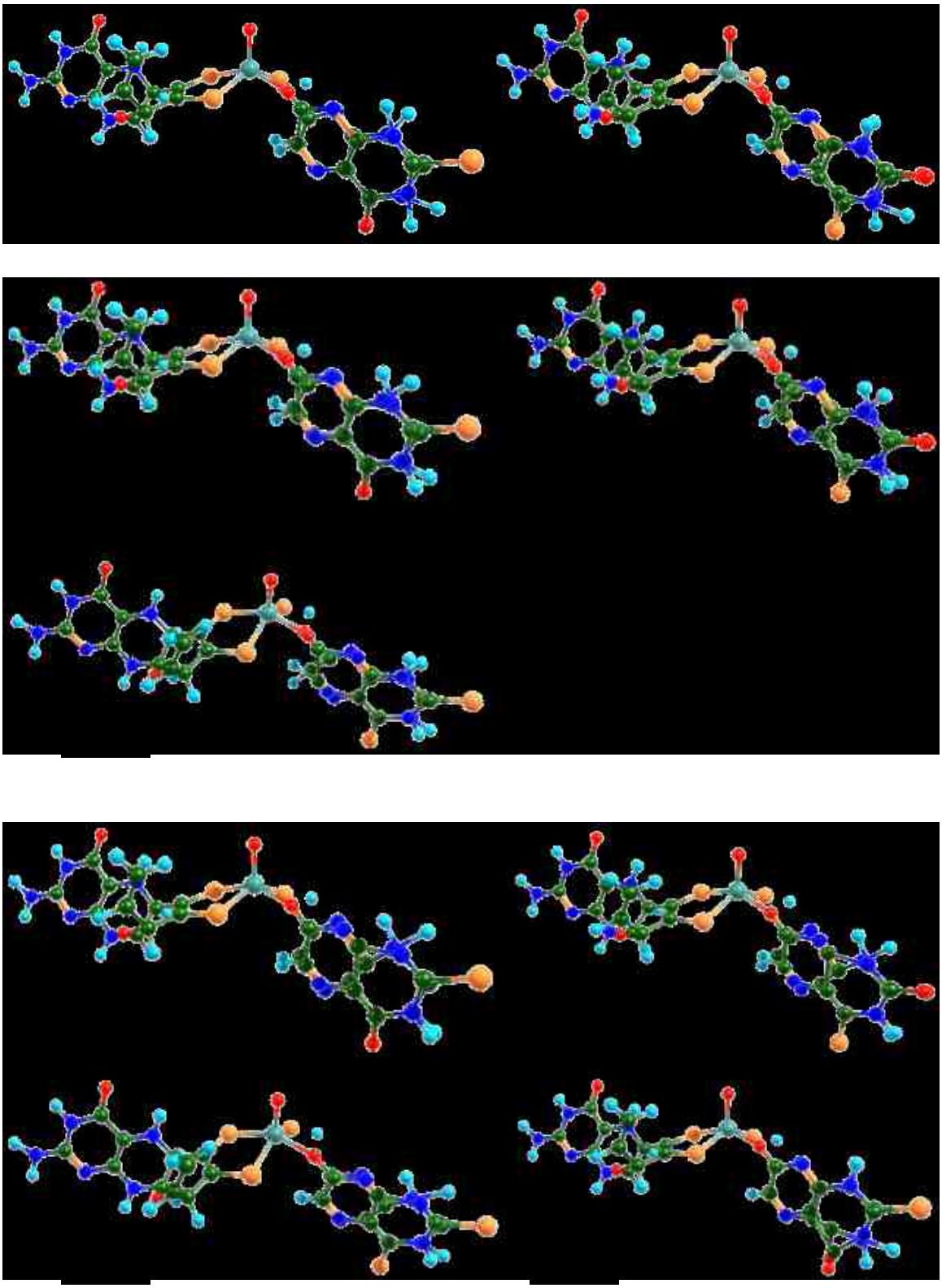

Figure 2.21 Plots of the vibrational modes for the XOr-violatperin derivatives.

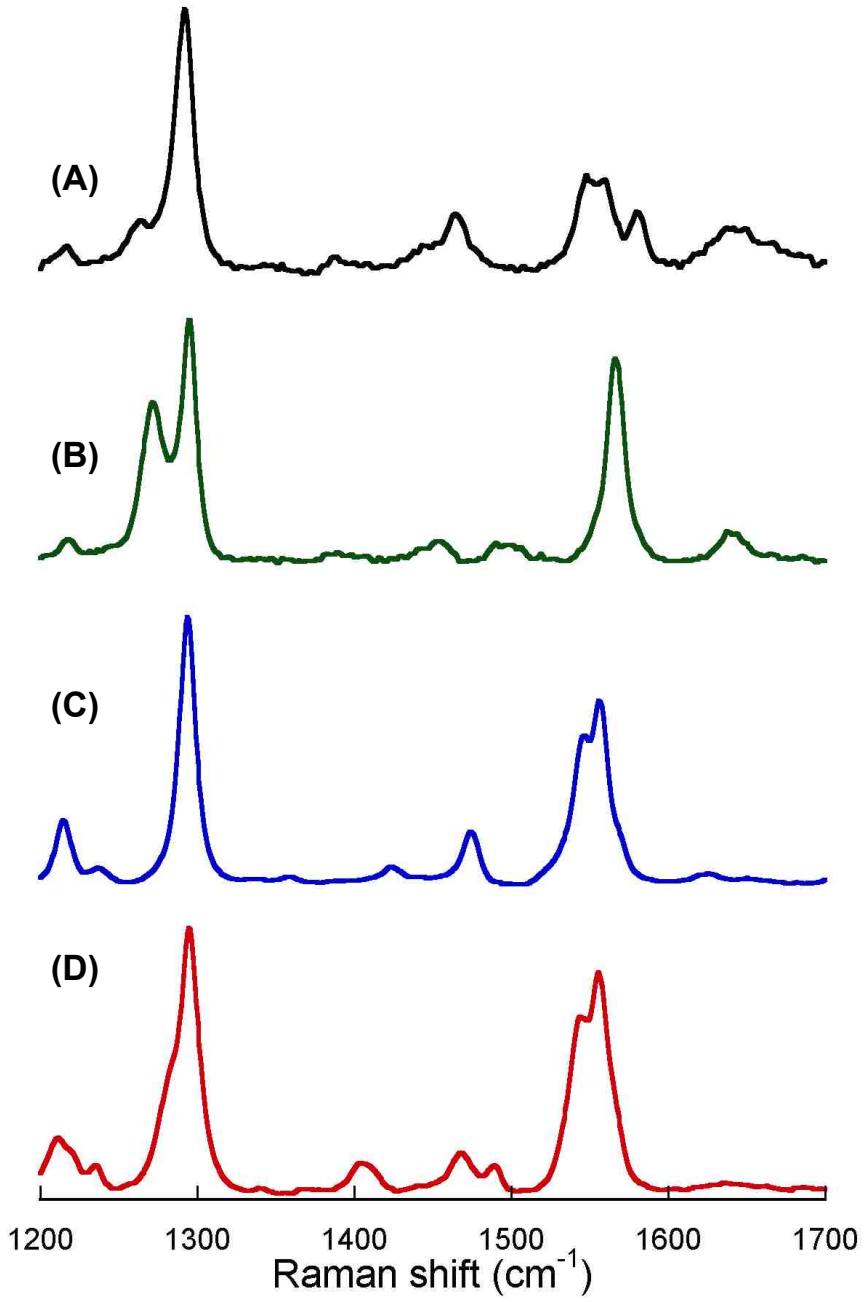

Figure 2.22 High frequency region of Raman spectra for XOr-violatperin derivatives.

2.4.2.3.2 High Frequency Region (1200-1700 cm^{-1})

In the high frequency region (1200 cm^{-1} to 1700 cm^{-1}), all of the samples show a similar pattern of two strongly enhanced peaks (~1290, and ~ 1560 cm^{-1}) and two medium medium enhanced peaks (~1215, 1465 cm^{-1})(Figure 2.22). As an example, XOr-2,4-dithioviolapterin displays Raman bands at 1556 cm^{-1}, 1543 cm^{-1}, 1489 cm^{-1}, 1467 cm^{-1} and 1294 cm^{-1}, and approximate 1277cm^{-1}. Computations yields similar bands at 1576 cm^{-1}, 1563 cm^{-1}, 1498 cm^{-1}, 1465 cm^{-1} and 1346 cm^{-1}, 1267 cm^{-1} respectively. Detailed vibrational mode descriptions are shown in Figure 2.21.

Table 2.5 High frequency region of the Raman spectra for XOr-violatperin derivatives. The labeled blue color signifies single bands in the experimental data can be linear combination of two bands.

XOr-2-thiovio			XOr-4-thiovio			XOr-2, 4-dithiovio		
Mode	Exp	Cal	Mode	Exp	Cal	Mode	Exp	Cal
101	1217	1186	98	1213	1197	101	1210	1219
104	1271	1263	101		1270	103	1277	1267
107	1294	1307	104	1293	1320	110	1294	1346
						117	1404	1429
116	1453	1461		1423	1447	119	1467	1465
120		1478	119	1474	1478	121	1489	1498
124	1493	1520	121		1507			
126		1575	123	1544	1556	125	1543	1563
127	1565	1578	124	1556	1574	126	1556	1576
132	1639	1668						

2.4.2.4 Transition State

A tetrahedral transition state (Figure 2.23 middle), which possesses a Mo-O-$C_{substrate}$ linkage, was found and confirmed by the observation of a single, imaginary, low-frequency vibrational mode that involves a $O_{hydoxyl}$-$C_{substrate}$-N

bend coupled to a $S_{sulfido}$-H stretching mode. The imaginary frequency frequency describes the H migration from $C_{substrate}$ to the sulfido, and the $C_{substrate}$ structure changes from sp^3 to sp^2 hybridized, which is consistent with a concerted mechanism involving involving nucleophilic attack of the Mo bound hydroxyl on the $C_{substrate}$ carbon of 4-thione-lumazine. Since a Mo-O-$C_{substrate}$ linkage is present at the transition state, it is of intense interest to understand the nature of this bonding scheme, particularly with respect to the two-electron oxidation of the substrate, the reduction of Mo(VI) to Mo(IV), and the transfer of the $C_{substrate}$-H hydrogen to the terminal sulfido ligand. The Mulliken charges on the $C_{substrate}$-H H-atom at the intermediate state (IM), transition state, and the XOr-product complexes are listed in Table 2.6. The data strongly suggests that the hydrogen that is transferred to the terminal sulfido possesses nearly neutral charge. The degree of Mo reduction along the reaction coordinate is strongly correlated to the degree of $C_{substrate}$-H bond cleavage, and the results strongly imply that the formation of a highly covalent Mo-O-$C_{substrate}$ bonding interaction. Analysis of the Mo(dxy) orbital character of the HOMO wave function for the points from IM to TS show that the Mo(IV)-product bound complex possesses 73.1% Mo(dxy) character. As a result we can calculate the degree of product formation along the reaction coordinate. The Mo(dxy) character in the HOMOs are 7.5% for IM and 27.7% for the TS respectively. The product formation is about 38% (27.7/73.1) complete at the transition state.

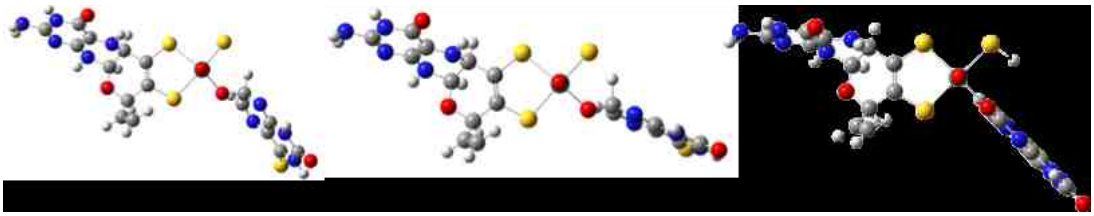

Figure 2.23 Optimized geometries of intermediate IM (left), transition state TS (middle) and intermediate II product (product bound reduced enzyme XO)(right).

Table 2.6 Atomic charge on the sulfido and the transferred hydrogen from the IM to TS using XOr-4-thioviolapterin and XOr-2, 4-dithioviolpaterin substrates.

XOr-4-thiovio	C-H (Å)	1.12 (IM)	1.22	1.24	1.262
	S	-0.43	-0.39	-0.37	-0.35
	H	0.123	0.098	0.086	0.072
XOr-2, 4-dithiovio	C-H (Å)	1.12 (IM)	1.22	1.24	1.27
	S	-0.41	-0.38	-0.37	-0.30
	H	0.073	0.053	0.048	0.045

2.4.2.5 Discussion

Directly probing the TS that is not possible because the TS is not spectroscopically accessible. However, spectroscopic studies of product bound reduced xanthine oxidase complexes, such as the Mo (IV)-4-thione-violapterin complex, that possesses a similar Mo-O-C linkage that may provide valuable insight into the nature of transition state and ultimately the mechanism of substrate hydroxylation by XO. Figure 2.24 shows the relationship between the intermediate I, the transition state, and the product complex (Intermediate II) along the reaction coordinate. The instability of ground state potential surface at

the TS directly results from the vibronic coupling with a stable excited state.

Figure 2.24 Reaction coordinate potential energy surface.

Therefore, spectroscopic studies on one electron transition to the related one-electron excited state potential energy surface can provide detailed information regarding the electronic structure contributions to the XO transition state and the overall reaction coordinate.

The high intensity of MLCT band results from appreciable Mo and product mixing as previously described, and this derives from large electron delocalization and covalency within the Mo-O-C linkage. From the electron density difference map the electron density moves from Mo center to the oxidized product in the MLCT excited state and involves the Mo-O-C bonding scheme. Here, electron flow is opposite that found along the ground state reaction coordinate during the oxidative hydroxylation of 4-dithiolumazine. The MLCT assignment is significant since the electron transfer direction going from the ground state to the MLCT excited state is from Mo to product resulting in a more “oxidized” Mo site and a bound violopterin that is more “reduced”.

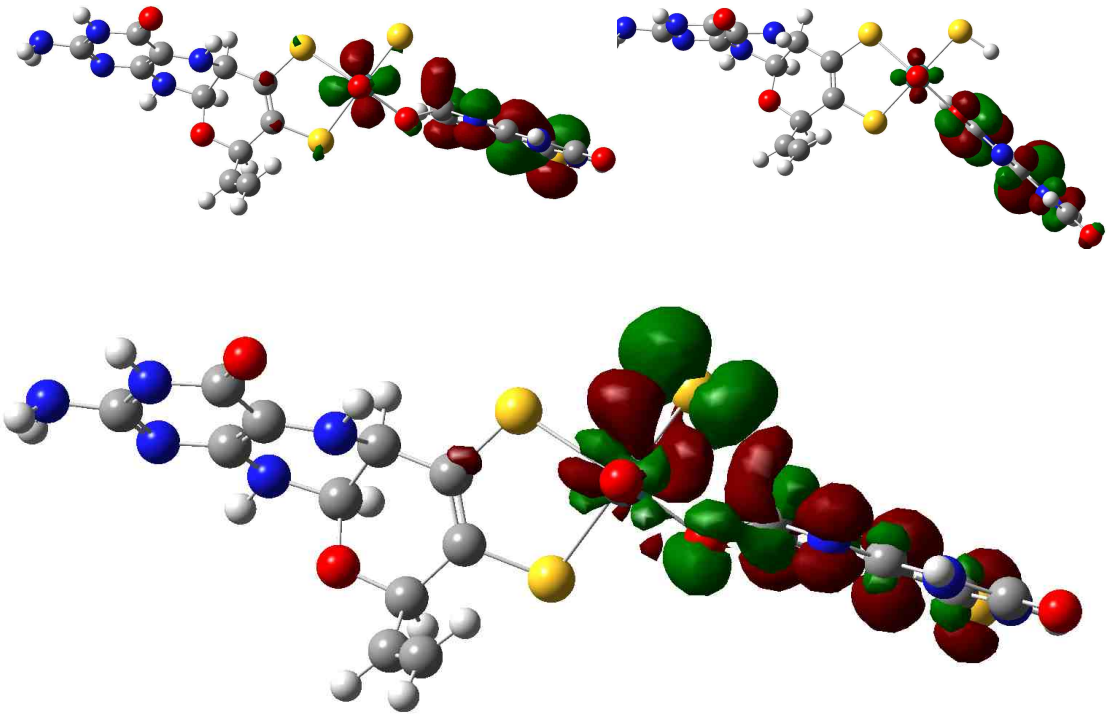

Figure 2.25 Top: comparison between HOMO of TS (left) and LUMO of XOr-P complex (right). Bottom: EDDM of TS.

A comparison between the TS HOMO wavefunction and the LUMO wavefunction for the Mo(IV)-P4-thioviolopterin complex is given in Figure 2.25. The remarkable similarity of these wavefunctions underscores the relationship between the MLCT state and the TS, and supports a through-bond Mo-O-$C_{substrate}$ pathway for Mo reduction, and proton transfer to a terminal sulfidothat becomes progressively more nucleophilic along the reaction coordinate. EDDM for transition state clearly indicates that electrons flow from substrate to Mo and sulfide where the Mo ion plays a double role as electron acceptor and electron donor. As such, our proposed spectroscopic studies extend early biochemical studies on XO where a Hammett plot was obtained for quinazoline oxidation activity.[46] This work showed that an increase in substrate electron density

facilitates a formal hydride transfer, which these researchers could not distinguish from a coupled 2e-/H+ transfer process.[47]

The intense MLCT band in XOr-violapterin derivatives not only helps us understand the electron transfer pathway during the oxidation of substrate, but also illuminates the utility of heavy atom substitution in the analysis of the Raman spectra. We expected that heavy atom congeners of lumazine would result in bathochromic shifts of the MLCT absorption maximum relative to the analogous complex formed with lumazine. The electronic absorption spectra for Mo-product complexes with 4-thioviolapterin (758 nm) and 2,4-dithioviolapteirn (778 nm) possess NIR absorbance maxima that are red shifted by ~3,000 cm^{-1} and ~4,000 cm^{-1}, respectively, relative to the XOr-violatperin MLCT complex.[25,26]

The bathochromic MLCT shift results in high quality rR data, since it effectively eliminates the dominant higher energy absorption contributions from the 2Fe2S and FAD centers, and deleterious contributions from free FAD fluorescence. The nature of the MLCT is such that optical pumping of this transition creates a transient hole at the Mo site that results in an excited state with appreciable Mo(V)-P•- character. Interrogation of this MLCT state by rR spectroscopy (Fig. 2.21 and table 2.4) provides important information regarding the nature of low-frequency Mo-PDT distortions that accompany the one electron oxidation of the Mo(IV) site during the initial ET event in the oxidative half reaction of the enzyme. To our knowledge, these are the first definitive assignments of a core Mo-dithiolene vibrational mode in a Mo hydroxylase enzyme. Additional support for this assignment is based on polarized rR spectra of the benchmark Mo-ditholene

complex Tp*Mo(bdt) (bdt = benzene-1,2-dithiolate), where the S-Mo-S symmetric stretch and bend are observed at 393 and 362 cm^{-1}, respectively[48,49]. Although low frequency rR data for pyranopterin molybdenum enzymes is sparse, vibrational data for enzymes of the DMSO reductase (DMSOR) family have been collected and analyzed [50,51]. In contrast to XO/XDH, DMSOR family enzymes possesses two PDTs bound to the Mo ion[52]. In the reduced form, $DMSOR_{red}$ displays S-Mo-S core vibrations at 352 cm^{-1} and 383 cm^{-1}, while for $DMSOR_{ox}$ these vibrations have been assigned at 350 cm^{-1} and 370 cm^{-1} [51,53]. Thus, the lower S-Mo-S frequencies for XO/XDH suggest a modified Mo-dithiolene bonding interaction when compared with the DMSOR enzymes, and this may be associated with their different functions (i.e. hydroxylation (XO/XDH) vs. oxygen atom transfer (DMSOR)) and respective redox partners.

The observation of PDT character in this mode indicates that the effect of instantaneous hole generation on Mo, induced by photoexcitation into the MLCT band, is felt at long distances from the Mo center. This supports the hypothesis that Mo(IV)→Mo(V) oxidation in the oxidative half reaction of XO/XDH is also coupled to PDT vibrational distortions, providing strong evidence for the direct involvement of the PDT in enzymatic ET. A similarly large number of low frequency vibrational modes have also been observed in the rR spectra of the blue copper proteins plastocyanin and azurin upon photoexcitation into the intense S_{Cys}→Cu LMCT band.[54] This has been explained by kinematic coupling of the coordinated cysteine side chain with the Cu-S_{Cys} stretching coordinate, underscoring the importance of an ET pathway that involves the coordinated

cysteine. Similarly, the four less intense vibrational modes in XO/XDH that are observed at frequencies below ~375 cm^{-1} all likely possess Mo-PDT character (Figure 2.21) and further support the hypothesis that the PDT functions as an effective conduit for ET between the reduced Mo center and the 2Fe2S clusters in the protein.

The product plane is essentially orthogonal to the square pyramidal basal ligand plane in reduced XO. This geometric orientation allows for efficient π type overlap between the product π system and the Mo dxy redox orbital, which effectively enables low a lying vacant MO on product to play a π acceptor role with respect to donating from Mo dxy. As a result, the ring in-plane modes involved in the π^* acceptor get enhanced in the higher energy region of resonance Raman spectra for the XOr-4-thioviolaperin and XOr-2, 4-dithioviolapterin complexes.

2.4.2.6 Conclusions

We have obtained high quality rR spectra of two new Mo(IV)-product complexes by exciting into the NIR Mo(IV)→product MLCT band. The use of S/O substitution for the violopterin product carbonyl oxygen atoms enables the assignment of resonantly enhanced low-frequency Mo-PDT modes. The observation of these PDT modes provides evidence for the PDT ligand being coupled to redox changes at the Mo site and serving as an ET conduit in the oxidative half reaction of XO/XDH.

2.4.3 Violapterin Derivatives that React with Reduced wtXDH and Specific Variants

The high resolution and quality rRman spectra of XOr-4-thiioviolapteirn and XOr-2, 4-dithioviolapterin provide us with an opportunity to study the role of the conserved amino acid residues at the active site spectroscopic-ally through the perturbation on the frequencies of vibrational modes by hydrogen bonding interactions. The amino acid residues E802, E1261 and R880 (Xanthine Oxidase) around the substrate-binding pocket are proposed to recognize and orientate substrate by hydrogen bonding interactions. The terminal amine group of the pyranopterin points toward the 2Fe/2S I cluster. Q102 is located between the pyranopterin and the 2Fe/2S I cluster and may hydrogen bonding with both. Due to the fact that the active sites of XO and XDH wild type *R. capsulatus* XDH are virtually identical, XDH variants have been used with luamzine derivatives.

2.4.3.1 Violapterin Derivatives React with Reduced wtXDH

Resonance Raman spectra of wtXDHr-4-thioviolatperin and wtXDHr-2, 4-dithioviolapterin charge transfer complexes were collected and compared with the XOr-product complexes. Figures 2.26 and 2.27 show the overlap of rRaman spectra for XOr-4-thiovolapterin and wtXDHr-4-thiovolapterin, XOr-2, 4-dithiovolapterin, and wtXDHr-2, 4-dithiovolapterin. Their identical rRaman spectra show the structural similarity of their active sites.

Control experiments were also preformed. The product 4-thioviolapterin and 2,4-dithioviolpaterin can be produce by XO and separated for “backward reaction” with reduced wtXDH. First the “backward” experiment is run to make sure that future experiments are practicable. The wtXDHr-4-thiovolapterin complex may be

taken as an example and is shown in Figure 2.28. The results indicated the designed plan works.

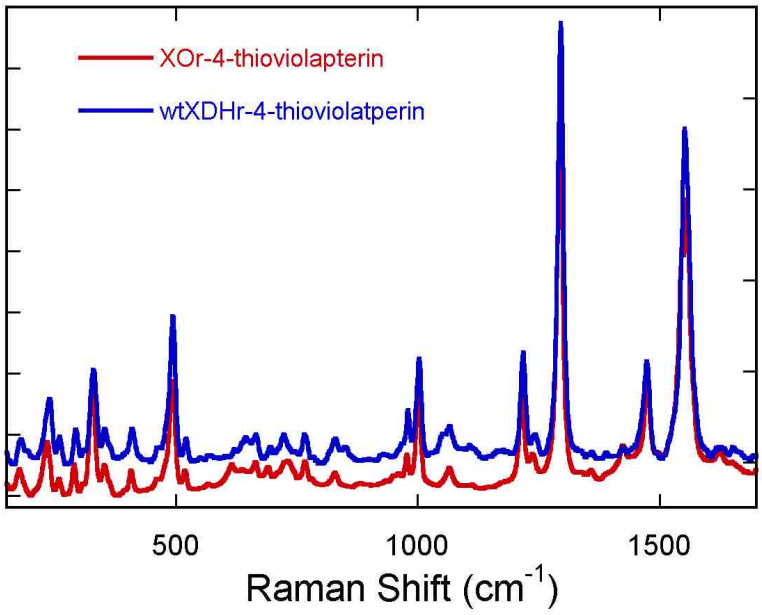

Figure 2.26 Overlap of rRaman spectra for XOr-4-thiovolapterin and wtXDHr-4-thiovolapterin (the 780nm laser is used to excite the absorption band).

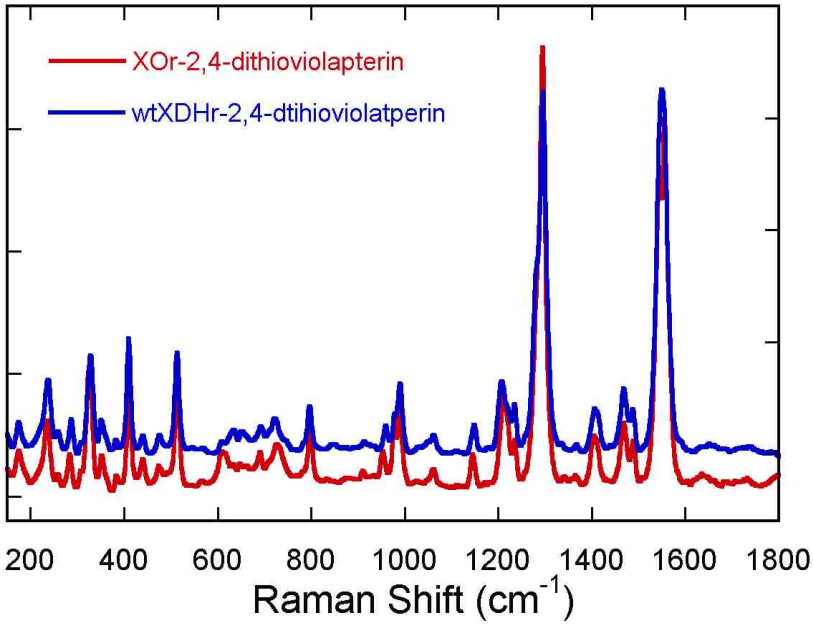

Figure 2.27 Overlap of rRaman spectra for XOr-2, 4-dithiovolapterin and wtXDHr-2, 4-dithiovolapterin (the 780nm laser is used to excite the absorption band).

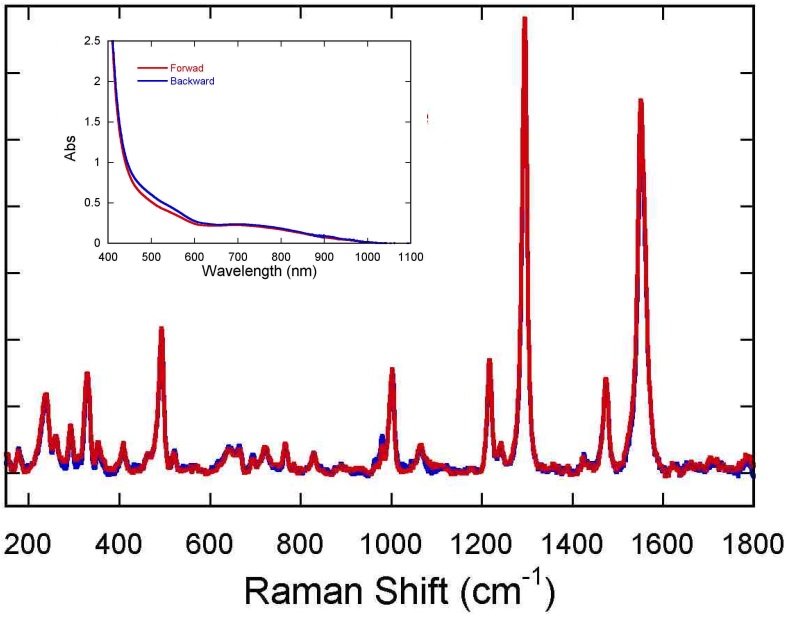

Figure 2.28 Overlap of rRaman spectra for the forward band backward reaction. Inset is the electronic absorption spectra for the forward and backward reaction. Forward: wtXDH, 4-thiolumazine and dithionite; Backward: wtXDH, dithionite and 4-thioviolapterin.

well, since the “backward reaction” can produce the same spectroscopic properties as the “forward reaction”. The strong rRaman enhancement arises from the product bound reduced enzyme as indicated in Figure 2.29.

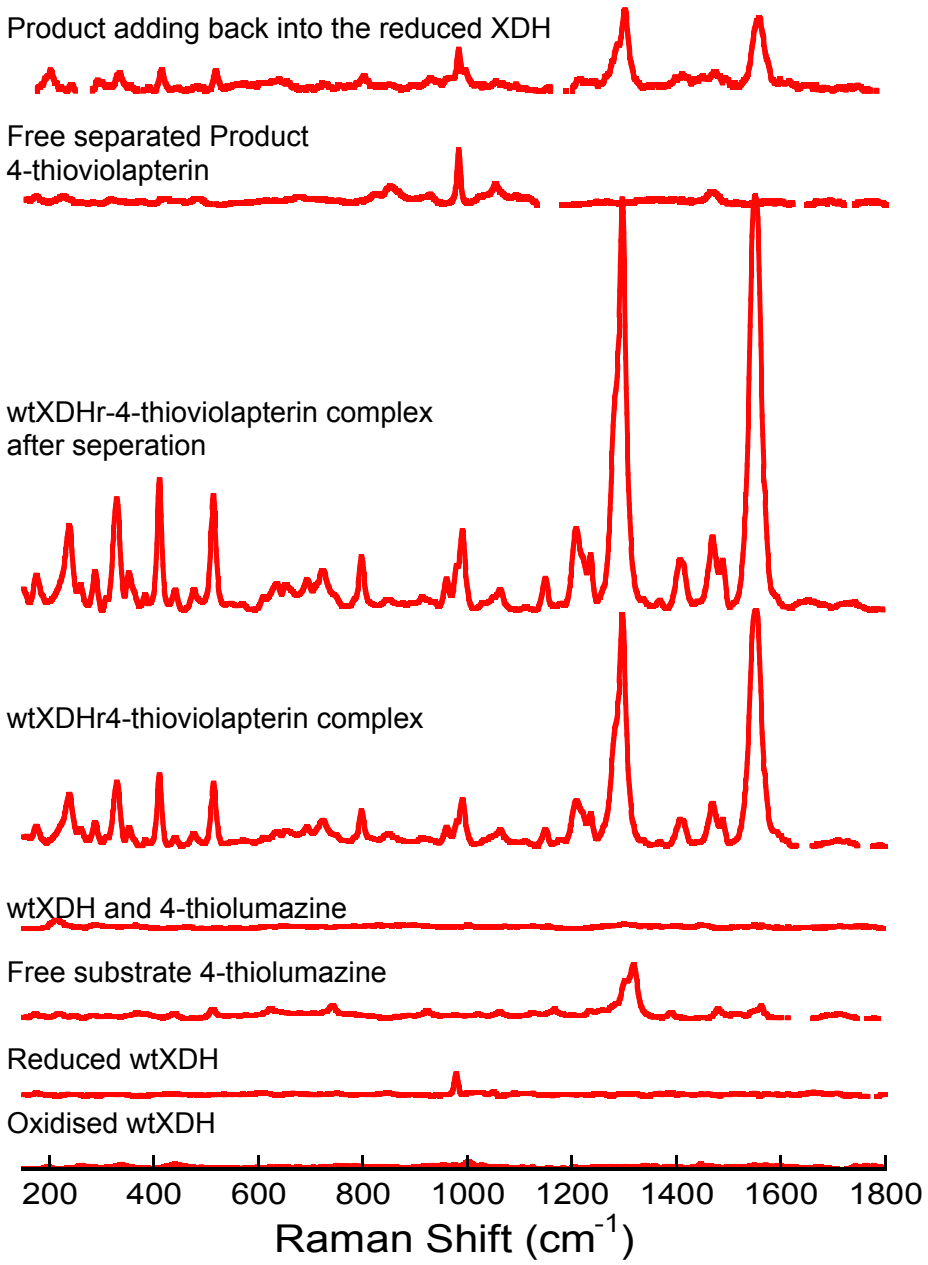

Figure 2.29 Control experiment for the origin of the rRaman signal.

2.4.3.2 4-thioviolapterin Reactivity

The electronic absorption spectra for the oxidized wtXDH and its variants are displayed in Figure 2.30 (top). As predicted, the electronic absorption spectra for

the wt-XDH and the four variants showed no difference in their oxidized forms. This indicates that the mutation of Glu232, Glu730 and Arg310 positions does not affect the overall electronic properties significantly. However, the difference spectra obtained from reduced enzyme-product complexes show a difference between the variants and the wt-XDH (Figure 2.30 (bottom)). Only the reduced wt-XDH protein bound with 4-thioviolapterin forms a broad band at 750 nm. All four reduced variants show no the formation of enzyme-product complexes.

2.4.3.3 Discussion and Conclusion

The product 4-thioviolapterin can't bind the reduced XDH variants with mutated amino residues at the substrate-binding pocket. Since glutamate and arginine are mutated to alanine, the carbon chain length changes and positive charge also disappears. Initially it was thought that the conformational changes were so greatly that the ability of hydrogen bonding from the conserved amino residues was lost in the variants. However, when reduced E730D was tested to react with 4-thioviolapterin this variant still can't form a charge transfer complex even though the substituted amino acid is only one carbon bond length shorter compared with E730.

In summary, even though the conformations of XDH variants change slightly, they all lose the substrate-binding ability as evidenced by the lack of an MLCT feature. Interestingly, E730 appears to play a significant role in substrate/product binding.[12,14]

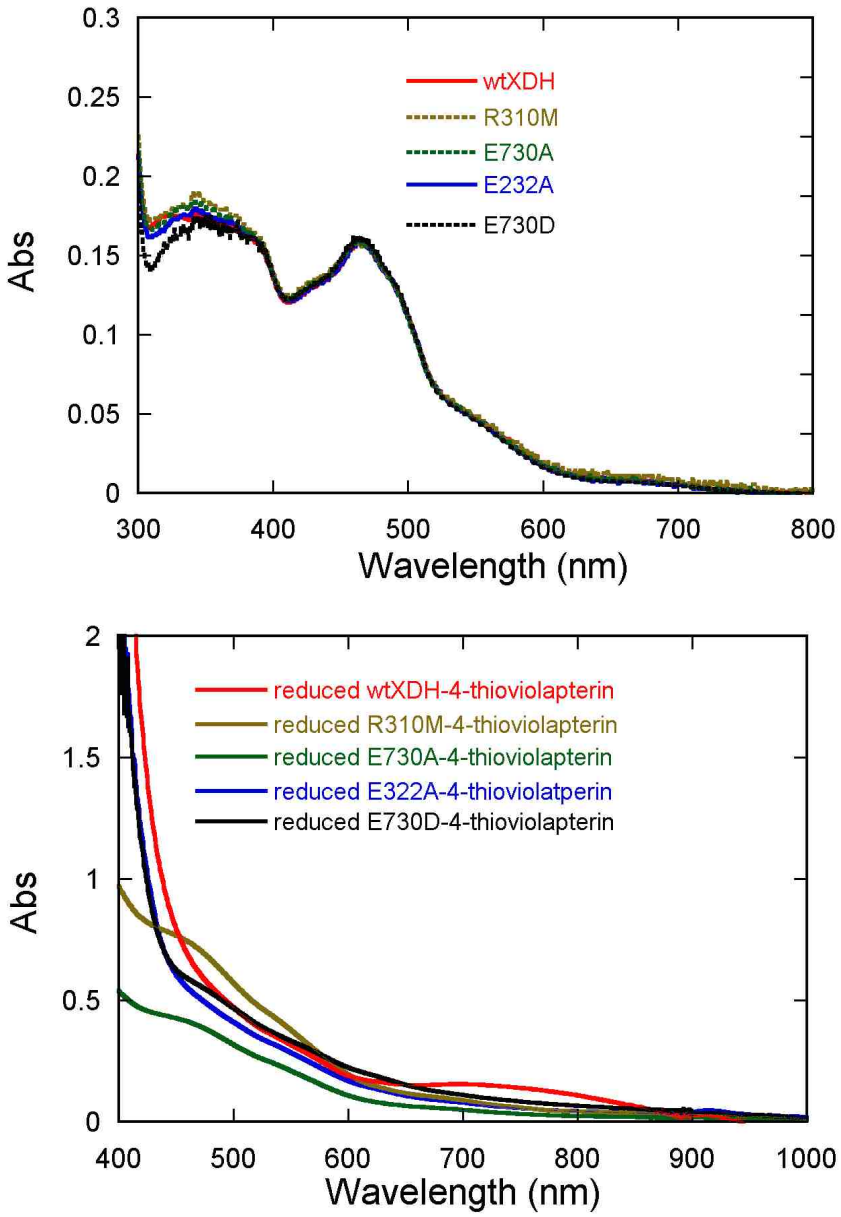

Figure 2.30 Room temperature electronic absorption spectra for oxidized wt-XDH and its variants: wt-XDH (red), variant E232A (blue), variant R310M (brown), variant E730D (black) and variant E730A (green) (top). Electronic absorption spectra obtained after product 4-thioviolapterin additions to reduced enzymes (bottom).

2.4.4 Probing the Q197A and Q102A Perturbation on the Mo-PDT

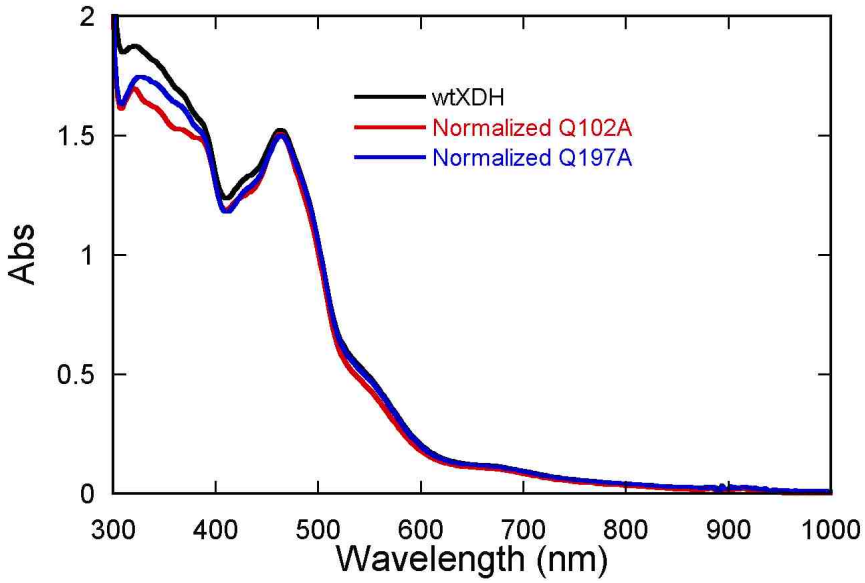

Figure 2.31 Room temperature electronic absorption spectra for oxidized wt-XDH and variants: wt-XDH (black), variant Q197A (blue), variant Q102A (red).

Vibrational modes of the Mo-PDT are observed in the low energy region of rRaman spectra. Q197 potentially interacts with the apical Mo-Oxo and Q102 potentially interacts with the terminal amino group of the pyranopterin. Here we study alanine variants to see if there is any hydrogen bonding perturbation on the vibrational frequencies of the Mo-PDT.

2.4.4.1 Charge Transfer Band

The electronic absorption spectra of wtXDH, Q197A and Q102A are very similar in the 400-600nm spectral range due to the strong absorption from the 2Fe2S clusters and FAD absorbance (Figure 2.31). The electronic absorption difference spectra shown in Figure 2.32 reveal that the MLCT band of the Q197Ar-product complex is blue shifted by about 20nm compared with the 750nm absorption of the reduced wild type enzyme product complex. The MLCT band of the Q102Ar-

product complex does not appear to shift relative to the reduced wild type enzyme product complex.

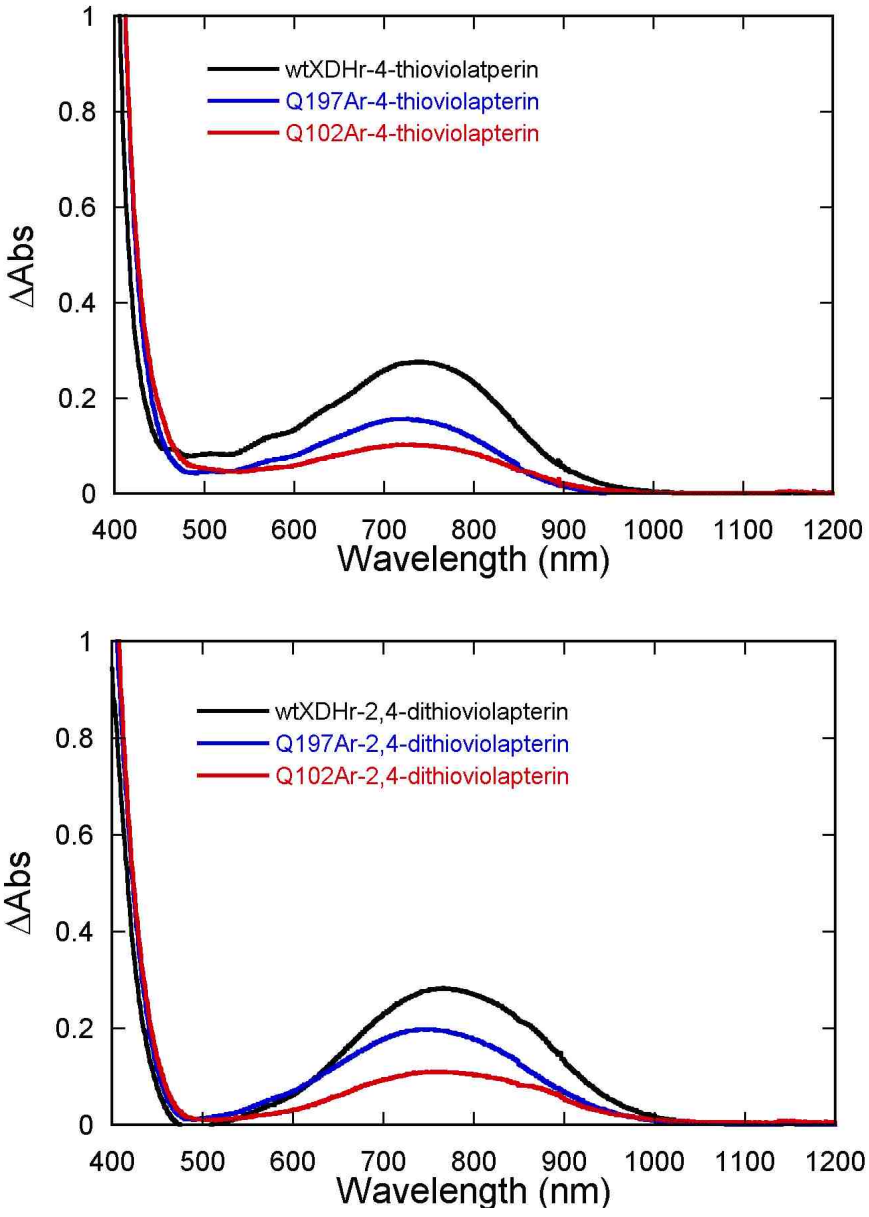

Figure 2.32 Room temperature electronic absorption spectra for reduced wt-XDH and variants: variant Q102A (red). XDH (black) and variants (Q197-blue and Q102-red) bound with 2, 4-dithioviolapterin and 4-thioviolapterin respectively. Difference spectra obtained from enzyme-product complex by subtracting reduced enzyme spectra.

2.4.4.2 Resonance Raman Spectra

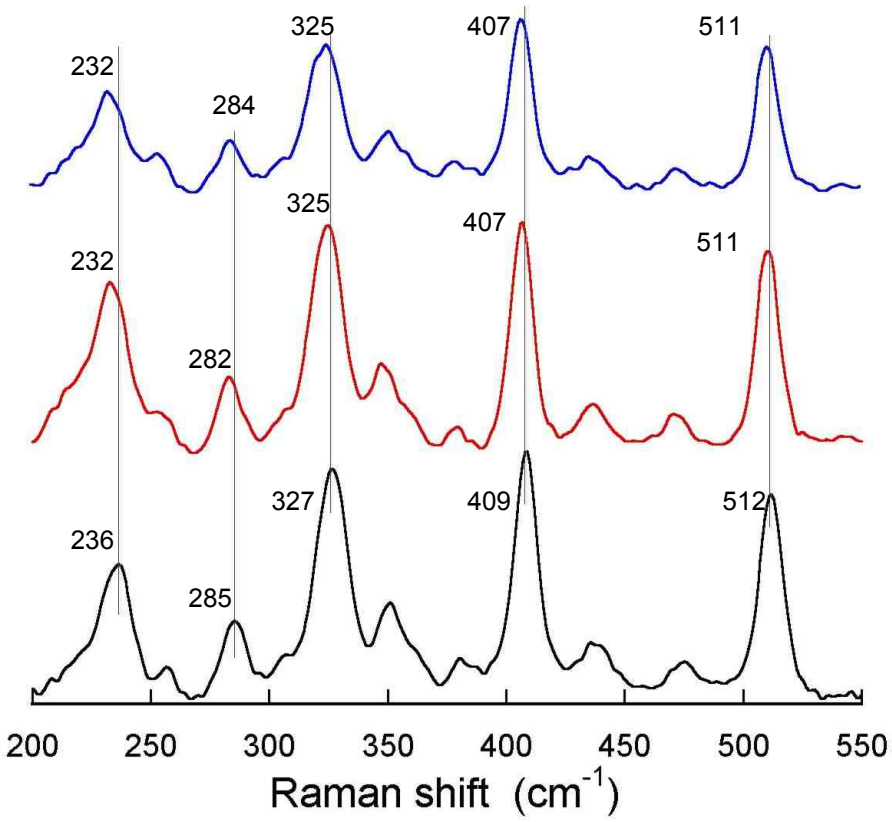

Figure 2.33 Comparative resonance Raman spectra in low frequency region of the reduced wild type XDH (black) and variants (Q197-blue and Q102-red) bound with 2, 4-dithioviolapterin.

The high-frequency region of the resonance Raman spectra for reduced wtXDH, Q197A and Q102A enzyme bound with 4-thioviolapterin and 2,4-dithioviolapterin respectively, are plotted in Figure 2.34. It can be observed that essentially no rR vibrational frequencies from product involved modes (band-shift greater than 1 cm^{-1}) are perturbed. The low frequency rR spectra (Figures 2.33 and 2.35) of the the Q198 variant shows band shifts of 3-4 cm^{-1} while the Q102A variant shows a smaller band shifts between 1-2 cm^{-1}.

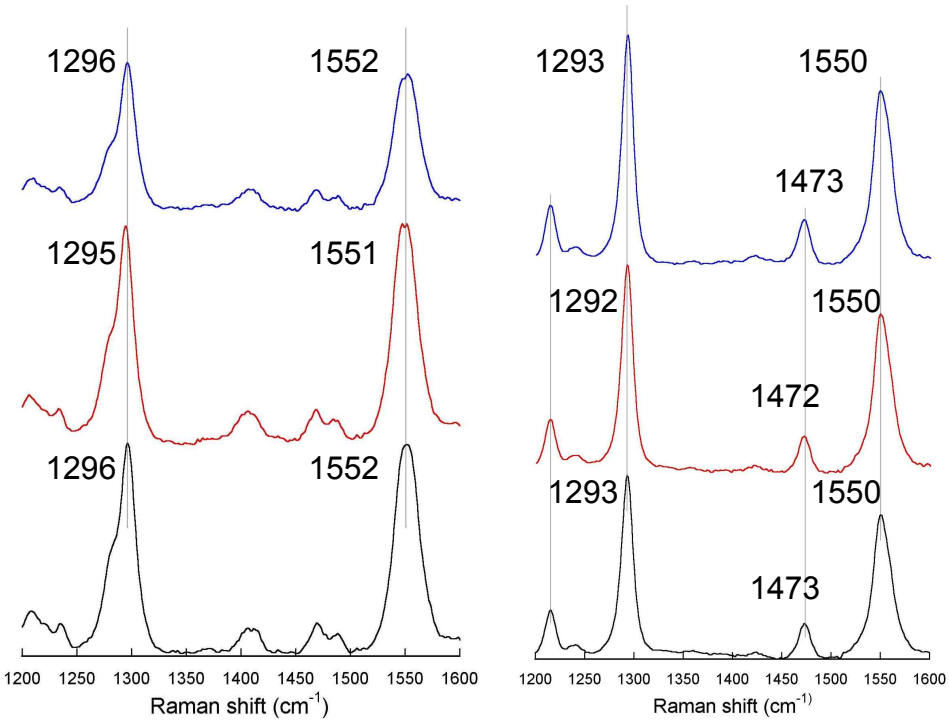

Figure 2.34 Comparative resonance Raman spectra in high-energy region of the reduced wild type XDH (black) and variants (Q197-blue and Q102-red) bound with 2, 4-dithioviolapterin (left) and 4-thioviolapterin (right).

2.4.4.3 Discussion and Conclusions

In high frequency region, the bands with highest remain virtually unchanged. However, in the low frequency region some bands do appear to shift. This indicates that hydrogen bonding effects these modes slightly. Q197 potentially interacts with the Mo-oxo, and with a 2.8 Å hydrogen bond length can directly perturb low frequency bending motions involving the Mo-oxo. However, Q102 is 7 Å away from the Mo-dithiolene and may be expected to have a markedly smaller perturbation. Analysis of the data indicates PDT is kinematic coupling

with the S-Mo-S stretching and bending modes. It is possible that EPR spectroscopy of the aldehyde inhibited paramagnetic species shows perturbations due to Q197 mutations since they may create a perturbation on the Mo geometry.

In summary Q197 possesses a relatively stronger hydrogen bonding interaction with Mo-oxo compared to the weaker Q102 hydrogen bonding with the amino group at the end of the PDT cofactor. It may be that Q197 modulates the molybdenum reduction potential while Q102 affects the PDT in a manner that facilitates electron transfer from Mo to 2Fe2S I.

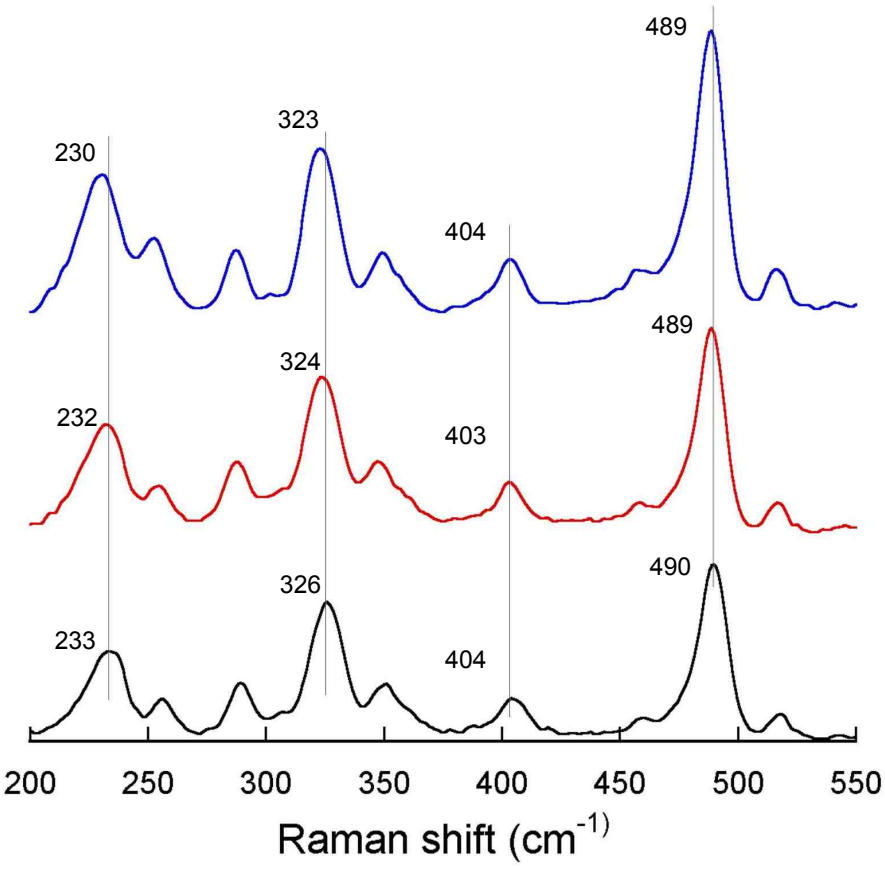

Figure 2.35 Comparative resonance Raman spectra of the reduced wild type XDH (black) and variants (Q197-blue and Q102-red) bound with 4-thioviolapterin.

2.4.5 Reactions of FYX051 and FYX051C with XO/XDH

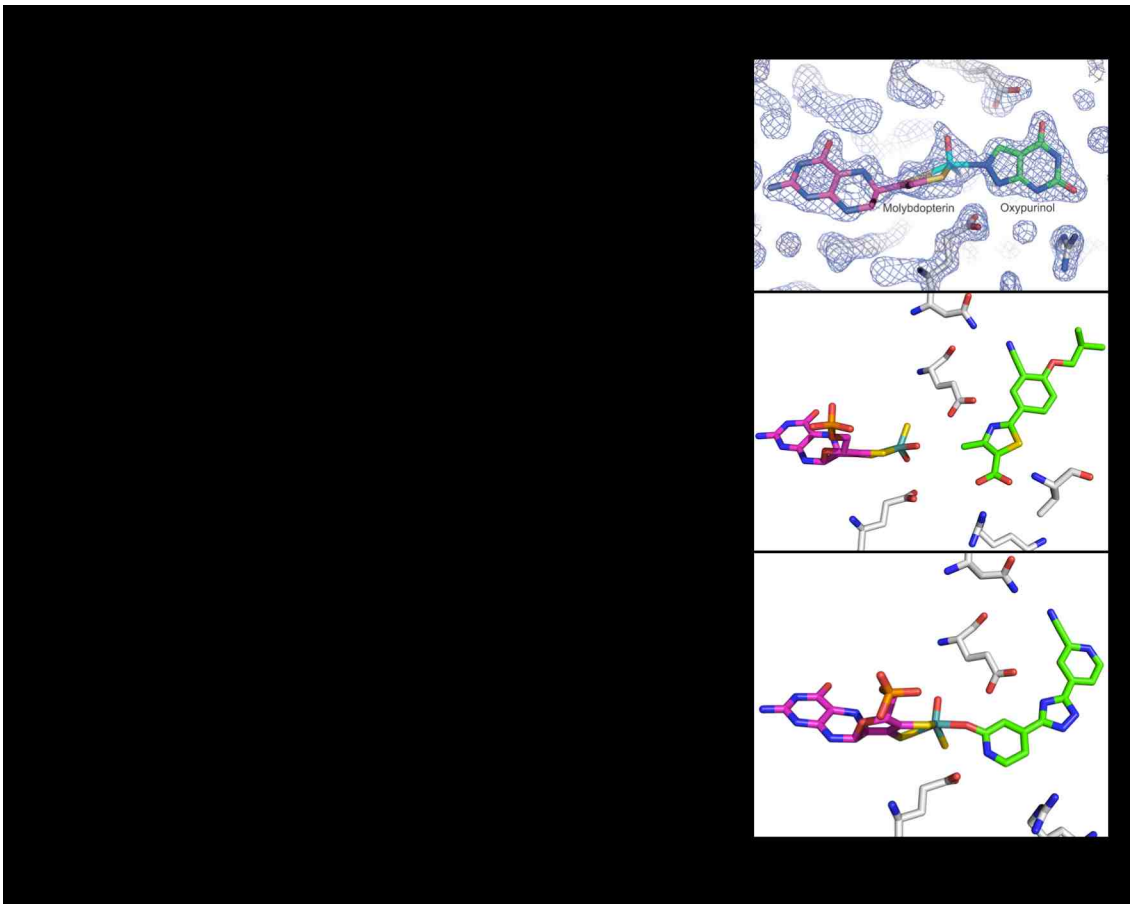

Figure 2.36 The development of molybdenum hydroxylase enzyme inhibitor FYX051 ($t_{1/2}$ is lifetime). [39,55,56]

Another reduced xanthine oxidase product bound species is found to have an intense charge transfer band at 590nm.[23] When the FYX051 substrate is hydroxylated, it binds the molybdenum center via a covalent linkage with oxygen and gives rise to a charge transfer band at 640nm.[22] After a prolonged the reaction time (120hours) an intense 590nm charge transfer band appears that originates from the tri-hydroxylation product bound to the reduced molybdenum

center. During this reaction the substrate sequentially hydroxylated to tri-hydroxy form. Finally the oxidized tri-hydroxy FYX051 product is coordinated to molybdenum. The di-hydroxy FYX051 species appears to have a 24h lifetime. FYX051 is a mechanism-based inhibitor and is used as a drug for treating gout, which arises from excessive uric acid crystallization in the blood vessels and joints (due to xanthine hydroxylation). It has been developed from structure-based inhibitors to result in a hybrid type structural/functional inhibitor (Figure 2.36).[18,23,39] In the substrate channel it is clearly seen that the hydrogen bonding interactions between FYX051 and conserved amino residues occur. The enzyme-product complex shown in Figure 2.37 (left) has potential hydrogen bonds with Glu802 and Arg880. Therefore, we have designed the analog of FYX051C (Figure 2.37 (right)) to probe these potential hydrogen bonding interactions.

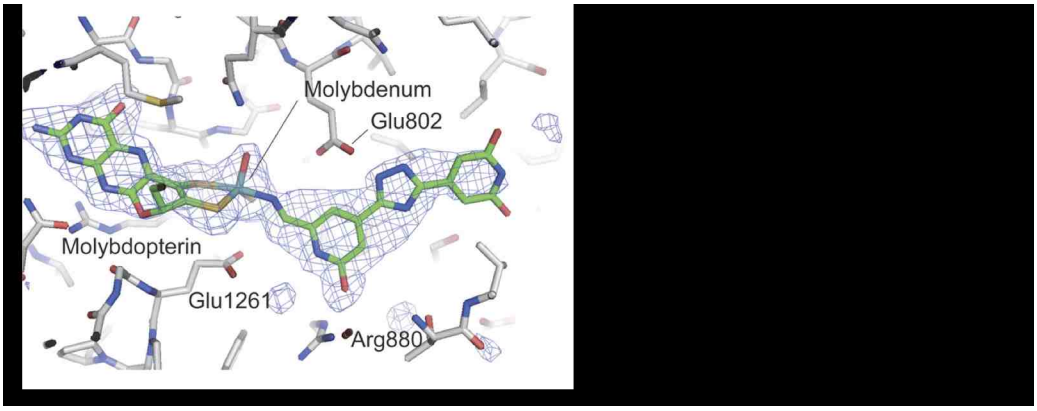

Figure 2.37 Left: crystal structure of XOR active site;[23] right: molecules FYX051 and FYX051C.

2.4.5.1 Electronic Absorption Spectra of XOr-FYX051 and XOr-FYX051C

The electronic absorption of XOr-FYX051 and XOr-FYX051C are shown in Figure 2.38. After 120h incubation, a broad peak is observed in both complexes. The electronic absorption spectra of reduced enzymes have also been collected in order to obtain the difference spectra. After spectral subtraction, we can see that the low-energy charge transfer band of XOr-FYX051C shifts to 605nm compared with the 586nm absorption of XOr-FYX051.

2.4.5.2 Discussion

Electronic absorption spectra indicate that the E232 variant located on the top of the substrate-binding pocket doesn't affect the final tri-hydroxy-FYX051 since we still observe the intense charge transfer band at 605nm. This may be due to the hybrid properties of substrate. It is very important to continue additional research efforts here. If we can observe the resonance Raman spectra of XOr-tri-hydroxy-FYX051 and XOR-tri-hydroxy-FYX051C enzyme product complexes, this will allow for direct comparison of the difference between them. Also the assignment of CN vibration may tell us whether the linkage to Mo is composed of CN or not. A large CN Raman shift will occur if the CN group is directly connected to the molybdenum center. Additionally the study of variants with FYX051 and FYX051C may show perturbations on vibrational modes from hydrogen bonding to key amino acid residues.

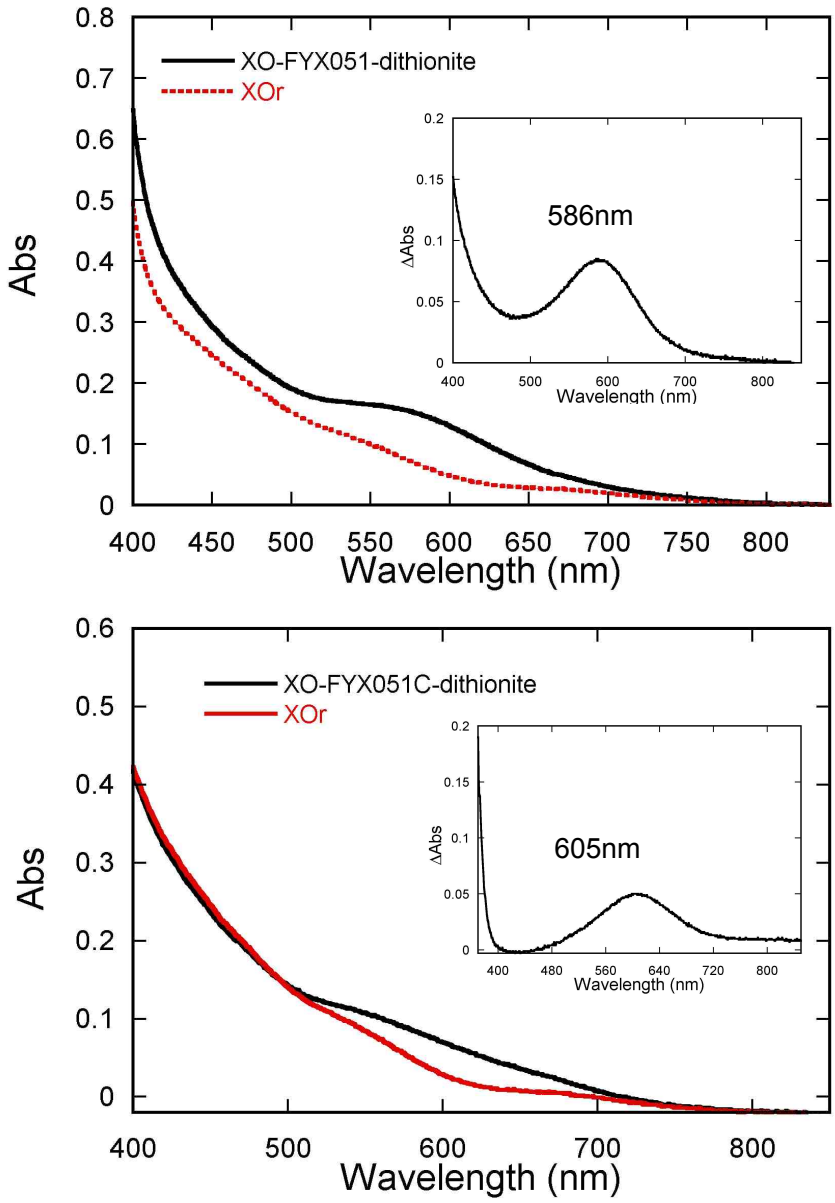

Figure 2.38 Electronic absorption spectra of XOr-tri-hydroxy-FYX051 (top) and XOr-tri-hydroxy-FYX051C (bottom) after 120h of incubations. Insets are the difference spectra of XOr-Product and XOr (27mM enzyme with excessive substrate).

2.4.6 EPR Spectra of Aldehyde Inhibited wtXDH and Its Variants

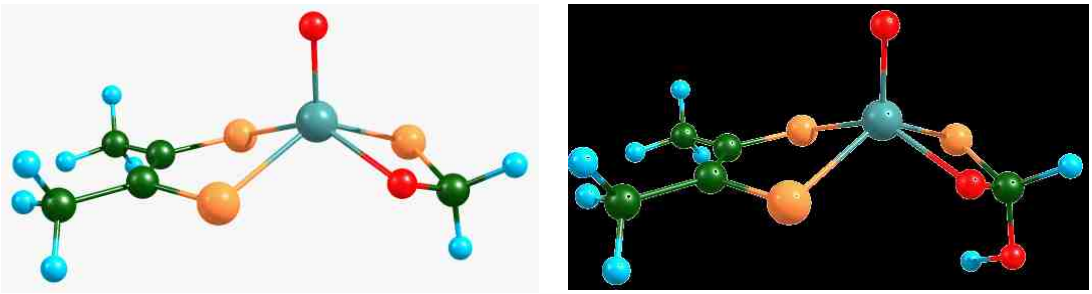

Figure 2.39 Proposed structures for aldehyde inhibited species.

Since the EPR spectrum is also sensitive to small structural changes, we have collected EPR spectra of specific binding pocket variants to see if there are perturbations on the electronic structure of the aldehyde inhibited species due to geometry changes brought about through changes in hydrogen bonding interactions. The inhibitors 3-pyridinecarboxyaldehyde (3-PA) and formaldehyde (FA) are employed for these EPR studies. In Figure 2.39, two models for the aldehyde-inhibited species with formaldehyde are shown.

2.4.6.1 EPR Spectra of Formaldehyde and 3-pyridinecarboxyaldehyde Inhibited wtXDH and Its Variants

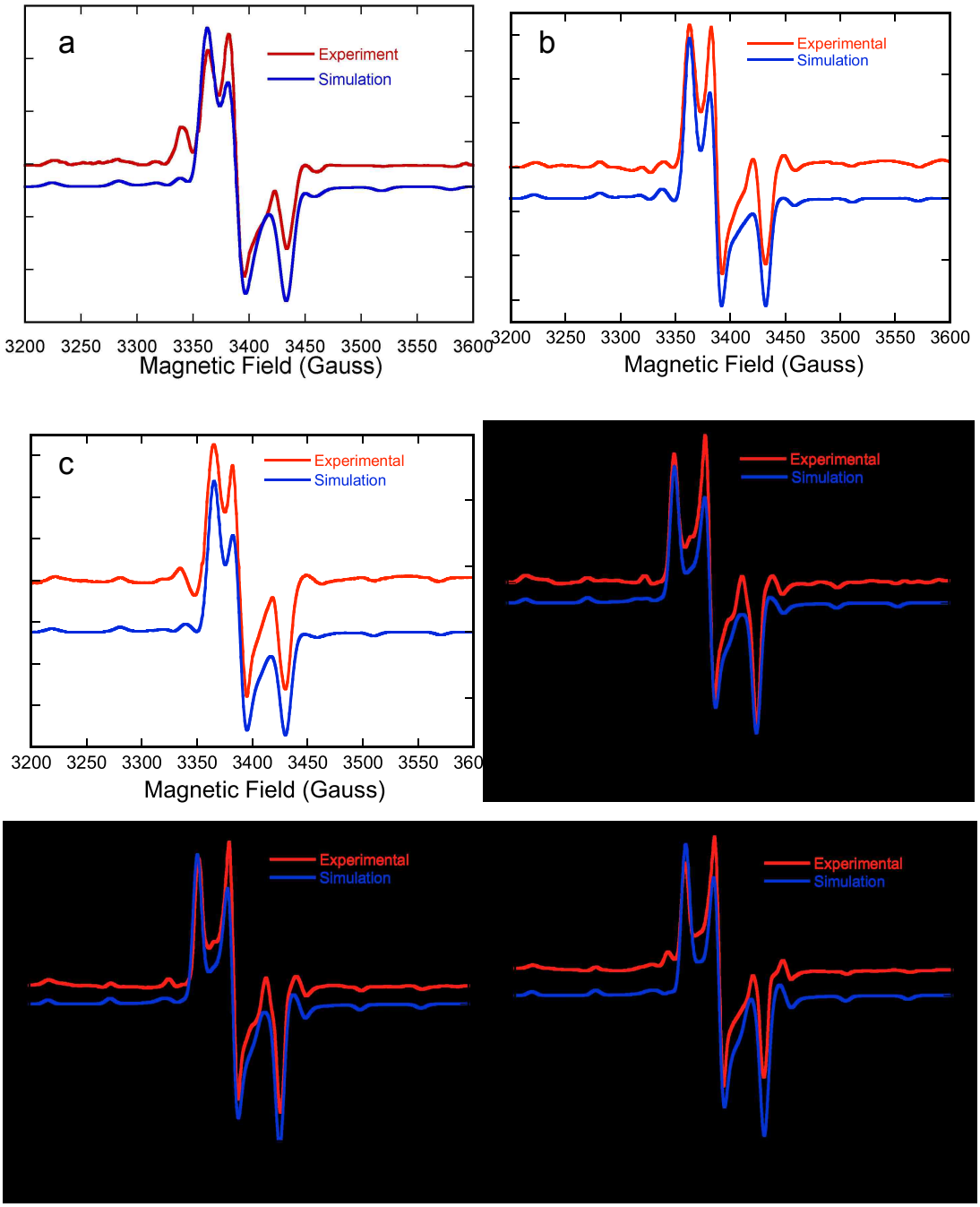

Figure 2.40 Electron paramagnetic resonance (EPR) signals for formaldehyde (a-c, a-wild type XDH, b-R310M, c-E232A) and 3-pyridinecarboxyaldehyde (3-PA) (d-f, d-wild type XDH, e-R310M, f-E232A) samples. The experimental parameters are: microwave frequency: 9.35GHz, modulation amplitude 10G, microwave power 10dB, 16scans, temperature is 100K, 10scans. Concentrations of inhibitors, wtXDH and its variants are 0.3M (FA), 0.03M (3-PA), 70μM (wtXDH), 87μM (E232A) and 70.4μM(R310M). The buffer is Bicine/NaOH with pH 8.3. The incubation time for the samples are FA 20 minutes and 3-PA 15minutes. The red color is for experimental data and data simulations are in blue.

The EPR spectra are shown in Figure 2.40. The wild type XDH and its E232A variant were incubated with 3-PA and FA respectively for a certain listed time. The well-resolved $^{95, 97}$Mo hyperfine splitting is due to the I=5/2 nucleus, and rhombic patterns are observed. Proton coupling appears in the EPR spectra of formaldehyde with XDH and its variants, but not for 3-pyrimidinecarboxyaldehyde.

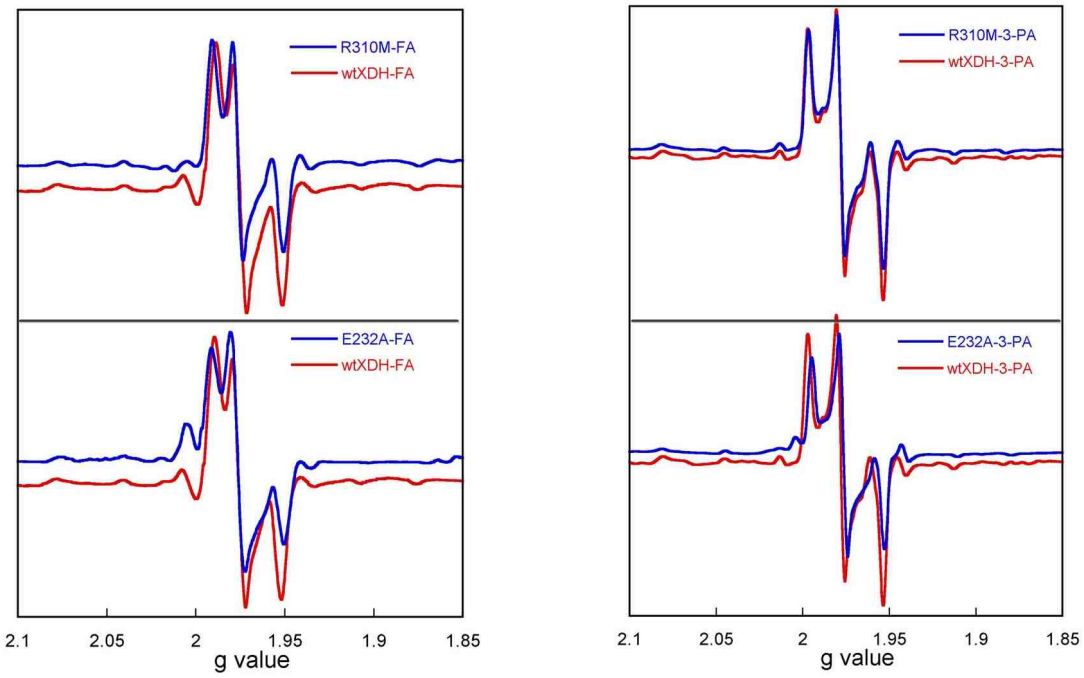

Figure 2.41 Overlap of EPR spectra for variants and wtXDH with 3-pyrimidinecarboxyaldehyde (3-PA) and formaldehyde (FA).

Table 2.7 EPR parameters of FA with wtXDH and its variants R310M and E232A. The hyperfine coupling constant units are in MHz. α, β, γ are Euler angles rotated as ZYZ axis; g_1, g_2, g_3 is equal to g_z, g_y, g_x.

	g_1	g_2	g_3	A_1	A_2	A_3	α	β	γ
wtXDH	1.989	1.975	1.951	181	63	55	160	42	0
R310M	1.991	1.977	1.951	178	65	55	160	44	0
E232A	1.992	1.976	1.951	180	65	55	160	48	0

Table 2.8 EPR parameters of 3-PA with wtXDH and its variants R310M and E232A. The hyperfine coupling constant unit are in MHz. α, β, γ are Euler angles rotated as ZYZ axis; g_1, g_2, g_3 is equal to g_z, g_y, g_x.

	g_1	g_2	g_3	A_1	A_2	A_3	α	β	γ
wtXDH	1.997	1.978	1.953	168	65	60	9	40	-27
R310M	1.997	1.978	1.953	169	65	60	7	40	-21
E232A	1.995	1.977	1.953	173	65	60	10	40	-21

The spin Hamiltonian parameters are listed in the table 2.7 and 2.8 for FA and 3-PA respectively. The hyperfine splitting and g values are modified going from formaldehyde (FA) to 3-ppyridinecarboxyaldehyde (3-PA).

The EPR spectra of variant E730A with 3-PA and FA are also collected and shown in Figure 2.42 which display “rapid type” signal.

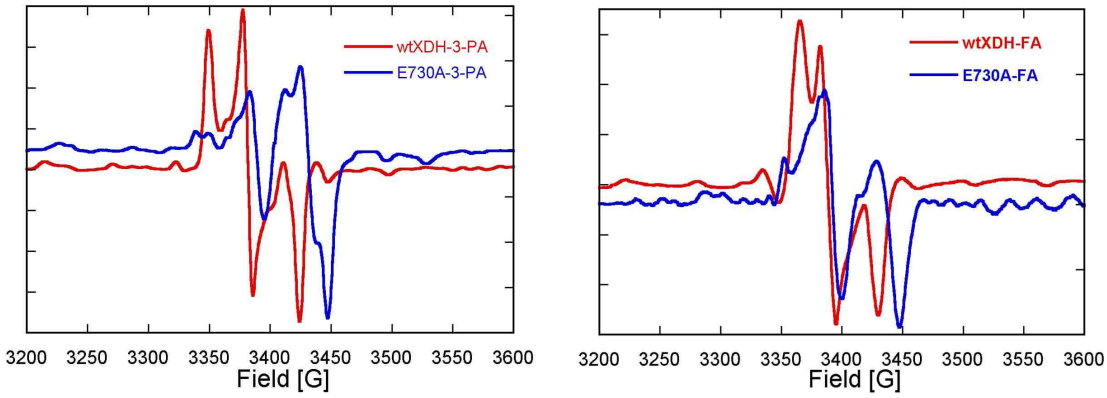

Figure 2.42 Electron paramagnetic resonance spectra of variant E730A with 3-pyrimidinecarboxyaldehyde (3-PA) and formaldehyde (FA).

2.4.6.2 EPR Spectra of ^{13}C-formaldehyde Inhibited wtXDH and Its Variants

Figure 2.43 shows both proton and carbon hyperfine splitting for ^{13}C-formaldehyde with wild type XDH. However, when incubating E730A with ^{13}C-formaldehyde for 10minutes with O_2 bubbling, no such proton or carbon hyperfine splitting is observed (Figure 2.44). The spectrum is the same as the regular formaldehyde produced EPR.

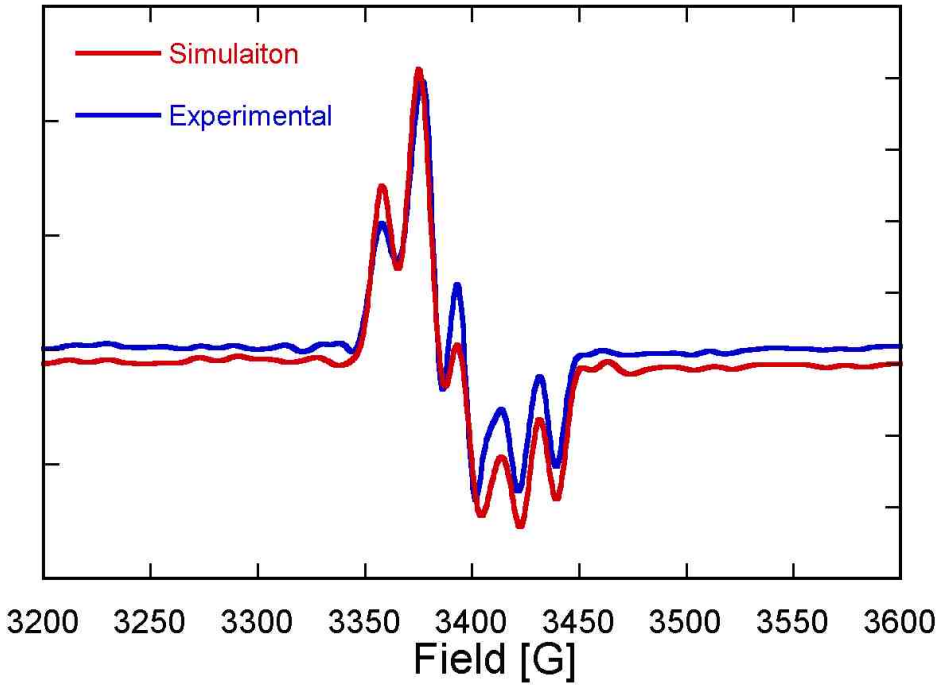

Figure 2.43 Electron paramagnetic resonance (EPR) signals for ^{13}C-formaldehyde with wild type XDH. The experimental parameters are: microwave frequency: 9.39GHz, modulation amplitude 10G, microwave power 10dB, 16scans, temperature is 100K. Concentrations are 0.3M (FA) and 70μM (wtXDH). The buffer is Bicine/NaOH with pH 8.2. The incubation time for the sample is 10 minutes. The red color is for experimental data and data simulation is in blue.

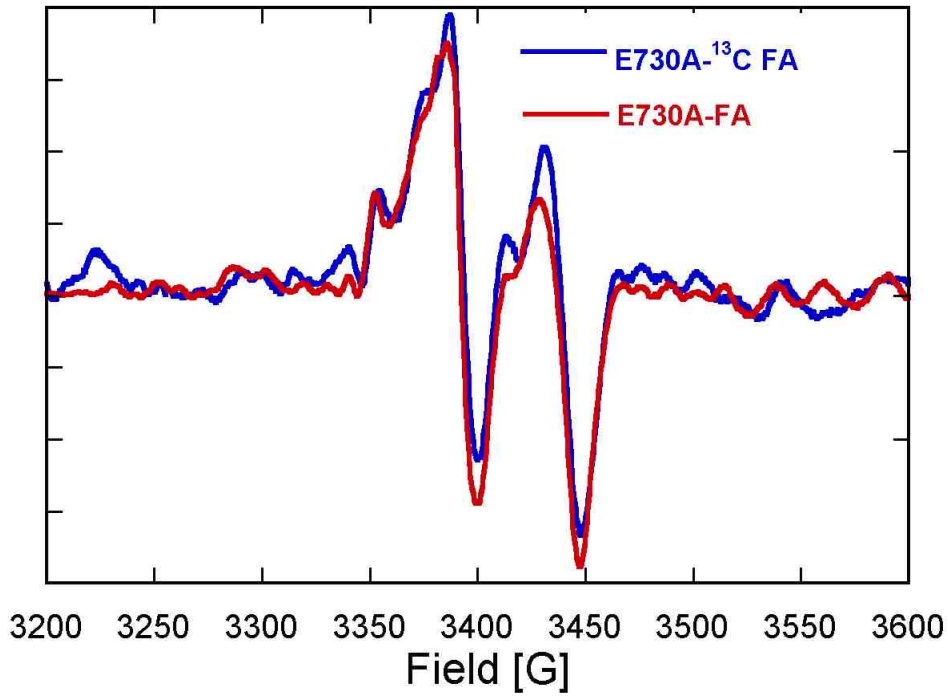

Figure 2.44 Electron paramagnetic resonance (EPR) spectra overlap of wild type XDH with ^{13}C-formaldehyde and formaldehyde as substrates. The experimental parameters are: microwave frequency: 9.39GHz, modulation amplitude 10G, microwave power 10dB, 16scans, temperature is 100K. Concentrations are 0.3M (FA) and 70mM (wtXDH). The buffer is Bicine/NaOH with pH 8.2. The incubation time for the sample is 10 minutes. The red color is for experimental data and data simulation is in blue.

Table 2.9 EPR parameters of ^{13}C-formaldehyde (FA) with wtXDH. The hyperfine coupling constant units are in MHz.

	z	y	x	α	β	γ
g	1.989	1.974	1.9515			
A (Mo)	180	78	69	0	43.5	0
A (^{13}C)	37	50	48	50	69.2	56.7
A (^{1}H)	10	10	15	9.5	102.3	-81.8

Comparing g values between formaldehyde inhibited wild type enzyme and specific variants in Table 2.6 and Figure 2.40 we see that E232A and R310M both exhibit a potential perturbation on the geometry of the aldehyde inhibited species. For model 1 (Figure 2.38 (left)), there should not be any perturbation resulting from a mutation of E232 and R310 since no hydrogen bonding interaction is formed. If structure 2 is correct, it is likely that the g vales shift compared to wild type enzyme due to an alternative orientation of inhibitor. However, R310 is located far from the inhibitor and it should not cause any perturbation on the g values. With respect to 3-pyridinecarboxyaldehyde as an inhibitor, the g value changes with E232A, but not with the R310M variant. 3-pyridinecarboxyaldehyde oriented in the upside geometry may form a hydrogen bond with E232A through an N-H interaction. However, proton splitting is not observed. This further supports the upside orientation of 3-pridinecarboxyaldehyde inhibited species.

The E730A variant displays a EPR spectra that are different from the classic aldehyde inhibited EPR signal, being more like the rapid type species. We suggest that E730 facilitates the formation of four members ring just like what is observed in purine type substrate oxidation. More experiments are needed to confirm these speculations. D_2O and ^{13}C-formaldehyde substrates incubated with E232 and R310 variants could be helpful to see if any proton coupling changes.

2.5 References

(1) Hille, R. *Eur. J. Inorg. Chem.* **2006**, *2006*, 1913–1926.

(2) Hille, R.; Hall, J.; Basu, P. *Chem. Rev.* **2014**, 140128065419006.

(3) Leimkühler, S.; Wuebbens, M. M.; Rajagopalan, K. V. *Coordination Chemistry Reviews* **2011**, *255*, 1129–1144.

(4) Romão, M. J.; Archer, M.; Moura, I.; Moura, J. J.; LeGall, J.; Engh, R.; Schneider, M.; Hof, P.; Huber, R. *Science* **1995**, *270*, 1170–1176.

(5) Kitamura, S.; Sugihara, K.; Ohta, S. *Drug Metab. Pharmacokinet.* **2006**, *21*, 83–98.

(6) Dobbek, H.; Gremer, L.; Kiefersauer, R.; Huber, R.; Meyer, O. *Proc. Natl. Acad. Sci. U.S.A.* **2002**, *99*, 15971–15976.

(7) Bonin, I.; Martins, B. M.; Purvanov, V.; Fetzner, S.; Huber, R.; Dobbek, H. *Structure* **2004**, *12*, 1425–1435.

(8) Pauff, J. M.; Cao, H.; Hille, R. *J. Biol. Chem.* **2009**, *284*, 8760–8767.

(9) Hille, R. *Chem. Rev.* **1996**, *96*, 2757–2816.

(10) Rothery, R. A.; Stein, B.; Solomonson, M.; Kirk, M. L.; Weiner, J. H. *Proc. Natl. Acad. Sci. U.S.A.* **2012**, *109*, 14773–14778.

(11) Leimkühler, S.; Hodson, R.; George, G. N.; Rajagopalan, K. V. *J. Biol. Chem.* **2003**, *278*, 20802–20811.

(12) Truglio, J. J.; Theis, K.; Leimkühler, S.; Rappa, R.; Rajagopalan, K. V.; Kisker, C. *Structure* **2002**, *10*, 115–125.

(13) Cao, H.; Pauff, J. M.; Hille, R. *Journal of Biological Chemistry* **2010**, *285*, 28044–28053.

(14) Dietzel, U.; Kuper, J.; Doebbler, J. A.; Schulte, A.; Truglio, J. J.; Leimkühler, S.; Kisker, C. *J. Biol. Chem.* **2009**, *284*, 8768–8776.

(15) Dent, C. E.; Philpot, G. R. *The Lancet* **1954**.

(16) Agarwal, A.; Banerjee, A. *Critical reviews in …* **2011**.

(17) Berry, C. E.; Hare, J. M. *The Journal of physiology* **2004**.

(18) Pacher, P.; Nivorozhkin, A.; SZABO, C. *Pharmacological reviews* **2006**, *58*, 87–114.

(19) Leimkühler, S. *Journal of Biological Chemistry* **2004**, *279*, 40437–40444.

(20) Davis, M. D.; Olson, J. S.; Palmer, G. *J. Biol. Chem.* **1982**, *257*, 14730–14737.

(21) Davis, M. D.; Olson, J. S.; Palmer, G. *J. Biol. Chem.* **1984**, *259*, 3526–3533.

(22) Okamoto, K.; Matsumoto, K.; Hille, R.; Eger, B. T.; Pai, E. F.; Nishino, T. *Proc. Natl. Acad. Sci. U.S.A.* **2004**, *101*, 7931–7936.

(23) Matsumoto, K.; Okamoto, K.; Ashizawa, N.; Nishino, T. *Journal of Pharmacology and Experimental Therapeutics* **2010**, *336*, 95–103.

(24) Maiti, N. C.; Tomita, T.; Kitagawa, T.; Okamoto, K.; Nishino, T. *J Biol Inorg Chem* **2003**, *8*, 327–333.

(25) Oertling, W. A.; Hille, R. *J. Biol. Chem.* **1990**, *265*, 17446–17450.

(26) Hemann, C.; Ilich, P.; Stockert, A. L.; Choi, E.-Y.; Hille, R. *J. Phys. Chem. B* **2005**, *109*, 3023–3031.

(27) Manikandan, P.; Choi, E.-Y.; Hille, R.; Hoffman, B. M. *JACS* **2001**, *123*, 2658–2663.

(28) P, M. J.; W, W. J.; C, B. R. **1981**.

(29) Ilich, P.; Hille, R. *J. Phys. Chem. B* **1999**, *103*, 5406–5412.

(30) Kirk, M. L.; Berhane, A. *Chem. Biodivers.* **2012**, *9*, 1756–1760.

(31) Sempombe, J.; Stein, B.; Kirk, M. L. *Inorg Chem* **2011**, *50*, 10919–10928.

(32) Karlin, K. D.; Stiefel, E. I. *Progress in Inorganic Chemistry, Dithiolene Chemistry*; John Wiley & Sons, 2004.

(33) Okamoto, K.; Kawaguchi, Y.; Eger, B. T.; Pai, E. F.; Nishino, T. *J. Am. Chem. Soc.* **2010**, *132*, 17080–17083.

(34) Enroth, C.; Eger, B. T.; Okamoto, K.; Nishino, T.; Nishino, T.; Pai, E. F. *Proc. Natl. Acad. Sci. U.S.A.* **2000**, *97*, 10723–10728.

(35) Pauff, J. M.; Zhang, J.; Bell, C. E.; Hille, R. *J. Biol. Chem.* **2008**, *283*, 4818–4824.

(36) Yamaguchi, Y.; Matsumura, T.; Ichida, K.; Okamoto, K.; Nishino, T. *J. Biochem.* **2007**, *141*, 513–524.

(37) Pauff, J. M.; Hemann, C. F.; Jünemann, N.; Leimkühler, S.; Hille, R. *J. Biol. Chem.* **2007**, *282*, 12785–12790.

(38) Metz, S.; Thiel, W. *J. Am. Chem. Soc.* **2009**, *131*, 14885–14902.

(39) Okamoto, K.; Eger, B. T.; Nishino, T.; Kondo, S.; Pai, E. F.; Nishino, T. *J. Biol. Chem.* **2003**, *278*, 1848–1855.

(40) Schneider, H.-J.; Pfleiderer, W. *Chem, Ber.* **1974**, *107*, 3377–3394.

(41) Taylor, E. C., Jr; Carbon, J. A.; Hoff, D. R. *JACS* **1953**, *75*, 1904–1908.

(42) Felczak, K.; Bretner, M.; Kulikowski, T.; Shugar, D. *Nucleosides & nucleotides* **1993**, *12*, 245–261.

(43) Gorizdra, T. E. *chemistry of heterocyclic compounds* **1969**, *5*, 677–680.

(44) Illán-Cabeza, N. A.; Peña-Ruiz, T.; Moreno-Carretero, M. N. *Journal of Molecular Modeling* **2012**, *18*, 815–824.

(45) Norrestam, R.; Stensland, B.; Soderberg, E. *Acta Cryst (1972). B28, 659-666 [doi:10.1107/S0567740872002985]* **1972**, 1–8.

(46) Skibo, E. B.; Gilchrist, J. H.; Lee, C. H. *Biochemistry* **2001**, *26*, 3032–3037.

(47) Stockert, A. L.; Shinde, S. S.; Anderson, R. F.; Hille, R. *J. Am. Chem. Soc.* **2002**, *124*, 14554–14555.

(48) Inscore, F. E.; Knottenbelt, S. Z.; Rubie, N. D.; Joshi, H. K.; Kirk, M. L.; Enemark, J. H. *Inorg Chem* **2006**, *45*, 967–976.

(49) Inscore, F. E.; McNaughton, R.; Westcott, B. L.; Helton, M. E.; Jones, R.; Dhawan, I. K.; Enemark, J. H.; Kirk, M. L. *Inorg Chem* **1999**, *38*, 1401–1410.

(50) Garton, S. D.; Temple, C. A.; Dhawan, I. K.; Barber, M. J.; Rajagopalan, K. V.; Johnson, M. K. *J. Biol. Chem.* **2000**, *275*, 6798–6805.

(51) Garton, S. D.; Hilton, J.; Oku, H.; Crouse, B. R.; Rajagopalan, K. V.; Johnson, M. K. *JACS* **1997**, *119*, 12906–12916.

(52) Schindelin, H.; KISKER, C.; Hilton, J.; Rajagopalan, K. V. *Science* **1996**.

(53) Johnson, M. K. *Progress in Inorganic Chemistry* **2004**.

(54) Qiu, D.; Kilpatrick, L.; Kitajima, N.; Spiro, T. G. *JACS* **1994**, *116*, 2585–2590.

(55) Okamoto, K.; Eger, B. T.; Nishino, T.; Pai, E. F.; Nishino, T. *Nucleosides Nucleotides Nucleic Acids* **2008**, *27*, 888–893.

(56) Okamoto, K.; Matsumoto, K.; Hille, R.; Eger, B. T.; Pai, E. F.; Nishino, T. *Proc. Natl. Acad. Sci. U.S.A.* **2004**, *101*, 7931–7936.

Chapter 3 Model Complex Studies of Electronic Stucture Contributions to Oxygen Atom Transfer in Arsenite Oxidase

3.1 Introduction

As a dimethyl sulfoxide reductase (DMSOR) family member, arsenite oxidase shares the characteristics of the DMSOR family: transferring oxygen from the water to arsenite and two pyranoperin dithiolene (PDT) ligands bound to the molybdenum ion. Arsenite oxidase is isolated from the bacteria *Alcaligenes faecalis* and is located in the periplasmic space, and performs the conversion of arsenite to less toxic arsenate with either azurin or cytochrome c as electron acceptor (equation 3.1).

$HAsO_3^{2-}+H_2O \rightarrow HAsO_4^{2-}+2H^+ +2e^-$……(3.1)

Its protein structure has been characterized by X-ray crystallography and EXAFS as shown in Figure 3.1.[1,2] The Mo active site and the 3Fe4S cluster are found in a large subunit while the 2Fe2S cluster is located in a small subunit. The molybdenum center is coordinated to two pyranopterin ditholene ligands and an oxo at 1.6Å. It possesses a square pyramidal geometry and is believed to be in its reduced state due to reduction in the X-ray beam.

Usually ser-O, cys-S, Asp-O and seleno-Se amino acid residues from side chains are coordinated to the molybdenum center at the active site of DMSOR family members.[3,4] Unlike most DMSOR family enzymes, in the arsenite oxidase active site the polypeptide ligand bound to molybdenum is replaced by a hydroxyl

ligand. EXAFS data reveals two asymmetric dioxo ligands or one oxo and one OH group, which possess the Mo-O bond lengths of 1.7Å and 1.83Å, respectively. The stretching vibrational mode for the oxo ligand occurs at 822cm^{-1}. This mode has a downshift of 35cm^{-1} when the single enzyme turnover is run in the D_2O, and it disappears in the reduced state. Two distinguished C=C stretching modesa are observed at 1525 cm^{-1} and 1598cm^{-1} and are assigned as two inequivalent PDTs.

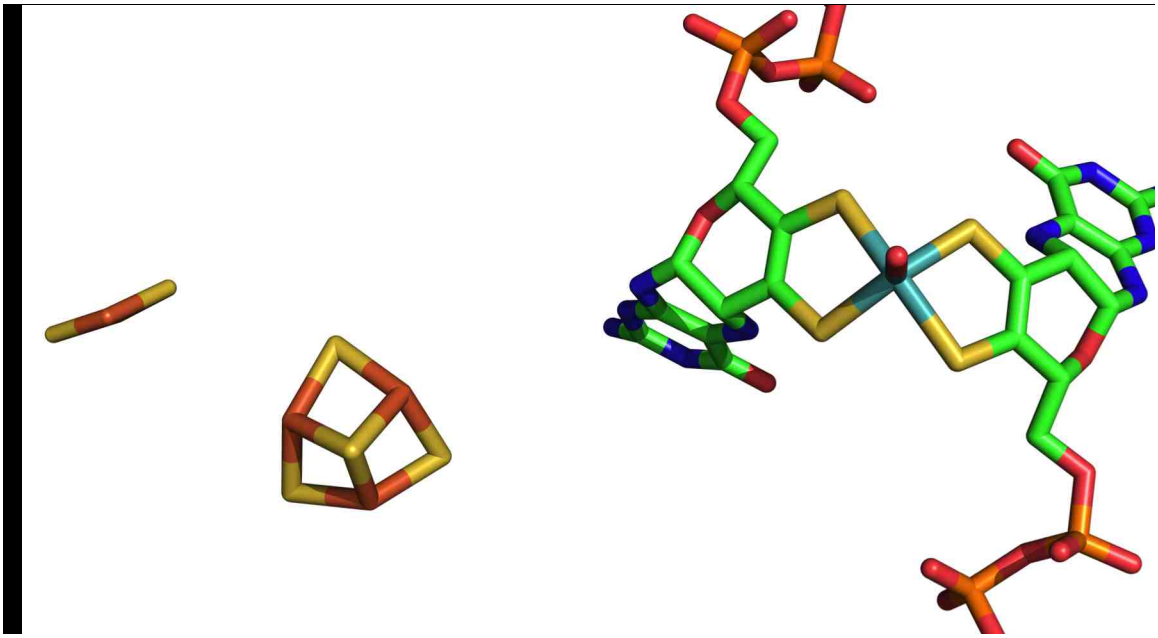

Figure 3.1 The structure of arsenite oxidase shown as an illustration of the molybdenum active site combined with two different types of iron sulfur clusters 3Fe-4S and 2Fe-2S (PDB code: 1G8K with 1.64Å).[1]

Based on the X-ray and EXAFS data the proposed oxygen atom transfer mechanism is as follows (Figure 3.2): a lone pair of electrons from arsenite attacks the labile Mo(VI)-oxo, and arsenite is reduced arsenate as two electrons are transferred to molybdenum. The reduced square-pyramidal Mo(IV) is re-

oxidized to Mo(VI) and an oxygen atom from a water molecule that is incorporated into the active site. This results in a new loss of $2e^-$ and H+. During the turnover no Mo(V) signal is detected.

Low energy S (ene-1, 2-dihiolate) → Mo charge transfer bands of considerable intensity are observed in the electronic absorption spectra of both Mo (VI) and Mo (IV) forms in *R. sphaeroides* and *R.capsulatus* DMSOR enzymes.[5] It is therefore of interest to understand how

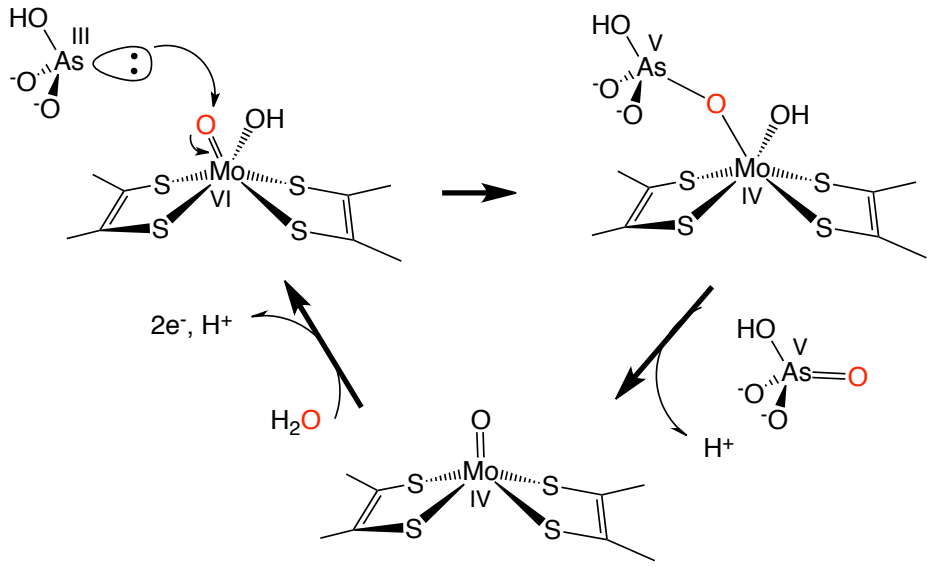

Figure 3.2 The proposed catalytic mechanism of arsenite oxidase (labile oxygen is labeled in red).[1]

bis(ene-1, 2-dihiolate) coordination in members of the DMSOR enzyme family affects electron and atom transfer reactivity during the course of catalysis. The presence of the low energy charge transfer bands is of particular interest since ene-1, 2-dihiolate and dithiolenes are known to be highly non-innocent ligands that have a dramatic effect on the electronic structure of their metal ion complexes.[6] The degree of π delocalization within the dithiolene unit and charge

donation to the metal can be probed by monitoring the frequency of the υ(C=C) stretching mode associated with the ene-1-2-dithiolate ligand (-S-C=C-S-). The information obtained from a combination of the υ(C=C) stretching frequency and the electronic origin of the low energy charge transfer band in DMSOR family enzymes can offer valuable insight into electronic structure contributions to the rich electron and atom transfer reactivity of DMSOR family enzymes. The intense absorption peaks from prosthetic groups such as Fe-S clusters or heme complicate the interpretation of optical spectra. For example the spectroscopic analysis of the arsenite oxidase is complicated by the presence of 3Fe-4S and 2Fe-2S clusters. Therefore structurally characterized model complexes that are free from the spectroscopic contributions of the prosthetic groups provide an important tool to evaluate enzyme spectra and developing key structure-function relationships.

Along these lines, more than two dozen $[Mo(IV)O(ene\text{-}1,2\text{-}dithiolate)]^{2-}$ complexes have been synthesized as analogues of reduced DMSOR family enzymes and characterized by IR and rR spectroscopies.[6-8] Recently, a Mo(IV)O complex with an ene-1, 2-dithiolate ligand and an aromatic dithiolene ligand, $(Et_4N)_2[Mo(IV)O(S_2C_2(CO_2Me)_2)(bdt)]$ ($S_2C_2(CO_2Me)_2$=1,2-dicarbo-methoxyethylene-1,2-ditholate, bdt=1,2 benzenedithiolate) was reported.[9] In contrast, Mo(VI) complexes with one or two ene-1,2-dithiolate ligands have been considered to be too unstable for isolation due to auto-redox reactions that may be facilitated by π-delocalization between the metal and ene-1,2-dithiolate ligands.[8,10,11] Isolated Mo(VI) $[Mo(VI)O_2(ene\text{-}1,2\text{-}dithiolate)_2]^{2-}$ complexes are

limited to $[MoO_2(mnt)_2]^{2-}$ (mnt = dicyano-ethylene-1,2-dithiolate),[12] which is believed to be stabilized by the very strong electron withdrawing nature of the CN substituents. Other $Mo(VI)O_2$ or Mo(VI)O(OR) bis(ene-1,2-dithiolate) complexes have been generated in situ.[13,14] Thus, there is a need for spectroscopic and electronic structure studies of structurally characterized model systems that do not have substituents in conjugation with the C=C unit of the ene-1, 2-dithiolate ligand, since the pyranopterin cofactor is not believed to be conjugated to the ene-1,2-dithiolate moiety in the enzymes.[15]

As shown in Figure 3.3 our collaborators in the Sugimoto group have synthesized, isolated and characterized the arsenite oxidase analog complexes $(Et_4N)(Ph_4P)[Mo(VI)O_2(S_2C_2(CO_2Me)_2)(bdt)]$ (**a**), its chlorine substituted aromatic dithiolene derivative $(Et_4N)(Ph_4P)[Mo(VI)O_2(S_2C_2(CO_2Me)_2)(bdtCl_2)]$ (**b**) and $(Et_4N)(Ph_4P)[Mo(VI)O_2(S_2C_2(CO_2Me)_2)_2]$ (**c**).

In this chapter we have used electronic absorption and resonance Raman spectroscopies in combination of DFT calculations to probe the basic electronic structure of the dioxo complexes, and this has provided insight into the relationship between their electronic structure properties and oxygen atom transfer reactivity.

3.2 Materials and Methods

The sample preparations for spectroscopic data collection were carried out anaerobically under a N_2 atmosphere.

3.2.1 Electronic Absorption Spectroscopy

Routine UV-vis spectra were recorded on a Shimazu-UV 2550 spectrometer. Additional solution electronic absorption spectra were collected using a Hitachi U-3501 UV-Vis-NIR dual-beam spectrometer capable of scanning a wavelength region between 185 and 3200 nm. Spectral samples were dissolved in dry, degassed dichloromethane, and the electronic absorption spectra were measured in a 1cm path length, 100 µL, black-masked, quartz cuvette (Starna Cells, Inc.) equipped with a Teflon stopper. All electronic absorption spectra were performed at room temperature and repeated at regular time intervals to ensure the structural stability and integrity of the complex in solution.

3.2.2 Resonance Raman Spectroscopy

Solid-state resonance Raman (rR) spectra and associated rR excitation profiles were collected using a system comprised of an PI/Acton SpectraPro SP-2500i 500 mm focal length imaging spectrograph with a triple grating turret and a PI/Acton Spec-10:100B back-illumi-nated 1340 100 pixel digital CCD spectroscopy system with a cryogenically cooled camera head. A Coherent Innova I302C Ar^+ ion laser was the excitation source. Samples were mixed with either NaCl or a NaCl/Na_2SO_4 mixture with Na_2SO_4 as an internal calibrant. The employed laser powers were kept below ~100 mW in order to exclude photo-degradation of the sample. Resonance Raman excitation profile was constructed by utilizing resonance Raman data collected at the 458, 488 and 514 nm Ar^+ laser lines.

3.2.3 Electronic Structure Calculations

Spin-restricted gas phase geometry optimizations and vibrational frequency calculations for compounds **a**, **b**, and **c** were performed at the density functional level of theory using the Gaussian 03W software package.[16] All calculations employed the B3LYP hybrid functional. A LANL2DZ basis set with an effective core potential was used for Mo and a 6-31G* basis set was used for all light atoms. Input files were prepared using the molecule builder function in the GaussView software package. Frontier molecular orbitals were generated for the optimized ground states of **a**, **b**, and **c**. Time-dependent DFT calculations were performed on the optimized ground state geometries, and the first 40 excited states were calculated. Electron density difference maps (EDDMs) were constructed using the Gauss-Sum suite of programs.[17]

3.3 Dioxo Model Complexes of Arsenite Oxidase

Figure 3.3 Model complex structures. **(a)** $[Mo(VI)O_2(S_2C_2(CO_2Me)_2)(bdt)]^{2-}$

;**(b)** $[Mo(VI)O_2(S_2C_2(CO_2Me)_2)(bdtCl)]^{2-}$; **(c)** $[Mo(VI)O_2(S_2C_2(CO_2Me)_2)_2]^{2-}$ **(**cation is $(Et_4N)(Ph_4P)$).

The Mo1 atom of **b** is coordinated by two oxo oxygen atoms (O1 and O2), two sulfur atoms (S1 and S2) from $bdtCl_2^{2-}$ and two additional sulfur atoms (S3 and S4) from $S_2C_2(CO_2Me)_2^{2-}$. The S2-S1-S3-S4 torsion angle describing the twist of the dithiolene ligands relative to one another is 94.1°, indicative of a distorted octahedral geometry about the Mo1 center.[18] Similar to the crystal structures of $(Ph_4P)_2[Mo(VI)O_2(bdt)_2]$,[19] $(Ph_4P)_2[Mo(VI)O_2(mnt)_2]$,[12,19] and $(Et_4N)_2[Mo(VI)O_2(bdtCl_2)_2]$,[20] the Mo1-S2 and Mo1-S4 bond distances (2.5537(19) and 2.6555(16) Å) are longer than the Mo1-S1 and Mo1-S3 distances (2.431(2) and 2.4059(18) Å) since S2 and S4 are oriented trans to the O1 and O2 oxo atoms. The structure of the $bdtCl_2^{2-}$ ligand in **b** is very similar to that of the $(Et_4N)_2[Mo(VI)O_2(bdtCl_2)_2]$ model,[20] reflecting the π-delocalization with the aromatic ring. Interestingly, the S3-C7 (1.731(9) Å) and S4-C8 (1.720(7) Å) bond distances for the $S_2C_2(CO_2Me)_2^{2-}$ ligand are remarkably similar and do not reflect whether the S-C bonds are oriented trans or cis relative to the O2 oxo atom. Large dihedral angles (30.3° and 75.7° for S3C7C8S3-O3C7O4 and S3C7C8S3-O5C11O6, respectively) are observed between the S3C7C8S3 and CO_2Me planes in **b**. This indicates reduced conjugation between the ene-1, 2-ditiolate and the CO_2Me substituents.

Two independent complexes (molecules 1 and 1') are found in the unit cell of **c**. The two complex anions differ in the orientation of their CO_2Me groups with

respect to the S-C-C-S plane. The stereochemistry about Mo1a is described as a distorted octahedron, and this is reflected by an S2aS1aS3aS4a dihedral angle (95.1°) close to 90°. The S2a-C2a (1.715(5) Å) and S4a-C8a (1.720(4) Å) bonds oriented trans to O1a and O2a are short due to the trans influence of the oxo ligands. By comparison, the S-C bonds oriented cis to O1a and O2a are 1.776(4) Å and 1.756(4) Å, respectively. Collectively, the structural results indicate that the $S_2C_2(CO_2Me)_2^{2-}$ of **c1** possesses a greater contribution of the dithione form than is observed for bdt^{2-} or $bdtCl_2^{2-}$. Although both **c1** and **c1'** possess $S_2C_2(CO_2Me)_2^{2-}$ ligands with some dithione character, the primary structural differences between them likely result from crystal packing forces.

3.4 Results and Discussions

3.4.1 Charge Transfer Band

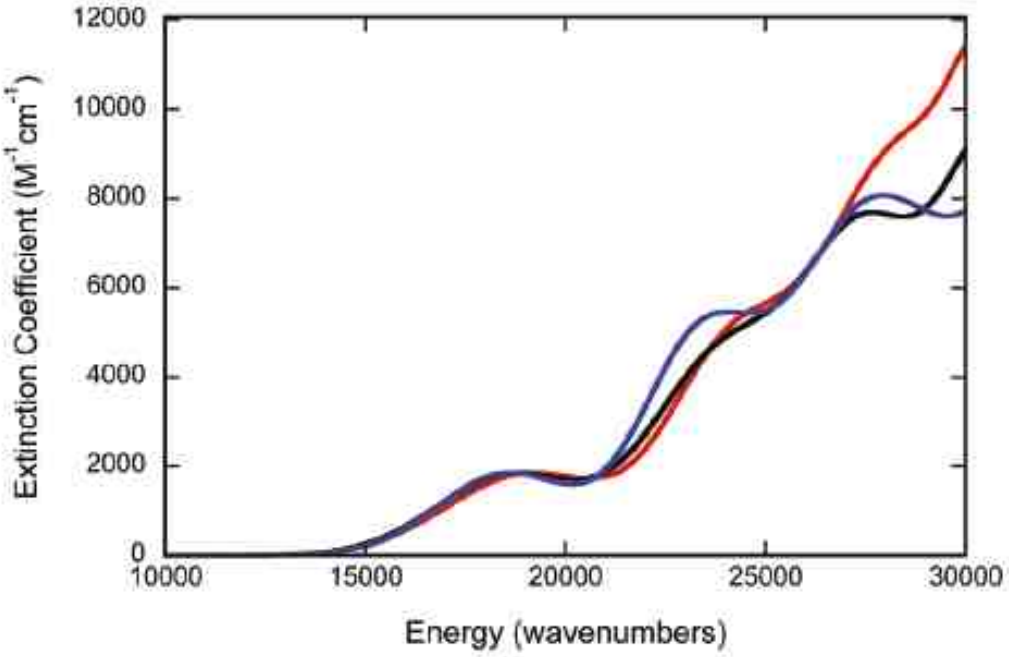

Figure 3.4 Solution electronic absorption spectra of **a** (black), **b** (red), and **c** (blue). Extinction coefficients have been normalized to the band at 18 000 cm^{-1} for comparative purposes.

Despite the different ligand sets in **a**, **b**, and **c**, the solution electronic absorption spectra of these complexes are remarkably similar and display three bands below 30000 cm^{-1} (Figure 3.4). The d^0 electron configuration of the M(VI) ion and the magnitude of the extinction coefficients (~2000-8000 M^{-1} cm^{-1}) for these three bands clearly identify the transitions in this energy range as ligand-to-metal charge transfer (LMCT) in nature. Because of the spectral similarity between complexes **a**, **b**, and **c**, we will focus this discussion on compound **c**, whose Gaussian-resolved solution electronic absorption spectrum is presented in Figure 3.5.

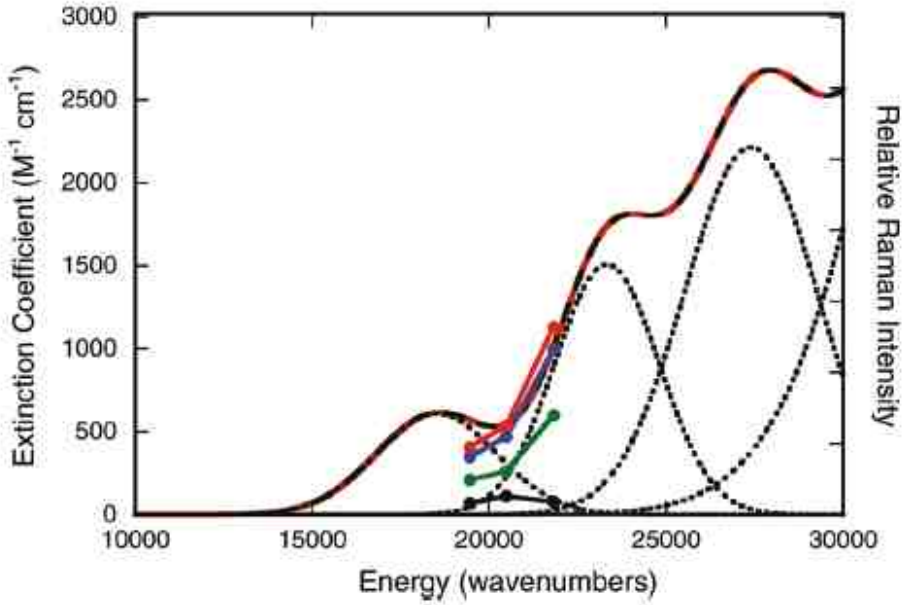

Figure 3.5 Gaussian resolved electronic absorption spectrum for **c**. Resonance Raman excitation profiles are shown for the 867 cm^{-1} symmetric O_{oxo}-Mo-O_{oxo} stretch (red), 1494 cm^{-1} C=C stretch (green), 1510 cm^{-1} C=C stretch (blue), and 834 cm^{-1} asymmetric O_{oxo}-Mo-O_{oxo} stretch (black).

3.4.2 Molecular Orbitals

Although **a**, **b**, and **c** possess no molecular symmetry, the dominant dioxo ligand field principally dictates the relative energies and the nature of the Mo d orbitals. These empty d molecular orbitals are the lowest energy acceptor orbitals and they are depicted for compounds **c** in Figure 3.6 for compound **c**. The orbital plots are shown at an isodensity value of 0.05 au to more clearly depict the nature of the Mo d orbital component in these low-lying virtual molecular orbitals. The four lowest-energy acceptor orbitals (LUMO – LUMO+3) possess d orbital functions that are π antibonding with respect to the two oxo ligands. The LUMO and LUMO+1 are the lowest energy orbitals because they possess weak π

interactions with the oxo ligands. Their relative energy ordering is a function of the O_{oxo}-Mo-O_{oxo} bond angle, with more acute angles leading to an orbital reversal between LUMO and LUMO+1. The LUMO+2 and LUMO+3 orbitals possess Mo d orbital functions that are more strongly π -antibonding with respect to the oxo ligands due to the increased directionality of the π -bond along the Mo-O_{oxo} bond axes, which leads to their higher energy. Additionally, the LUMO+2 and LUMO+3 orbitals possess dithiolene C=C antibonding character, which is not present to a large degree in the LUMO and LUMO+1. Thus, one-electron promotions to the LUMO+2 and LUMO+3 acceptor orbitals should result in large excited state distortions along the C=C and symmetric O_{oxo}-Mo-O_{oxo} stretching coordinates.

The bonding calculations indicate that the two highest occupied molecular orbitals (HOMOs) of the bis-dithiolene ligand set comprise in-phase and out-of-phase combinations of out-of-plane symmetric dithiolene sulfur p orbitals (HOMO and HOMO-1 in Figure 3.6), and this is in agreement with earlier work on mono-oxomolybdenum dithiolene complexes.[21] The HOMO-2 function is at deeper binding energy and can be described as an out-of-phase in-plane p orbital primarily localized on the cis dithiolene sulfur atoms (Figure 3.6). The HOMO-3 and HOMO-4 functions are out-of-phase linear combinations of in-plane and out-of-plane p orbitals on dithiolene sulfur atoms. Further inspection of the calculated orbital energies indicates that HOMO and HOMO-1 are relatively close in energy (ΔE = 2800 cm^{-1}), while LUMO and LUMO+1 are nearly isoenergetic

(ΔE = 1400 cm^{-1}) (Figure 3.6 and Table 3.1). The near degeneracy of the LUMO and LUMO+1 orbitals in **a**, **b**, and **c** is markedly different from what is observed in the 5-coordinate dioxo active site of sulfite oxidase, where a large splitting between the LUMO and LUMO+1 is observed.[22,23]

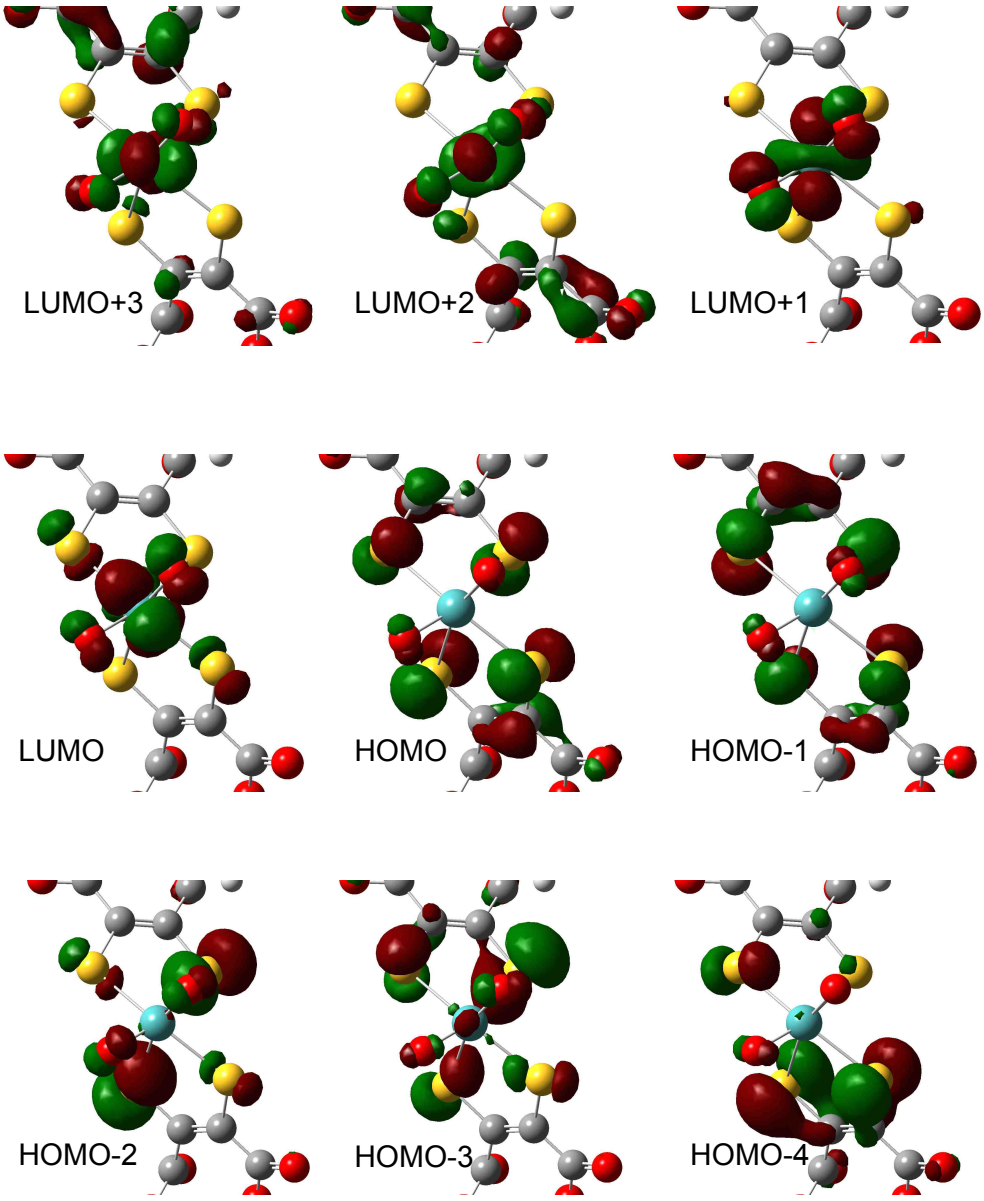

Figure 3.6 Calculated active space HOMO and LUMO wave function for **c** depicted at an isodensity value of 0.05au.

The relevant HOMO and LUMO orbitals for **a** and **b** are virtually identical to those of **c** and are provided in the Figures 3.7-3.8 and Tables 3.2 and 3.3.

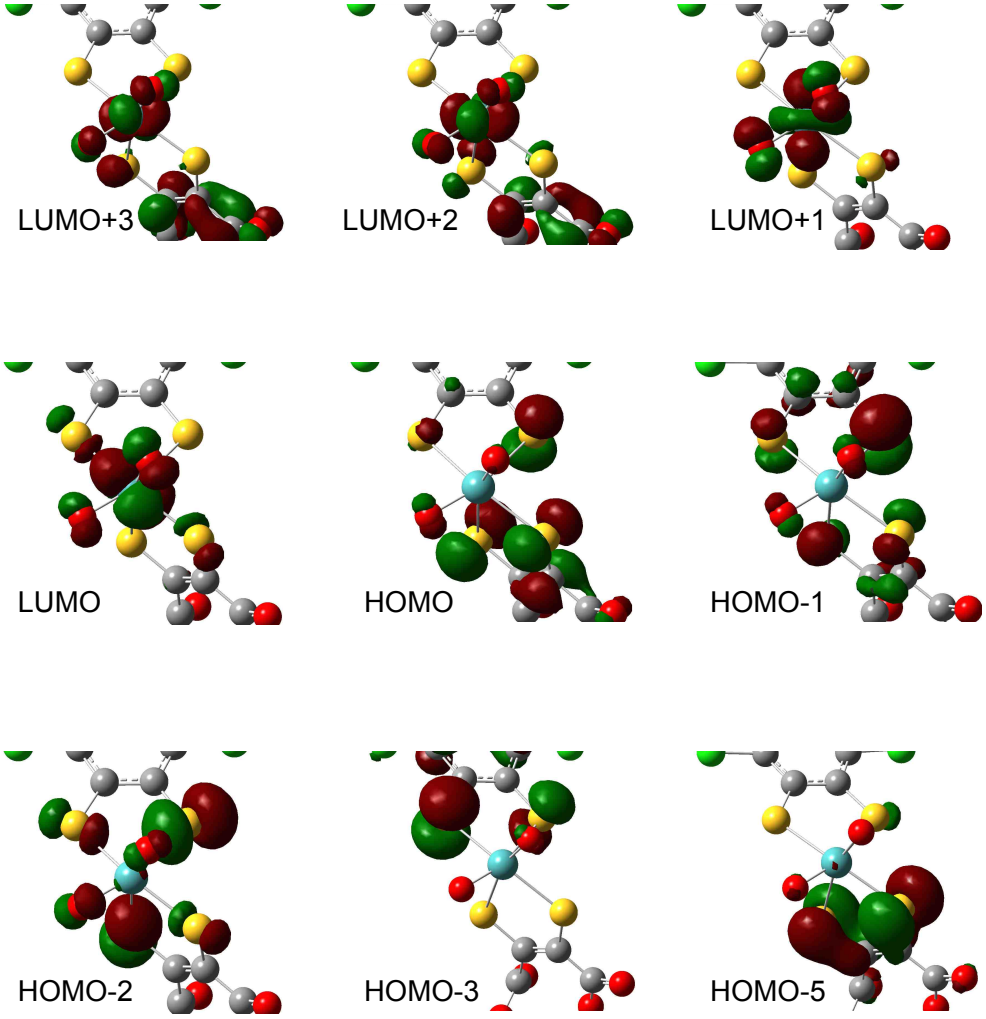

Figure 3.7 Calculated active space HOMO and LUMO wave function for **b** depicted at an isodensity value of 0.05au.

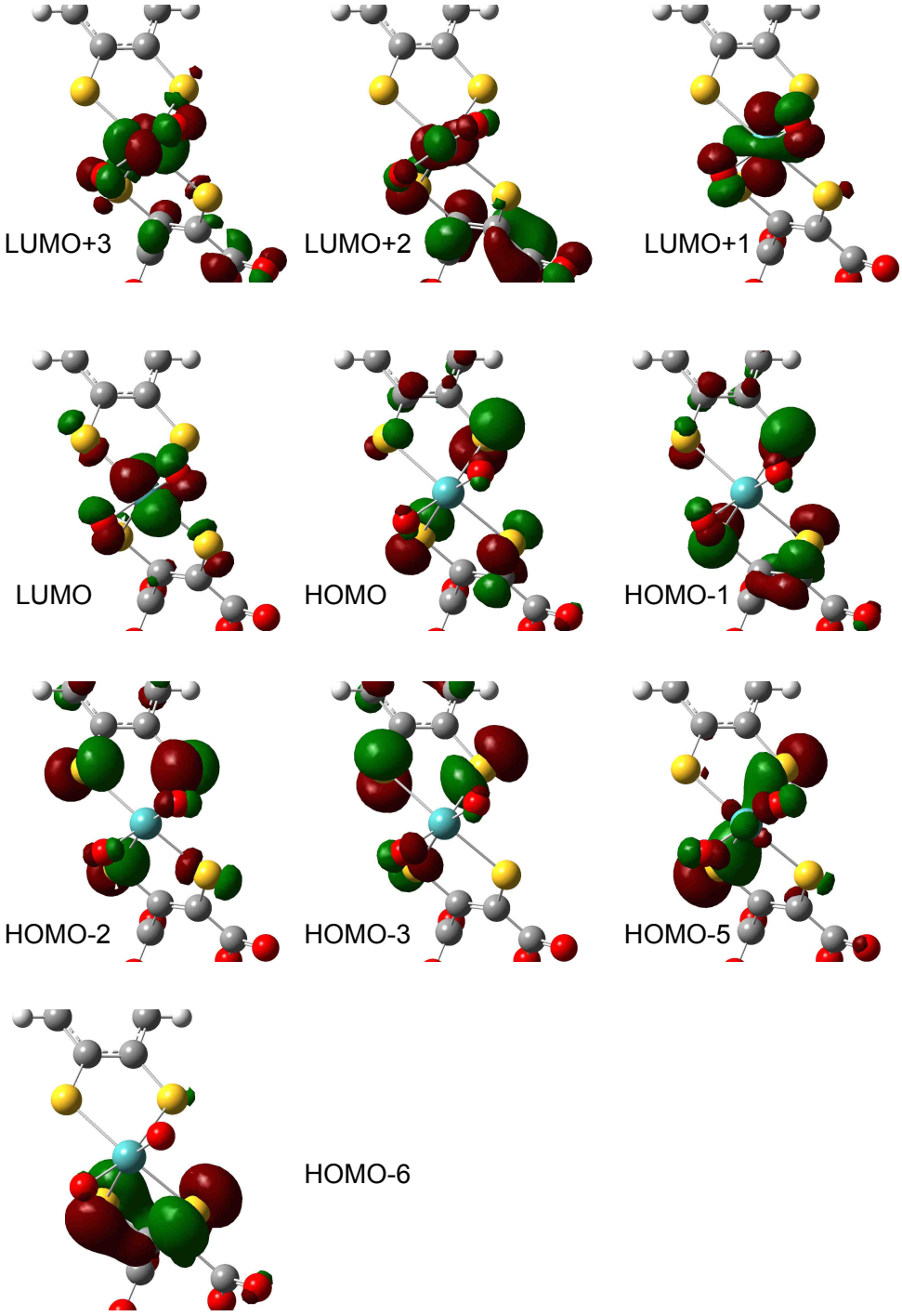

Figure 3.8 Calculated active space HOMO and LUMO wave function for **a** depicted at an isodensity value of 0.05au.

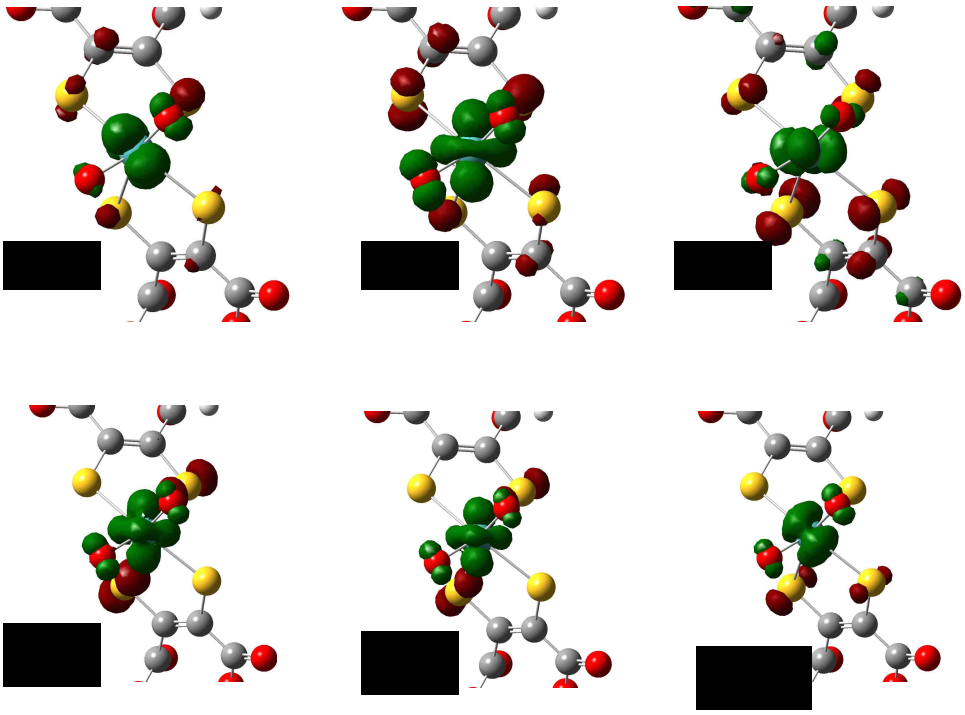

Figure 3.9 Calculated electron density difference maps (EDDMs) of transitions 3, 4, 5, 8, 9, and 15 for **c** depicted at an isodensity value of 0.005 au. Transitions 3 and 4 are the dominant contributors to band 1, and transitions 5, 8 and 9 are the dominant contributors to band 2. Transition 15 dominates for band 3. Red regions indicate a loss of electron density in a transition to the excited state and green regions indicate a gain of electron density in a transition to the excited state.

3.4.3 Band Assignments

Having described an active space of metal and ligand frontier orbital functions, we can now begin to describe the nature of the lowest energy LMCT transitions in **a**, **b**, and **c**. Energy considerations indicate that the lowest- energy LMCT excitations should occur between the HOMO-1, HOMO, LUMO, and LUMO+1. Thus, there are four possible one-electron promotions that can occur between these orbitals and they should dominantly contribute to the lowest energy band. This is supported by the results of time-dependent DFT (TDDFT) calculations where it is found that two LMCT transitions (T3 and T4) are linear combinations

of HOMO-1→LUMO and HOMO-1→LUMO+1 one-electron promotions. These possess the highest oscillator strengths and dominate in their contribution to band 1. The nature of the LUMO and LUMO+1 indicate that one-electron promotions to these acceptor orbitals will result in excited state distortions along the totally symmetric O_{oxo}-Mo-O_{oxo} bend and weaker excited state distortions along the symmetric O_{oxo}-Mo-O_{oxo} stretch. The mixing of these two one-electron promotions is clearly evident in the electron density difference maps (EDDMs) that are shown in Figure 3.9 and Table 3.1. Transitions 5, 8 and 9 are the LMCT transitions that principally contribute to the absorption envelope of band 2. The calculations indicate that HOMO→LUMO+2 and HOMO→LUMO+3 (T5) one-electron promotions contribute to the low energy side of band 2. The dominant transitions (T8 and T9) that contribute to band 2 are principally composed of HOMO→LUMO+2 and HOMO→LUMO+3 mixed with HOMO-2→LUMO+1 one-electron promotions respectively. The nature of the dominant LMCT transitions that comprise band 2 are summarized in the EDDMs shown in Figure 3.9. The electronic origin of band 3 is a transition from the much-deeper sulfur out-of-phase in-plane combination with out-of-plane p orbitals of dithiolene. Calculations indicate that the main contribution to the intensity of band 3 is one dominant transition that is a linear combination of HOMO-3→LUMO and HOMO-3→LUMO+1 one-electron promotions.

Table 3.1 Calculated band energies, oscillator strengths f, and percentage of transition and nature of transition for **c**.

Band	Excitation Energy cm^{-1}	f	%	Principal nature of Transition
1	14948	0.0010	0.69	HOMO→LUMO
	16474	0.0033	0.59	HOMO→LUMO+1
	17730(TS3)	0.017 *	0.59	HOMO-1→LUMO
	19646(TS4)	0.0079*	0.67	HOMO-1→LUMO+1
2	21053(TS5)	0.0373*	0.52	HOMO→LUMO+2
			0.44	HOMO→LUMO+3
	23095(TS8)	0.0411*	0.46	HOMO-2→LUMO+1
			0.34	HOMO→LUMO+2
			-0.38	HOMO→LUMO+3
	24096(TS9)	0.0257*	0.52	HOMO-2→LUMO+1
			0.35	HOMO→LUMO+3
3	28169(TS15)	0.0408*	0.39	HOMO-3→LUMO
			0.20	HOMO-3→LUMO+1

Comparison of the molecular orbitals and EDDMs shown in Figure 3.6-3.11 and the time-dependent DFT data in Table 2.1-3.3 for **a**, **b**, and **c** indicates that the transitions of band 1 utilize the redox orbital for **a**, **b**, and **c**. The difference between models **a**, **b**, and **c** is the nature of lower energy sulfur-based orbital HOMO-3. Both **a** and **b** have noticeably less of the dithiolene sulfur out-of-phase in-plane combination with out-of-plane p orbital character in HOMO-3 than is observed for **c**. This difference in the HOMO-3 composition HOMO-3→LUMO transition that contributes to band 2 for **a** and **b,** and is due to **a** and **b** possessing two relatively inequivalent dithiolene ligands and thus a slightly more distorted geometry than **c.** The crystal structure data torsional angle S2S1S3S4 (94.1° of

b and 95.1°/99.7° of **c**, **c'**) and DFT-calculated dihedral angle of S2MoS4 (83.40° of **a**, 83.20° **b** of and 82.34° of **c**) support this conclusion.

Table 3.2 Calculated band energies, oscillator strengths f, and percentage of transition and nature of transition for **b**.

Band	Excitation Energy cm^{-1}	f	%	Principal nature of Transition
1	15123	0.0008	0.68	HOMO→LUMO
	17153(TS2)	0.0195*	0.66	HOMO→LUMO+1
	18797(TS3)	0.0136*	0.67	HOMO-1→LUMO
	20833(TS4)	0.0076*	0.66	HOMO-1→LUMO+1
2	21552(TS5)	0.0315*	0.55	HOMO→LUMO+2
	24691(TS8)	0.0233*	0.48	HOMO-1→LUMO+2
	25381(TS9)	0.0459*	0.40	HOMO-3→LUMO
			0.37	HOMO→LUMO+3
3	28249(TS14)	0.0223*	-0.34	HOMO-1→LUMO+2
			0.42	HOMO-1→LUMO+3
	28986(TS16)	0.0163*	0.63	HOMO-5→LUMO

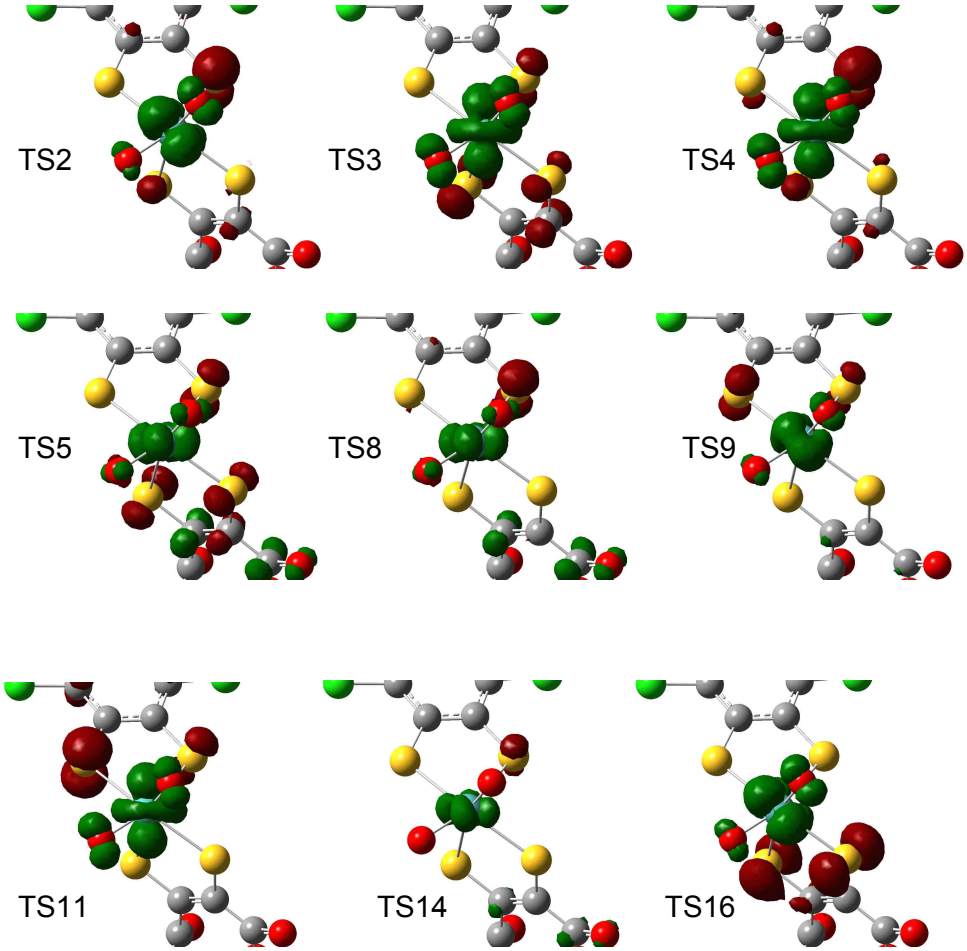

Figure 3.10 Calculated electron density difference maps (EDDMs) of transitions 2, 3, 4, 5, 8, 10, 11, 14 and 16 for **b** depicted at an isodensity value of 0.005 au. Transitions 2 and 3 are the dominant contributors to band 1, and transitions 5, 8,10 and 11 are the dominant contributors to band 2. Transitions 14 and 16 dominates for band 3.

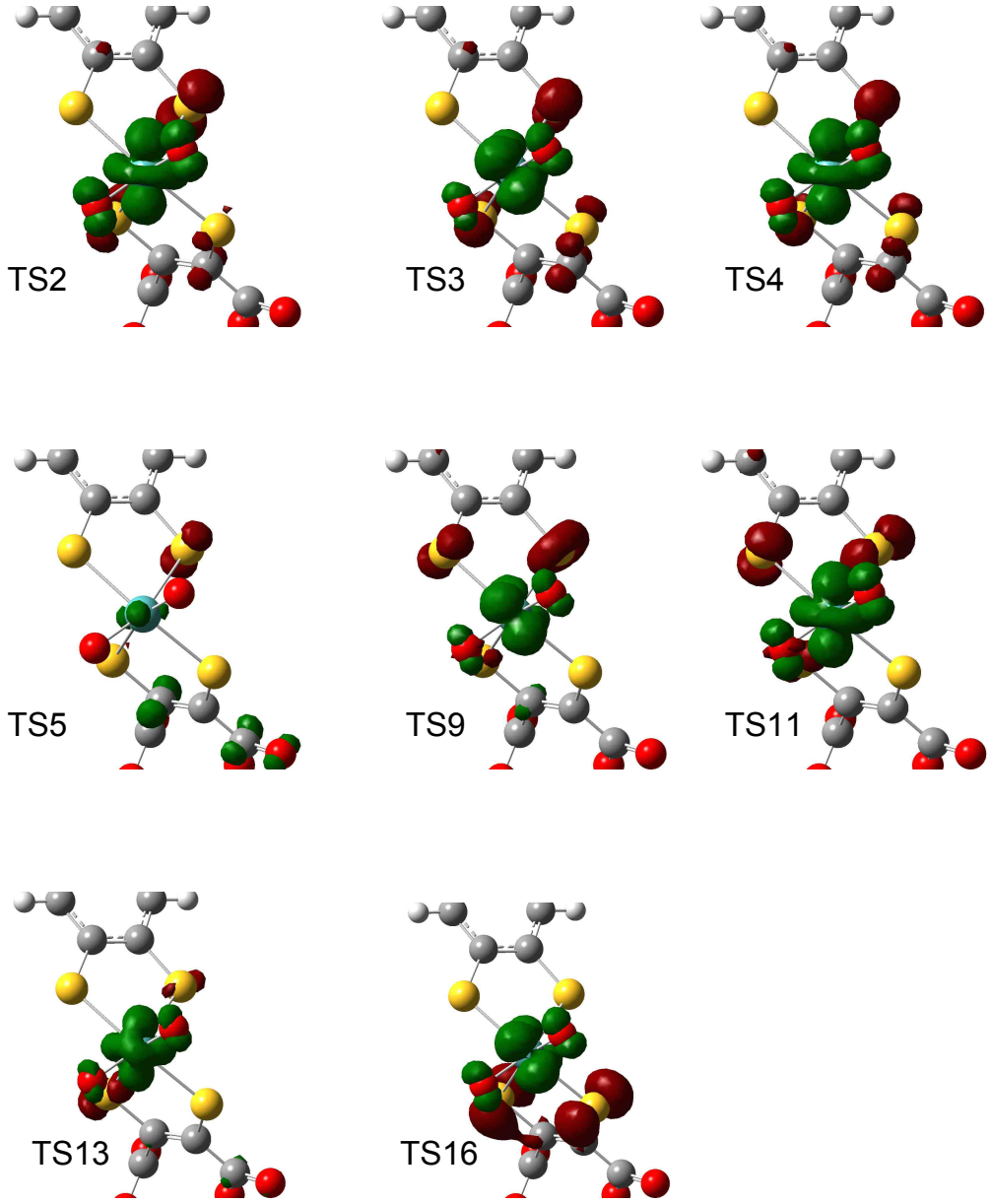

Figure 3.11 Calculated electron density difference maps (EDDMs) of transitions 2, 3, 4, 5, 9, 11, 13 and 16 for **a** depicted at an isodensity value of 0.005 au. Transitions 2 and 3 are the dominant contributors to band 1, and transitions 5, 9 and 11 are the dominant contributors to band 2. Transitions 13 and 16 dominates for band 3.

Table 3.3 Calculated band energies, oscillator strengths (f), percentage of transition and nature of transition for **a**.

Band	Excitation Energy cm^{-1}	f	%	Principal nature of Transition
1	14706	0.0010	0.69	HOMO→LUMO
	16420(TS2)	0.012*	0.66	HOMO→LUMO+1
	17986(TS3)	0.0149*	0.65	HOMO-1→LUMO
	20367(TS4)	0.0096*	0.66	HOMO-1→LUMO+1
2	21142(TS5)	0.0355*	0.49	HOMO→LUMO+2
	23866(TS9)	0.0224*	0.40	HOMO-3→LUMO
			0.43	HOMO-2→LUMO
	25773(TS11)	0.0292*	0.47	HOMO-3→LUMO+1
			0.43	HOMO-2→LUMO+1
3	28249(TS13)	0.0187*	0.41	HOMO-4→LUMO+1
	28986(TS16)	0.0185*	0.63	HOMO-5→LUMO

3.4.4 Resonance Raman Spectra

The resonance Raman spectrum of **c** using 458nm excitation is presented in Figure 3.12. We have observed Mo-$(S_{dt})_4$ and O_{oxo}-Mo-O_{oxo} metal-ligand stretching modes as well as ligand based ene-1,2-dithiolate C-S and C=C stretches, and their corresponding vibrational frequencies are listed in table 3.4. The frequency assignments have been assisted by direct spectral comparison with previously published Raman data for various DMSO reductase family enzymes as well as data for relevant $[Mo(VI)O_2(dithiolene)_2]^{2-}$ model complexes.[6] In general, the experimental vibrational frequencies for **a**, **b**, and **c** are in reasonable agreement with the DFT-calculated frequencies for these modes (Table 4 and Figures 3.12-3.14). Resonance Raman excitation profiles have been constructed for the dithiolene C=C stretches and the symmetric and antisymmetric O_{oxo}-Mo-O_{oxo} stretches for compound **c**. The excitation profiles are shown superimposed on the Gaussian-resolved electronic absorption spectrum in Figure 3.5. Collectively the resonance Raman enhancement profile provides strong support for our LMCT assignments and the nature of the lowest-lying Mo-based acceptor orbitals. Specifically, the observed larger resonance enhancement of the symmetric O_{oxo}-Mo-O_{oxo} stretch upon excitation into the low energy side of band 2 is fully consistent with the population of acceptor orbitals (LUMO+2, +3) being strongly π-antibonding with respect to both oxo ligands. The resonance Raman excitation profiles for the two ene-1, 2-dithiolate C=C stretches in **c** indicate that both of the ene-1, 2-dithioates are involved in LMCT transitions to the Mo center.

Table 3.4 Summary of resonance Raman Data for **a**, **b** and **c.**

Compound **a**		
Vibrational mode	Frequency (cm^{-1}) (observed)	Frequency (cm^{-1}) (calculated)
Mo-$(S_{dt})_4$	360	352
O_{oxo}-Mo-O_{oxo}(sym)	870	945
O_{oxo}-Mo-O_{oxo}(antisym)	834	920
C-S stretch	764	763
C=C stretch	1497	1508
Compound **b**		
Vibrational mode	Frequency (cm^{-1}) (observed)	Frequency (cm^{-1}) (calculated)
Mo-$(S_{dt})_4$	360	353
O_{oxo}-Mo-O_{oxo}(sym)	871	948
O_{oxo}-Mo-O_{oxo}(antisym)	838	923
C-S stretch	765	764
C=C stretch	1497	1512
Compound **c**		
Vibrational mode	Frequency (cm^{-1}) (observed)	Frequency (cm^{-1}) (calculated)
Mo-$(S_{dt})_4$	360	356
O_{oxo}-Mo-O_{oxo}(sym)	867	948
O_{oxo}-Mo-O_{oxo}(antisym)	838	927
C-S stretch	764	764
C=C stretch	1494/1510	1515/1524

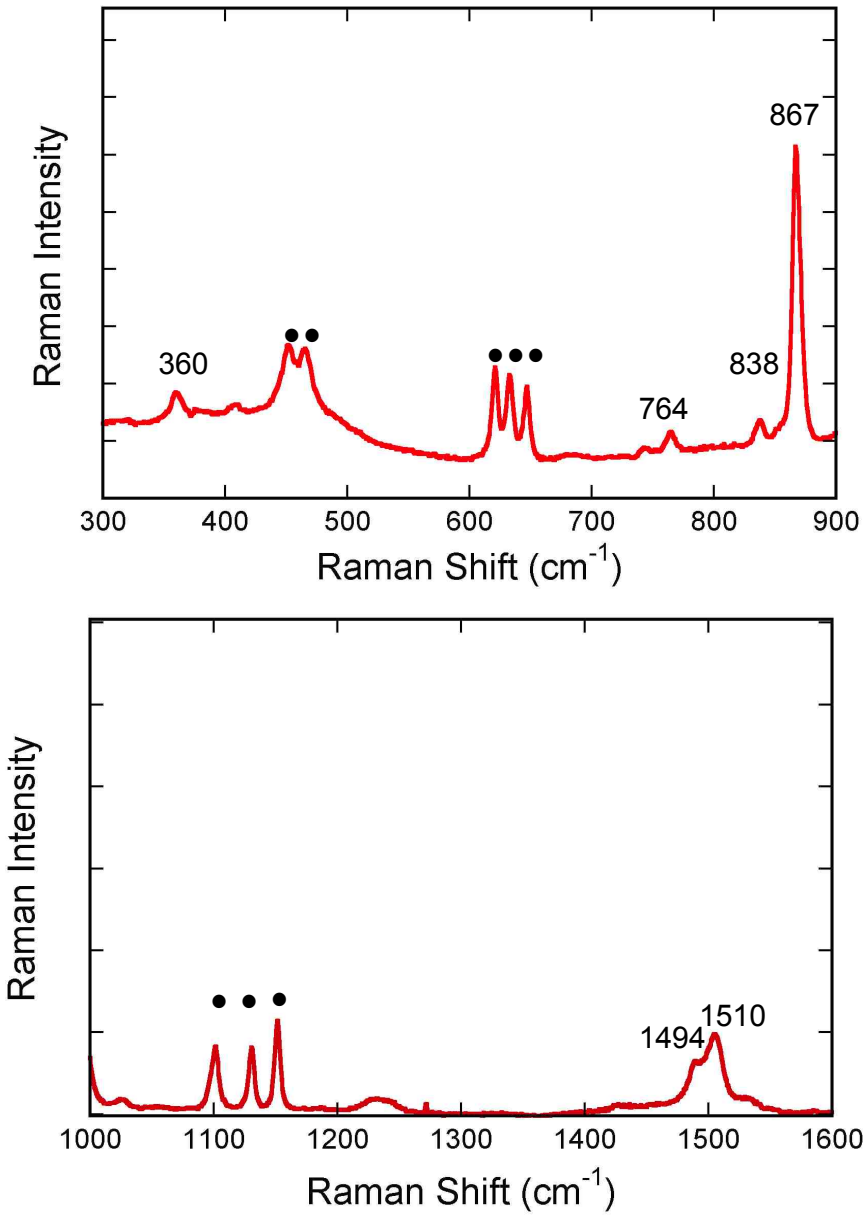

Figure 3.12 Low frequency (top) and high frequency (bottom) resonance Raman spectra of **c** using 458nm excitation. Raman bands for the Na_2SO_4 internal standard are indicated with black dots. Vibrational assignments are given in table 3.4.

Bands 1-3 result from $S_{dithiolene}$→Mo charge transfer transitions, and their intensities are a direct reflection of the degree of $S_{dithiolene}$→Mo charge donation

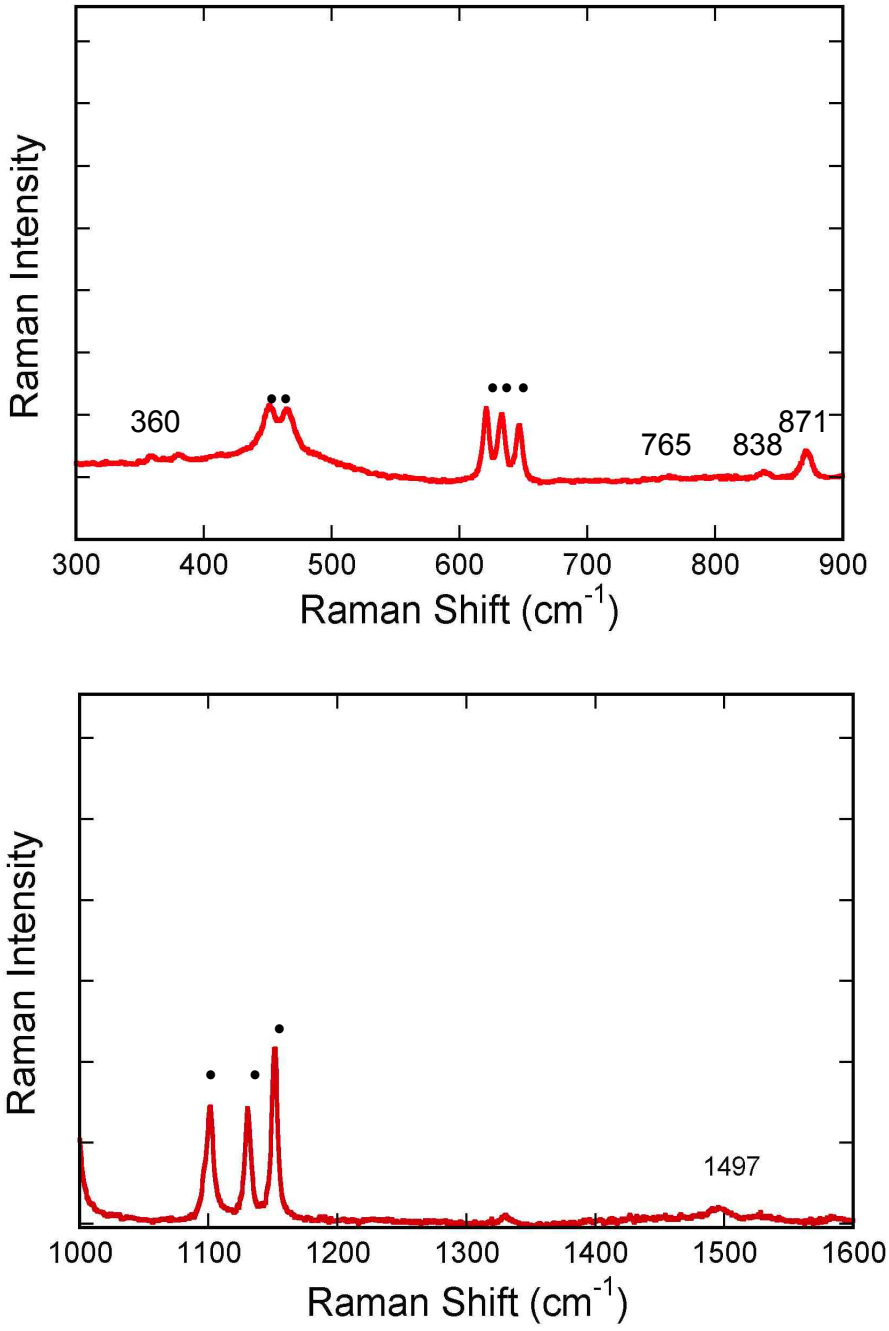

Figure 3.13 Low frequency (top) and high frequency (bottom) resonance Raman spectra of **b** using 458nm excitation. Raman bands for the Na_2SO_4 internal standard are indicated with black dots. Vibrational assignments are given in Table 3.4.

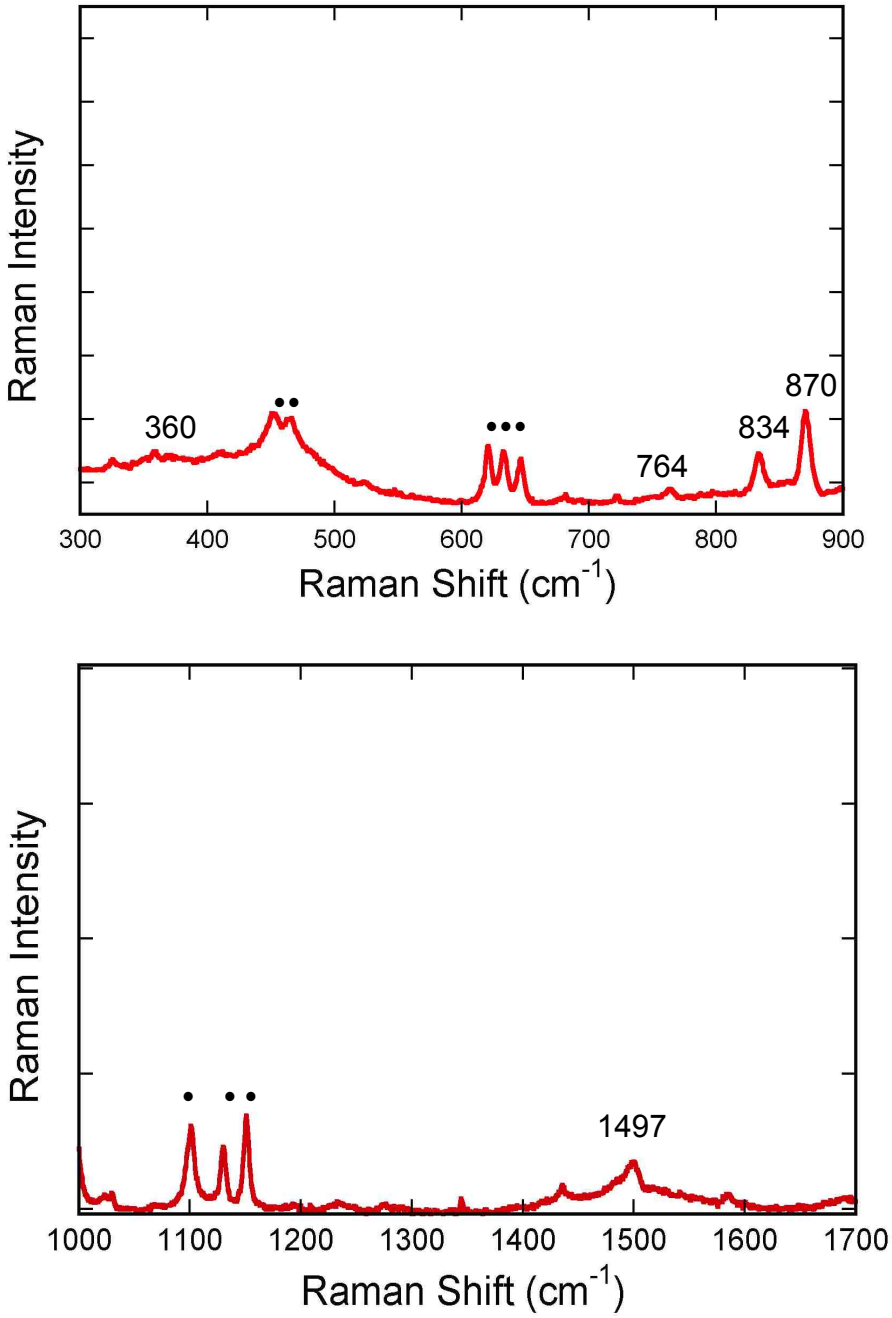

Figure 3.14 Low frequency (top) and high frequency (bottom) resonance Raman spectra of **a** using 458nm excitation. Raman bands for the Na_2SO_4 internal standard are indicated with black dots. Vibrational assignments are given in table 3.4.

present in $[MoO_2(dithiolene)_2]^{2-}$ complexes. It is this charge donation that reflects Mo(VI) contributions to the Mo(VI/V) redox couple by reducing the hard donor

stabilization of the Mo(VI) oxidation state and facilitating reductive processes at the metal. Oxygen atom transfer from $[MoO_2]^{2+}$ centers to oxygen atom acceptors represents a two-electron reductive process at the Mo site, and it has been observed that a linear correlation exists between $E_{1/2}$ and the rate of oxygen atom transfer to PPh_3.[24,25] The implication here is that the activation energy for oxygen atom transfer possesses a considerable contribution from partial electron occupancy of the Mo(VI) LUMO at the transition state. Therefore, Mo-dithiolene covalency can modulate the reduction potential of $[MoO_2]^{2+}$ complexes by reducing the hard donor stabilization of the Mo(VI) state, leading to an increase in the rate of oxygen atom transfer to oxygen atom acceptors. Additionally, electron occupation of the LUMO along the reaction coordinate will assist in the cleavage of the Mo=O bond in oxygen atom transfer reactions with oxo acceptors because of the O=Mo=O π^*-character of the LUMO. Since both the low-energy LUMO and LUMO+1 are weakly O=Mo=O π-antibonding in these pseudo C_2 symmetry dioxo complexes, electron occupation of the LUMO and LUMO+1 orbitals will not make a substantial contribution to lowering the activation energy for oxygen atom transfer to yield a Mo(IV) mono-oxo complex. This is in marked contrast to the situation proposed for the five coordinate active site found in sulfite oxidizing enzymes, where the LUMO is strongly π-antibonding with respect to a single equatorial oxo ligand.[22,23] The similar LMCT spectra for **a**, **b**, and **c** imply very similar ligand field splitting patterns and similar degrees of Mo-dithiolene covalency.

3.4.5 Oxygen Atom Transfer Rates

The Sugimoto group performed the atom transfer reactions from the $Mo(VI)O_2$ complexes to AsO_2^-, which is a native substrate of the DMSOR family enzyme arsenite oxidase. Compounds **b** and **c** transfer a single oxygen atom to AsO_2^- to yield the corresponding MoI(V)O species and AsO_3^- stoichiometrically. In contrast, **a** disproportionate to 0.5 equivalents of $[Mo(VI)O_2(bdt)_2]^{2-}$ and 0.5 equivalents of **c**. Therefore, only the oxygen atom transfer rates of **b** and **c** were able to be determined. It is observed that the rates of reaction for **b** and **c** (k_{obs}, s^{-1}) with AsO_2^- are proportional to the AsO_2^- concentration and follows a second order reaction rate law since no saturation kinetics are observed even even at high AsO_2^- concentration. The OAT rate of **b** and **c** are calculated to be $2.7x10^{-2}M^{-1}s^{-1}$. In molybdenum complexes that show a reversible Mo(VI)/ Mo(V) redox process, the reduction potential provides a good indication of their relative oxygen atom transfer reaction rates.[26-28] Although irreversible redox behavior is observed for **b** and **c**, the small difference in their redox potential values support their identical reaction rates. This result is consistent with the observation of similar low energy LMCT spectra for these complexes as well as similar Mo=O bond strengths inferred from their O_{oxo}-Mo-O_{oxo} stretching frequencies (871 cm^{-1} for **b** and 867 cm^{-1} for **c**).

3.5 Conclusions

The crystallographic, computational, and spectroscopic results presented here indicate the presence of considerable π-delocalization between the $Mo(VI)O_2$ and

($S_2(C_2(CO_2Me)_2^{2-}$) ligand units. This is interpreted to result in a greater Mo(VI)-S bond covalency in **a**, **b**, and **c** as compared with $[Mo(IV)O(S_2(C_2(CO_2Me)_2)_2]^{2-}$. Solution electronic absorption spectra and resonance Raman excitation profiles have allowed for the assignment of the lowest energy LMCT transitions in **a**, **b**, and **c** as transitions from S_{op} orbitals to Mo d orbitals. Finally, the kinetic studies of the $MO(VI)O_2$ complexes have provided insight into the relationship between the electronic structure and OAT reactivity of our model complexes. For **b** and **c** there are key similarities in their electronic structures of the metal ligand complex, namely the lowest energy charge transfer bands (band 1), their O=Mo=O π -antibonding LUMOs, and the frequencies of vibrational modes (O_{oxo}-Mo-O_{oxo} symmetric stretch). These key similarities in the electronic structures of **b** and **c** correlate with the OAT rates of the complexes.

3.6 References

(1) Ellis, P. J.; Conrads, T.; Hille, R.; Kuhn, P. *Structure* **2001**, *9*, 125–132.

(2) Conrads, T.; Hemann, C.; George, G. N.; Pickering, I. J.; Prince, R. C.; Hille, R. *JACS* **2002**, *124*, 11276–11277.

(3) Romão, M. J. *Dalton Trans.* **2009**, 4053–4068.

(4) Pushie, M. J.; George, G. N. *Coordination Chemistry Reviews* **2011**, *255*, 1055–1084.

(5) Cobb, N. *Journal of Biological Chemistry* **2005**, *280*, 11007–11017.

(6) Johnson, M. K. *Progress in Inorganic Chemistry* **2004**.

(7) Sugimoto, H.; Tsukube, H. *Chem. Soc. Rev.* **2008**, *37*, 2609.

(8) Enemark, J. H.; Cooney, J. J. A.; Wang, J.-J.; Holm, R. H. *Chem. Rev.* **2004**, *104*, 1175–1200.

(9) Sugimoto, H.; Suyama, K.; Sugimoto, K.; Miyake, H.; Takahashi, I.; Hirota, S.; Itoh, S. *Inorg Chem* **2008**, *47*, 10150–10157.

(10) Sugimoto, H.; Harihara, M.; Shiro, M.; Sugimoto, K.; Tanaka, K.; Miyake, H.; Tsukube, H. *Inorg Chem* **2005**, *44*, 6386–6392.

(11) Lim, B. S.; Willer, M. W.; Miao, M.; Holm, R. H. *J. Am. Chem. Soc.* **2001**, *123*, 8343–8349.

(12) Das, S. K.; Biswas, D.; Maiti, R.; Sarkar, S. *JACS* **1996**, *118*, 1387–1397.

(13) Oku, H.; Ueyama, N.; Nakamura, A. *Inorg Chem* **1997**, *36*, 1504–1516.

(14) Oku, H.; Ueyama, N.; Nakamura, K. *Inorg Chem* **1995**, *34*, 3667–3676.

(15) Hille, R. *Chem. Rev.* **1996**, *96*, 2757–2816.

(16) Frisch, M. J.; Trucks, G. W.; Schlegel, H. B.; Scuseria, G. E.; Robb, M. A.; Cheeseman, J. R.; Montgomery, J. A., Jr.; Vreven, T.; Kudin, K. N.; Burant, J. C.; Millam, J. M.; Iyengar, S. S.; Tomasi, J.; Barone, V.; Mennucci, B.; Cossi, M.; Scalmani, G.; Rega, N.; Petersson, G. A.; Nakatsuji, H.; Hada, M.; Ehara, M.; Toyota, K.; Fukuda, R.; Hasegawa, J.; Ishida, M.; Nakajima, T.; Honda, Y.; Kitao, O.; Nakai, H.; Klene, M.; Li, X.; Knox, J. E.; Hratchian, H. P.; Cross, J. B.; Bakken, V.; Adamo, C.; Jaramillo, J.; Gomperts, R.; Stratmann, R. E.; Yazyev, O.; Austin, A. J.; Cammi, R.; Pomelli, C.; Ochterski, J. W.; Ayala, P. Y.; Morokuma, K.; Voth, G. A.; Salvador, P.; Dannenberg, J. J.; Zakrzewski, V. G.; Dapprich, S.; Daniels, A. D.; Strain, M. C.; Farkas, O.; Malick, D. K.; Rabuck, A. D.; Raghavachari, K.; Foresman, J. B.; Ortiz, J. V.; Cui, Q.; Baboul, A. G.; Clifford, S.; Cioslowski, J.; Stefanov, B. B.; Liu, G.; Liashenko, A.; Piskorz, P.; Komaromi, I.; Martin, R. L.; Fox, D. J.; Keith, T.; Al-Laham, M. A.; Peng, C. Y.; Nanayakkara, A.; Challacombe, M.; Gill, P. M. W.; Johnson, B.; Chen, W.; Wong, M. W.; Gonzalez, C.; Pople, J. A. Gaussian 03; Gaussian, Inc.: Pittsburgh, PA, **2003**.

(17) O'Boyle, N. M.; Tenderholt, A. L.; Langner, K. M. *J Comput Chem* **2008**, *29*, 839–845.

(18) Webster, C. E.; Hall, M. B. *JACS* **2001**, *123*, 5820–5821.

(19) Ueyama, N.; Oku, H.; Kondo, M.; Okamura, T.-A.; Yoshinaga, N.; Nakamura, A. *Inorg Chem* **1996**, *35*, 643–650.

(20) Sugimoto, H.; Tano, H.; Suyama, K.; Kobayashi, T.; Miyake, H.; Itoh, S.; Mtei, R. P.; Kirk, M. L. *Dalton Trans.* **2011**, *40*, 1119.

(21) Inscore, F. E.; Knottenbelt, S. Z.; Rubie, N. D.; Joshi, H. K.; Kirk, M. L.; Enemark, J. H. *Inorg Chem* **2006**, *45*, 967–976.

(22) Peariso, K.; McNaughton, R. L.; Kirk, M. L. *J. Am. Chem. Soc.* **2002**, *124*, 9006–9007.

(23) Hemann, C.; Hood, B. L.; Fulton, M.; Hänsch, R.; Schwarz, G.; Mendel, R. R.; Kirk, M. L.; Hille, R. *JACS* **2005**, *127*, 16567–16577.

(24) TOPICH, J. *Inorg Chem* **1981**, *20*, 3704–3707.

(25) Basu, P.; Nemykin, V. N.; Sengar, R. S. *Inorg Chem* **2009**, *48*, 6303–6313.

(26) Izumi, Y.; Glaser, T.; Rose, K.; McMaster, J.; Basu, P.; Enemark, J. H.; Hedman, B.; Hodgson, K. O.; Solomon, E. I. *J. Am. Chem. Soc.* **1999**, *121*, 10035–10046.

(27) Sung, K.-M.; Holm, R. H. *JACS* **2002**, *124*, 4312–4320.

(28) Kail, B. W.; Pérez, L. M.; Zarić, S. D.; Millar, A. J.; Young, C. G.; Hall, M. B.; Basu, P. *Chemistry* **2006**, *12*, 7501–7509.

Chapter 4 Spectroscopic and Computational Studies of Model Complexes For Sulfite Oxidase Family Enzymes

4.1 Introduction

As one of the mononuclear molybdenum enzyme families the sulfite oxidase enzyme family is found extensively in animal, plant and bacterial species.[1,2] Chicken sulfite oxidase (CSO),[3] plant sulfite oxidase (PSO)[4] and sulfite dehydrogenase (SDH)[5] from *Starkeya novella* catalyze the conversion of sulfite to sulfate to remove its toxicity to the cell or to degrade sulfur containing amino acids in the terminal step of the organism's mechanism (Figure 4.1). The active sites of sulfite oxidase family enzyme possess a nearly square pyramidal geometry constructed by the coordination of molybdenum with an equatorial dithiolene from the pyranopterin cofactor, a thiolate ligand from a cysteine amino acid and two oxo ligands in a cis orientation (Figure 4.1.D). The catalytic cycle is well understood as shown in Figure 4.2, and is initiated by the attack of the lone pair of sulfur of sulfite on the equatorial oxo leading to the transfer of the oxygen atom to the substrate and reduction of Mo (VI) to Mo (IV).[6] A water then binds at the empty coordination Mo(IV) site. In the oxidative half reaction the Mo (IV) species with the bound water ligand undergoes two consequential proton-coupled electron transfers to a cytochrome via the b-type heme, returning to Mo (VI) resting state.[7]

Electron paramagnetic resonance spectroscopy is widely used for characterization of paramagnetic Mo (V) species of model complexes[8-16] and enzymes.[17-24] In particular, in the oxidative half reaction for sulfite oxidase the one electron oxidation of Mo (IV) to Mo (V) produces EPR silent Fe (II) from Fe (III). Continuous wave and pulsed EPR spectroscopies have been employed to probe the molybdenum center and its coordination environment in sulfite oxidase enzymes. Since the low pH and high pH EPR signals from CSO were first reported,[25] numerous pulsed EPR studies on the Mo (V) forms of sulfite oxidase enzyme have been reported by the Enemark group.[7,26-31] ENDOR and ESEEM experiments confirm an easily exchangeable equatorial OH group in the Mo (V) form of the enzyme, but also detected a slowly exchangeable apical oxo in the high pH of the enzyme.[27,29] The distance of between the molybdenum and the proton of Cα from Mo-bound Cys in CSO and HSO varies from 2.8Å at low pH to 3.3Å at high pH, which indicates a change in the O_{oxo}-Mo-$S_{thiolate}$(cysteine)-C dihedral anlge.[26]

It is the change in the dihedral angle O_{oxo}-Mo-$S_{thiolate}$(cysteine)-C that leads to the variation in the g_{max} value of 2.003 for CSO at low pH to 1.987 at high pH[25], and this is due to decreased Mo-S(thiolate) covalency. The effect of O_{oxo}-Mo-$S_{thiolate}$(cysteine)-C dihedral angle on the Mo-S covalency is probed by the molybdenum oxo model complexes that vary in the number of sulfur donor ligands from three to four.[12,32-35] When the dihedral angle is ~90° the out-of-plane p orbital of the thiolate S is poorly mixed into the singly occupied Mo $d_{xy/dx2-y2}$ orbital, which results in very low intensity for this lowest charge transfer band.

Deviationof the dihedral angle from 90° leads to greater S-Mo covalency and an increase in the intensity of the S→Mo charge transfer band,[12,32,33] which is responsible for the $g_{max} > g_e$.[9,36] This appreciable Mo-S(cysteine) covalency is also observed in bacterial YedY enzyme with g_{max} 2.030.[20]

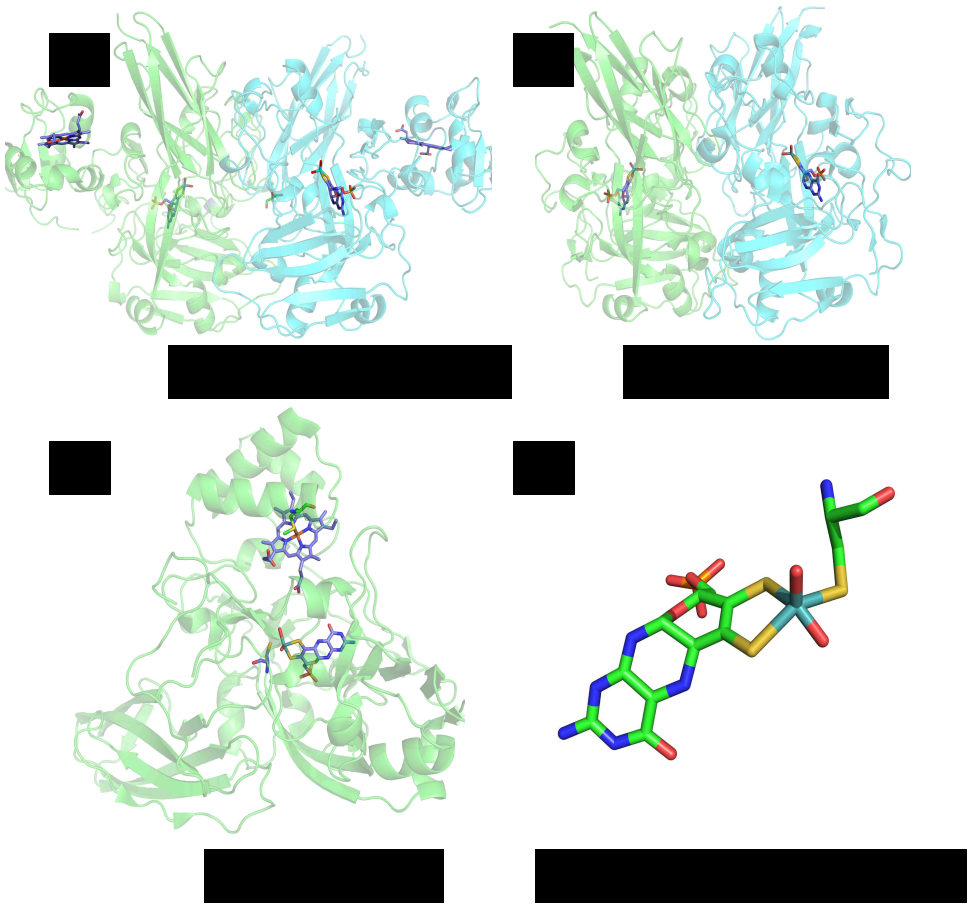

Figure 4.1 Representatives of sulfite oxidase family members. A: Vertebrate sulfite oxidase (chicken sulfite oxidase, pdb ID: 1SOX, 1.7Å) is composed of homodimeric subunits with 110kDa. A b-type-heme and a Moco domain are in each subunit and are connected by a flexible peptide tether. B: Plant sulfite oxidase (*A. thaliana* SO, pdb ID: 1OGP, 2.6Å) of 99kDa possesses only Moco in each subunit with O_2 as electron acceptor. C: Bacterial SDH (50kDa, pdb ID: 2BLF, 1.8Å) possesses hetero-dimeric subunits with Moco and c-type heme respectively. Moco and heme center are displayed in sticks. D: Sticks representation of fully oxidized Moco center.

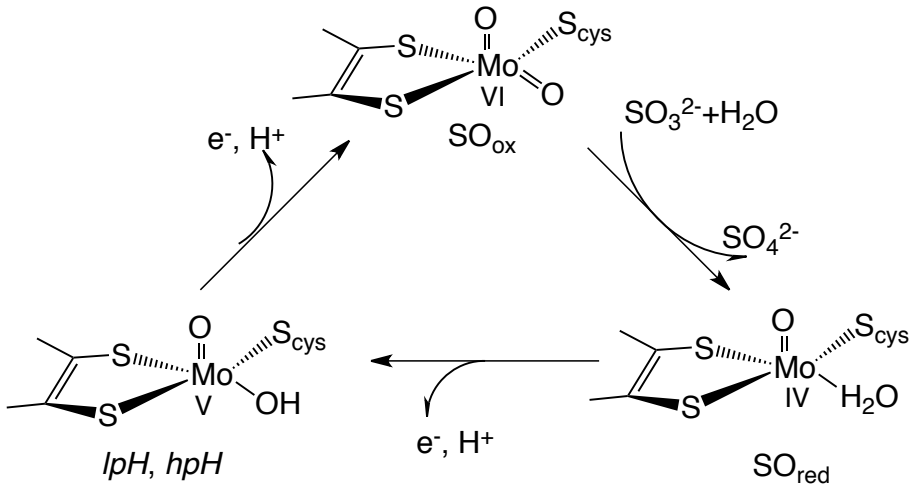

Figure 4.2 Proposed catalytic mechanism of sulfite oxidase. SOox: oxidized SO; SOred: reduced SO; *lpH* and *hpH* are Mo (V) species with EPR signals at high pH and at low pH, respectively.

Recently exchange of cysteine with selenocysteine in HSO has been reported.[37] Upon substitution of cysteine with selenocysteine the g_{max} shifts from 2.0003 to 2.022 at low pH when it remains unchanged at high pH. The smaller effect of substitution of cysteine with selenocysteine at high pH in comparison with that at low pH correlates with a lower S/Se-Mo covalency at high pH compared with at low pH. Here, molybdenum oxo complexes with a series of equatorial O/S/Se donors that possess an ~90° O_{oxo}-Mo-O/S/Se-C dihedral angle have been synthesized and employed to investigate the effects of ligand substitution on Mo-E(O/S/Se) covalency in HSO at high pH.

4.2 Experimental

4.2.1 Synthesis

Physical/General Methods

All air-sensitive manipulations were performed with standard Schlenk techniques

under N_2 flow. All solvents were dried prior to use. Tp*$MoOCl_2$ was prepared by the method from literature reference[14] and the ligand 2-selenolbenzyl alcohol (sba) was prepared as described elsewhere.[38] The other two ligands 2-mercaptobenzyl alcohol (mba) and 2-hydroxybenzyl alcohol (hba) were purchased from Aldrich and used as received without further purification. Tp*MoO(mba) was prepared as previously described in the literature.[39] Elemental analysis was performed at Galbraith Laboratories in Knoxville, TN, and the ESI mass spectrum was collected at the UNM Mass Spectrometry Facility in the Department of Chemistry and Chemical Biology at the University of New Mexico.

Tp*MoO(sba)

sba was produced by reducing diselenide (139mg, 0.37mmol) with $NaBH_4$ (70mg, 1.85mmol) in methanol (3 mL) at 0°C. It was added into a solution of Tp*$MoOCl_2$ (0.37mmol, 178mg) in a dry toluene (50 mL) at 70°C, then this is followed by addition of a dry toluene solution of triethylamine (103μL, 0.74mmol). After stirring for 14h at 70°C under the protection of an N_2 atmosphere the reaction mixture was filtered and evaporated to dryness, then dissolved in a minimum amount of toluene and hexane (2:1) and chromatographed on silica gel with the same ratio of toluene and hexane as an eluant. The third dark brown band was the expected product (60mg). The slow evaporation of saturated dichloromethane from crude product affords the crystals of Tp*MoO(sba). Anal. Calc. for $C_{22}H_{28}N_6O_2SeBMo$ (595 g/mol): C, 44.37; H, 4.71; N, 14.12. Found: C, 44.73; H, 5.05; N; 13.74. MS (ESI): m/z=596 (M+H), 618(M+Na), 634 (M+K).

Tp*MoO(hba)

The compound Tp*MoO(hba) was prepared in same way as Tp*MoO(mba) using 0.258g (2.08mmol) of H_2hba instead of H_2mba. After 3 hours, the color of the reaction mixture changed from lime green to a dark orange. The dark orange solution was filtered and concentrated to form a brown colored powder under vacuum, which was re-dissolved in minimum amount of toluene and chromatographed on sillica gel with an eluent of toluene. The sixth band was the desired product Tp*MoO(hba). The evaporation of this brown colored eluate yielded 0.221g of sand colored powder. The recrystallization of the compound occurred by layering an acetonitrile solution of Tp*MoO(hba) with hexane (5:1 hexane : acetonitrile) This provided the crystals of Tp*MoO(hba). Anal. Calc. for $C_{22}H_{28}N_6O_3BMo$ (531.25 g/mol): C, 49.72; H, 5.27; N, 15.82. Found: C, 49.68; H, 5.42; N; 15.60. MS (ESI): m/z=532 (M+H), 554(M+Na), 570 (M+K).

4.2.2 Spectroscopy

4.2.2.1 Electronic Absorption Spectroscopy

Solution electronic absorption spectra were collected using a Hitachi-3501 UV-vis-NIR single beam spectrophotometer with 1cm path length, black-masked quartz cuvettes at room temperature. Samples were prepared in dichloromethane solvent.

4.2.2.2 Magnetic Circular Dichroism (MCD) Spectroscopy

Low temperature MCD spectra were collected on a system consisting of track-mounted Jasco J-810 (185-900 nm) and Jasco J-730 (700-2000 nm) spectropolarimeters, an Oxford Instruments SM4000-7T superconducting

magnetooptical cryostat (0-7T, 1.4-300 K), and an ITC503 Oxford Instruments temperature controller. The spectrometer was calibrated for circular dichroism intensity with camphorsulfonic acid, and the wavelength was calibrated using Nd-doped glass. The films of samples were prepared by dissolving the compounds in a mixture of dichlomethane and polystyrene. Concentrations for the model compounds in the film samples used for MCD were determined by electronic absorption spectroscopy. The depolarization of the incident radiation was monitored by comparison of the intrinsic circular dichroism of a standard Ni (+)-tartrate solution positioned in front of and behind each sample. The spectra were collected at a temperature of 5 K in an applied magnetic field of 7T.

4.2.2.3 EPR Measurements and Spectral Simulations

The room-temperature solution and frozen-solution EPR spectra were measured at X-band (about 9.4 GHz) with a rectangular cavity and Q band (about 34GHz) with a cylindrical cavity resonator using a Bruker EMX spectrometer. For low temperature measurements, the temperature was kept constant at 77 K in an Oxford Instruments liquid helium flow cryostat. The toluene is used as for the solvent for collecting EPR data for three model compounds. Simulations of spectra were performed using the Easy Spin 3.1.0 software package.[40]

4.2.2.4 X-ray Crystallography

The crystal structures of Tp*MoO(sba) and Tp*MoO(hba) were obtained at The University of New Mexico X-ray Laboratory located in the Department of Chemistry and Chemical Biology. Samples were mounted on a standard Bruker

X8 Apex2 CCD-based X-ray diffractometer equipped with an Oxford Cryostream 700 low temperature device, monochromator and normal focus Mo-target X-ray tube (λ = 0.71073 Å) operated at 1500 W power (50 kV, 30 mA). The X-ray intensities were measured at 202(2) K; the detector was placed at a distance 4.500 cm from the crystal. Data were collected assuming a triclinic cell. The frames were measured for 25 sec instead of 20 [first data set] for 8 runs and 3130 frames. The frames were integrated as monoclinic with the Bruker SAINT software package with a narrow frame algorithm. The integration of the data yielded a total of 58303 reflections of which 9080 were independent in a monoclinic cell to a maximum 2θ value of 65.21°. The final monoclinic cell constants were based on the xyz centers of 9934 reflections above 20σ(I). Analysis of the data showed negligible decay during data collection; the data were processed with SADABS and corrected for absorption. The structure was solved and refined with the Bruker SHELXTL (version 6.12) software package, using the monoclinic space group P2(1)/c. The unique part of the structure is the asymmetric unit. The asymmetric unit is the molecule. The space group symmetry generates four of these units per unit cell. There are no solvent molecules present. All non-hydrdogen atoms refined anisotropically. The carbon hydrogen atoms were included in calculated positions with fixed isotropic U set to 1.5Uequiv of parent atom for terminal methyl groups and 1.2Uequiv for other carbon hydrogen atoms.

4.2.3 Computational Studies

4.2.3.1 Geometry Optimization and EPR Parameters Calculations

The spin-unrestricted density functional theory geometry optimizations and EPR parameter calculations were carried out uding the ORCA 2.8.0.0 package.[41-44] Becke's three-parameter exchange hybrid functional and the correlation functional of Lee-Yang-Parr (B3LYP) implemented in the Gaussian code (B3LYP/G) were used. The polarized-triple-ζ valence with two-polarization functions basis set (TZVPP) and the TZVPP/J auxiliary basis set were employed for the molybdenum and the sulfur and oxygen atoms, while polarized-split-valence SV (P) basis set and SV(P)/J auxiliary basis set were used for all other atoms. The coordinate system is illustrated in Figure 4.3 with the X, Y axes oriented between the metal-ligand bonds. The plots of molecular orbitals were produced with the Chemcraft program using an isosurface value of 0.04au. The g and A tensor orientations relative to molecular orbitals were visualized by VMD and the built-in Tachyon ray-tracer.[45]

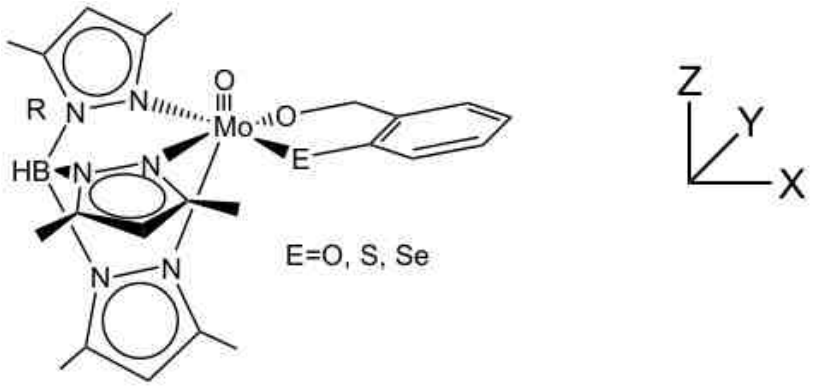

Figure 4.3 Structure of Tp*MoOL2. L2 is chalcogen benzylalcohol and E=O (hba), S (mba), Se (sba). X, Y, Z coordinates label the molecular frame axes; the Z axis directs along the Mo-Oxo bond and the X axis is defined to bisect the equatorial bidentate ligand. Lowercase x, y, z and x', y', z' are employed to designate the principal axes of **g** and **A** tensors.

4.2.3.2 Origin of g-tensor Anisotropy

The Amsterdam Density Functional (ADF) software package (2010. 10.01.) [46]was used to analyze the electronic origin of the g values with a Becke-Perdew exchange-correlation functional (BP86) and a standard triple-ζ STO basis with one set of polarization function for all atoms at the optimized geometry of models. The relativity and frozen core were not considered during the calculations. The g tensor was reoriented to the molecular frames by aligning the three coordinates of g-tensor to the X, Y and Z axes.

4.2.3.3 Time Dependent DFT Calculations (TD-DFT)

All TD-DFT calculations were performed with the ORCA 2.8[41] software package using the functional B3LYP/G based on the optimized model geometries as mentioned above. The basis SVP and auxiliary set SVP/C was used for all atoms except molybdenum, for which TZVPP and TZVPP/C were used. The electron density difference maps (EDDMs) generated from the ORCA program

and visualized with the Chemcraft program using an isodensity value of 0.0004 au, and were employed to probe the nature of key calculated electronic transitions including ligand field transitions and charge transfer transitions.

4.3 Results

4.3.1 Molecular Crystal Structures

The crystal structures of Tp*MoO(sba) and Tp*MoO(hba) are shown in Figure 4.4. The selected bond lengths and bond angles are presented in Table 4.1. The six coordinate distorted Mo (V) complexes possess a lengthened Mo-N3 bond due to the trans effect from the apical oxo ligand that has also been observed for the Tp*MoOL2 complex.[47] The Mo-N1 bond length is similar to the average value observed in [(L3S)MoO(bdt)], [(L3S)MoO$(SPh)_2$][12], and the Tp* analogues [Tp*MoO(bdt)] and [Tp*MoO$(SPh)_2$].[8] The Mo-N5 bond in Tp*MoO(hba) is about 0.2Å shorter than that in Tp*MoO(mba) and Tp*MoO(sba). It arises from the trans effect from the longer Mo-O2 in Tp*MoO(hba) by comparison to Tp*MoO(mba) and Tp*MoO(sba). The Mo-E the bond length exhibits the trend of Se>S>O (Figure 4.5). The Mo-O bond length is shorter than those of Mo-S and Mo-Se due to the smaller atomic radius. We observed an decrease of Mo-E-C in Tp*MoO(hba), Tp*MoO(mba) and Tp*MoO(sba) as listed in table 4.1. Interestingly the O-Mo-E-C dihedral angle is remarkably close to 90°, as observed in the crystal structure of the chicken SO enzyme.[3]

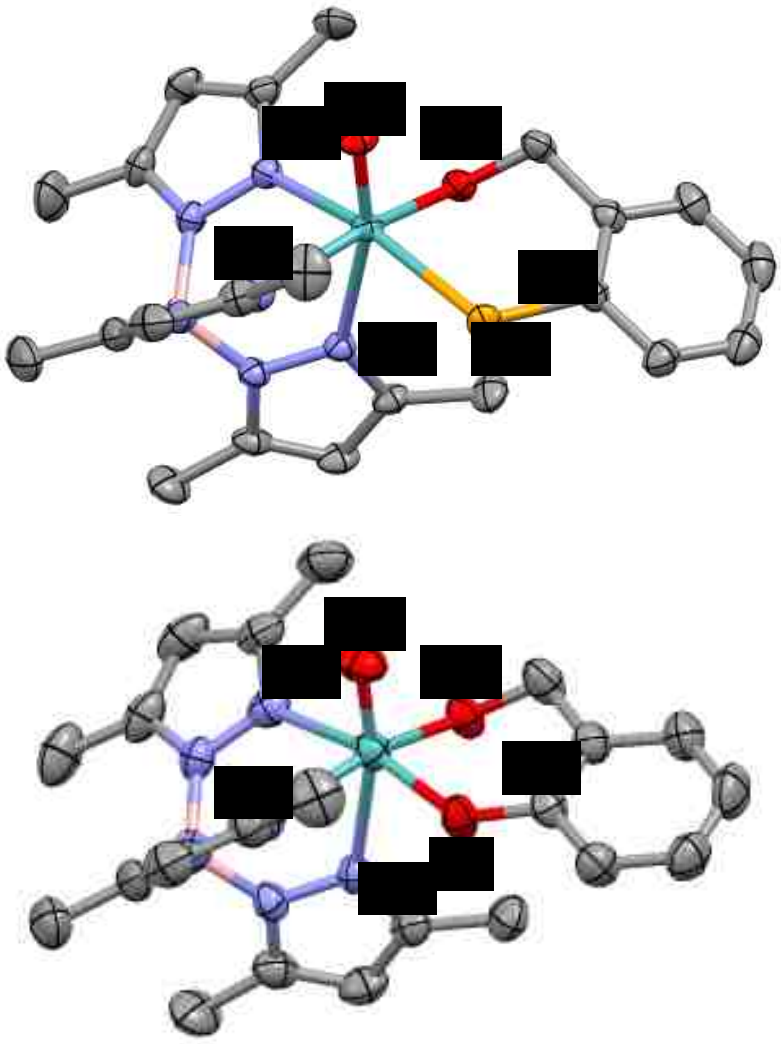

Figure 4.4 Crystal structure of Tp*MoO(sba) and Tp*MoO(hba): Red: O; Grey: C; Brown is Se; Pink: B; Cyan: N. Hydrogen atoms removed for clarity.

4.3.2 Electronic Absorption Spectra

An overlay of the electronic absorption spectra of the three complexes is shown in Figure 4.6 **(**top). The similarity between Tp*MoO(mba) and Tp*MoO(sba) is indicated by a weak low energy absorption band and two strong absorption

Table 4.1 Selected Bond Distances and Bond Angles for the three complexes.

Complex		Tp*MoO(hba)	Tp*MoO(mba)	Tp*MoO(sba)
Bond Distances	Mo-N1	2.186	2.187	2.187
	Mo-N5	2.188	2.205	2.208
	Mo-N3	2.340	2.341	2.343
	Mo-O1	1.675	1.676	1.682
	Mo-O2	1.917	1.903	1.906
	M-E	1.954	2.397	2.534
Bond Angles	O1-Mo-E-C1	-79.5	-95.5	-99.0
	Mo-O-C1	128	110	106
	O1-Mo-E	103.0	102.1	101.8
	O2-Mo-E	88.1	87.8	87.4
	O1-Mo-N3	167.2	164.7	165
	N1-Mo-N5	86.1	86.7	86.3

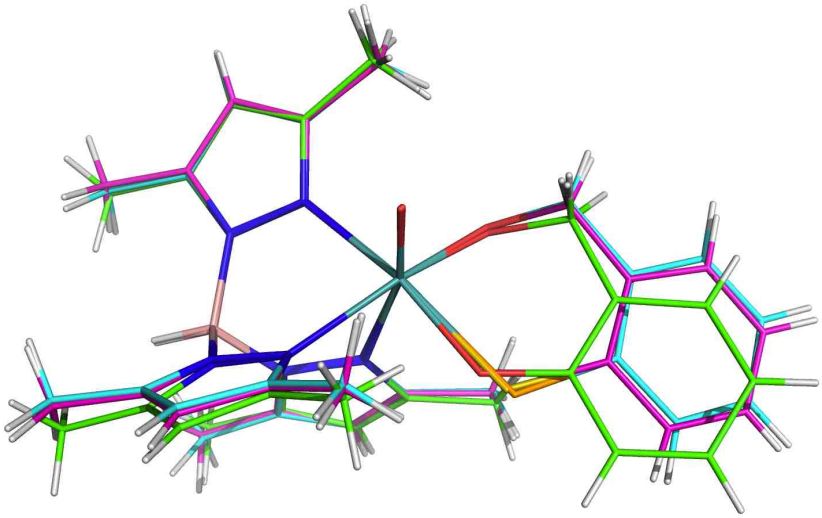

Figure 4.5 Overlay of crystal structures of for the three complexes. Green is Tp*MoO(hba), pink is Tp*MoO(mba) and cyan is Tp*MoO(sba), E: Red O; Yellow S; Brown Se.

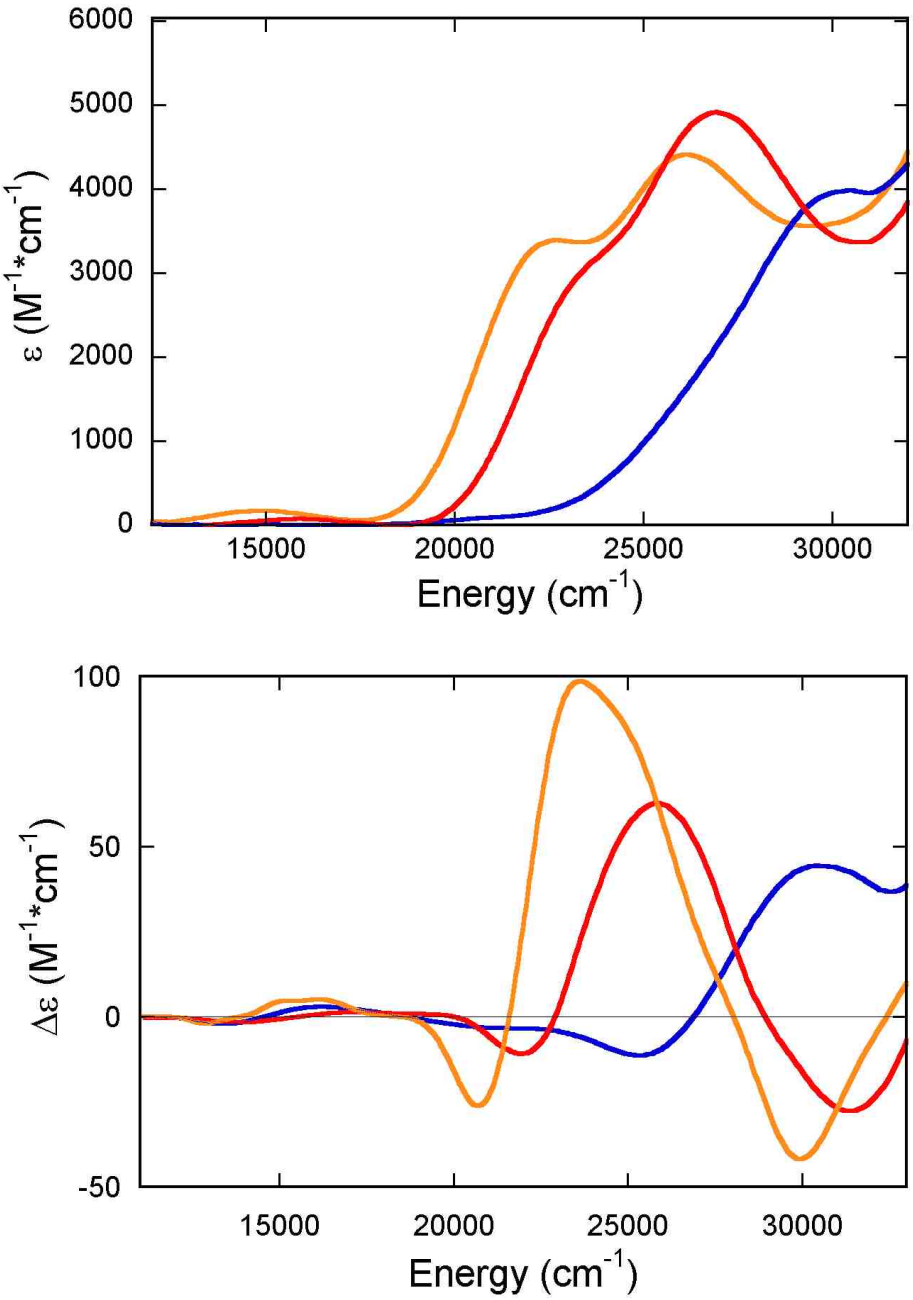

Figure 4.6 Overlay of electronic absorption spectra for the three complexes (top) and MCD spectra (bottom). Blue, Tp*MoO(hba); red, Tp*MoO(mba) and orange Tp*MoO(sba).

bands at ~16000cm^{-1} (ε≈150 M^{-1} cm^{-1}), ~22500 cm^{-1} (ε ≈3000 M^{-1} cm^{-1}) and 27000 cm^{-1} (ε ≈4900 M^{-1} cm^{-1}) for Tp*MoO(mba) and these correspond to slightly red shifted bands at ~14500cm^{-1} (ε ≈175 M^{-1} cm^{-1}), ~21000 cm^{-1} (ε ≈3500 M^{-1}

cm^{-1}) and 26000 cm^{-1}($\varepsilon \approx 4500\ M^{-1}\,cm^{-1}$) for Tp*MoO(sba). When the equatorial E donor changes from Se or S to O, the absorption spectrum changes noticeably, where the low energy absorption band at ~15000 cm^{-1} ($\varepsilon \approx 75\ M^{-1}\,cm^{-1}$) is lower in intensity (not observable in low concentration samples) and at higher energies we observed a broad shoulder underneath of the intense band at 30000 cm^{-1} ($\varepsilon \approx 4000\ M^{-1}\,cm^{-1}$).

4.3.3 MCD Spectra

The 5K MCD spectra of the three complexes are overlayed in Figure 4.6 **(**bottom). The MCD spectra of Tp*MoO(mba) and Tp*MoO(sba) are also very similar as observed for the electronic absorption spectra of these two complexes . The MCD spectrum of Tp*MoO(mba) with relatively smaller $\Delta\varepsilon$ values is shifted to higher energy relative to Tp*MoO(sba) by several hundreds of wavenumbers in the low energy region and 1000-2000 cm^{-1} in the high energy region, analogous to what was observed in the absorption data. Both temperature-dependent C-term and pseudo A-term components are displayed in the observed MCD dispersion of these two complexes with a negative-positive-negative-positive-negative pattern. The MCD spectrum of Tp*MoO(hba) displays a negative-negative-positive pattern above 20000 cm^{-1} and a symmetric negative-positive pseudo A-term feature at 15000 cm^{-1}.

4.3.4 Time Dependent Calculations

Time-dependent DFT calculations have been used to understand the band energies and intensities for the three complexes as shown in Figure 4.7. The calculated absorption spectra for Tp*MoO(sba), Tp*MoO(mba) and Tp*MoO(hba)

do not match the experimental data with respect to the band energies. This is especially true for the low energy bands below 20,000cm^{-1}. This is often observed for the ligand field transitions and LMCT transitions in the Tp*MoOL2 system. The bulky Tp* is always considered as a spectroscopically innocent ligand in its transition metal complexes since its absorption peaks appear above 30, 000cm^{-1} experimentally.[48] However, as a negative charged ligand Tp* causes perturbations on the energy levels of various molecular orbitals of the other non-innocent ligands in TD-DFT calculations, which leads to the unreasonable transition energies in calculated electronic absorption spectra.

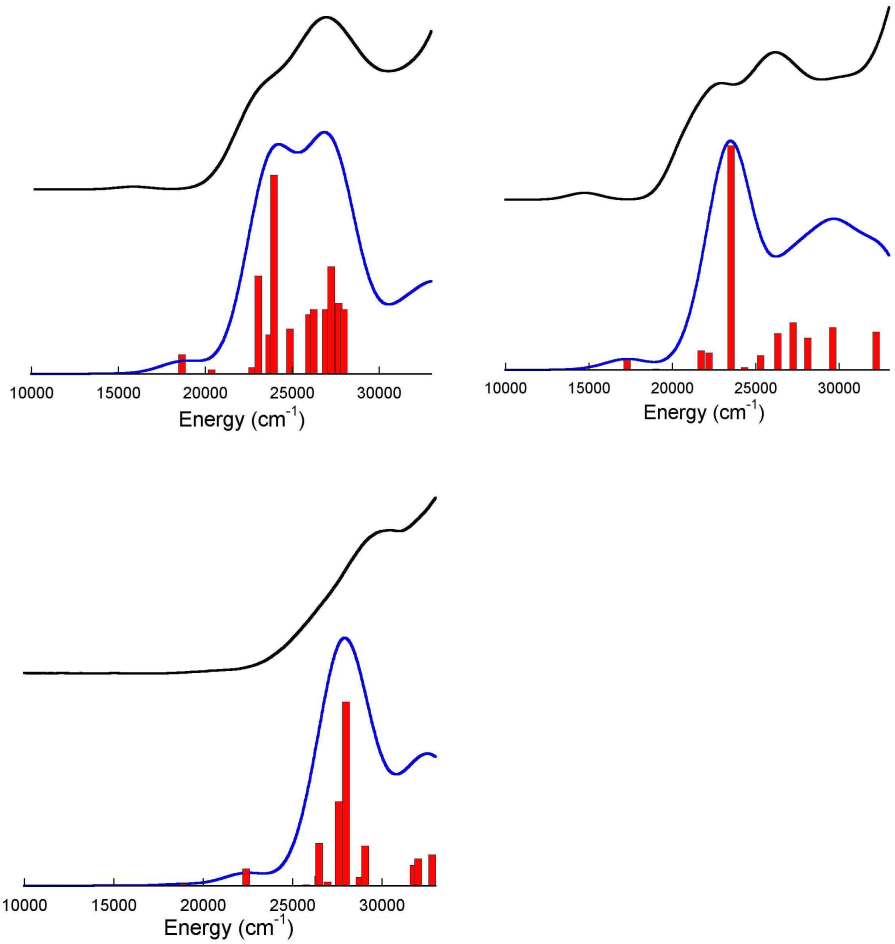

Figure 4.7 Experimental (black) and TD-DFT calculated (blue with red oscillator strength bars) absorbance for Tp*MoO(sba) (left top), Tp*MoO(mba) (right top) and Tp*MoO(hba) (bottom).

4.3.5 EPR Spectra

Experimental EPR data

The room temperature solution X-band EPR spectra (Figure 4.8) of the three complexes are typical for Mo(V) species with a primary ^{98}Mo (I=0; 74.53% abundance) signal central resonance at g ~2 and six hyperfine lines from $^{95, 97}$Mo (I=5/2; 25.38% abundance). The isotropic g and A values show small shifts between Tp*MoO(sba) and Tp*MoO(mba), and a larger shift relative to Tp*MoO(hba). The 77 K frozen-solution EPR spectra of the three complexes in toluene (Figure 4.9 left) display a rhombic g-value pattern consistent with their low symmetry (C_1) geometry. The rhombicity of the EPR signal is more obvious as E changes from oxygen to sulfur and selenium, which is clearly shown in the Q-band EPR spectra that provide a high resolution determination for the g values (Figure 4.9 right).

Spin-Hamiltonian Parameters

The spin-Hamiltonian equation (1) is employed to simulate the collected frozen-solution EPR spectra. Here, β is the Bohr magnetron and B is the applied magnetic field. $\hat{S}$ and $\hat{I}$ are the electron spin operator and the nuclear spin operator respectively. g and A are the principal axes of the g-tensor and A-tensor (nuclear hyperfine coupling constant), respectively.

$$H = \beta B(g_{xx'}\hat{S}_x + g_{yy}\hat{S}_y + g_{zz}\hat{S}_z) + A_{x'x'}\hat{S}_{x'}\hat{I}_{x'} + A_{y'y'}\hat{S}_{y'}\hat{I}_{y'} + A_{z'z'}\hat{S}_{z'}\hat{I}_{z'} \quad (1)$$

Computational simulations of X-band and Q band EPR spectra provide the spin-Hamiltonian parameters in Table 4.2. The g and A values for Tp*MoO(mba) and Tp*MoO(sba) are almost identical. By comparison, Tp*MoO(hba) possesses a less rhombic spectrum with smaller g_{min} and g_{max} values. The g_{max} for all three Mo compounds is less than the free electron value (g_e=2.0032). As for the nuclear hyperfine splitting the similar pattern and magnitude are shown in all three complexes. The Euler angles are represented α as a rotation with 'z' axis, β as a rotation with new 'y' axis and γ as a rotation with new 'z' axis. Underlined g values in Table 4.2 were calculated for the model complexes using the ADF program. The main contribution to the g shift (equation 2) is described in equation (3):

$$g_{ij} = g_e + \Delta g_{ij} \quad (2)$$

$$\Delta g^{ia} = -\frac{1}{S}\sum_i\sum_a \frac{<\psi_i|l_\mu|\psi_a><\psi_i|h_{SOC}|\psi_a>}{\varepsilon_i^\alpha - \varepsilon_a^\alpha} + \frac{1}{S}\sum_i\sum_a \frac{<\psi_i|l_\mu|\psi_a><\psi_i|h_{SOC}|\psi_a>}{\varepsilon_i^\beta - \varepsilon_a^\beta} \quad (3)$$

where S=1/2, h_{SOC} is the spatial part of spin-orbit operator, l_μ is the one-electron angular momentum operator, ε_i and ε_a are the energies of occupied orbital ψ_i and virtual orbital ψ_a respectively.[11] The negative contribution from the first item in equation (3) contains α spin transitions: SOMO→VMO (d→d) and DOMO→VMO (LMCT-occupied ligand orbitals to virtual orbitals). The second item contributes positively within β spin transitions DOMO→VMO (LMCT-

occupied ligand orbitals to virtual orbitals). The sum of various contributions to the calculated g-tensor shifts are listed in the Table 4.3 but do not show a rhombic pattern as observed in the experimental EPR data of the model compounds. Individual contribution from excited states being formed from one electron excited from singly occupied and doubly occupied orbitals to virtual orbitals, respectively are exhibited in the Tables 4.4-4.6. The contribution of selected MOs with SFO orbital population to the net g shifts is dominated by the transitions between d components of the manifold. It is worth mentioning that the $d_{X2-Y2} \rightarrow d_{YZ}$ transition not only contributes primarily to the g_{xx} shift but also g_{zz} shift and off-diagonal g_{xz} term. The LMCT transitions do not contribute significantly, as reported previously for the Tp*MoOL2 system.[11]

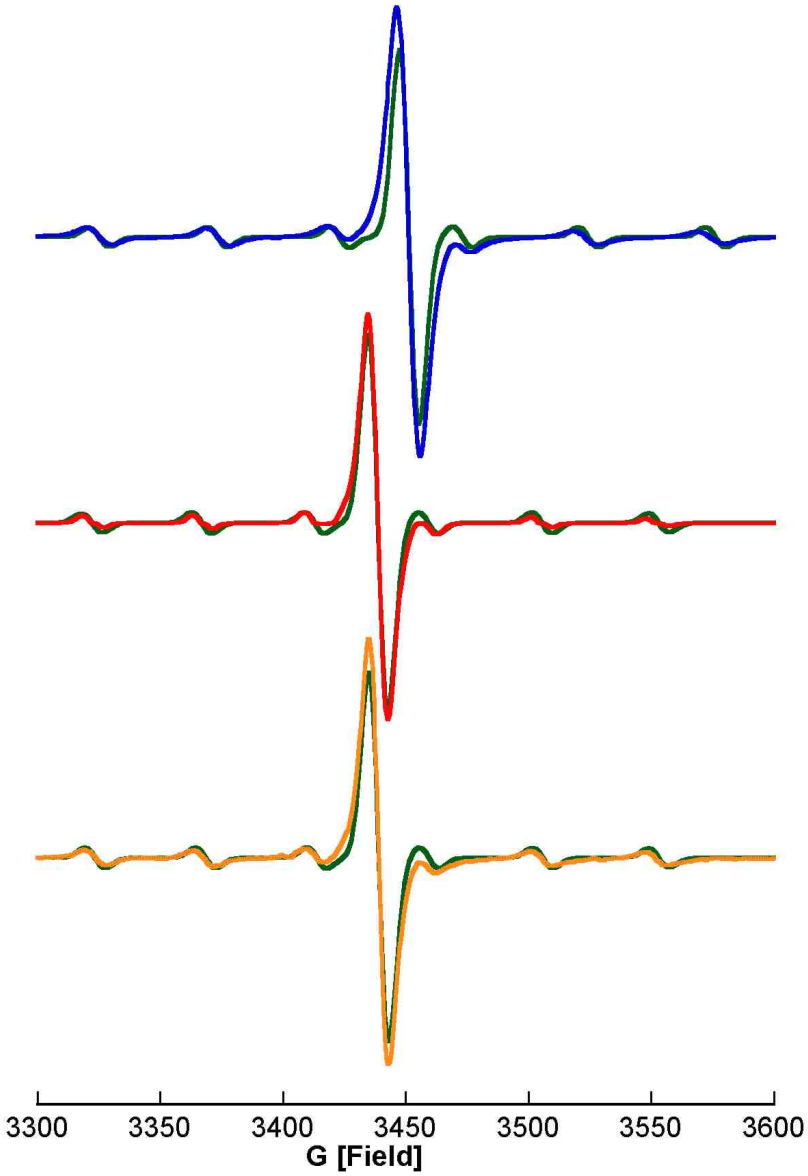

Figure 4.8 Overlay of room temperature EPR spectra for the three complexes. Green, simulated spectrum; Blue, Tp*MoO(hba) with g_{iso}=1.948 and A_{iso}=136GHz; red, Tp*MoO(mba) with g_{iso}=1.9594 and A_{iso}=125.67GHz and orange Tp*MoO(sba) with g_{iso}=1.9597 and A_{iso}=125MHz.

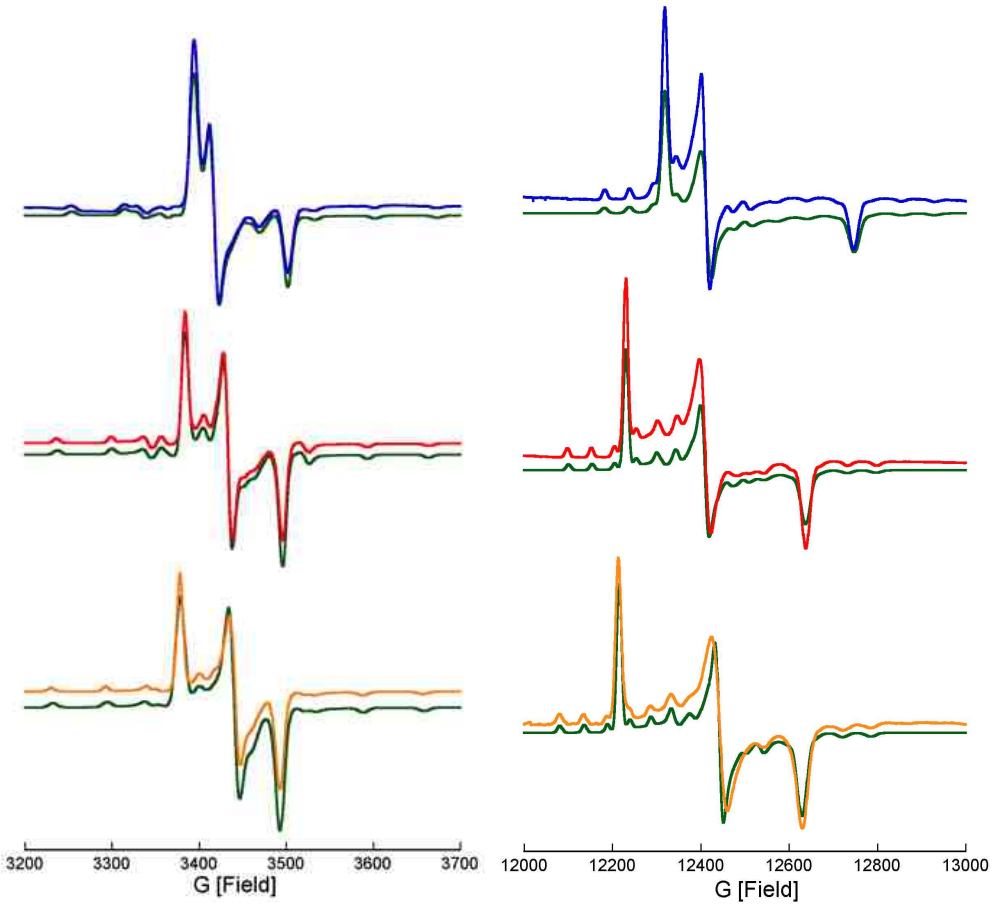

Figure 4.9 Frozen glass (toluene) X-band and Q-band EPR spectra of Tp*MoOL2 complexes: Blue Tp*MoO(hba); Red Tp*MoO(mba); Brown Tp*MoO(sba); Green is the spectral simulation.

Table 4.2 Experimental and calculated (italic, ORCA) spin-Hamiltonian parameters for the three complexes (underlined values are the calculated g values from the analysis of g-tensor shifts with ADF). Hyperfine coupling constant units are in MHz.

Complex	($\alpha/\beta/\gamma$)			($g_{xx}/g_{yy}/g_{zz}$)			($A_{xx}/A_{yy}/A_{zz}$) (GHz)		
Tp*MoO(sba)	-20.7	53	-23.4	1.927	1.956	1.992	83	90	202
	-20.7	*54.9*	*-23.4*	*1.921*	*1.951*	*1.991*	*67*	*73*	*178*
				1.926	1.955	1.999			
Tp*MoO(mba)	22.8	55	20.6	1.925	1.960	1.989	85	90	203
	22.8	*55.7*	*20.6*	*1.923*	*1.957*	*1.988*	*68*	*73*	*180*
				1.929	1.962	1.996			
Tp*MoO(hba)	-16.8	58.3	-13.5	1.907	1.956	1.973	95	95	218
	-16.8	*60*	*-13.5*	*1.908*	*1.960*	*1.976*	*75*	*76*	*192*
				1.913	1.964	1.984			

Table 4.3 Contributions to the g tensor shift (in units of PPM) from spin orbit coupling between occupied orbitals and virtual orbitals.

Complex		Transition	Δg_{XX}	Δg_{YY}	Δg_{ZZ}	Δg_{XZ}	Δg_{YZ}	Δg_{XY}
Tp*MoO(sba)	α	SOMO→VMO	-50042	-40647	-70966	58270	25845	-10104
	α	DOMO→VMO	-100127	-91189	-53005	-9678	12563	-26561
	β	DOMO→VMO	95536	83334	82910	7940	-15073	23831
	SUM		-54633	-48502	-41061	56532	23335	12834
Tp*MoO(mba)	α	SOMO→VMO	-46994	-42881	-71133	59014	26496	3888
	α	DOMO→VMO	-70729	-65755	-29257	-1277	-20400	17093
	β	DOMO→VMO	67531	66291	60569	5645	12008	-13615
	SUM		-50192	-42345	-39821	63382	18104	7366
Tp*MoO(hba)	α	SOMO→VMO	-52680	-45549	-84088	69268	21659	-10542
	α	DOMO→VMO	-55553	-44623	-15524	-8448	-20092	-2118

	β	DOMO→VMO	51507	47474	38948	1828	8423	9466
	SUM		-56726	-42698	-60664	62648	9990	3194

Table 4.4 Orbital populations of selected α and β orbitals for Tp*MoO(hba). Individual contributions of these transitions to the g-tensor shift (in units of PPM) by SOC between occupied and virtual orbitals.

Tp*MoO(hba)											
ΔE(cm^{-1})	MO(α)	%Mo	%Oxo	%O	%O (benzylate)	Δg_{XX}	Δg_{YY}	Δg_{ZZ}	Δg_{XZ}	Δg_{YZ}	Δg_{XY}
35360	L+8	16.5(d_{XY} 15.4; $d_{X^2-Y^2}$ 1.1)	0	1.8	1.2	2	-1729	-18434	-960	11298	305
33976	L+6	35.8(d_{XY} 29.1; d_{YZ} 1.5; d_{XZ} 1.2; d_{Z^2} 2.3; d_{X2-Y2} 1.7)	0	4.5	3.4	52	-2810	-32131	-1098	19036	373
15224	L+1	56.7(d_{XZ} 47.4; $d_{X^2-Y^2}$ 1.1; d_{Z^2} 4.9; d_{XY} 3.3)	23.7	1.5	5.7	42	-36115	-1438	100	-15064	-238
13840	LUMO	55.5(d_{YZ} 34.8; $d_{X^2-Y^2}$ 7.5; d_{XZ} 3.7; d_{Z^2} 9.5)	24.6	2.4	1.4	-50966	-275	-23945	70563	5164	-7729
0	HOMO	65($d_{X^2-Y^2}$ 51; d_{YZ} 6.1; d_{XY} 7.9)	3	3.6	10						
-4880	H-1	1.5 d_{YZ}	4.2	20	0	-1382	-2275	-1430	-215	3623	2508
-10408	H-7	1.4 $d_{X^2-Y^2}$	0	0	4.4	-44	-1755	-954	-36	325	599
-13880	H-9	2.5 $d_{X^2-Y^2}$	2.9	18.7	37.6	-2233	197	-3645	-612	-443	146
-17360	H-10	1.1 d_{XY}	0	12.7	35.2	-6528	-884	117	-1334	-1460	-1982
-20504	H-11	0	1.5	29.4	1.9	-1493	-1877	-192	172	-1374	857
-24424	H-12	10.2(d_{YZ} 1.8; $d_{X^2-Y^2}$ 7.3; d_{XY} 1.1)	4.5	25.3	20.4	-3152	-2900	-2074	-5566	88	3687
-25880	H-13	2.2 $d_{X^2-Y^2}$	13.2	21.4	2.7	-74	-1845	350	23	146	-738
-31656	H-17	12(d_{YZ} 1.8; $d_{X^2-Y^2}$ 7.3; d_{Z^2} 2.9)	6	1.8	1.9	-2793	-342	250	-826	-1213	-2250
-32344	H-18	4.2(d_{XZ} 2.0; d_{Z^2} 2.2)	4.6	0	0	-1891	-2161	102	-142	-32	-2614
-33576	H-20	10.8(d_{YZ} 1.1; $d_{X^2-Y^2}$ 7.7; d_{XY} 2)	18.4	3.9	0	-1599	-3473	-617	-60	-2333	3141
-37728	H-25	3.2(d_{XY} 1.2; d_{Z^2} 2)	7.2	0	0	-3908	-1711	-591	-943	-1204	-2248
-39840	H-28	17.6(d_{YZ} 3.4; d_{Z^2} 14.2)	28.1	0	0	-18292	-16438	-2636	2445	-10261	-1172
ΔE(cm^{-1})	MO(β)	%Mo	%Oxo	%O	%O(benzylate)	Δg_{XX}	Δg_{YY}	Δg_{ZZ}	Δg_{XZ}	Δg_{YZ}	Δg_{XY}
0	LUMO	75.9($d_{X^2-Y^2}$ 59; d_{YZ}	1.1	2.8	6	-7004	10890	29380	-565	-14032	1670

		7.6;dxy 9.3)									
-14320	HOMO	0	3.9	20.7	0	68	1812	409	-1015	-1539	-1353
-22720	H-8	1.2 d_{XY}	7.8	15.9	41.4	528	-186	2701	1135	-90	13
-26488	H-9	3 $d_{X^2-Y^2}$	1.1	12	36.4	6521	2136	5442	5204	-3136	257
-30152	H-10	0	25.3	1.6	1.7	1291	1629	192	-122	1242	-706
-32288	H-11	5.88 $d_{X^2-Y^2}$	4.4	30	25.4	1718	2827	1621	3777	229	-467
-35280	H-12	0	20.2	22.4	0	1250	1156	-326	-54	-417	784
-40000	H-15	2.7 d_{XY}	0	0	0	832	1014	3637	-1291	-1763	-457
-40800	H-16	13.6(d_{YZ} 7.2; $d_{X^2-Y^2}$ 3.4; d_{Z^2} 3)	40.2	1.7	1.5	5869	2303	1735	-3482	4663	-1038
-41776	H-17	4.8(d_{XZ} 3.0; d_{Z^2} 1.8)	14.1	0	0	2498	3347	1055	-2537	-2125	3951
-42400	H-18	5 d_{XZ}	9.5	0	0	1711	3461	198	-247	1364	-200
-42840	H-19	6.9(d_{XY}2.4; d_{XZ} 4.5)	14.6	5.2	0	1128	2625	2880	1759	3986	-862
-43816	H-20	5.3(d_{XZ} 2.2; d_{YZ} 1.8; d_{Z^2} 1.3)	11.7	6.1	5.5	203	1318	224	692	-423	150
-45088	H-21	3.5(d_{XZ} 1.5; d_{XY} 2.0)	2.7	1.2	0	749	-226	1296	1331	584	391
-46704	H-23	2.0 d_{XY}	0	1.1	0	884	699	2648	-1288	-1025	-151
-47168	H-24	3.0 d_{Z^2}	8.4	0	0	4618	2651	1260	886	1211	1438
-48408	H-27	15.7 (d_{Z^2} 12.3; d_{YZ} 3.4)	27.4	0	0	16403	15550	2195	-2070	10051	428

Table 4.5 Orbitals populations of selected α and β orbitals for Tp*MoO(mba) individual contributions of these transitions to the g-tensor shift (in units of PPM) by SOC between occupied and virtual orbitals.

Tp*MoO(mba)											
ΔE(cm^{-1})	MO(α)	%Mo	%Oxo	%S	%O (benzylate)	Δg_{XX}	Δg_{YY}	Δg_{ZZ}	Δg_{XZ}	Δg_{YZ}	Δg_{XY}
31408	L+6	33.1(d_{XY} 26.8; d_{YZ} 1.8; d_{Z^2} 4.5)	1	10.6	1.6	-177	-641	-26513	-5094	9208	1092
29880	L+5	15.2 d_{XY}	0	5	1.3	-246	-697	-8301	2856	6072	-1048
28128	L+2	3 d_{XY}	0	0	0	-9	92	-7088	676	-999	108
15072	L+1	55.2(d_{YZ} 1.9; d_{XY} 1.1; d_{XZ} 49.6; d_{Z^2} 2.6)	24	1.2	4.5	-2947	-36304	51	1371	-3888	21023
13984	LUMO	55.1(d_{YZ} 47.4; d_{XY} 1.4; d_{XZ} 3; $d_{X^2-Y^2}$ 2.1; d_{Z^2} 1.2)	23	5.9	1.1	-42700	-1191	-18065	56615	9753	-14375
0	HOMO	59.7($d_{X^2-Y^2}$ 57.3;	2.7	0	15.1						

		d_{YZ} 2.4)									
-2072	H-1	3.8 (d_{XZ} 1.3; d_{YZ} 2.5)	6.2	47.6	0	-2954	-3182	-2964	-2566	-4497	4977
-10240	H-4	0	0	17.1	2.2	-3747	-1043	-1868	1369	-1819	4054
-12720	H-9	6.1 ($d_{X^2-Y^2}$ 3.5; d_{XY} 2.6)	2.4	36	4.1	-7873	-3304	-7616	6973	-6816	5530
-16048	H-10	4 ($d_{X^2-Y^2}$ 2.3; d_{XY} 1.7)	4.4	7.9	41.8	-6964	-2004	-1289	-2006	-79	427
-20232	H-12	2.6 $d_{X^2-Y^2}$	27.4	3.6	8.4	-3122	-846	-2014	-1541	-318	-97
-21368	H-13	8.7 $d_{X^2-Y^2}$	6.4	8.5	25.4	-183	-5786	-2504	-3753	1556	1506
-27752	H-14	4.8 $d_{X^2-Y^2}$	0	10.8	1.1	-1493	-686	-5007	1547	-2338	988
-29824	H-17	8 (d_{XY} 1.6; d_{XZ} 2.1; d_{YZ} 4.7)	15.8	0	0	-2239	-2334	-497	689	-1158	-3703
-32488	H-20	14 (d_{YZ} 12.7; P_Y1.3)	35.7	1	4.1	-2839	-1013	-1319	-1525	-1214	1262
-33064	H-21	18.5 d_{XZ}	33.5	1.2	3.6	-3181	-7892	-500	-1411	-2435	3285
-36584	H-25	1.1 d_{XZ}	5	0	0	-1404	-1655	27	300	-595	1656
-36784	H-26	4.5 d_{XY}	1.3	0	1	-2562	-1353	-119	-134	-1085	-1200
-37696	H-28	1.8 d_{Z^2}	6.3	0	0	-2631	-1955	-107	-138	-940	-1627
-38600	H-29	14.7 (d_{XZ} 1.3; d_{Z^2} 13.4)	21.9	0	0	-14662	-13200	-1046	1584	-3837	-2055
-41592	H-34	4.7 (d_{Z^2} 3.6; d_{XY} 1.1)	1.8	7.2	1.9	-1946	-4319	382	-512	629	3921
$\Delta E(cm^{-1})$	MO(β)	%Mo	%Oxo	%S	%O(benzylate)	Δg_{XX}	Δg_{YY}	Δg_{ZZ}	Δg_{XZ}	Δg_{YZ}	Δg_{XY}
0	LUMO	74.1($d_{X^2-Y^2}$ 70.1; d_{YZ} 2.8; d_{XY} 1.2)	1	0	10.4	8119	9975	39494	2591	-10392	2811
-11728	HOMO	3.2 (d_{XZ} 1.4; d_{YZ} 1.8)	5.4	48.8	0	1602	3359	1926	947	-1032	-2303
-18648	H-3	1.1 d_{XY}	0	18.2	6	4448	1373	5379	-1224	1309	-5156
-20792	H-8	4 (d_{XY} 1.8; $d_{X^2-Y^2}$ 2.2)	4.5	26.2	9.7	4731	2164	6594	-2289	5239	-3827
-24256	H-9	3.8 (d_{XY} 2; $d_{X^2-Y^2}$ 1.8)	4.8	13.1	39	7068	1717	8584	7618	1442	-1770
-28224	H-11	4.1 $d_{X^2-Y^2}$	21.45	5.8	24.7	1923	826	3049	3103	-908	155
-35992	H-13	2.5 $d_{X^2-Y^2}$	1.3	17.9	2.2	1209	1890	3736	-813	1692	-2575
-38280	H-15	8.8 (d_{XY} 2.3; d_{XZ} 1.9; d_{YZ} 4.6)	16.4	0	0	4697	3372	3656	-5455	4390	1906
-39472	H-17	7.8 (d_{XY} 3.5; d_{XZ} 1.6; d_{YZ} 2.7)	9.5	0	1.8	2819	2343	5209	-5782	-4992	-3102
-40768	H-19	11.2 (d_{XY} 1.3;d_{YZ} 9.9)	35.7	1.3	3.2	4286	1187	2233	4783	777	-1036
-41200	H-20	16.9 d_{XZ}	36.7	1.5	3.4	3136	10134	418	2363	2481	-908
-45208	H-24	1.5 d_{XY}	3.9	0	0	1801	2178	1843	-1152	-130	-2435

-45368	H-25	3.2 d_{XY}	2.8	0	0	2721	1402	3486	-863	-464	2588
-46208	H-26	3.3 (d_{Z^2} 1.2; d_{YZ} 1.1)	4.1	0	0	1917	1813	217	-48	1265	-332
-46328	H-27	2.1 d_{Z^2}	6.6	0	0	2577	2330	67	-44	783	1612
-46872	H-28	12.8 (d_{Z^2} 11.6; d_{XZ} 1.2)	18.5	0	0	12470	11857	735	-1394	1988	1346

Table 4.6 Orbitals populations of selected α and β orbitals for Tp*MoO(sba) individual contributions of these transitions to the g-tensor shift (in units of PPM) by SOC between occupied and virtual orbitals

Tp*MoO(sba)											
ΔE(cm^{-1})	MO(α)	%Mo	%Oxo	%Se	%O (benzylate)	Δg_{XX}	Δg_{YY}	Δg_{ZZ}	Δg_{XZ}	Δg_{YZ}	Δg_{XY}
30496	L+6	20.6(d_{XY} 15.7; d_{YZ} 2.5; d_{Z^2} 2.4)	1	7.3	0	-282	54	-16180	-4324	706	53
29248	L+5	22.7(d_{XY} 21.5; d_{Z^2} 1.2)	0	7.2	1.7	-641	-7	-13880	6119	-2608	450
27648	L+2	6 d_{XY}	0	1.9	0	-136	-164	-12374	2671	19036	373
14704	L+1	55.3 d_{XZ}	23.5	2.3	5.1	-5548	-35952	-764	-4243	-11614	-28788
13720	LUMO	55.6(d_{YZ} 54.3; d_{XY} 1.3;)	23.4	6.9	1.4	-42619	-1313	-16220	53108	-10529	16075
0	HOMO	60($d_{X^2-Y^2}$ 57.9; d_{XZ} 2.1)	2.7	0	15.1						
-1344	H-1	3.5 (d_{XZ} 1; d_{YZ} 2.5)	6.2	57.1	0	-11824	-11870	-3720	-4158	-8048	-2474
-11112	H-4	1.4 d_{XY}	0	27.6	2.8	-14729	-3704	-5778	1586	5964	-11588
-11984	H-7	0	3.3	4.8	9.4	-2432	-1415	-159	-3035	-2620	-2498
-12840	H-9	5.7 (d_{XZ} 1.3; $d_{X^2-Y^2}$ 4.4)	1.1	22.8	0	-13057	-3395	-16024	4820	9447	-6924
-16152	H-10	4.6($d_{X^2-Y^2}$ 2.9; d_{XY} 1.7)	4.4	5.8	39.6	-3823	-2603	-3287	-1950	5263	-1675
-16336	H-11	0	0	16.3	5.9	-3048	-958	5426	3293	-1947	509
-20392	H-12	2.2 $d_{X^2-Y^2}$	27.4	1.9	8.2	-2486	-441	-393	398	-237	1784
-22368	H-13	7.9 $d_{X^2-Y^2}$	6.7	6.4	27.8	-120	-8305	-4701	-628	-3051	-2288
-26336	H-14	7.6 $d_{X^2-Y^2}$	0	24.2	4.1	-1734	-4233	-8426	-1447	4694	-803
-30088	H-17	8.6(d_{XY} 1.2; d_{XZ} 3.3; d_{YZ} 4.1)	13.3	0	0	-1723	-2669	-119	369	938	2964
-31240	H-18	7.9(d_{XY} 4.8; d_{XZ} 3.1)	4.7	0	1.4	-2035	-1416	-511	559	-303	2810
-32776	H-20	16.7 (d_{YZ} 15.5; P_Y1.2)	40.1	0	3.3	-4310	-2421	-726	-2472	1122	-1683
-33336	H-21	18.9 d_{XZ}	35.2	1.1	4.2	-3364	-7630	5	-1520	586	-2368
-36976	H-25	1.1 d_{XY}	4.2	0	0	-1692	-1617	14	250	428	-2138
-37136	H-26	4 d_{XY}	1.2	0	0	-2071	-2051	-5	-365	959	2825

-37960	H-27	1.8 d_{Z^2}	4.6	0	0	-2235	-2055	-123	-110	1081	446
-38872	H-29	11.9 d_{Z^2}	18.7	2.2	0	-12518	-11415	-1052	1081	1295	2972
-40128	H-30	4.5(d_{YZ} 1.3; d_{Z^2} 3.2)	4.5	3	1.3	-3836	-4732	965	-1457	-2007	-5064
-40704	H-31	1.7 d_{Z^2}	0	2.6	0	-2042	-2453	-322	-1022	-2017	-2473
$\Delta E(cm^{-1})$	MO(β)	%Mo	%Oxo	%Se	%O(benzylate)	Δg_{XX}	Δg_{YY}	Δg_{ZZ}	Δg_{XZ}	Δg_{YZ}	Δg_{XY}
0	LUMO	73.2($d_{X^2-Y^2}$ 71.1; d_{XZ} 2.1)	1	0	10.5	9175	7406	42428	1450	-1850	-3874
-11608	HOMO	3(d_{XZ} 1.1; d_{YZ} 1.9)	4.3	58.6	0	9686	10934	2903	-1184	4603	1673
-16776	H-2	0	5.3	0	0	1958	482	1767	-446	-1261	1722
-18432	H-3	1.6 d_{XY}	0	30.9	5.4	15317	4123	10954	683	-8138	11684
-20464	H-6	0	2.3	4.6	7.8	1874	1015	-85	3157	1777	514
-20976	H-7	2.6 $d_{X^2-Y^2}$	1.9	14.6	1.9	7589	2354	12146	-602	-6832	5127
-24124	H-9	3.9($d_{X^2-Y^2}$ 2; d_{XY} 1.9)	5.3	9.9	37.5	4273	3239	9276	5846	-8159	1446
-24864	H-10	0	1.6	14.3	10.2	2617	1022	6295	-511	2668	-1077
-28256	H-11	4.8 $d_{X^2-Y^2}$	17.5	5	29.2	195	1447	3878	1169	-242	-601
-30008	H-12	0	15.5	5.8	10.3	1442	4021	914	-324	1812	1626
-34440	H-13	3 $d_{X^2-Y^2}$	0	26.3	2.8	1712	5111	5379	2617	-1529	705
-38512	H-15	9.6 (d_{XY} 1.4; d_{XZ} 3.8; d_{YZ} 4.4)	17.9	0	0	3879	2704	2470	-4601	-3535	-11
-39736	H-17	9.6 (d_{XY} 4.4; d_{YZ} 3.6)	7.7	0	1.5	2814	1156	6587	-6654	3306	-3702
-41008	H-19	14.8 (d_{XY} 1.2; d_{XZ} 1.5; d_{YZ} 12.1)	41.4	1	2.1	6386	2163	1668	5120	-1667	229
-41424	H-20	16.1 d_{XZ}	36.1	1.1	3.9	2608	9139	-217	1669	-41	1276
-45568	H-24	2.3 d_{XY}	2.4	0	0	2446	1804	2773	-1342	-203	3353
-45688	H-25	3.4 (d_{Z^2} 1.1; d_{XY} 2.3)	4.1	0	0	2856	2239	2498	-619	-54	-3385
-46536	H-26	3.5 d_{Z^2}	8.5	0	0	4027	4017	107	-9	-1389	-940
-47168	H-27	11.0 d_{Z^2}	15.4	0	0	11572	10609	666	-388	212	-974
-48408	H-28	4.6(d_{Z^2} 2.4; d_{YZ} 1.1; d_{XY} 1.1)	2.5	6.9	1.9	3109	5262	670	2443	2854	4258

4.4 Analysis

Mono-oxo molybdenum oxo complexes possess a characteristic d orbital energy splitting pattern dominated by the ligand field of the terminal oxo as shown in Figure 4.10 A. This molybdenum d orbital splitting has the d_{X2-Y2} lowest in energy and singly occupied as a result of the strong σ and π interactions with the oxo

donor ligand. The large splitting between d_{X2-Y2} and d_{XZ}, d_{YZ} has been characterized by spectroscopic methods and is in the range of ~13000-16000 cm^{-1}.[49] Therefore, the LMCT transition to d_{XZ},d_{YZ} are expected to occur at energies that are at least 13000 cm^{-1} higher than the lowest LMCT to d_{X2-Y2}. The mono-thiolate bonding scheme with molybdenum is shown in Figure 4.10 B-E. An ~90° O_{oxo}-Mo-E-C dihedral angle precludes the mixing of the out-plane p orbital of E (Se/S/O) with the molybdenum $d_{X2-Y2.}$ while a 0°/180° of O_{oxo}-Mo-E-C dihedral angle maximizes the overlap of E_{OP}-d_{X2-Y2} giving rise to strong π type interactions. The mixing of the p orbital of E and the Mo d_{X2-Y2} mediates the energy of the redox orbital and the effective nuclear charge of the molybdenum center to affect the reduction potential of the metal. [50]

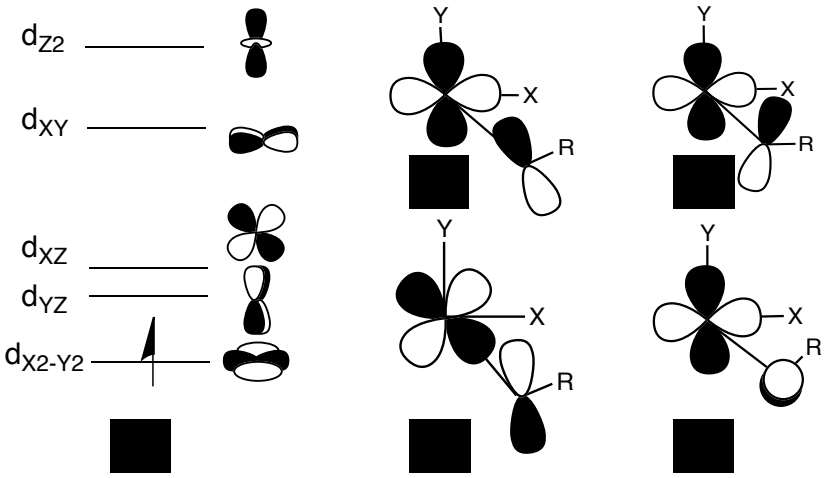

Figure 4.10 Schematic molecular orbital diagram for Tp*MoOL2 (A). B-E: bonding schemes of Mo-S(monothiolate). B and C: in-plane p orbital of E (Se/S/O) anti-bonding interaction with molybdenum in-plane d_{X2-Y2} orbital with 110° and 130° of Mo-E-C angles. D: in-plane Se/S pseudo σ anti-bonding with molybdenum in-plane d_{XY} orbital. E: out-of-plane E p orbital overlaps with molybdenum in-plane d_{X2-Y2} orbital.

4.4.1 Gaussian Resolution and Band Assignments

The Gaussian resolved the MCD and electronic absorption spectra are shown in Figure 4.13, where the MCD data is resolved into seven bands. The energies of these bands and their assignments are presented in Table 4.7. A very high similarity is displayed in the MCD and electronic absorption spectra of Tp*MoO(sba) and Tp*MoO(mba). In combination with data for Tp*MoO(hba), this allows for detailed band assignment below 33000 cm^{-1}. Thus the results of bonding calculations could be evaluated by the spectra assignments of the three complexes. Various analog complexes of sulfite oxidase with two, three or four thiolate ligands have been spectroscopically studied.[12,13,32,34,51] Here the chalcogen ligands (one thiolate ligand analog of sulfite oxidase) provide the opportunity to probe the role of a single thiolate ligand with dihedral angle of ~90˚ and a Mo-S-C angle of ~110˚ and to compare with MCD data for sulfite oxidase.[52]

Bands 1, 2 and 3

The Figure 4.11 (top) shows the Gaussian-resolved MCD and electronic absorption spectra of Tp*MoO(sba). The broad low energy absorption peak at 14900 cm^{-1} ($\varepsilon \approx 175$ M^{-1} cm^{-1}) is dominated by the $Se_{op} \rightarrow d_{YZ}$ (α) CT transition which corresponds to band 2 at 14918 cm^{-1} in the MCD while negative band 1 at 12900 cm^{-1} and positive band 3 at 16166 cm^{-1} are assigned as the ligand field transitions $d_{X2-Y2} \rightarrow d_{YZ}$ and $d_{X2-Y2} \rightarrow d_{XZ}$ respectively. In the Gaussian-resolved MCD and electronic absorption spectra of Tp*MoO(mba) (Figure 4.11 middle) the $S_{op} \rightarrow d_{YZ}$ (α) CT transition is responsible for the broad peak in the absorption

spectrum at 16000 cm^{-1}, and is not observed in the MCD. The pseudo A term (negative–positive pattern) at 13990 cm^{-1} (band 1) and 17141 cm^{-1} (band 2) arises from ligand field transitions $d_{X2-Y2} \rightarrow d_{YZ}$ and $d_{X2-Y2} \rightarrow d_{XZ}$. Selenium possesses a much larger spin orbit coupling constant of ~1800 cm^{-1} compared to that of sulfur (382 cm^{-1}), which results in CT transitions from selenium-based ligand orbitals having a higher MCD intensity than those from S-based ligand orbitals for an analogous transition. The electronic absorption spectrum of Tp*MoO(hba) (Figure 4.11 bottom) shows a weak absorption peak at 14618 cm^{-1} ($\varepsilon \approx 75$ M^{-1} cm^{-1}) assigned dominantly as the $O_{op}(E) \rightarrow d_{X2-Y2}$ transition that is resolved in the MCD as bands 2. The opposite negative component (band 1) and positive component (band 3) in the MCD are assigned as $d_{X2-Y2} \rightarrow d_{YZ}$ and $d_{X2-Y2} \rightarrow d_{XZ}$ transition respectively. The nature of ligand field transitions and CT transitions is evident in electron density difference maps (EDDMs) shown in Figure 4.12. The ligand field transition energy does not follow the trend of Se>S>O as expected for a high symmetry O_h ligand field, which is consistent with the strong ligand π orbital interaction of the apical oxo with molybdenum d_{YZ} and d_{XZ} orbitals. The low symmetry (C_1) of the three complexes alters the energy of the ligand field transitions, and the experimentally observed trend of transition energies for the chalcogen substitutions results from the configurational mixing of these ligand field transition states with CT transition states.

Bands 4-8.

Bands 4-6 in the MCD spectra of the Tp*MoO(sba) and Tp*MoO(mba) complexes are negative-positive-positive C-terms. The Gaussian-resolved

absorption peaks at 21040 cm^{-1}, 22616 cm^{-1} of Tp*MoO(sba), 22499 cm^{-1}, 23930 cm^{-1} for Tp*MoO(mba) correspond to two bands (4 and 5) in the MCD (negative-positive components) arising from the one electron excitation from $E_{op}\rightarrow d_{XZ}$, d_{YZ} (β)and $E_{ip}\rightarrow d_{X2-Y2}$ (β) respectively. The resonance Raman enhancement profile (Figure 4.13) of Mo≡O at 935 cm^{-1} confirms the assignment of a $Se/S_{op}\rightarrow d_{XZ}$, d_{YZ} CT transition since a one electron promotion to the Mo $d_{YZ,XZ}$ orbitals leads to a large distortion along Mo≡O bond due to the anti-bonding nature of the acceptor orbitals. The single positive C-term at 25623 cm^{-1} in the MCD spectra of Tp*MoO(sba) and Tp*MoO(mba) is assigned as arising from an $E_{op}(\beta)\rightarrow d_{YZ}$, d_{XZ} transition. Analogous to the $S/Se_{op}\rightarrow d_{YZ}$ (α) transition (band 4) for Tp*MoO(sba) and Tp*MoO(mba), we can assign the transition at 21261 cm^{-1} in the MCD of Tp*MoO(hba) as $O_{op}(E)\rightarrow d_{YZ}$, which is shifted ~5000 cm^{-1} to higher energy for Tp*MoO(hba) following the optical electro-negativity trends of the chalcogens. Band 5 and 7 in the MCD of Tp*MoO(hba) are assigned as $O_{op}(E)\rightarrow d_{XZ}$, d_{YZ} (β) CT transitions, and are resolved into various energies corresponding to different linear combination of the d_{XZ} and d_{YZ} acceptor orbitals at 26663 cm^{-1} and 28491 cm^{-1} in the absorption spectrum. Band 6 for Tp*MoO(hba) is assigned as a $O_{ip}\rightarrow d_{X2-Y2}$ (β) transition and possesses a higher intensity due to better overlap of the O_{ip} orbital with the molybdenum d_{X2-Y2} orbital. Band 7 in Tp*MoO(sba) and Tp*MoO(mba) is shown as a negative MCD feature and corresponds to band 8 in Tp*MoO(hba). They are assigned as transitions out of Tp*-based orbitals as well as other high energy CT transitions. Collectively, bands 4-8 can be assigned as LMCT transitions as shown in the EDDM plots (Figure 4.12), and

their transition energies follow the expected optical electronegativity of the chalcogen donors (Se<S<O, Table 4.7).

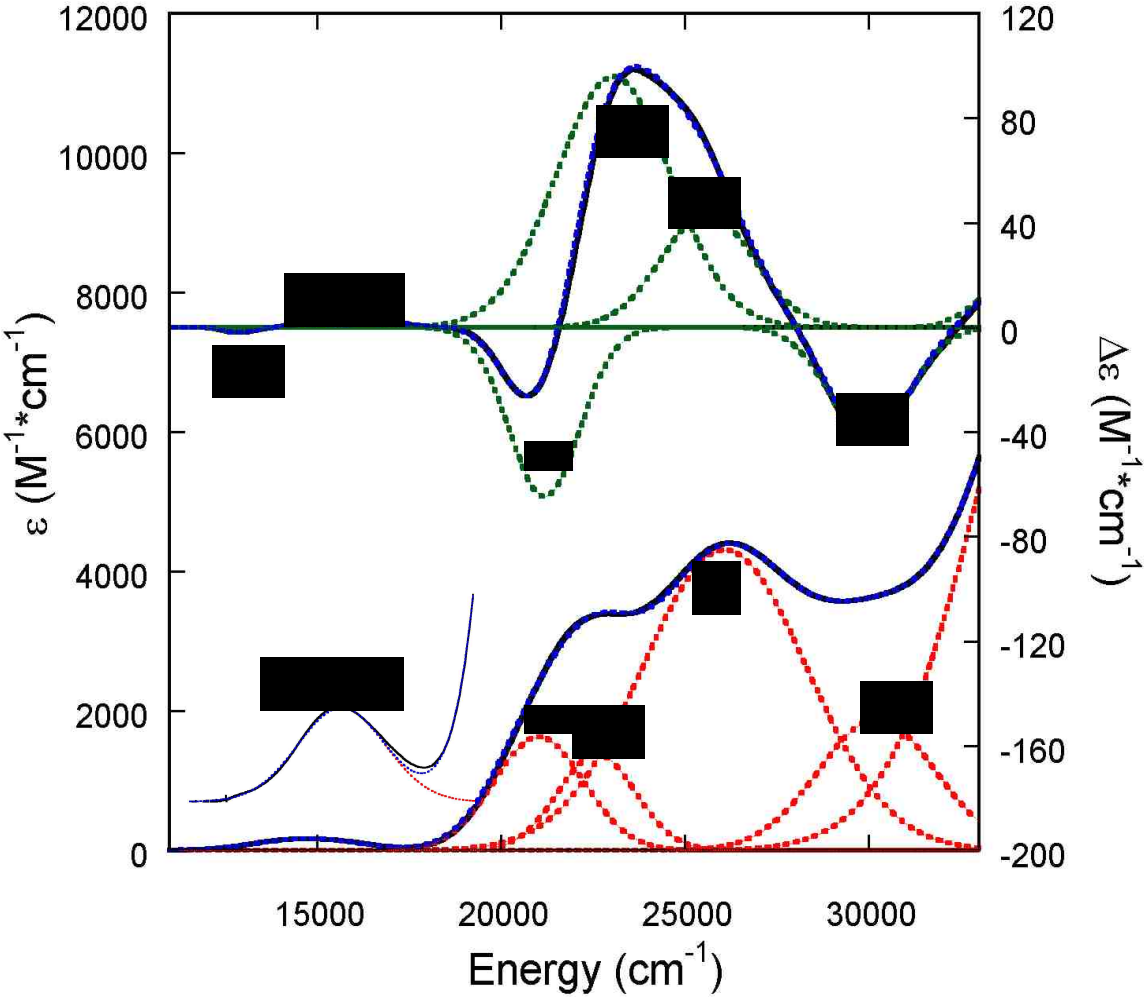

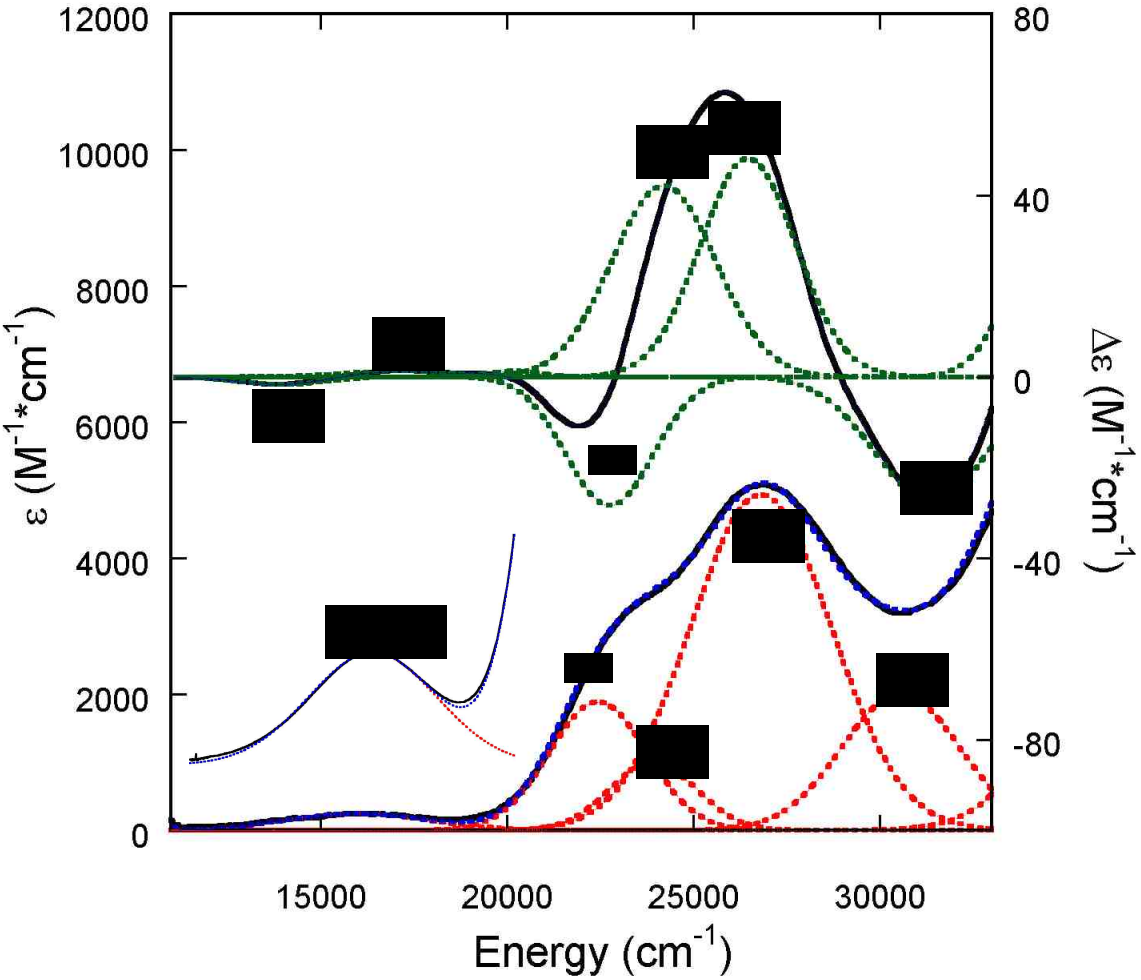
12000
10000
8000
6000
4000
2000
0
80
40
0
-40
-80
15000
20000
25000
30000
ε (M-1*cm-1)
Δε (M-1*cm-1)
Energy (cm-1)

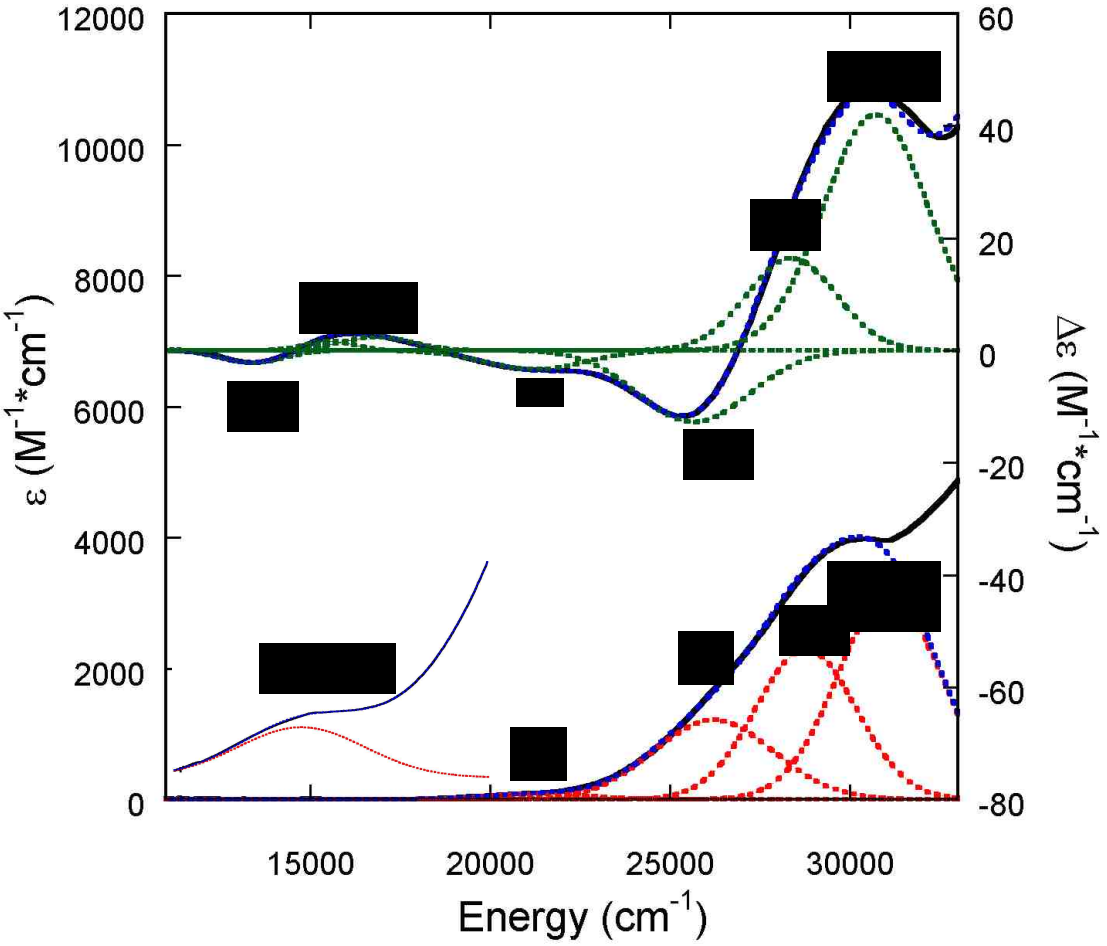

Figure 4.11 Overlay of Gaussian resolved electronic absorption and MCD spectra for the three complexes (top: Tp*MoO(sba); middle: Tp*MoO(mba); bottom: Tp*MoO(hba)) (inset are the high concentration absorption peak at low energy).

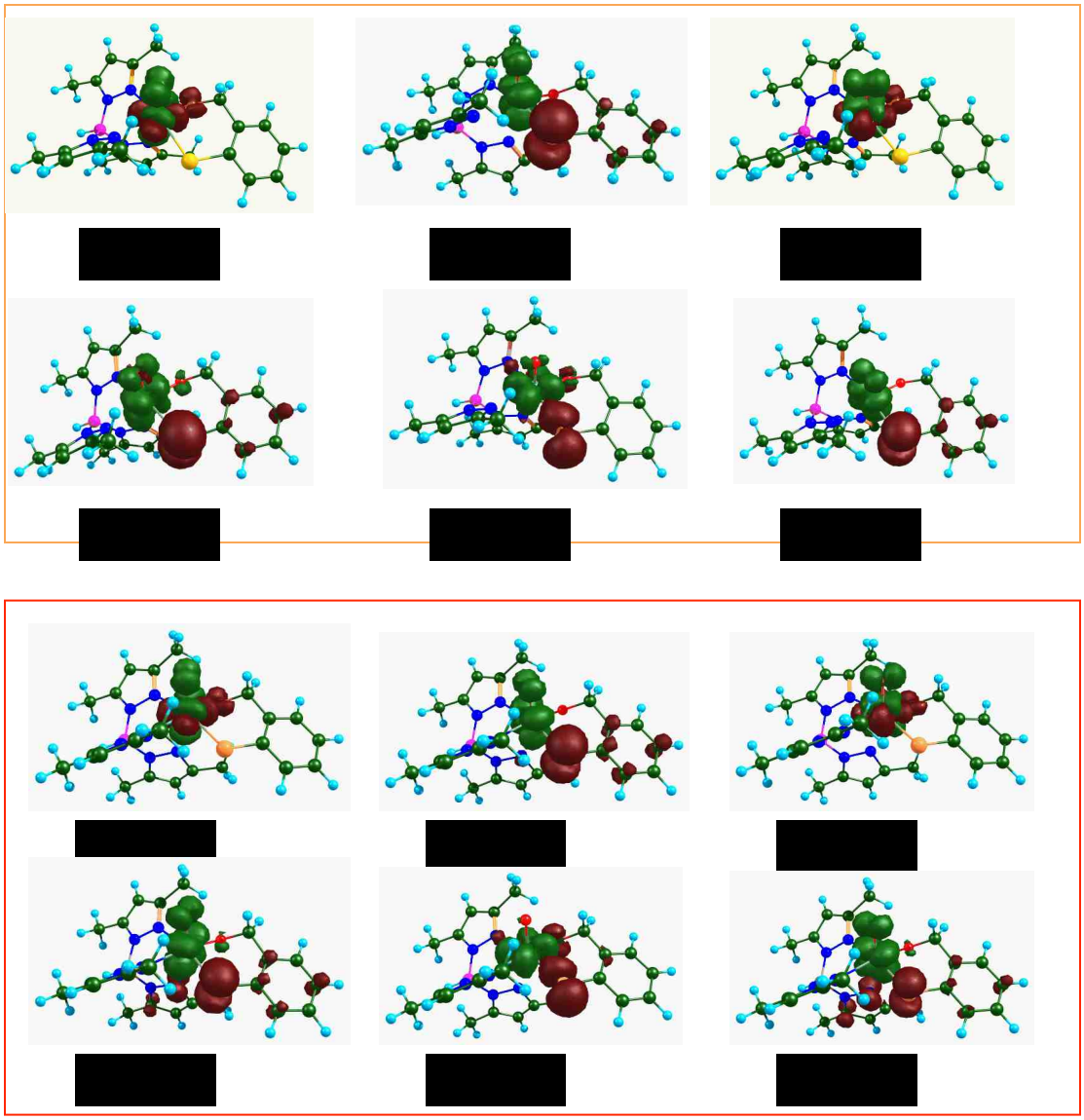

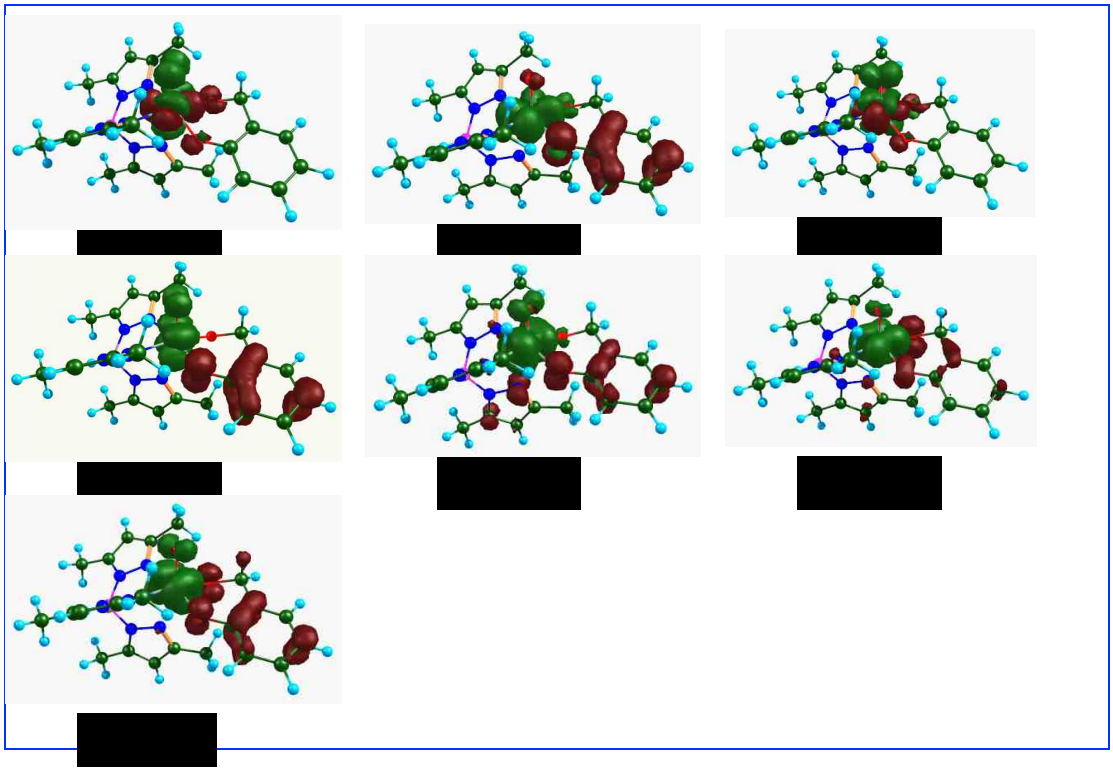

Figure 4.12 Electron density difference maps (top: Tp*MoO(sba); middle: Tp*MoO(mba); bottom: Tp*MoO(hba). (Iso-surface value is 0.004).

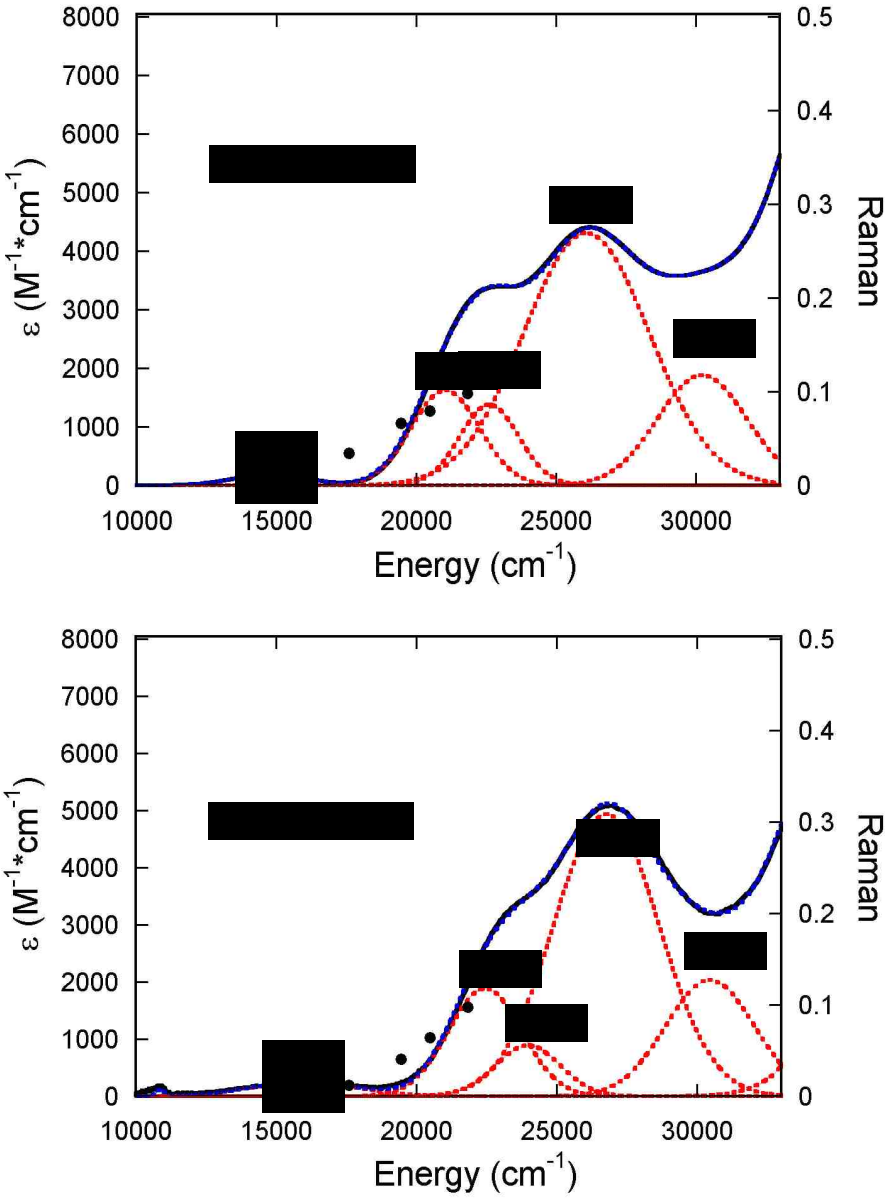

Figure 4.13 Resonance Raman enhancement profile of Mo≡O 935 cm^{-1} stretch for Tp*MoO(sba) (top) and Tp*MoO(mba) (bottom).

Table 4.7 MCD and electronic absorption bands for the three complexes. NA: not observable; * presents bands from Tp* involved in LMCT and other high CT transitions.

Band	Energy (cm^{-1})		Oscillator strength f (x10-3)		Assignment
	EAS	MCD	Exp	Cal	
Tp*MoO(sba)					
1		12900		0.1	$d_{X2-Y2} \rightarrow d_{YZ}$
2	14900	14918	2.8	4.2	$Se_{op} \rightarrow d_{YZ}(\alpha)$
3		16166		0.2	$d_{X2-Y2} \rightarrow d_{XZ}$
4	21040	21195	21.6	7.3	$Se_{op} \rightarrow d_{YZ}(\beta)$ $Se_{op} \rightarrow d_{XZ}(\beta)$
5	22616	23070	15.8	6.4	$Se_{ip} \rightarrow d_{X2-Y2}(\beta)$
6	26088	25623	104.5	84	$Se_{op} \rightarrow d_{YZ}(\beta)$ $Se_{op} \rightarrow d_{XZ}(\beta)$
7*	30229	30021			Tp*→Mo and Other high energy CT transitions
Tp*MoO(mba)					
1		13990		0.1	$d_{X2-Y2} \rightarrow d_{YZ}$
2	16000	NA	2.8	5.6	$S_{op} \rightarrow d_{YZ}(\alpha)$
3		17141		0.1	$d_{X2-Y2} \rightarrow d_{XZ}$
4	22449	22763	26.7	28	$S_{op} \rightarrow d_{YZ}(\beta)$ $S_{op} \rightarrow d_{XZ}(\beta)$
5	23930	24213	12.6	11.3	$S_{ip} \rightarrow d_{X2-Y2}(\beta)$
6	26816	26478	100	56.8	$S_{op} \rightarrow d_{YZ}(\beta)$ $S_{op} \rightarrow d_{XZ}(\beta)$
7*	30567	31387			Tp*→Mo and Other high energy CT transitions
Tp*MoO(hba)					
1		13411		0.1	$d_{X2-Y2} \rightarrow d_{YZ}$
2	14617	15556	1.4	1.1	$O_{op}(E) \rightarrow d_{X2-Y2}(\beta)$
3		16848		0.05	$d_{X2-Y2} \rightarrow d_{XZ}$
4	21345	21261	1.3	7.8	$O_{op}(E) \rightarrow d_{YZ}(\alpha)$
5	26207	26255	22	19.4	$O_{op}(E) \rightarrow d_{YZ}(\beta)$ $O_{op}(E) \rightarrow d_{XZ}(\beta)$
6	28782	28196	34.7	38.1	$O_{ip}(E) \rightarrow d_{X2-Y2}(\beta)$
7&8*	31098	30722			$O_{op}(E) \rightarrow d_{YZ}(\beta)$ $O_{op}(E) \rightarrow d_{XZ}(\beta)$; Tp*→Mo and Other high energy CT transitions

4.4.2 Electronic Origin of the Spin-Hamiltonian Parameters

The magnitudes and orientations of g- and A-tensors are dependent on the metal orbitals that are allowed to mix under a given point group symmetry of a metal

complex. As for the molybdenum-oxo complexes, C_s symmetry or higher requires at least one of the g- and A-tensor to be coincident. This is not necessary true in the lower C_1 symmetry of these complexes because of molybdenum d orbitals mixing.

Nuclear hyperfine splitting

The principal A-tensor components and their orientations are primarily determined by the composition of the ground-state orbital.[53] In Table 4.2 the principal A(^{95,97}Mo) hyperfine splitting values are nearly identical for Tp*MoO(sba) and Tp*MoO(mba) and show a small deviation for Tp*MoO(hba). The pattern of two small and one large hyperfine coupling constant indicates that these complexes have similar ground state wavefunctions (e.g. d_{X2-Y2}). With low C_1 symmetry in the three complexes trigged by the asymmetric bidentate ligands, molybdenum d_{XZ} and d_{YZ} orbital mixing results in better overlap with ligand out-plane p orbitals along the Mo-E bond (Figure 4.14). This gives rise to the A tensor rotating away from the molecular axes as shown in Figure 4.15**.**

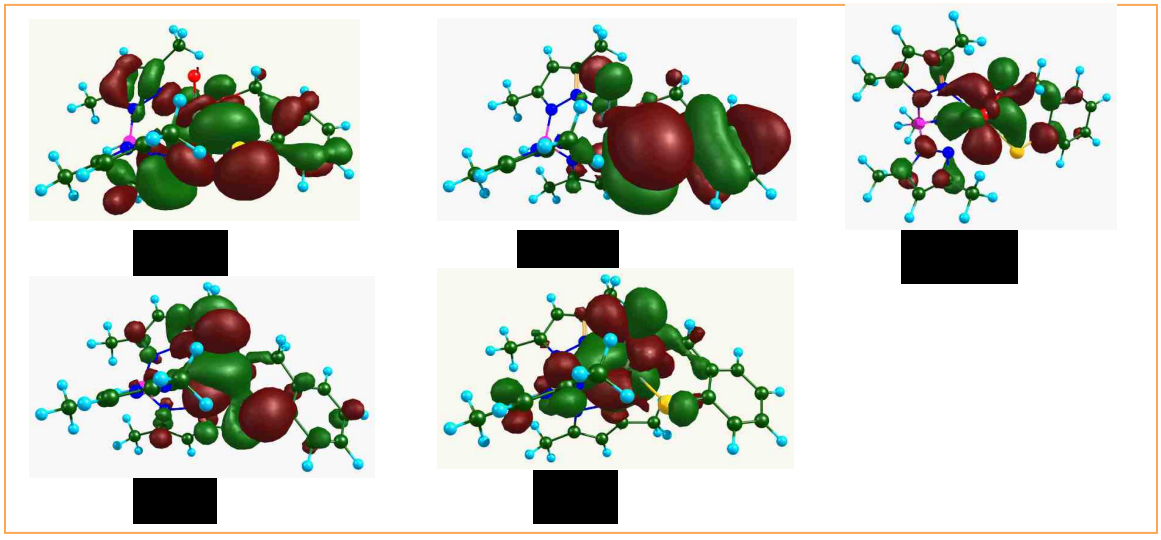

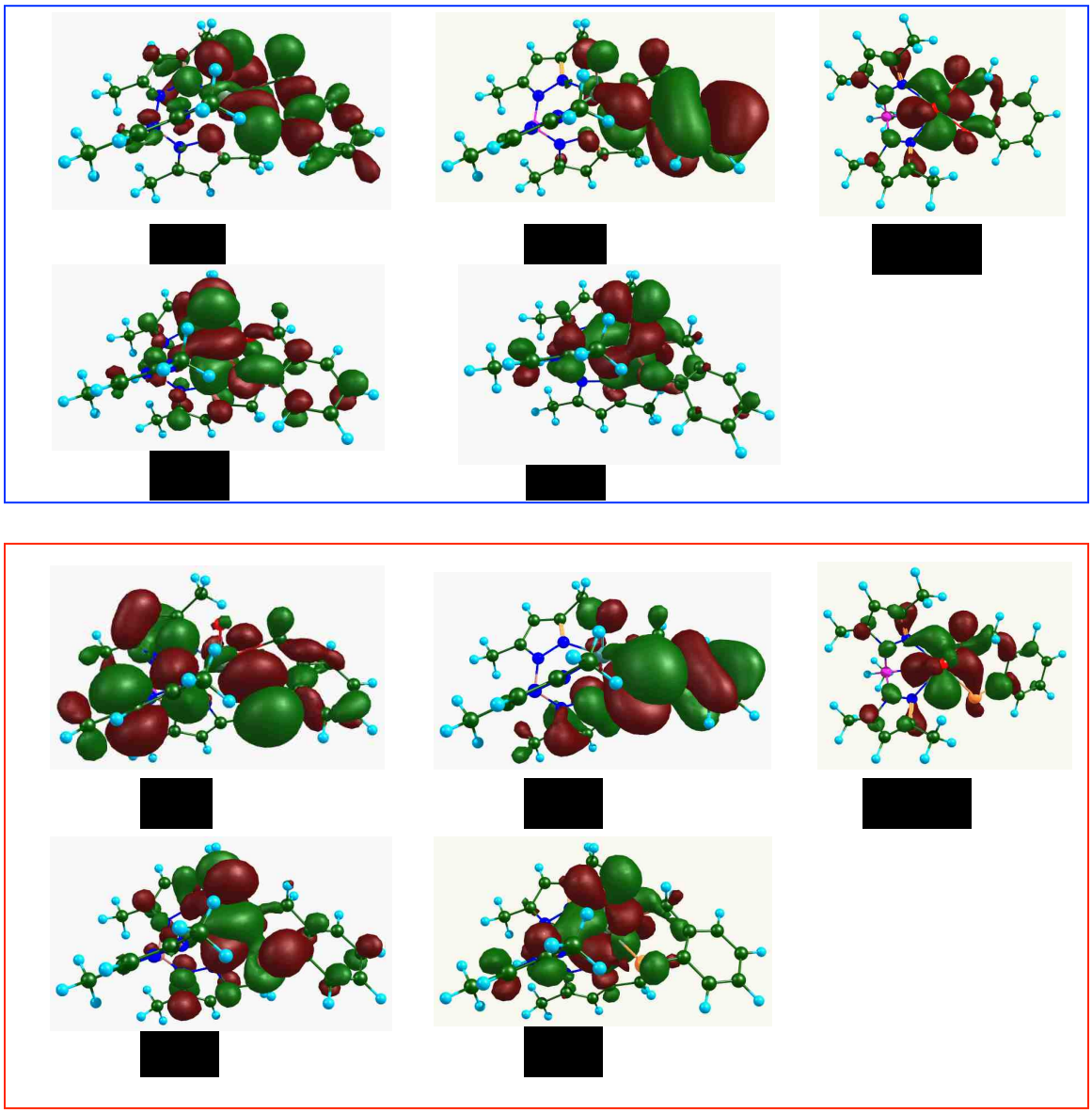

Figure 4.14 Molecular orbitals involved transitions (top: Tp*MoO(sba); middle: Tp*MoO(mba); bottom: Tp*MoO(hba). (Iso-surface value is 0.02).

Calculated g tensors and Euler angles

At the B3LYP/G level (ORCA) the calculated principal values of the g-tensor and the Euler angles agree very well with the experimental frozen solution values

(Table 4.2). For BP86 calculations (ADF), the calculated principal values of the g tensor are also in good agreement with experimental values. The consistence of the magnitude and orientation between calculation and experiment indicates that electronic structure calculations can provide valuable insight into the electronic origin of the g-tensor and its orientation.

Origin of g tensor Anisotropy

The g-tensor shifts depend on the ligand field transition energies and orbital compositions of molecular orbitals for the ground and excited states. The low (C_1) symmetry of the three complexes gives rise to d orbitals mixing and results in ligand field transition energies that do not follow the expected trend for the chalcogen series in an octahedral ligand field. From Tables 4.5-4.6 d-d transitions between d_{X2-Y2} and d_{YZ}, d_{XZ} take place from 13000 to 16000 cm^{-1} with the trend of Se<O<S that is in good agreement with both MCD and electronic absorption data. The orbital populations of the ground state and excited states are 60-65% d_{X2-Y2}, and 55-56% d_{YZ}, d_{XZ} respectively. In addition, less than 10% of d_{YZ}, d_{XZ} or d_{XY} character is mixed into the ground state. It is the d orbital mixing into the excited states that make the $d_{X2-Y2} \rightarrow d_{YZ}$ transition contribute significantly to both the g_{xx} and g_{zz} shifts. Therefore, large off-diagonal Δg_{xz} terms appear as a rotation of g_{xx} and g_{zz} away from the molecular frame (Figure 4.16), which is the origin of the large Euler angle β labeled as g_{zz} rotated away from A_{zz} (Figure 4.17).

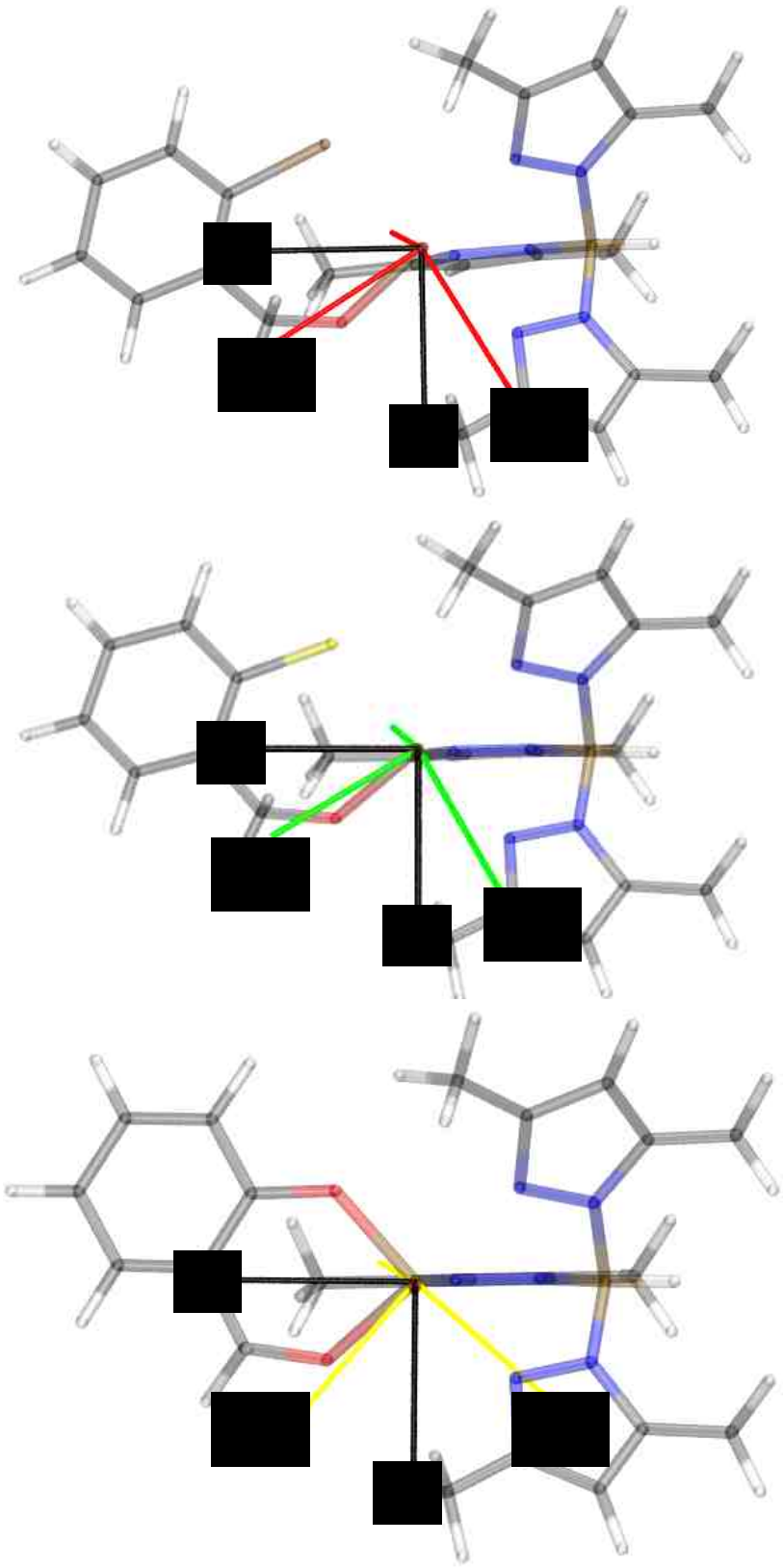

Figure 4.15 A tensors in the molecular frame for the three complexes viewed along Mo≡O bond (top: Tp*MoO(sba); middle: Tp*MoO(mba); bottom: Tp*MoO(hba)).

Table 4.8 Coordinates of the g and A tensors in the molecular frame.

Tp*MoO(sba)	g(min, mid, max)*3			A(min, mid, max)*3		
X	-2.3469	0.9771	X	-2.3469	0.9771	X
Y	0.2170	2.6823	Y	0.2170	2.6823	Y
Z	1.8561	0.9219	Z	1.8561	0.9219	Z
Tp*MoO(mba)	g(min, mid, max)*3			A(min, mid, max)*3		
X	2.2305	1.0767	1.6926	-1.4826	2.5671	0.4599
Y	-0.2828	2.6748	-1.3287	2.5968	1.5285	-0.2474
Z	-1.986	0.8286	2.0904	-0.4461	0.2718	-2.9541
Tp*MoO(hba)	g(min, mid, max)*3			A(min, mid, max)*3		
X	-2.1327	0.735	-1.9776	-2.2182	1.9536	0.5769
Y	0.0945	2.8425	0.9546	1.9494	2.2761	-0.142
Z	2.1075	0.6165	-2.0439	-0.5295	0.2699	-2.9406

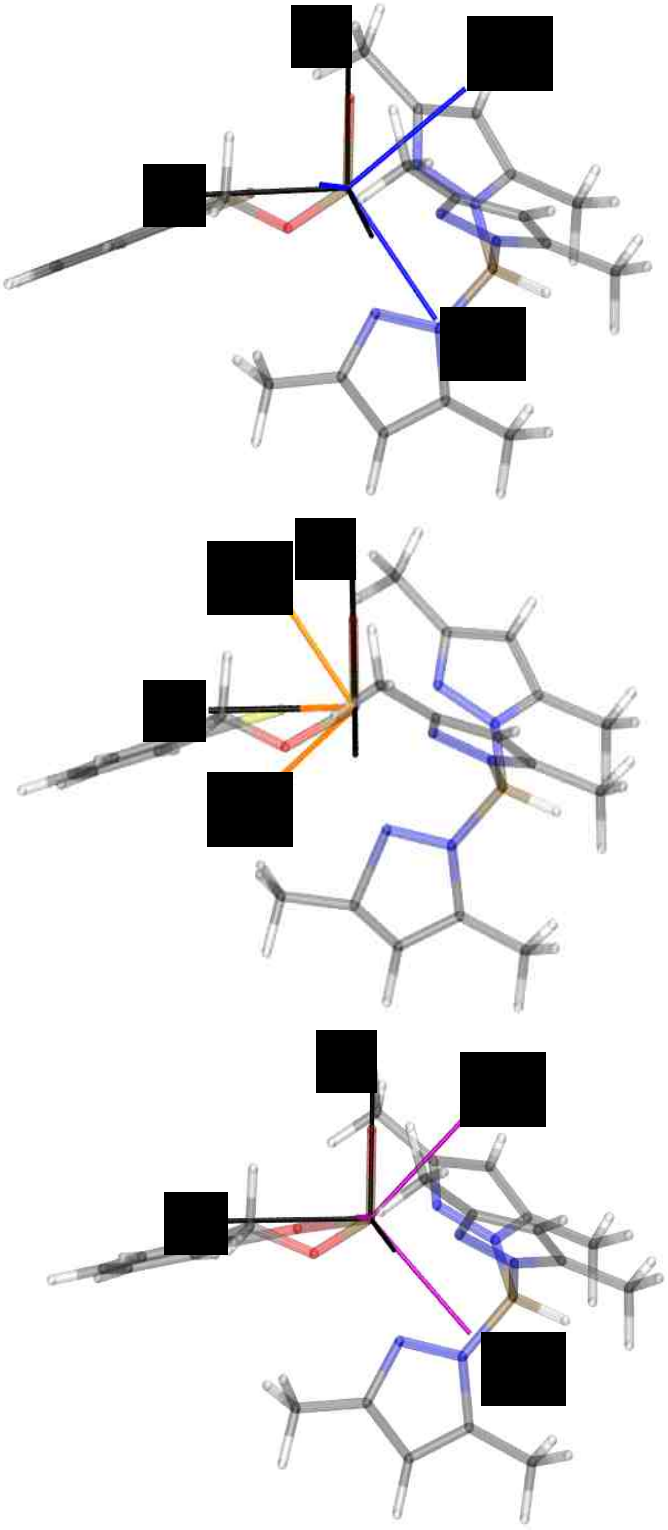

Figure 4.16 The g tensors in the molecular frame for the three complexes viewed along the Y axis (top: Tp*MoO(sba); middle: Tp*MoO(mba); bottom: Tp*MoO(hba)).

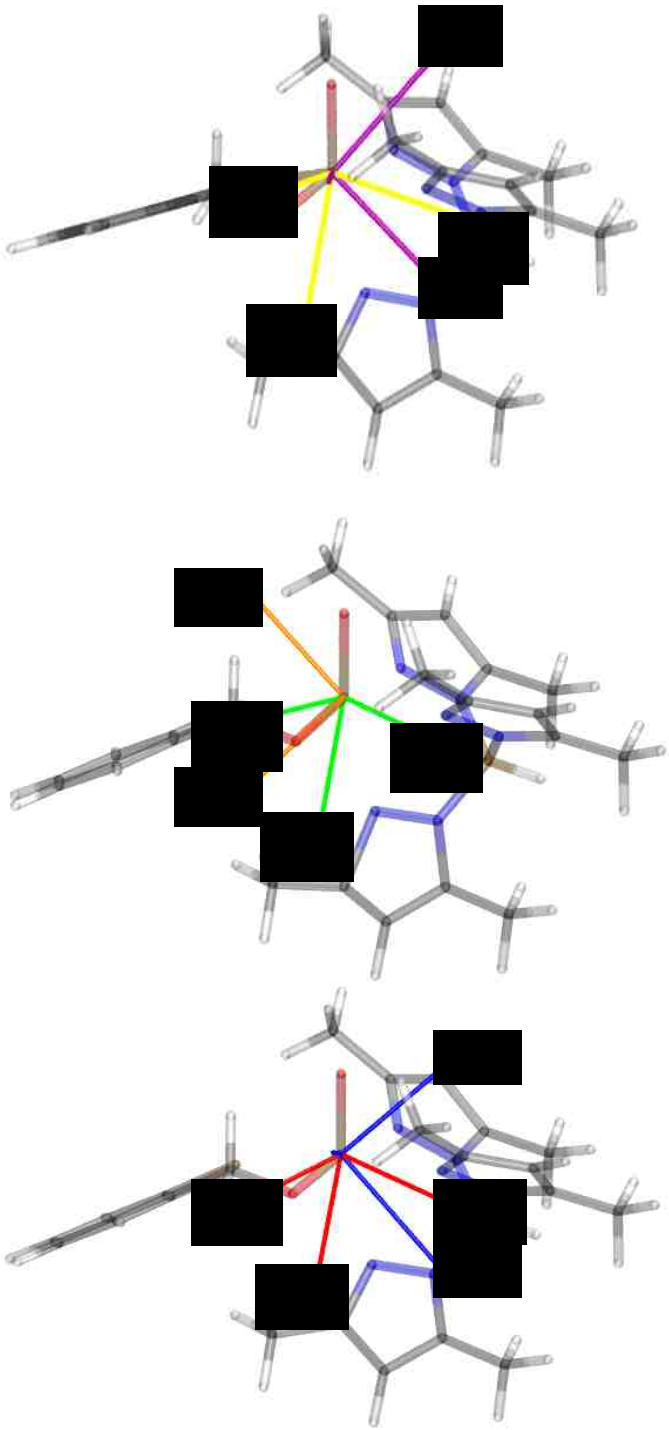

Figure 4.17 Orientations of g and A tensors in the molecular frame for the three complexes viewed along g_{yy} (top: Tp*MoO(sba); middle: Tp*MoO(mba); bottom: Tp*MoO(hba)).

In order to obtain a rhombic g-tensor shift pattern related to the experimental principal g values, an alignment of the g tensors with the molecular axes is performed. The new calculated contributions to the principal g-tensor shift are shown in the Table 4.9, where the contribution from d-d fold transitions is still shown to dominate compared to that from LMCT transitions. The three complexes display rhombic principal g-tensor shifts in agreement with the experimental g values. The charts in Figure 4.18 indicate the change in the principal g-tensor shifts from non-rhombic to rhombic.

Table 4.9 Contributions to the g tensor shift (in units of PPM) from coupling between occupied orbitals and virtual orbitals after alignment of the g-tensor with the molecular frame.

Complex		Transition	Δg_{XX}	Δg_{YY}	Δg_{ZZ}	Δg_{XZ}	Δg_{YZ}	Δg_{XY}
Tp*MoO(sba)	a	SOMO→VMO	-84804	-48892	-27818	35867	-13059	18202
		DOMO→VMO	-77523	-92126	-70962	-30493	8191	-47164
	b	DOMO→VMO	83706	87354	89333	128	5951	32800
		SUM	-78620	-53663	-9447	5502	1082	3838
Tp*MoO(mba)	a	SOMO→VMO	-87633	-43916	-29034	-33759	-13041	-15374
		DOMO→VMO	-45430	-63600	-45887	34221	8898	29868
	b	DOMO→VMO	55106	61724	65194	-5635	3975	-15985
		SUM	-77957	-45792	-9727	-5173	-169	-1491
Tp*MoO(hba)	a	SOMO→VMO	-105286	-41173	-33503	-30656	7324	9451
		DOMO→VMO	-27712	-48429	-38849	38752	-9730	-4465
	b	DOMO→VMO	35530	46182	46896	-7255	3182	1313
		SUM	-97468	-43420	-25456	841	775	6298

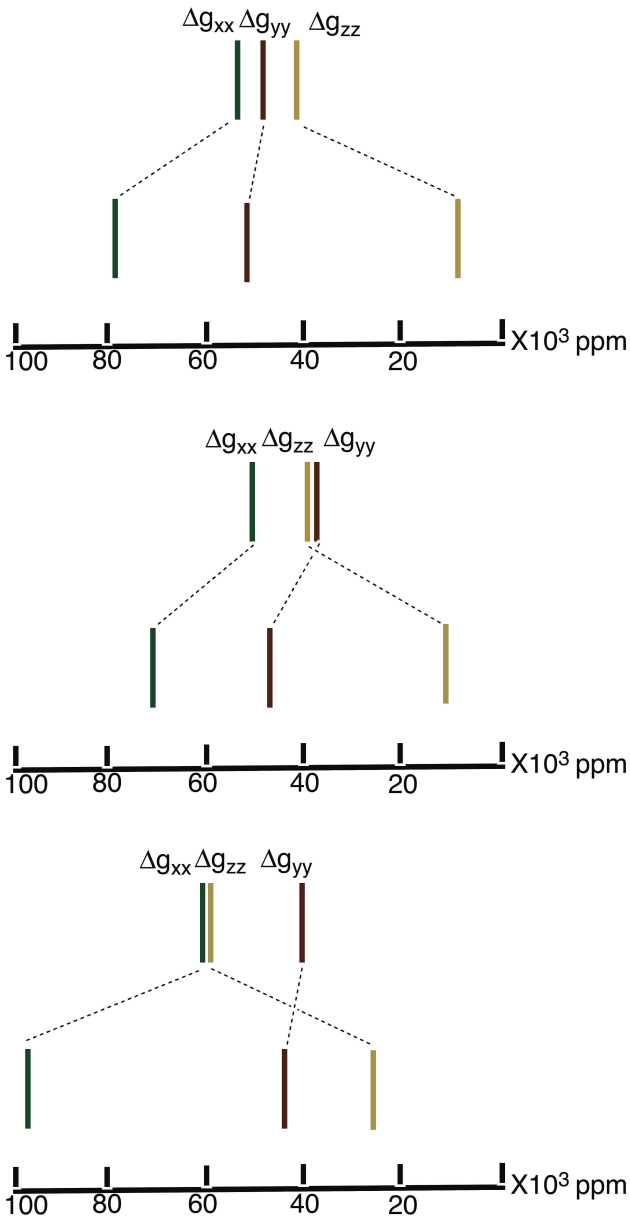

Figure 4.18 Diagrams of Δg shifts for Tp*MoO(sba) (top), Tp*MoO(mba) (middle), and Tp*MoO(hba) (bottom) before and after alignment of the g-tensor frame with the molecular frame.

4.5 Discussions

4.5.1 Spin Density Plots and Metal-Ligand Covalency

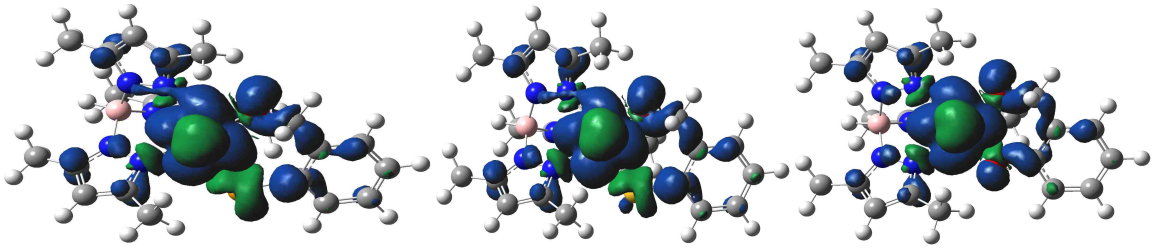

Figure 4.19 Plotted spin densities of the three complexes (left: Tp*MoO(sba); middle: Tp*MoO(mba); right: Tp*MoO(hba).

Calculated spin densities for the three complexes are presented in Figure 4.19 The calculations show net negative spin populations on the Se and S donor and net positive spin population on the O donor. This is due to a spin polarization mechanism from configurational mixing of CT excited states as described in Figure 4.20. The dominant contribution from an α (spin-up) electron promotion from doubly occupied Se/S_{ip} orbital to empty d_{XY} orbital leaves a spin-down electron that contributes to a negative spin population on the Se/S donor. However, only the spin-down (β) electron can be promoted to the singly occupied d_{X2-Y2} orbital in a low energy charge transfer configuration resulting in contributions to the positive spin population on the O donor. This is due to the better overlap for O_{ip}-Mo_{dX2-Y2} and Se/S_{ip}-Mo_{dXY} as shown in the bonding interaction descriptions detailed in Figure 4.10 C and D. A small degree of Se/S_{ip}-Mo_{dX2-Y2} covalency arises from the constraints of the Mo-Se/S-C bending angle.

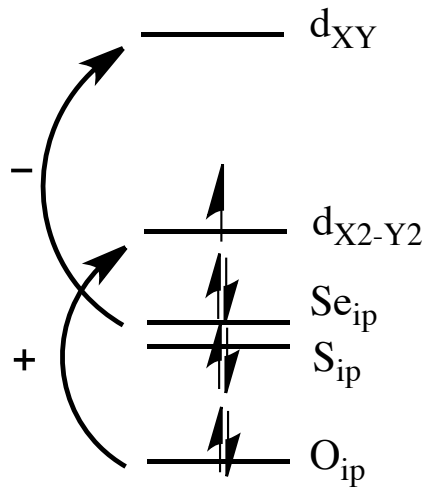

Figure 4.20 Schematic diagram of various transitions contributing to negative and positive spin densities on O and Se/S respectively. ip represents in plane and op represents out-of-plane.

4.5.2 Electronic Absorption Spectroscopy and Band Assignments

The $Se/S/O_{op} \rightarrow Mo_{dYZ,\ dXZ}$ and $Se/S/O_{ip} \rightarrow Mo_{dX2-Y2}$ CT transitions contribute intense bands that are clearly observed in the MCD and EAS spectra. No $Se/S_{op} \rightarrow Mo_{dX2-Y2}$ LMCT transitions are identified at energies below ~17000 cm^{-1}. This is due to poor Se/S_{op}-Mo_{dX2-Y2} covalency resulting from a O_{oxo}-Mo-Se/S-C dihedral angle close to 90°, which is consistent with the MCD spectrum for chicken sulfite oxidase enzyme, which also does not show a cysteine $S_{op} \rightarrow Mo_{dX2-Y2}$ CT transition.[52] The low symmetry of our model complexes leads to ground state Mo_{dXY} orbital mixing into the ground state Mo_{dX2-Y2} orbital. The resolved $Se/S/O_{ip} \rightarrow Mo_{dX2-Y2}$ CT bands in the electronic absorption and MCD spectra for the three model complexes confirm the band assignment at 22500

cm^{-1} as a $S_{ip} \rightarrow Mo_{dX2-Y2}$ CT transitions in the MCD spectrum of hpH chicken SO enzyme.

4.5.3 g Values from EPR

The analysis of the electronic origin of g tensor anisotropy shows that the ligand field transitions dominate the observed g-tensor shifts (Tables 4.3-4.6) for these three complexes. The O_{oxo}-Mo-Se/S-C dihedral angle ~90° results in orthogonal Se/S_{op} and Mo_{dX2-Y2} orbitals (Figure 4.10 E). Therefore, the $Se/S_{op} \rightarrow Mo_{dX2-Y2}$ CT transition possesses very low absorption intensity and does not contribute significantly to a positive g shift. As such, the observed g values are smaller than g_e. The g_{zz} values of 1.992 and 1.989 from the EPR spectra for Tp*MoO(sba) and Tp*MoO(mba) are similar to the reported g_{max} =1.987 from selenocysteine substituted and wt cysteine HSO enzymes.[37] The latter is due to poor cysteine Se/S_{op}- Mo_{dX2-Y2} covalency at high pH. At low pH, the g_{max} shifts from 2.003 to 2.022 when cysteine is substituted by selenocysteine in the HSO enzyme. The increased Se/S_{op}-Mo Mo_{dX2-Y2} covalency responsible for the g_{max} shift from smaller g_e to larger than g_e likely results from the O_{oxo}-Mo-Se/S-C dihedral angle appreciably varying from ~90°. Interestingly bacterial YedY enzyme possesses g_{max} =2.030 with a 65° O_{oxo}-Mo-$S_{cysteine}$-C dihedral angle at low pH.

4.6 Conclusion

Our spectroscopic studies of chalcogen donor substitution in molybdenum complexes with O_{oxo}-Mo-E-C dihedral angle of ~90° show that the models possess poor $Se/S/O_{op}$- Mo_{dX2-Y2} covalency. This is consistent with S K-edge X-

ray absorption spectroscopy (XAS) studies of Tp*MoO(mba). This ~90° O_{oxo}-Mo-E-C dihedral angle is responsible for negligible change in EPR spectra of Tp*MoO(sba) and Tp*MoO(mba). This strongly suggests that at high pH the poor covalency between Se/S and Mo_{dX2-Y2} derives from an ~90° O_{oxo}-Mo-E-C ~90° dihedral angle, and this results in a negligible change in g_{max} as shown in EPR studies of selenocysteine substituted human SO enzymes at high pH.

Our MCD and EAS data support the assignment of a $S_{ip} \rightarrow Mo_{dX2-Y2}$ CT transition is located at 22500 cm^{-1} in the MCD spectrum of molybdenum CSO enzyme at high pH, where the O_{oxo}-Mo-$S_{cysteine}$-C dihedral angle has been hypothesized to be ~90°.

Our spectroscopic studies of these SO model complexes suggest that a combination of spectroscopic methods such as EAS, EPR and MCD are valuable tools to probe the electronic structures of SO family enzymes and models. [54,55]

4.7 References

(1) Hille, R. *Chem. Rev.* **1996**, *96*, 2757–2816.

(2) Hille, R.; Hall, J.; Basu, P. *Chem. Rev.* **2014**, 140128065419006.

(3) KISKER, C.; Schindelin, H.; Pacheco, A.; Wehbi, W. A.; Garrett, R. M.; Rajagopalan, K. V.; Enemark, J. H.; Rees, D. C. *Cell* **1997**, *91*, 973–983.

(4) SCHRADER, N.; FISCHER, K.; THEIS, K.; MENDEL, R.; SCHWARZ, G.; KISKER, C. *Structure* **2003**, *11*, 1251–1263.

(5) Kappler, U.; Bailey, S. *J. Bio. Chem.* **2005***, 280,* 24999-25007.

(6) Peariso, K.; McNaughton, R. L.; Kirk, M. L. *J. Am. Chem. Soc.* **2002**, *124*, 9006–9007.

(7) Feng, C.; Tollin, G.; Enemark, J. H. *Biochimica et Biophysica Acta (BBA) - Proteins and Proteomics* **2007**, *1774*, 527–539.

(8) Dhawan, I. K.; Enemark, J. H. *Inorg Chem* **1996**, *35*, 4873–4882.

(9) Nipales, N. S.; Westmoreland, T. D. *Inorg Chem* **1997**, *36*, 756–757.

(10) Drew, S. C.; Hill, J. P.; Lane, I.; Hanson, G. R.; Gable, R. W.; Young, C. G. *Inorg Chem* **2007**, *46*, 2373–2387.

(11) Drew, S. C.; Young, C. G.; Hanson, G. R. *Inorg Chem* **2007**, *46*, 2388–2397.

(12) Peariso, K.; Chohan, B. S.; Carrano, C. J.; Kirk, M. L. *Inorg Chem* **2003**, *42*, 6194–6203.

(13) MADER COSPER, M.; Neese, F.; ASTASHKIN, A. V.; Carducci, M. D.; RAITSIMRING, A. M.; Enemark, J. H. *Inorg Chem* **2005**, *44*, 1290–1301.

(14) Young, C. G.; Collison, D.; Mabbs, F. E.; Enemark, J. H. *Inorg Chem* **1987**, *26*, 2925–2927.

(15) Gourlay, C.; Nielsen, D. J.; White, J. M.; Knottenbelt, S. Z.; Kirk, M. L.; Young, C. G. *JACS* **2006**, *128*, 2164–2165.

(16) Greenwood, R. J.; Wilson, G. L.; Pilbrow, J. R.; Wedd, A. G. *JACS* **1993**, *115*, 5385–5392.

(17) González, P. J.; Rivas, M. G.; Brondino, C. D.; Bursakov, S. A.; Moura, I.; Moura, J. J. G. *J Biol Inorg Chem* **2006**, *11*, 609–616.

(18) Santos-Silva, T.; Ferroni, F.; Thapper, A.; Marangon, J.; González, P. J.; Rizzi, A. C.; Moura, I.; Moura, J. J. G.; Romao, M. J.; Brondino, C. D. *JACS* **2009**, *131*, 7990–7998.

(19) González, P. J.; Rivas, M. G.; Mota, C. S.; Brondino, C. D.; Moura, I.; Moura, J. J. G. *Coordination Chemistry Reviews* **2013**, *257*, 315–331.

(20) Yang, J.; Rothery, R.; Sempombe, J.; Weiner, J. H.; Kirk, M. L. *J. Am. Chem. Soc.* **2009**, *131*, 15612–15614.

(21) Mtei, R. P.; Lyashenko, G.; Stein, B.; Rubie, N.; Hille, R.; Kirk, M. L. *J. Am. Chem. Soc.* **2011**, *133*, 9762–9774.

(22) Shanmugam, M.; Zhang, B.; McNaughton, R. L.; Kinney, R. A.; Hille, R.; Hoffman, B. M. *J. Am. Chem. Soc.* **2010**, *132*, 14015–14017.

(23) Wilcoxen, J.; Snider, S.; Hille, R. *J. Am. Chem. Soc.* **2011**, *133*, 12934–12936.

(24) Doonan, C. J.; Wilson, H. L.; Rajagopalan, K. V.; Garrett, R. M.; Bennett, B.; Prince, R. C.; George, G. N. *JACS* **2007**, *129*, 9421–9428.

(25) Lamy, M. T.; Gutteridge, S.; Bary, R. C. *Biochem. J.* **1980**, *185*, 397–403.

(26) ASTASHKIN, A. V.; RAITSIMRING, A. M.; Feng, C.; Johnson, J. L.; Rajagopalan, K. V.; Enemark, J. H. *JACS* **2002**, *124*, 6109–6118.

(27) ASTASHKIN, A. V.; Feng, C.; RAITSIMRING, A. M.; Enemark, J. H. *JACS* **2005**, *127*, 502–503.

(28) ASTASHKIN, A. V.; Klein, E. L.; Ganyushin, D.; Johnson-Winters, K.; Neese, F.; Kappler, U.; Enemark, J. H. *Phys. Chem. Chem. Phys.* **2009**, *11*, 6733–6742.

(29) ASTASHKIN, A. V.; Johnson-Winters, K.; Klein, E. L.; Feng, C.; Wilson, H. L.; Rajagopalan, K. V.; RAITSIMRING, A. M.; Enemark, J. H. *J. Am. Chem. Soc.* **2008**, *130*, 8471–8480.

(30) Johnson-Winters, K.; Tollin, G.; Enemark, J. H. *Biochemistry* **2010**, *49*, 7242–7254.

(31) Klein, E. L.; ASTASHKIN, A. V.; RAITSIMRING, A. M.; Enemark, J. H. *Coordination Chemistry Reviews* **2013**, *257*, 110–118.

(32) McNaughton, R. L.; Helton, M. E.; Cosper, M. M.; Enemark, J. H.; Kirk, M. L. *Inorg Chem* **2004**, *43*, 1625–1637.

(33) McNaughton, R. L.; Tipton, A. A.; Rubie, N. D.; Conry, R. R.; Kirk, M. L. *Inorg Chem* **2000**, *39*, 5697–5706.

(34) Kirk, M. L.; Peariso, K. *POLYHEDRON* **2004**, *23*, 499–506.

(35) McNaughton, R. L.; Mondal, S.; Nemykin, V. N.; Basu, P.; Kirk, M. L. *Inorg Chem* **2005**, *44*, 8216–8222.

(36) Swann, J.; Westmoreland, T. D. *Inorg Chem* **1997**, *36*, 5348–5357.

(37) Reschke, S.; Niks, D.; Wilson, H.; Sigfridsson, K. G. V.; Haumann, M.; Rajagopalan, K. V.; Hille, R.; Leimkühler, S. *Biochemistry* **2013**, *52*, 8295–8303.

(38) Tripathi, S. K.; Patel, U.; Roy, D.; Sunoj, R. B.; Singh, H. B.; Wolmershäuser, G.; Butcher, R. J. *J. Org. Chem.* **2005**, *70*, 9237–9247.

(39) Peariso, K.; Helton, M. E.; Duesler, E. N.; Shadle, S. E.; Kirk, M. L. *Inorg Chem* **2007**, *46*, 1259–1267.

(40) Stoll, S.; Schweiger, A. *J. Magn. Reson.* **2006**, *178*, 42–55.

(41) Neese, F. *An ab Initio, Density Functional and Semiempirical Program Package version* **2009**, *2*.

(42) Neese, F. *J Chem Phys* **2001**, *115*, 11080–11096.

(43) Neese, F. *J. Phys. Chem. A* **2001**, *105*, 4290–4299.

(44) Neese, F. *J Chem Phys* **2003**, *118*, 3939–3948.

(45) Humphrey, W.; Dalke, A.; Schulten, K. *J Mol Graph* **1996**, *14*, 33–8–27–8.

(46) Velde, Te, G.; Bickelhaupt, F. M. *Journal of …* **2001**.

(47) Cleland, W. E., Jr; Barnhart, K. M.; Yamanouchi, K.; Collison, D.; Mabbs, F. E.; Ortega, R. B.; Enemark, J. H. *Inorg Chem* **1987**, *26*, 1017–1025.

(48) Carducci, M. D.; Brown, C.; Solomon, E. I.; Enemark, J. H. *JACS* **1994**, *116*, 11856–11868.

(49) Inscore, F. E.; McNaughton, R.; Westcott, B. L.; Helton, M. E.; Jones, R.; Dhawan, I. K.; Enemark, J. H.; Kirk, M. L. *Inorg Chem* **1999**, *38*, 1401–1410.

(50) Holm, R. H.; Solomon, E. I. *Chem. Rev.* **1997**, 1–76.

(51) Inscore, F. E.; Knottenbelt, S. Z.; Rubie, N. D.; Joshi, H. K.; Kirk, M. L.; Enemark, J. H. *Inorg Chem* **2006**, *45*, 967–976.

(52) Helton, M. *J. Inorg. Biochem.* **2000**, *80*, 227–233.

(53) Sempombe, J.; Stein, B.; Kirk, M. L. *Inorg Chem* **2011**, *50*, 10919–10928.

(54) Raaijmakers, H.; Macieira, S.; Dias, J. M.; Teixeira, S.; Bursakov, S.; Huber, R.; Moura, J. J. G.; Moura, I.; Romao, M. J. *Structure* **2002**, *10*, 1261–1272.

(55) Jormakka, M.; Törnroth, S.; Byrne, B.; Iwata, S. *Science* **2002**, *295*, 1863–1868.

Chapter 5 Appendix NMR and Mass Spectroscopy

5.1 Appendix A: NMR Spectra

5.1.1 Lumazine Derivatives

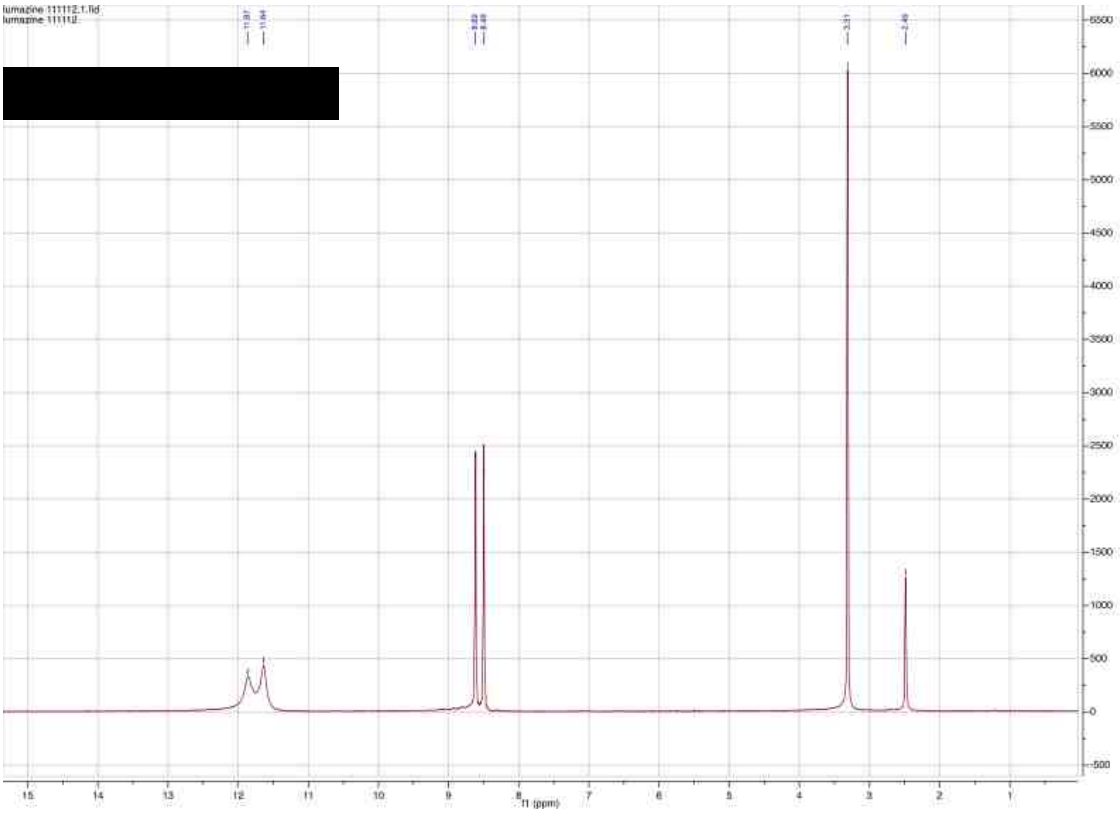

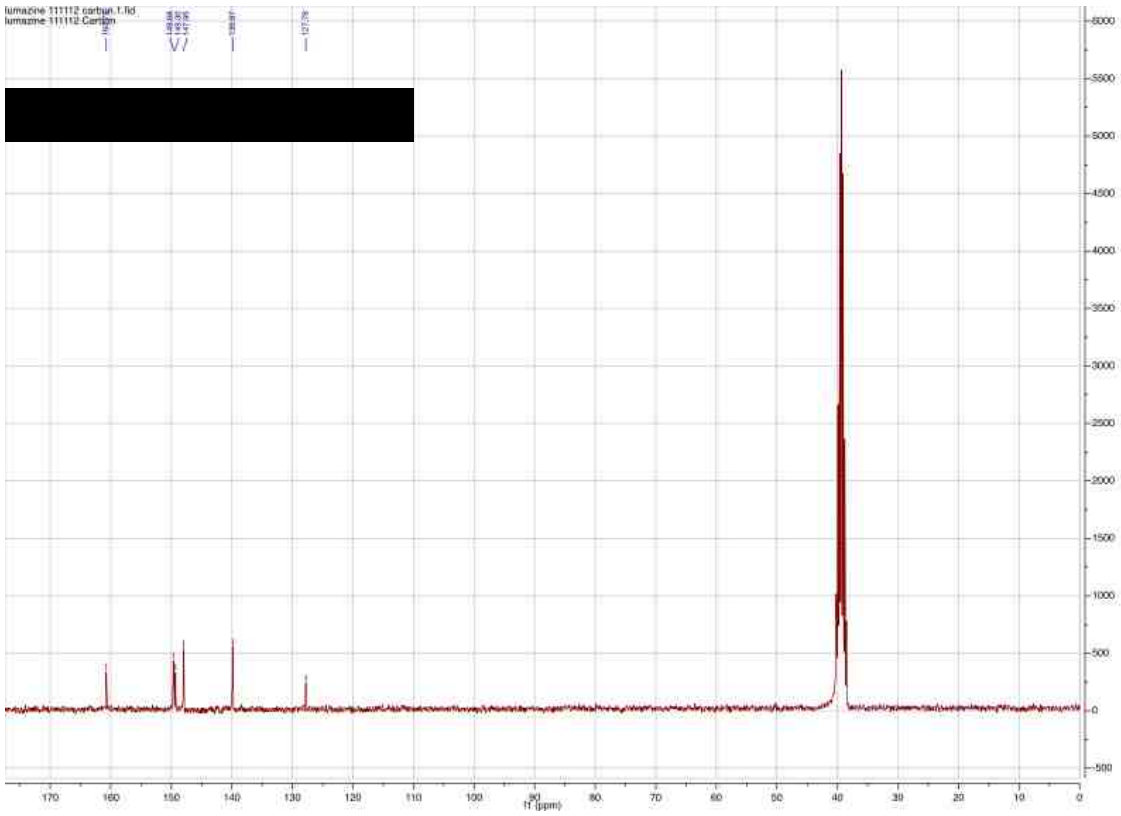
[redacted]

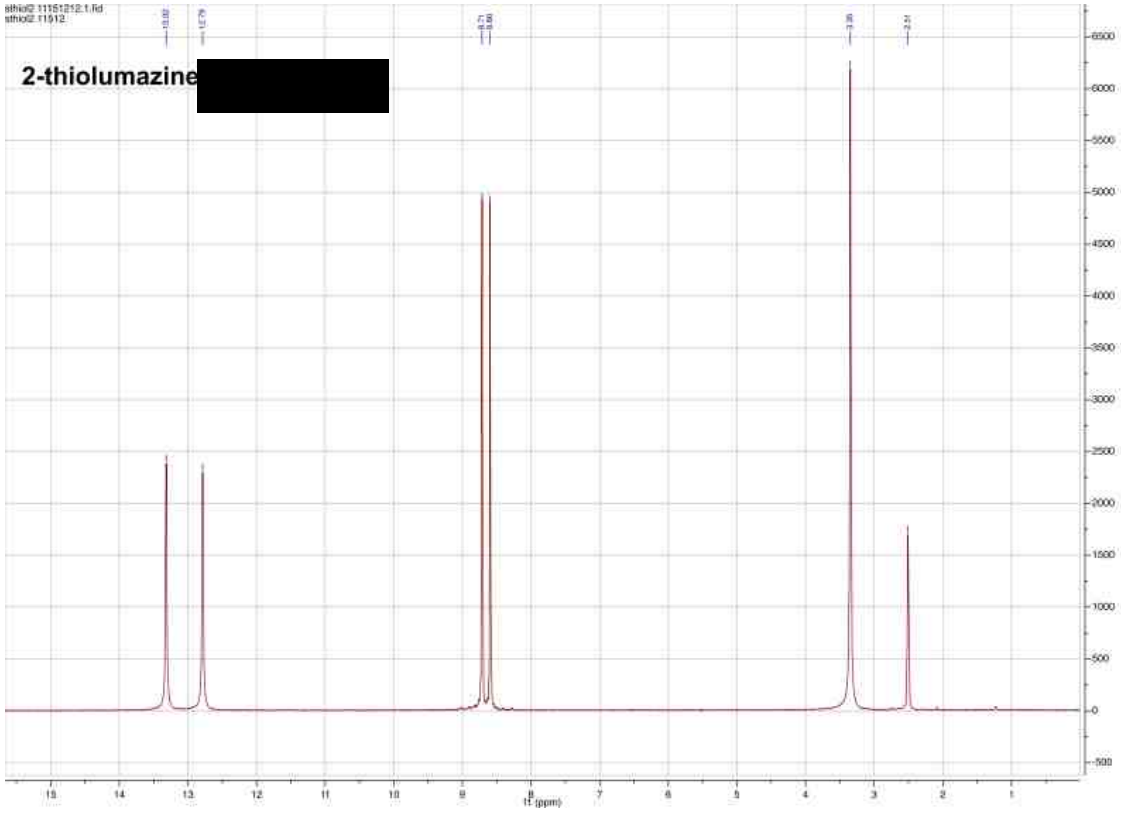
2-thiolumazine
[redacted]

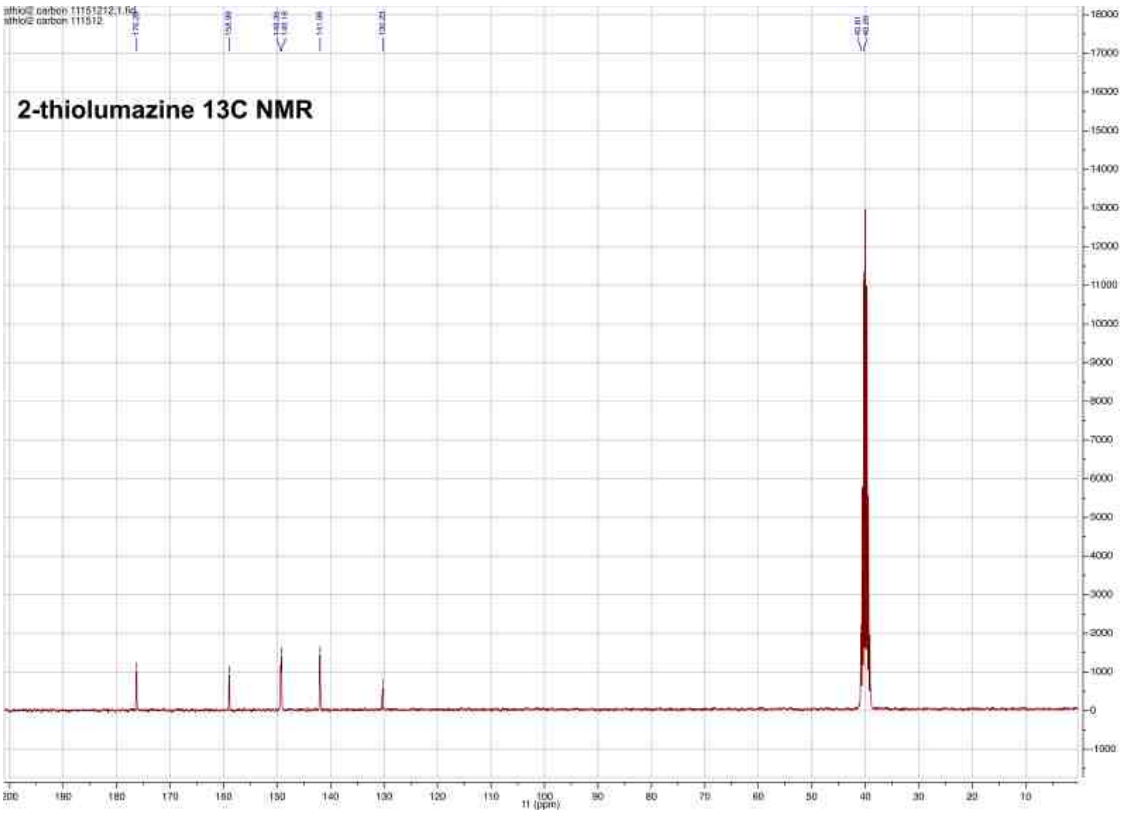
2-thiolumazine 13C NMR
f1 (ppm)

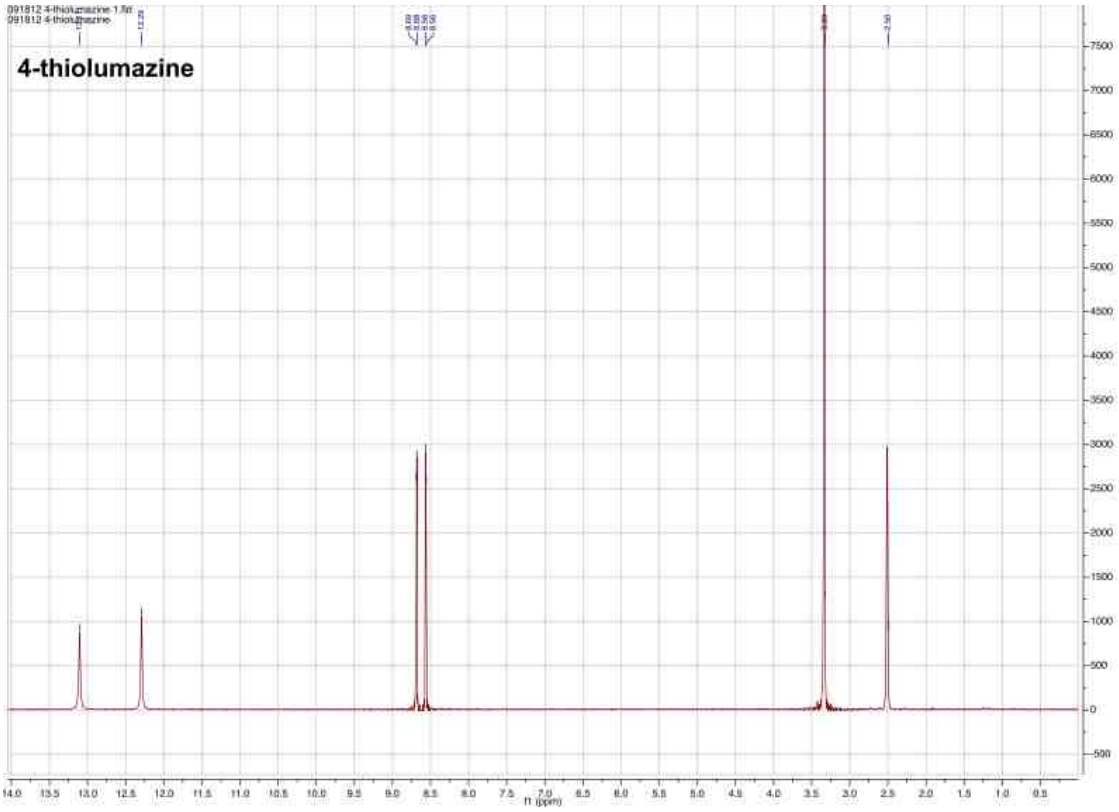
4-thiolumazine
f1 (ppm)

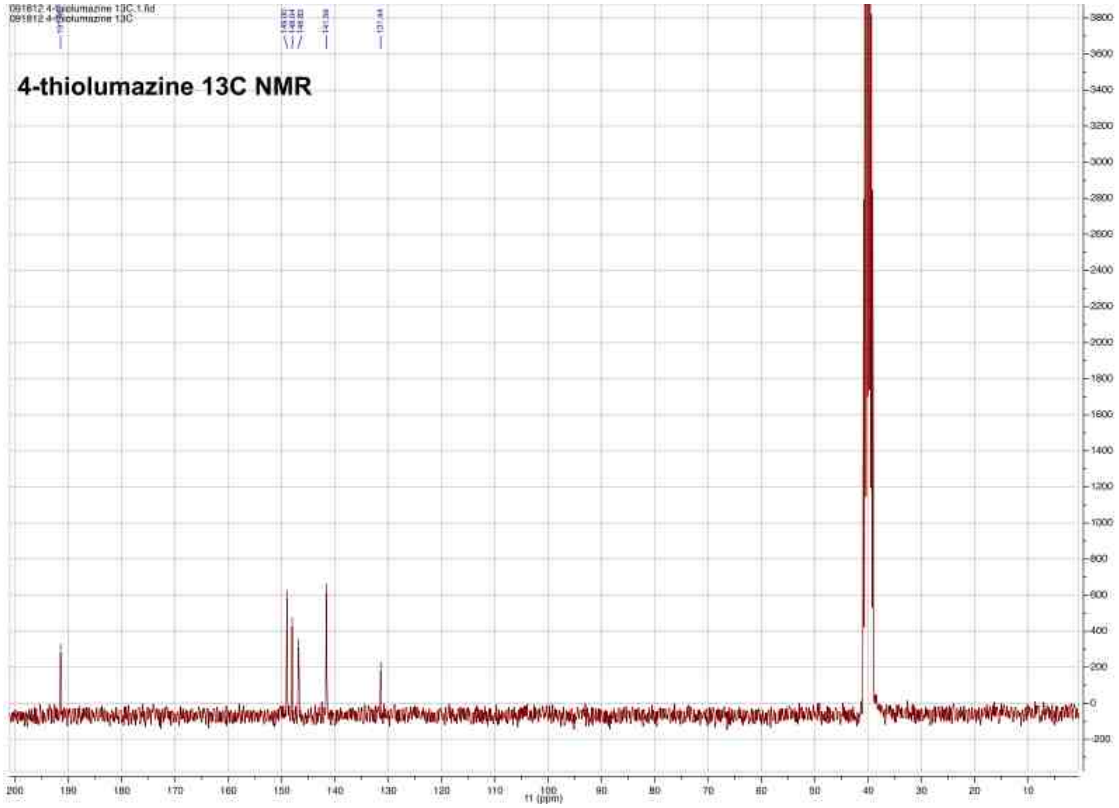
4-thiolumazine 13C NMR
f1 (ppm)

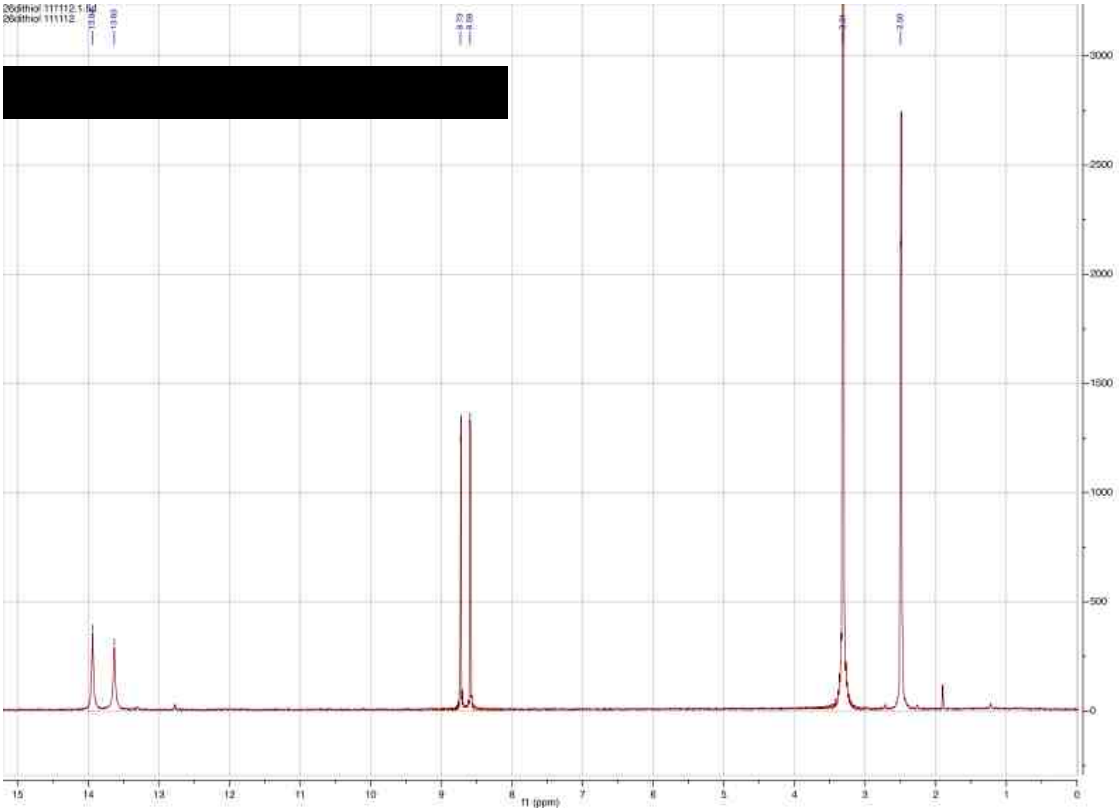
f1 (ppm)

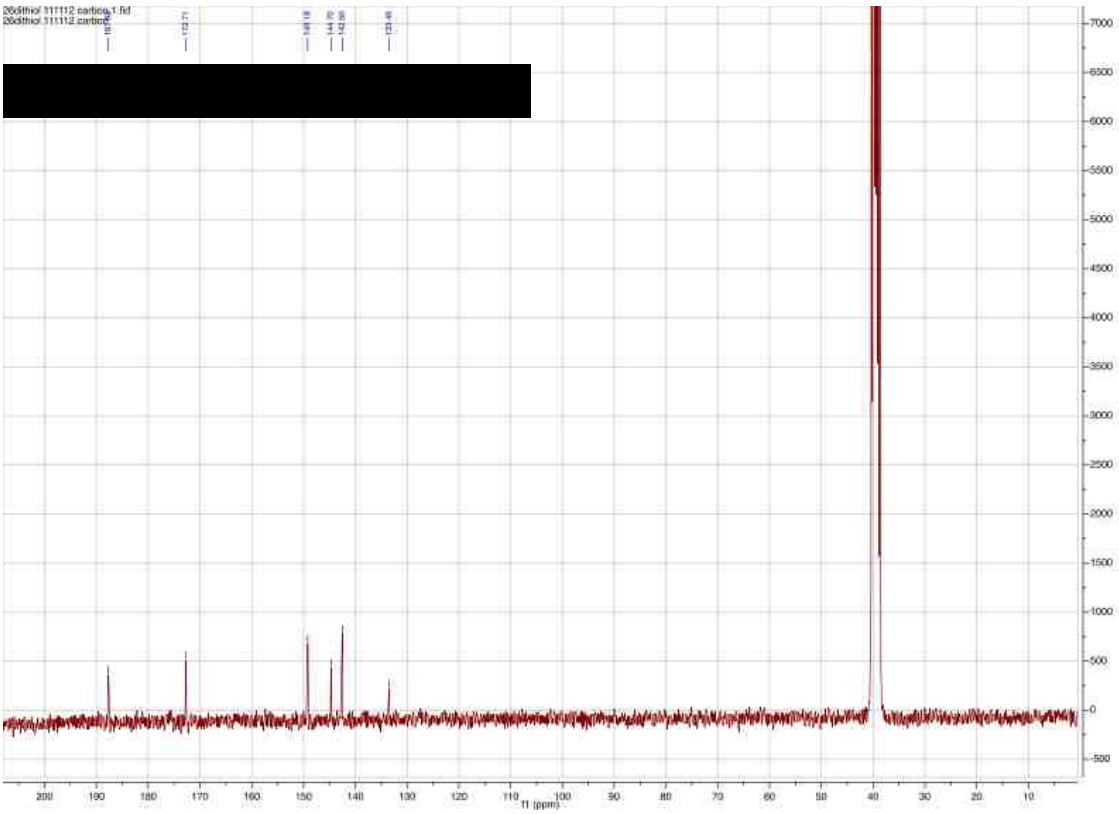
26d8thiol 111112 carbon_1.fid
26d8thiol 111112 carbon
168.57
172.71
149.18
144.70
142.99
133.48
[redacted]
7000
6500
6000
5500
5000
4500
4000
3500
3000
2500
2000
1500
1000
500
0
-500
200
190
180
170
160
150
140
130
120
110
100
90
80
70
60
50
40
30
20
10
f1 (ppm)

5.1.2 FYX051 and FYX051C

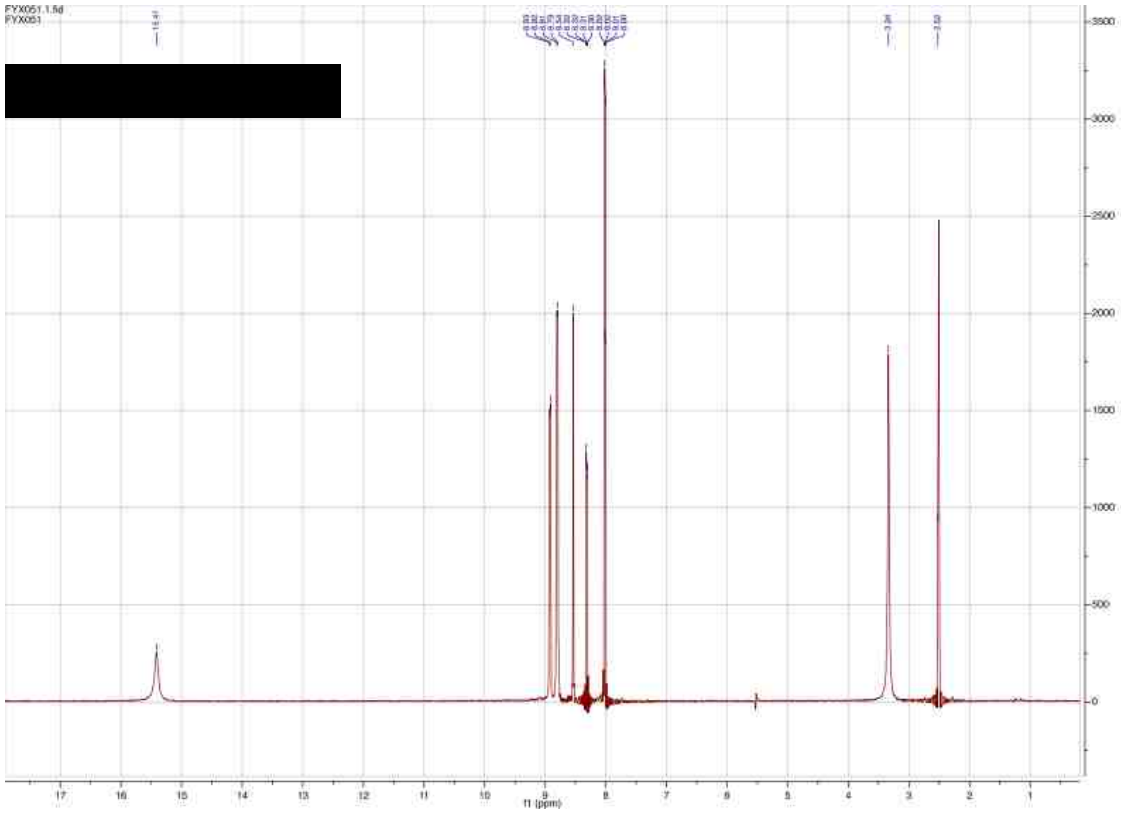

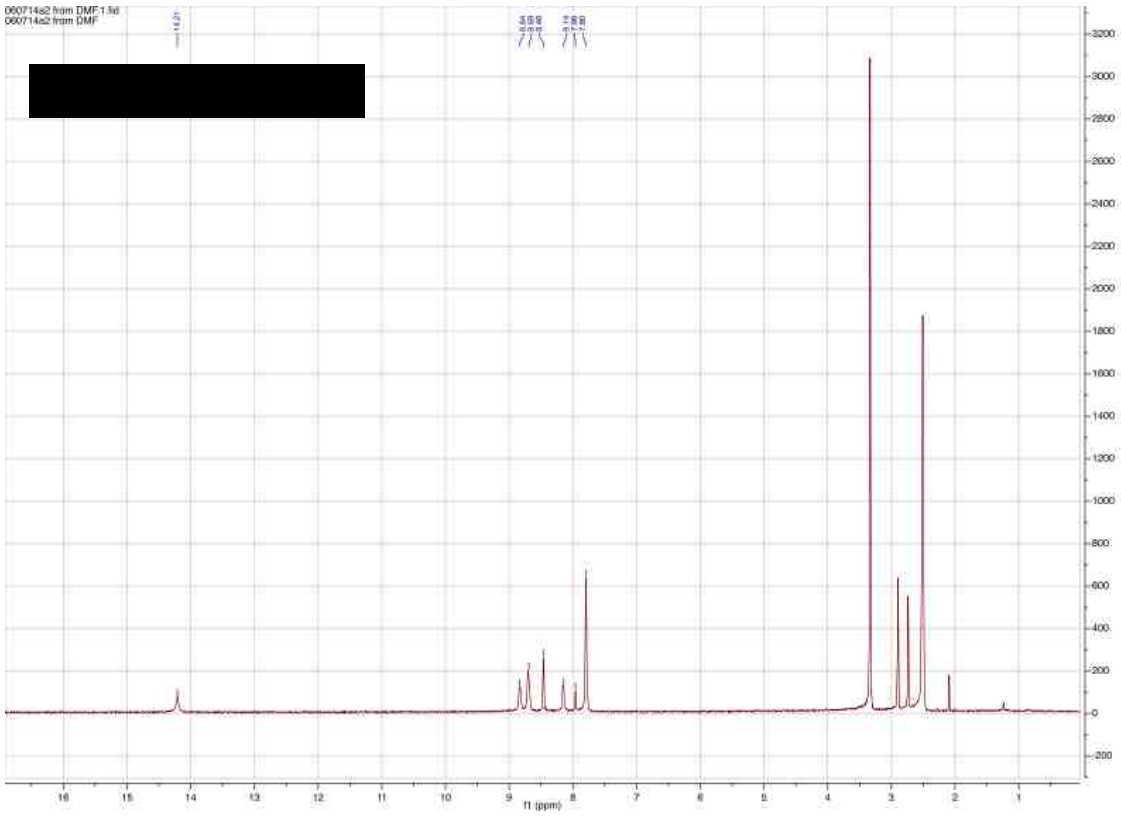
060714s2 from DMF.1.fid
060714s2 from DMF
[redacted]
f1 (ppm)

5.1.3 sba dimer

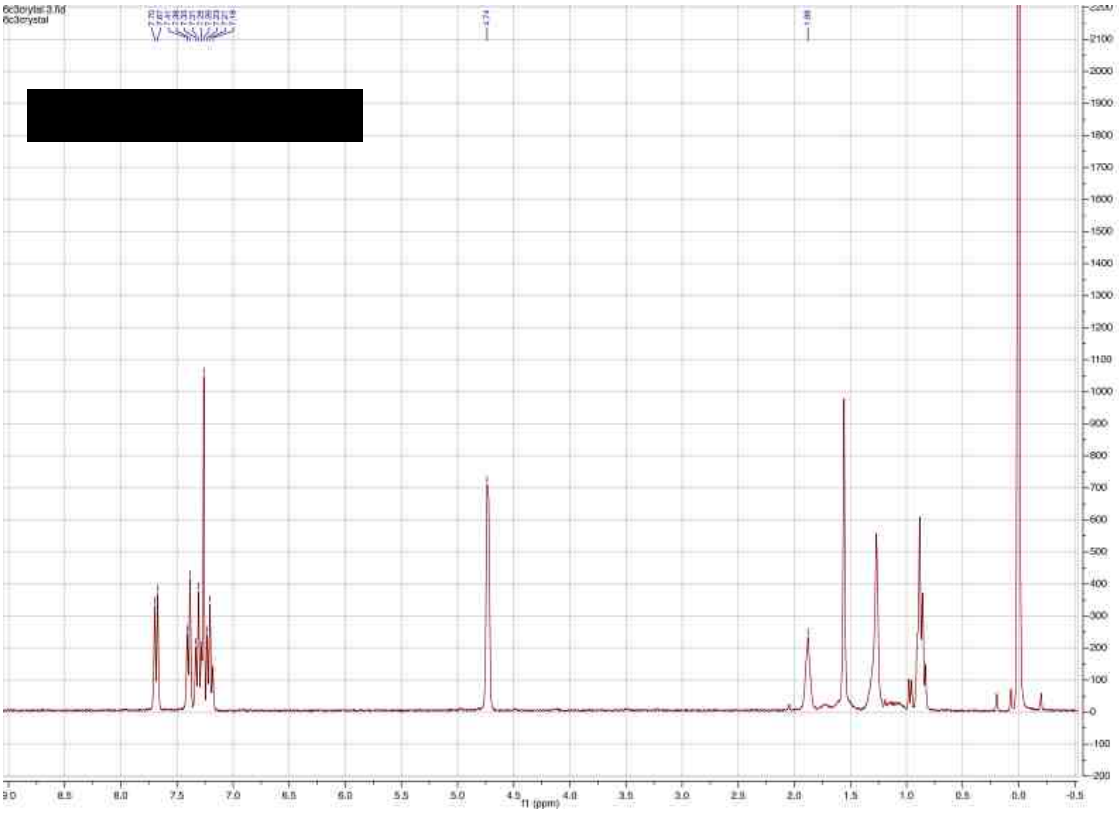

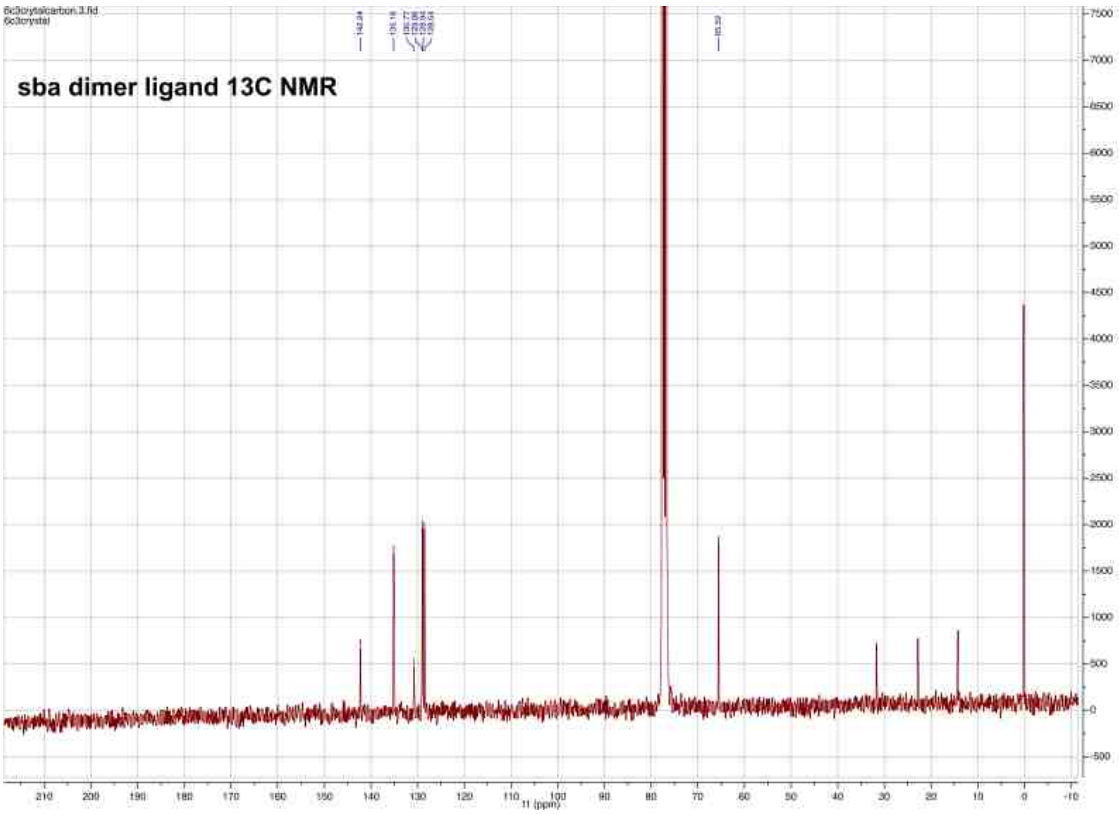
sba dimer ligand 13C NMR
142.84
135.19
130.77
130.66
129.94
128.64
85.33
f1 (ppm)

5.2 Appendix B: Mass Spectra

5.2.1 Lumazine Derivatives

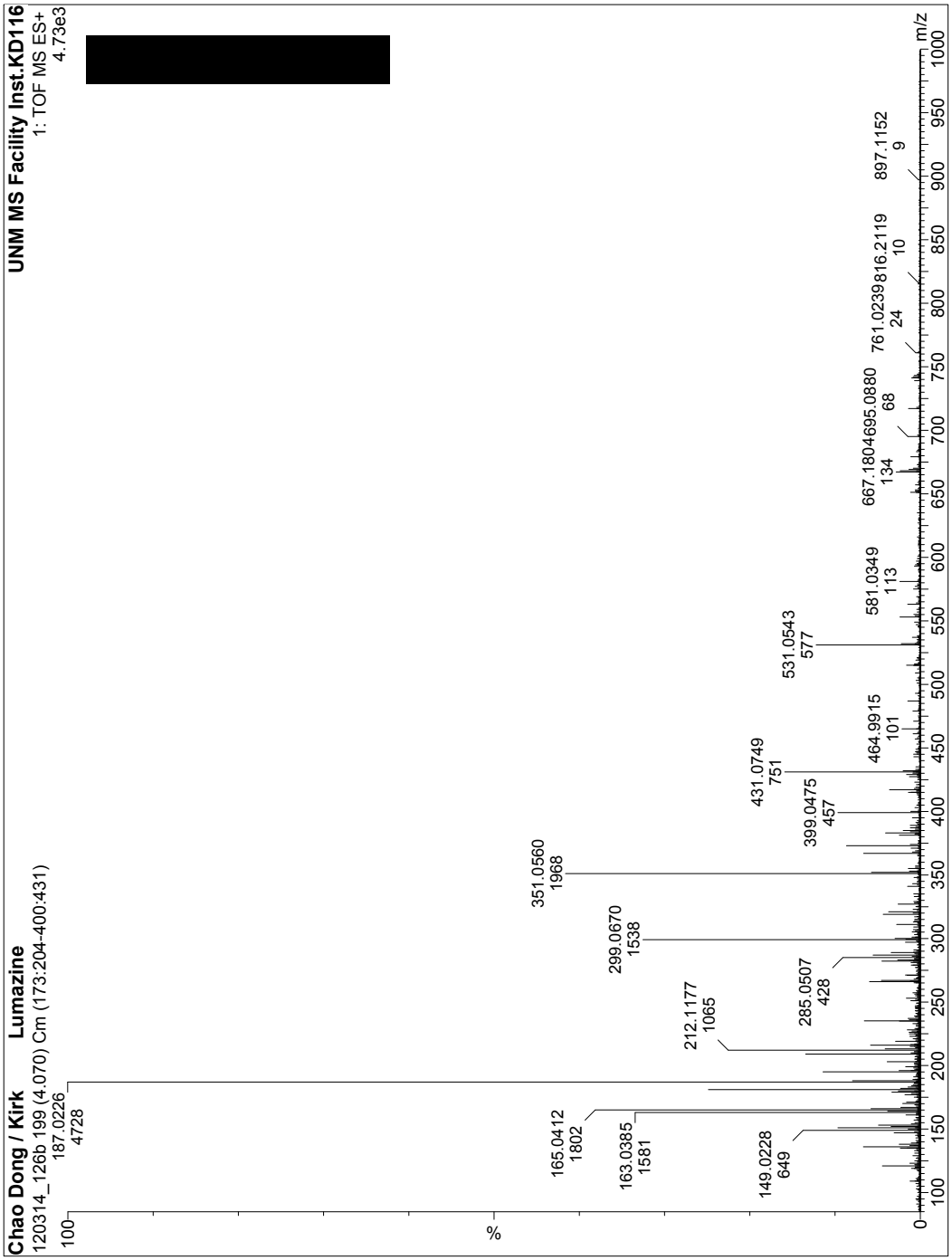

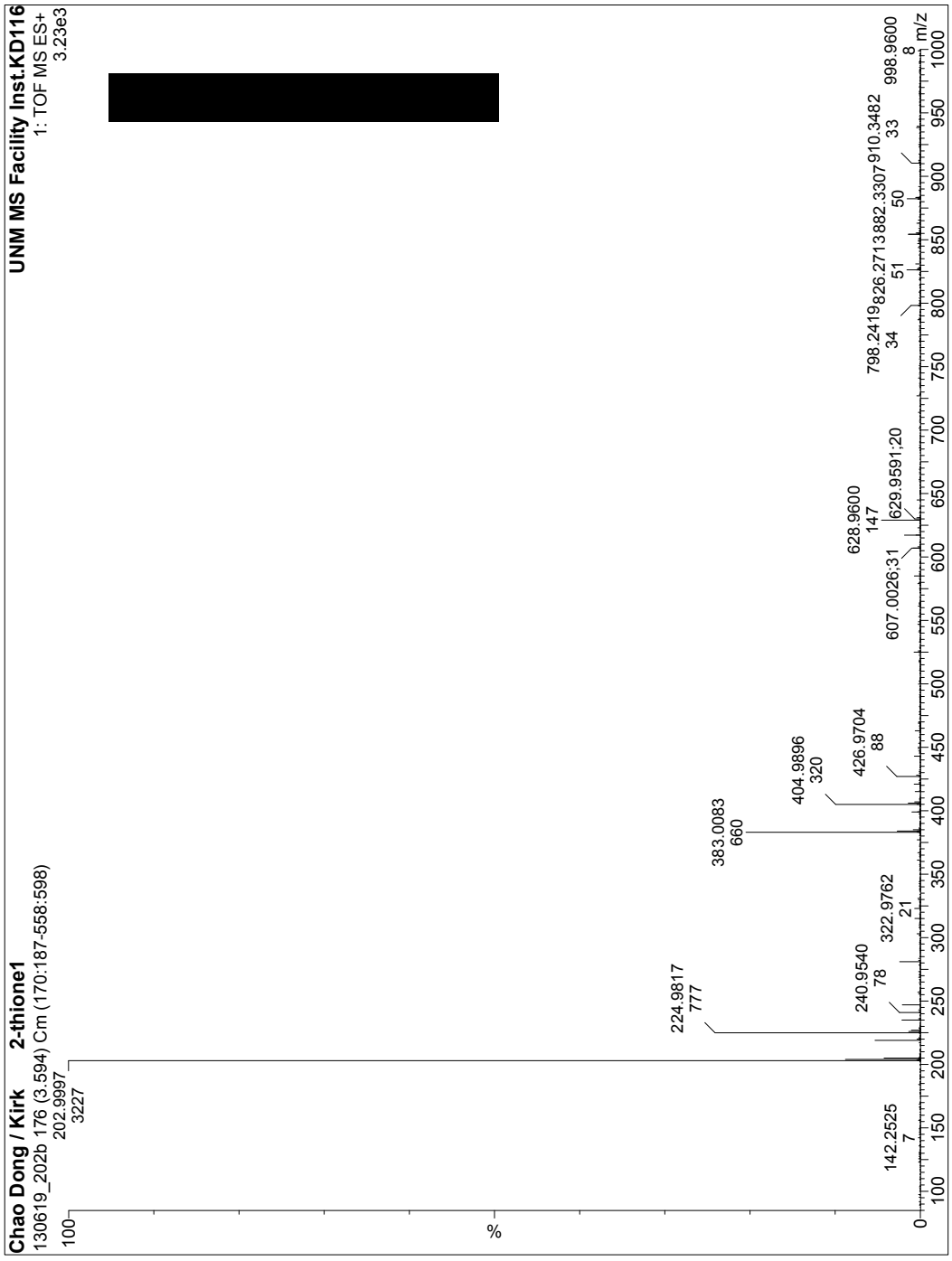
Chao Dong / Kirk 2-thione1
130619_202b 176 (3.594) Cm (170:187-558:598)
UNM MS Facility Inst.KD116
1: TOF MS ES+
3.23e3
100
%
0
202.9997
3227
142.2525
7
224.9817
777
240.9540
78
322.9762
21
383.0083
660
404.9896
320
426.9704
88
607.0026;31
628.9600
147
629.9591;20
798.2419
34
826.2713
51
882.3307
50
910.3482
33
998.9600
8
100 150 200 250 300 350 400 450 500 550 600 650 700 750 800 850 900 950 1000 m/z

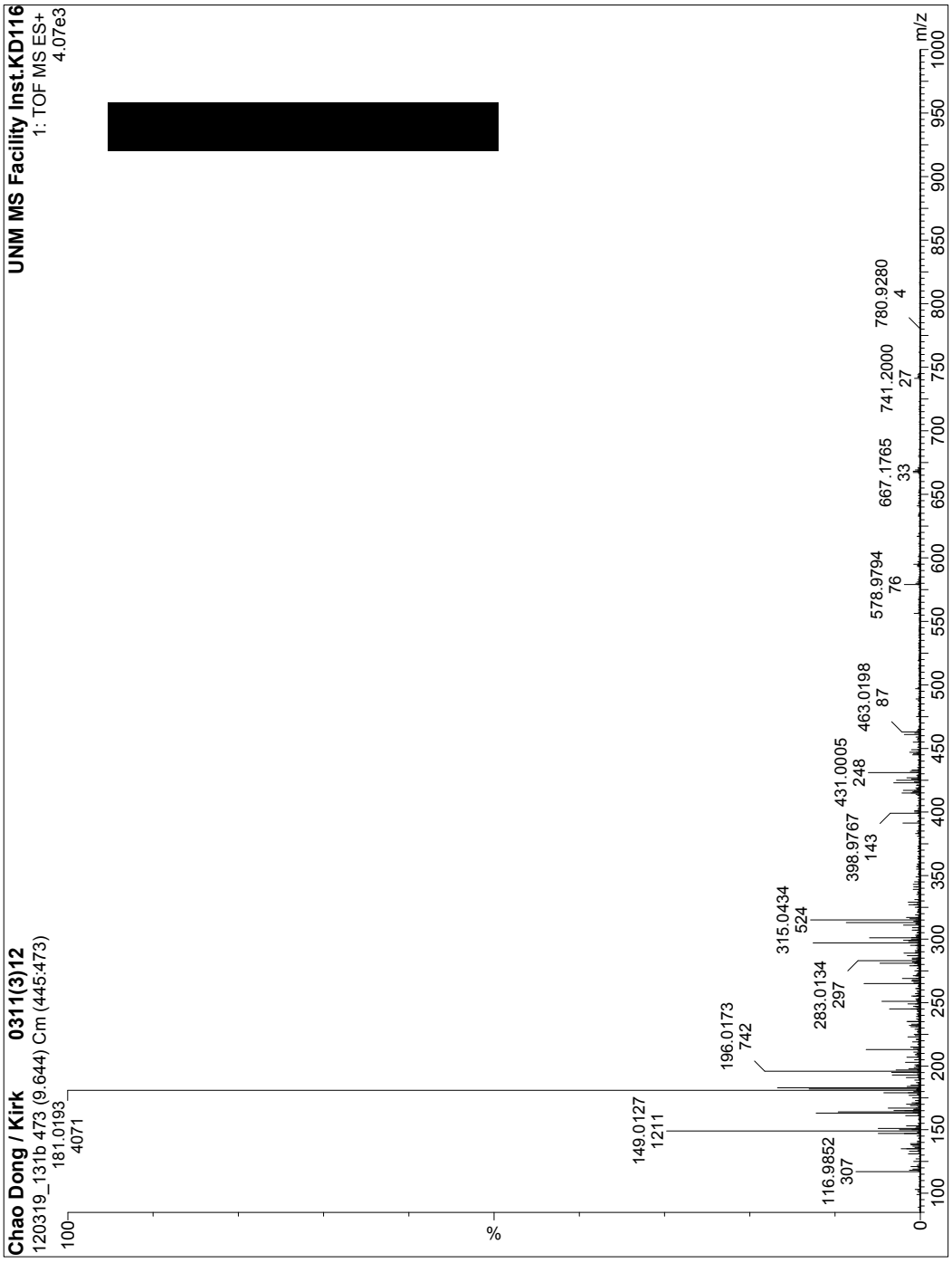
Chao Dong / Kirk 0311(3)12
120319_131b 473 (9.644) Cm (445:473)
181.0193
4071
149.0127
1211
196.0173
742
116.9852
307
283.0134
297
315.0434
524
398.9767
143
431.0005
248
463.0198
87
578.9794
76
667.1765
33
741.2000
27
780.9280
4
UNM MS Facility Inst.KD116
1: TOF MS ES+
4.07e3
100
%
0
100
150
200
250
300
350
400
450
500
550
600
650
700
750
800
850
900
950
1000
m/z

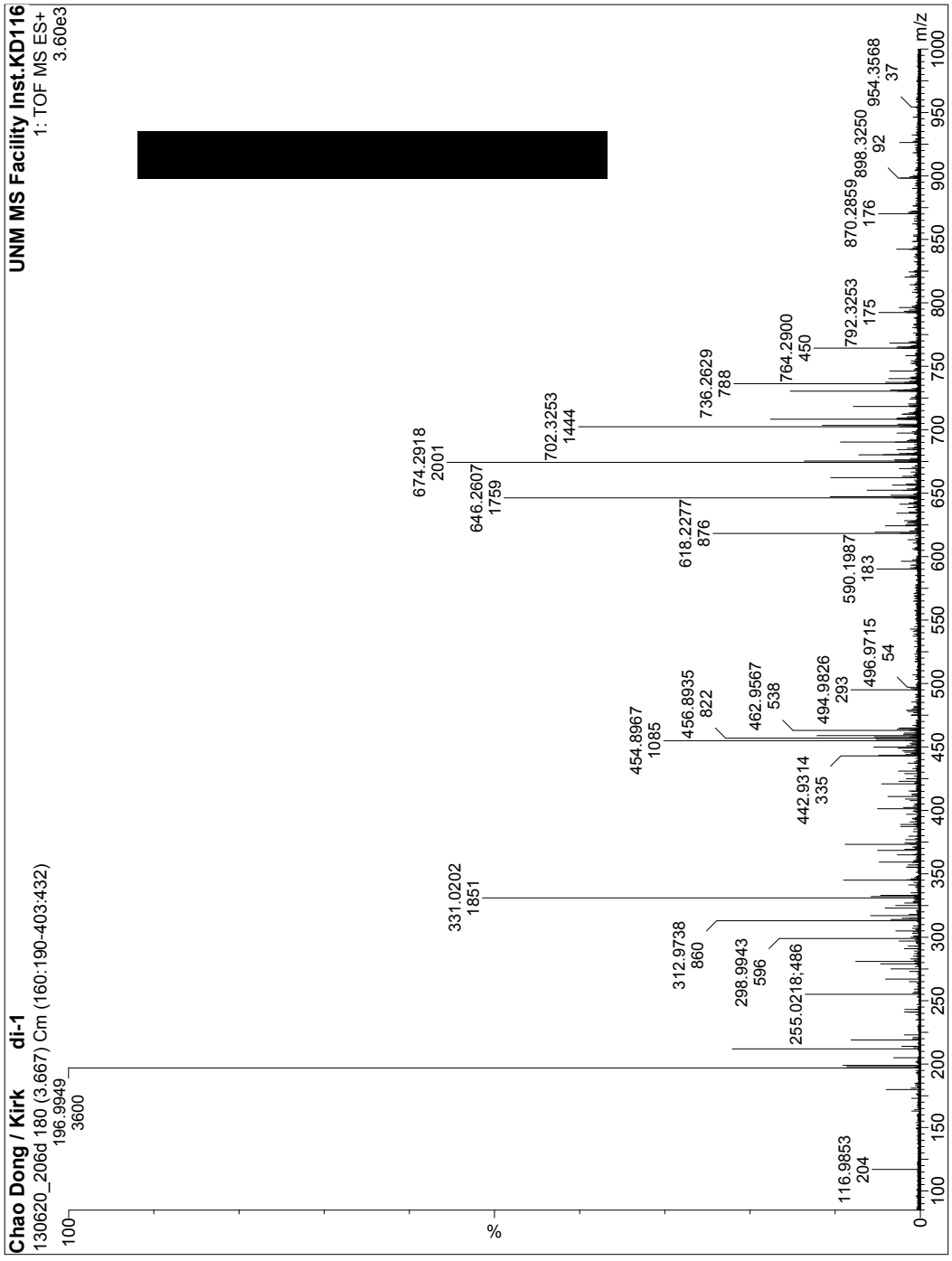
UNM MS Facility Inst.KD116
Chao Dong / Kirk di-1
130620_206d 180 (3.667) Cm (160:190-403:432)
1: TOF MS ES+
3.60e3
100
%
0
m/z
196.9949
3600
116.9853
204
255.0218;486
298.9943
596
312.9738
860
331.0202
1851
442.9314
335
454.8967
1085
456.8935
822
462.9567
538
494.9826
293
496.9715
54
590.1987
183
618.2277
876
646.2607
1759
674.2918
2001
702.3253
1444
736.2629
788
764.2900
450
792.3253
175
870.2859
176
898.3250
92
954.3568
37

5.2.2 FYX051 and FYX051C

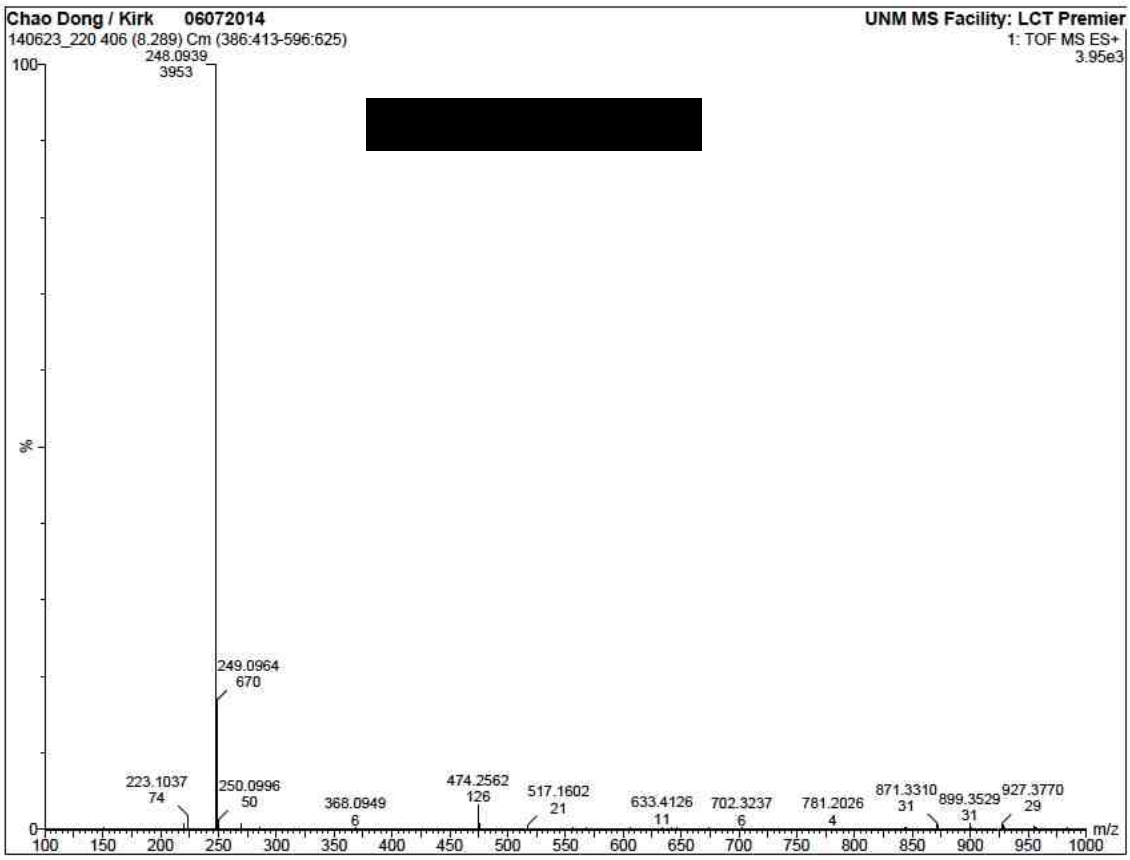

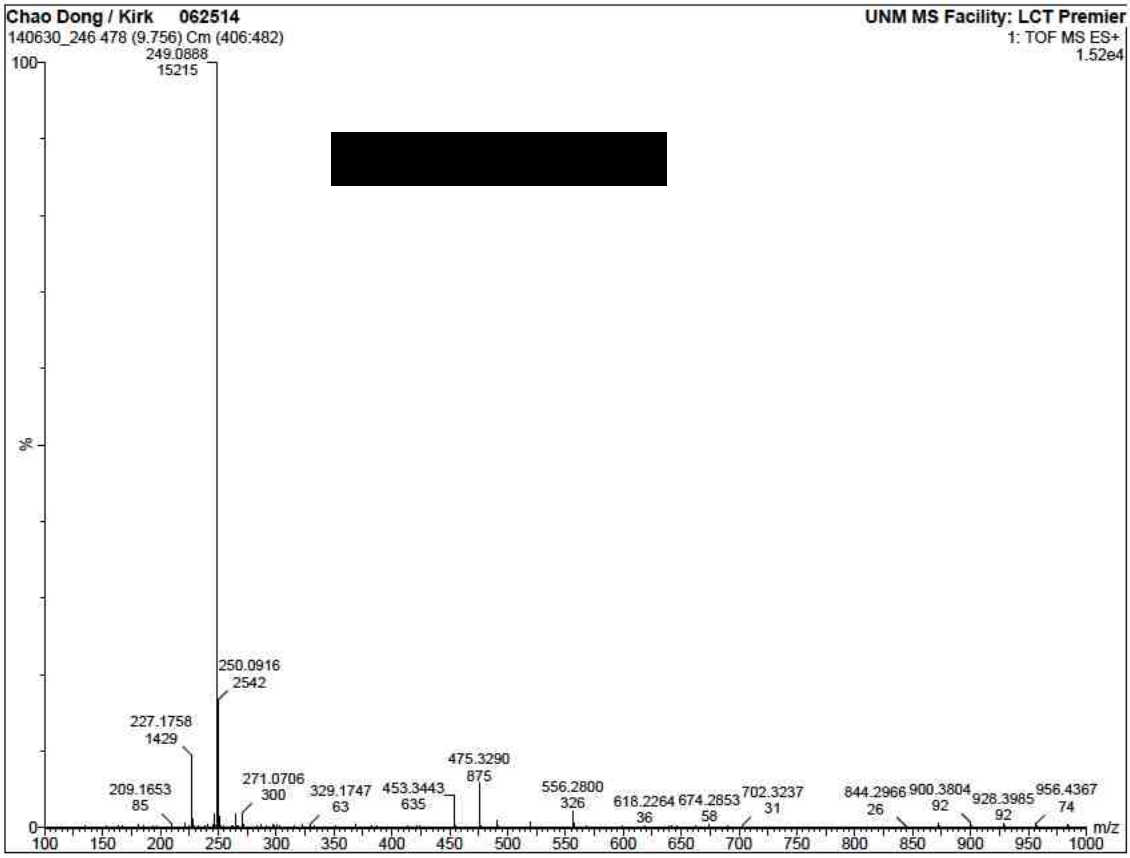

5.2.3 sba dimer, Tp*MoO(hba), Tp*MoO(mba) and Tp*MoO(sba)

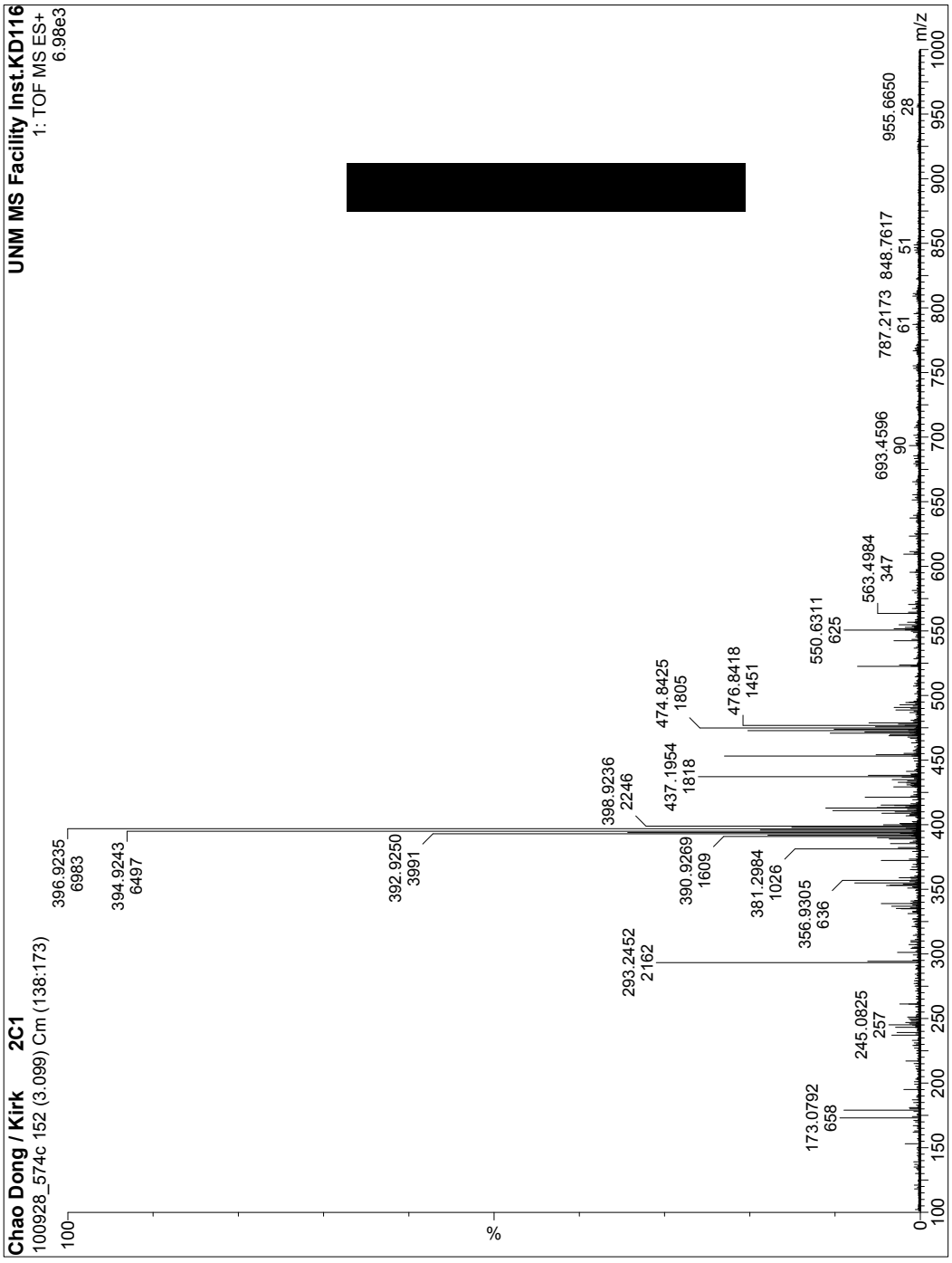
Chao Dong / Kirk 2C1
100928_574c 152 (3.099) Cm (138:173)
UNM MS Facility Inst.KD116
1: TOF MS ES+
6.98e3
100
%
0
100 150 200 250 300 350 400 450 500 550 600 650 700 750 800 850 900 950 1000
m/z
396.9235 6983
394.9243 6497
392.9250 3991
398.9236 2246
437.1954 1818
474.8425 1805
476.8418 1451
550.6311 625
563.4984 347
693.4596 90
787.2173 61
848.7617 51
955.6650 28
390.9269 1609
381.2984 1026
356.9305 636
293.2452 2162
245.0825 257
173.0792 658

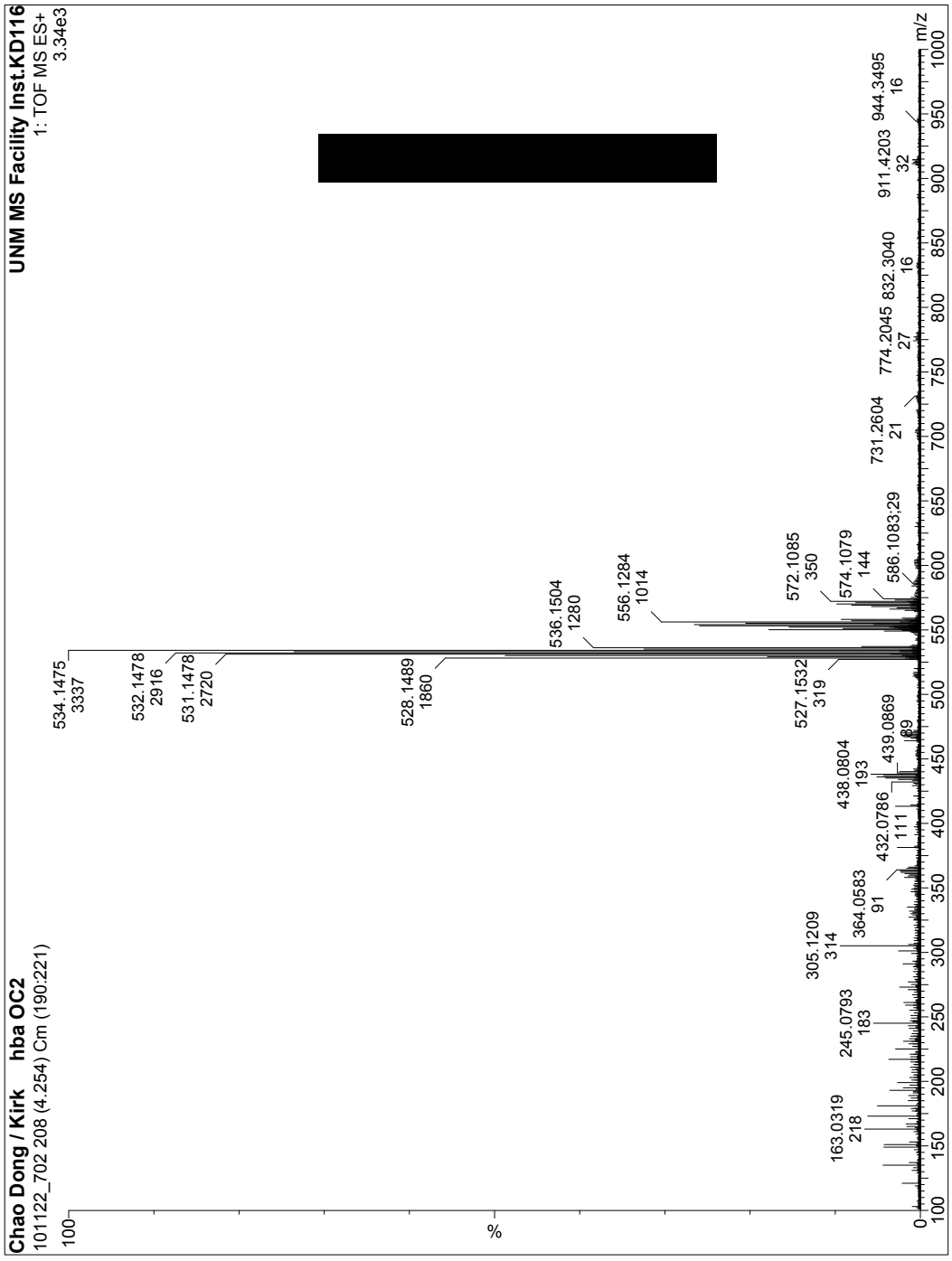
UNM MS Facility Inst.KD116
1: TOF MS ES+
3.34e3
Chao Dong / Kirk hba OC2
101122_702 208 (4.254) Cm (190:221)
100
%
0
100
150
200
250
300
350
400
450
500
550
600
650
700
750
800
850
900
950
1000
m/z
534.1475
3337
532.1478
2916
531.1478
2720
528.1489
1860
536.1504
1280
556.1284
1014
572.1085
350
574.1079
144
586.1083;29
731.2604
21
774.2045
27
832.3040
16
911.4203
32
944.3495
16
527.1532
319
439.0869
89
438.0804
193
432.0786
111
364.0583
91
305.1209
314
245.0793
183
163.0319
218

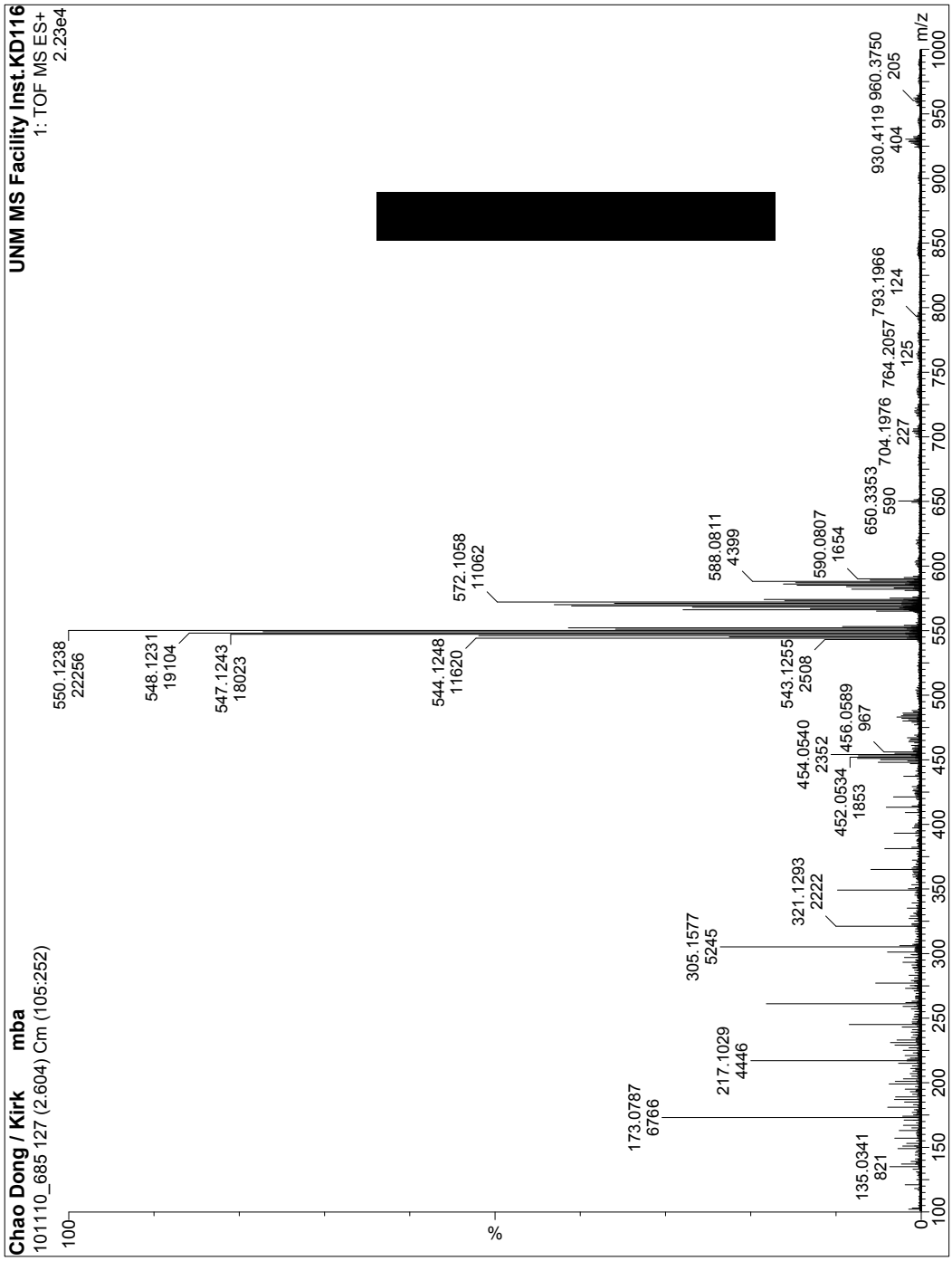
UNM MS Facility Inst.KD116
1: TOF MS ES+
2.23e4
Chao Dong / Kirk mba
101110_685 127 (2.604) Cm (105:252)
100
%
0
m/z
550.1238 22256
548.1231 19104
547.1243 18023
544.1248 11620
572.1058 11062
543.1255 2508
588.0811 4399
590.0807 1654
650.3353 590
704.1976 227
764.2057 125
793.1966 124
930.4119 404
960.3750 205
454.0540 2352
456.0589 967
452.0534 1853
321.1293 2222
305.1577 5245
217.1029 4446
173.0787 6766
135.0341 821

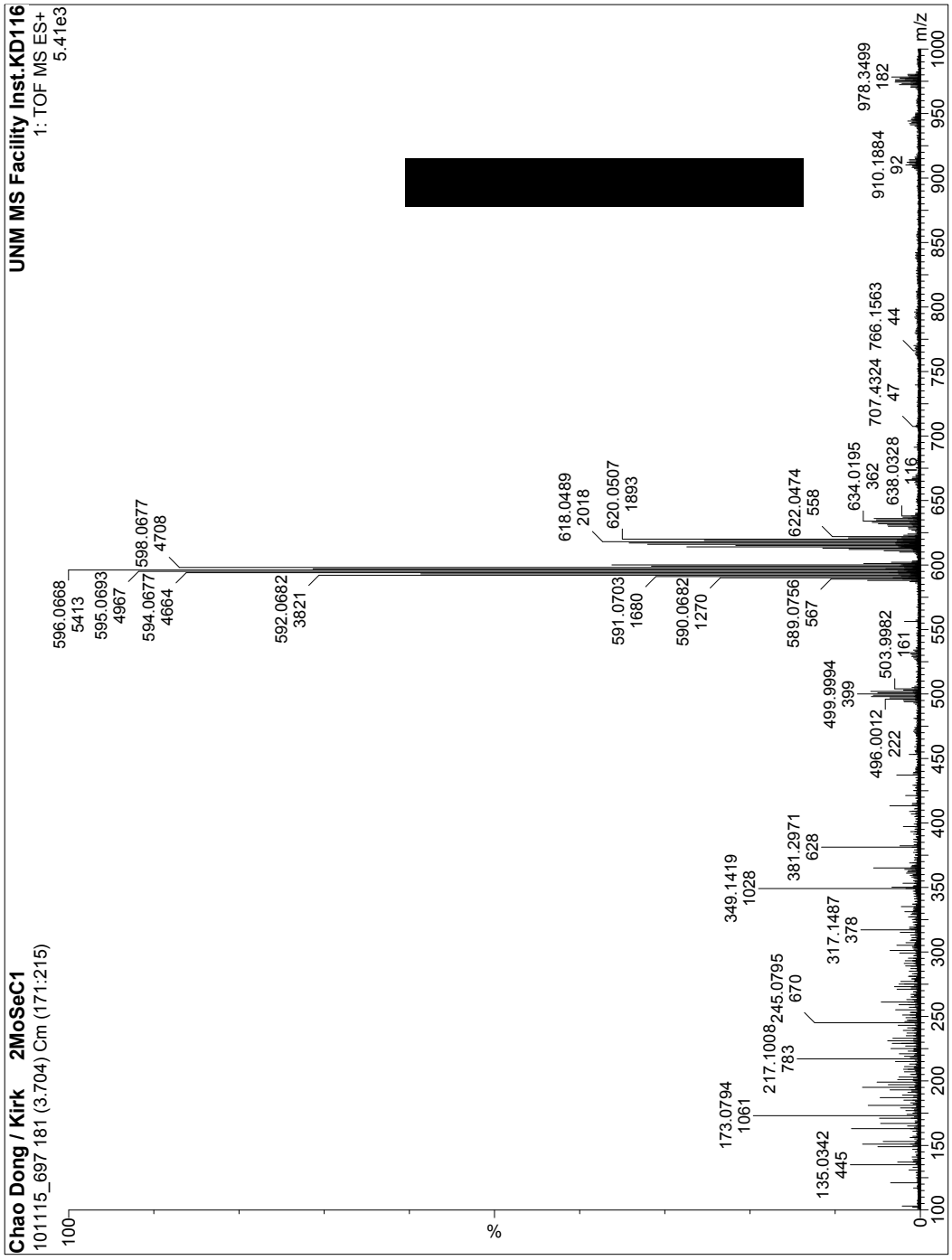
Chao Dong / Kirk 2MoSeC1
101115_697 181 (3.704) Cm (171:215)
UNM MS Facility Inst.KD116
1: TOF MS ES+
5.41e3
100
%
0
596.0668 5413
595.0693 4967
594.0677 4664
598.0677 4708
592.0682 3821
618.0489 2018
620.0507 1893
591.0703 1680
590.0682 1270
622.0474 558
589.0756 567
634.0195 362
638.0328 116
707.4324 47
766.1563 44
910.1884 92
978.3499 182
503.9982 161
499.9994 399
496.0012 222
381.2971 628
349.1419 1028
317.1487 378
245.0795 670
217.1008 783
173.0794 1061
135.0342 445
100 150 200 250 300 350 400 450 500 550 600 650 700 750 800 850 900 950 1000
m/z